NASA CR-120936

R-8973-2

(NASA-CR-120936) SPACE STORABLE PROPELLANT PERFORMANCE PROGRAM COAXIAL INJECTOR CHARACTERIZATION R.J. Burick (Rocketdyne) Oct. 1972 223 p CSCL 21I

N72-33731

Unclas
G3/27 44254

SPACE STORABLE PROPELLANT PERFORMANCE PROGRAM
COAXIAL INJECTOR CHARACTERIZATION

by

R. J. Burick

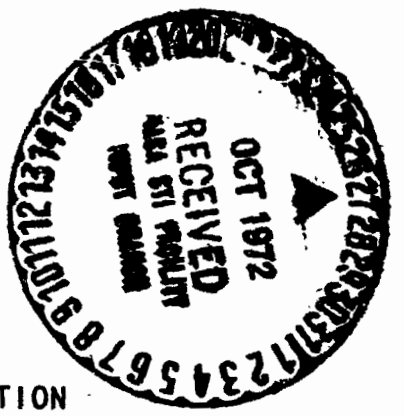

ROCKETDYNE
A DIVISION OF NORTH AMERICAN ROCKWELL CORPORATION
6633 CANOGA AVENUE, CANOGA PARK, CALIFORNIA

prepared for

NATIONAL AERONAUTICS AND SPACE ADMINISTRATION

NASA-Lewis Research Center
NAS3-12051
Larry H. Gordon, Project Manager

FOREWORD

The work described herein was conducted for NASA-Lewis Research Center, Cleveland, Ohio, by the Advanced Programs Department, Rocketdyne, a division of North American Rockwell Corporation. The study was performed in accordance with Contract NAS3-12051, Rocketdyne G. O. 09222.

This report (R-8973-2), which covers primarily the coaxial injector characterization portion of the contract, is one of three reports on the subject contract:

R-8973-1 - Like-Doublet Injector Characterization

- R-8973-2 - Coaxial Injector Characterization

R-8973-3 - Design Manual for Both Injector Types

Mr. L. H. Gordon on the Lewis Research Center served as NASA Technical Project Manager. The Rocketdyne Program Manager was Mr. H. G. Diem. Technical guidance of the program was provided by Mr. S. D. Clapp and Dr. D. T. Campbell.

Rocketdyne personnel contributing to the technical portion of the program were A. Y. Falk, J. T. Sabol, D. Zwald, D. Hemperly, R. Stitt, and R. Barnsdale.

CONTENTS

ABSTRACT

An experimental program was conducted to characterize the circular coaxial injector concept for application with the space storable gas/liquid propellant combination FLOX(82.6% F_2)/CH_4(g) at high pressure. The primary goal of the program was to obtain high characteristic velocity efficiency ($\eta_{C^*} \geq 99$ percent) in conjunction with acceptable injector/chamber compatibility.

A series of subscale (single-element) cold-flow and hot-fire experiments was employed to establish design criteria for a 3000-lbf (sea level) engine operating at 500 psia. The subscale experiments characterized both high performance "core" elements and "peripheral" elements with enhanced injector/chamber compatibility.

The full-scale injector which evolved from the study demonstrated a performance level of 99 percent of the theoretical shifting characteristic exhaust velocity with low chamber heat flux levels. At the design condition (P_C = 500 psia), measured heat flux levels were approximately 2 to 3 Btu/in.^{2}-sec in the cylindrical chamber. The injector demonstrated dynamic stability by exhibiting a 15-millisecond recovery to an induced 1100-psi chamber overpressure pulse.

A 44-second-duration firing demonstrated the durability of the injector. Performance during the test ($P_C \approx 500$ psia) varied between 98 and 100 percent of theoretical c*. The steady-state injector face temperature was approximately 50 F. The FLOX and CH_4(g) were supplied at LN_2 (-310 F) and ambient (70 F) temperatures, respectively.

Parametric data are presented that are applicable for the design of circular, coaxial injectors that operate with injection dynamics (fuel and oxidizer velocity, etc.) similar to those employed in the work reported herein.

ILLUSTRATIONS

TABLES

1.0 SUMMARY

Presented herein are the results of an experimental program to characterize circular coaxial injector concepts for high-pressure FLOX/CH_4(g) application. To establish design criteria for a full-scale injector, cold-flow and hot-fire experiments were conducted with single-element models.

Cold-flow experiments were employed to investigate the element geometric and operating variables with the intent of maximizing element performance. The use of cold-flow techniques permitted systematic variation of the controlling variables; a similar approach employing hot-firing techniques would have been prohibitively expensive.

The performance levels of the elements were based on the assumption that overall c* performance was the product or a mixing-limited efficiency, $\eta_{c^*,mix}$, and a vaporization-limited efficiency, $\eta_{c^*,vap}$. Cold-flow mixing data were employed in conjunction with a multi-streamtube mixing model as a measure of $\eta_{c^*,mix}$ whereas the results of the atomization experiments were utilized as input data for a computerized combustion model for the determination of $\eta_{c^*,vap}$.

Experiments were conducted with recessed oxidizer post configurations which were intended for use in the inner "core" region of the full-scale injector. Two types of chamber compatibility configurations were characterized for use in the "peripheral" zone of the full-scale injector. These were a boundary layer coolant (BLC) model and a scarfed post with oxidizer swirl configuration.

Mixing experiments conducted with the "core" configurations showed that the element mixing levels expressed as the Rupe mixing factor, E_M, was a function of the parameter:

$$E_M = f\left[(\rho_g V_g)^2/(MR \cdot V_L)\right]$$

where

ρ_g = the gas phase density
V_g = the fuel velocity in the element annuli
MR = the injected mixture ratio (o/f)
V_L = the liquid injection velocity

The "core" atomization data was correlated as:

$$\bar{D}/D_L = f\left[(V_g - V_L)/MR \cdot V_L)\right]$$

where

$\bar{D}$ = the mass medium drop size
D_L = the diameter of the liquid jet

Cold-flow mixing experiments revealed that the two "peripheral" configurations possessed distinctly different wall region mass and mixture ratio distribution. The BLC configuration produced low wall zone mixture ratio (MR < MR injected) accompanied by high wall zone mass flux. The scarfed post element produced high wall zone mixture ratios (MR > MR injected) with low wall zone mass flux. Single-element hot-fire experiments conducted with both configurations showed that the BLC element with a low mixture ratio, high mass flux wall region resulted in lower chamber wall heat flux levels.

Single-element hot-fire tests conducted with the "core" elements were employed to substantiate the cold-flow data and to investigate combustion effects such as oxidizer post burning. Tests with post-recess values up to 3 liquid jet diameters (≈0.40 in.) resulted in no oxidizer post burning. The performance results from these tests were in essential agreement with the cold-flow data which showed little performance improvement with post recess. Maximum performance with the "core" single-element model was 92 percent of theoretical c* in a 40 in L* chamber.

The results of the single-element cold-flow/hot-fire study were utilized to configure a 3000-pound full-scale injector. Recessed (0.204 in.) oxidizer post elements were utilized in the "core" region of the injector and the BLC element in the peripheral zone. The injector was tested in a 40-in. L* graphite chamber which was instrumented to determine local values of chamber wall heat flux.

The performance level of the 3000-pound full-scale injector was 99 percent of theoretical c* at the design condition (P_c = 500 psia, MR = 5.25, no BLC). Parametric tests conducted with varying amounts of boundary layer coolant (BLC) showed a 1-percent reduction in performance with approximately 6 percent of the total methane flow as BLC. Increased BLC flowrate resulted in lower overall chamber heat load (approximately 50-percent reduction with 9 percent of the total fuel flow as BLC); however, with no BLC, average chamber heat flux (averaged from injector to start of nozzle convergence) was only 2.29 Btu/in.^{2}-sec. Average chamber wall heat flux rates measured in the full-scale studies were nearly equivalent to those measured in the single-element hot-firings.

Throttling tests conducted over a 5:1 range resulted in reduced performance levels (≈4 percent) when no BLC was employed, but performance was nearly independent of throttling when BLC was used. Throttling to 100 psia revealed no instabilities discernible by the available instrumentation.

The full-scale injector was tested for dynamic stability by subjecting the injector to an 1100-psi overpressure. Recovery to normal operation was achieved in approximatley 15 milliseconds.

A 44-second duration test was conducted to ascertain the durability of the full-scale injector. Performance during the test varied from 98 to 100 percent of theoretical shifting c*. The test was conducted in a graphite-lined thrust chamber which exhibited almost no chamber erosion from the duration firing. Nozzle throat area erosion was only 0.75 percent. Posttest inspection of the injector revealed no damage of any kind. Injector face temperature (≈50 F steady-state) during the test showed that injector face cooling is not required. Thus, the full-scale injector met the primary program goals of a dynamically stable high-performance injector with acceptable injector-chamber compatibility.

2.0 INTRODUCTION

The work presented herein is the result of an 18-month program of analysis, design, and experiments to evaluate the coaxial injector concept for high performance space storable rocket engine applications. The present work marks the fourth, in a sequence of applied research programs at Rocketdyne to establish design criteria for high performance gas/liquid propulsion systems (Ref. 1 through 3). In this work, the specific space storable propellants were liquid FLOX (82.6% F_2, 17.4% O_2) and gaseous methane (CH_4) with a design chamber pressure of 500 psia.

The effort of the subject program (NAS3-12051) involved the study of two injector types. The initial effort was concerned with characterizing the self-impinging (like-doublet) injector concept for FLOX/CH_4(g) propellants. The results of that study are reported in a separate volume (Ref. 4). An add-on effort was initiated in July 1970 to characterize circular coaxial injector concepts, and the results of that study are reported herein.

The primary object of the coaxial injector add-on effort was to provide supporting technology for the FLOX/CH_4 breadboard engine. In addition to providing basic technology, an injector design evolved from the program which possibly could have been utilized with modifications as a flight weight configuration.

In general, coaxial injector concepts consist of a central liquid (usually oxidizer) jet which is surrounded by an annulus of high-velocity gas (usually fuel). In this study both the geometric and operating variables of the coaxial element were systematically investigated to determine their effect on the performance and chamber wall heat flux characteristics of the element.

These results complement the findings of NAS3-12001 (Ref. 3) wherein large-thrust-per-element (≈2000 lbf) circular coaxial elements were characterized for space storable propellant application. The present study was concerned with injectors having thrust-per-element values on the order of 70 lbf.

The nominal design ground rules for the program are shown in Table I.

TABLE I. SYSTEM DESIGN GUIDELINES

Propellants	Gaseous Methane/Liquid FLOX (82.6% F_2)
Propellant Temperatures	Ambient Methane, FLOX at LN_2 (-320F)
Overall Injected Mixture Ratio	5.25 to 5.75
Chamber Pressure (nominal	500 psia
Cylindrical Chamber Contraction Ratio	ϵ_c = 3:1
Chamber L*	40 inches

The major objectives of the work reported herein were to:

1. Design a 3000-lbf (sea level thrust) circular coaxial element injector with a performance goal of 99 percent of the theoretical shifting characteristic exhaust velocity.

2. Configure the injector to provide acceptable injector-chamber wall compatibility.

3. Prove inherent dynamic combustion stability.

4. Establish design criteria which would allow extrapolation to other gas/liquid propellant combinations.

To accomplish the above-listed objectives, a program was established that involved both cold-flow simulation and hot-firing techniques. Previous programs at Rocketdyne have employed an analogous approach to establish design criteria for liquid/liquid systems (Ref. 5 and 6). Therefore, this effort, along with the previously cited work (Ref. 1 through 3), represents a logical extension of these cold-flow/hot-fire techniques to establish design criteria for high performance gas/liquid systems.

As in the referenced programs listed above, the overall characteristic velocity efficiency, η_{c*}, (i.e., performance) was assumed to be represented by the product of a mixing-limited efficiency ($\eta_{c*,\ mix}$) and a vaporization-limited efficiency ($\eta_{c*,vap}$). The two separate effects were investigated by employing cold-flow techniques directed at simulating the hot-fire mixing and atomization processes. The cold-flow mixing data were employed in conjunction with a multi-stream tube mixing model as a measure of hot-fire mixing performance ($\eta_{c*,\ mix}$) whereas the atomization data were used in conjunction with a computerized vaporization limited combustion model to determine hot-fire vaporization efficiency ($\eta_{c*,vap}$).

To investigate chamber wall heat transfer characteristics of candidate elements, cold-flow mixing experiments were conducted to determine wall zone mass and mixture ratio distributions. Previous programs at Rocketdyne have shown that wall zone mass and mixture ratio distributions are the controlling variables for chamber wall heat flux levels (Ref. 7).

Figure 1 presents the general chronological sequence of the major technical phases of the program. As indicated, a single-element cold-flow investigation was employed to characterize the circular gas/liquid coaxial element. These element configurations were grouped into two categories: (1) performance elements intended for ultimate use in an injector inner core, and (2) chamber compatibility elements which would be utilized in the peripheral zone of the injector which is adjacent to the chamber wall. To substantiate and complement the results of the cold-flow investigation, single-element hot-firing experiments were conducted. Single-element hot-firing experiments were deemed to be an essential effort of the program since cold-flow techniques cannot provide information in regard to combustion effects which occur in recessed post coaxial elements. That is, burning within the cup* region of recessed post element can significantly alter the atomization and mixing characteristics of the element due to generation of combustion gases within the confined cup region. In addition, combustion within the cup region can lead to oxidizer post burning effects which cannot be simulated in cold-flow experiments.

*The cup region of a recessed post element is defined as the cylindrical region between the exit of the oxidizer post and the face of the injector.

SPACE STORABLE PROPELLANT PERFORMANCE

-COAXIAL INJECTOR CHARACTERIZATION PROGRAM-

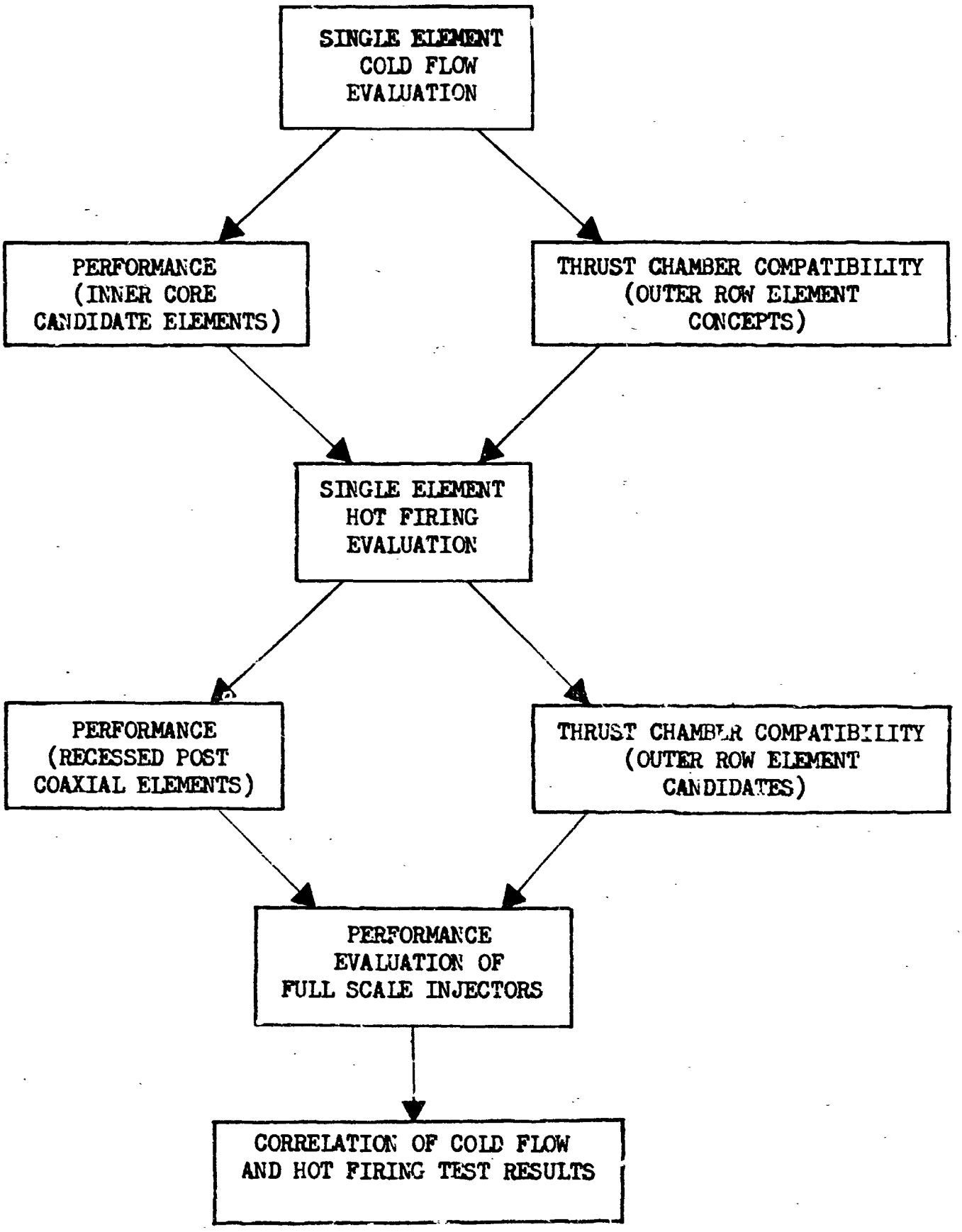

Figure 1. Sequence of Major Tasks in Program

3.0 PARAMETRIC COMBUSTION ANALYSIS

Rational design of rocket engine components using fundamental engineering principles requires a basic understanding of combustion and its relationship to the physical processes which control it. For most gas/liquid bipropellant systems, of which FLOX/CH_4(g) is typical, c* efficiency is affected by both propellant vaporization and mixing. These two processes can be considered independently (Ref. 7) in their effects on efficiency. A close approximation of overall efficiency can be obtained from

$$\eta_{c^*} = \eta_{c^* \text{ vap}} \times \eta_{c^*,\text{mix}} \quad (1)$$

where

η_{c^*} = the overall c* efficiency

$\eta_{c^*,\text{vap}}$ = the c* efficiency which would be obtained if propellant mixing were completely uniform, and the only losses were caused by incomplete propellant vaporization

$\eta_{c^*,\text{mix}}$ = the c* efficiency which would be obtained if propellant vaporization were entirely complete, and the only losses were caused by nonuniform propellant mixing.

Analysis of the parameters which affect c* efficiency is, therefore, logically divided into considerations of $\eta_{c^*,\text{vap}}$ and $\eta_{c^*,\text{mix}}$.

To assess the influence of $\eta_{c^*,\text{vap}}$ and $\eta_{c^*,\text{mix}}$ on the overall performance of the FLOX/CH_4(g) system, a parametric analytical study was conducted. The results of the study defined injector mixing levels and resultant mean drop sizes which would be required to meet the program performance goal of η_{c^*} = 99 percent.

3.1 PROPELLANT VAPORIZATION

The effects of incomplete propellant vaporization on c* efficiency can be quantitatively studied by means of an analytical propellant combustion model formulated at Rocketdyne several years ago by Lambiris, Combs, and Levine (Ref. 8) and further developed (e.g., Ref. 9) and used at Rocketdyne since that time. This combustion model, termed K-PRIME, exists in the form of a Fortran IV Computer Program written for the IBM-360 computer. A discussion of the essential feature of the K-PRIME combustion model is presented in Appendix A

A more sophisticated combustion model, termed CSS, has been developed recently at Rocketdyne (Ref. 10). However, to date, the model is operable only with the LOX/gaseous hydrogen propellant combination.

Figure 2 presents K-PRIME combustion model results for FLOX/CH_4(g) which shows the effect of propellant drop size and chamber geometry on characteristic velocity

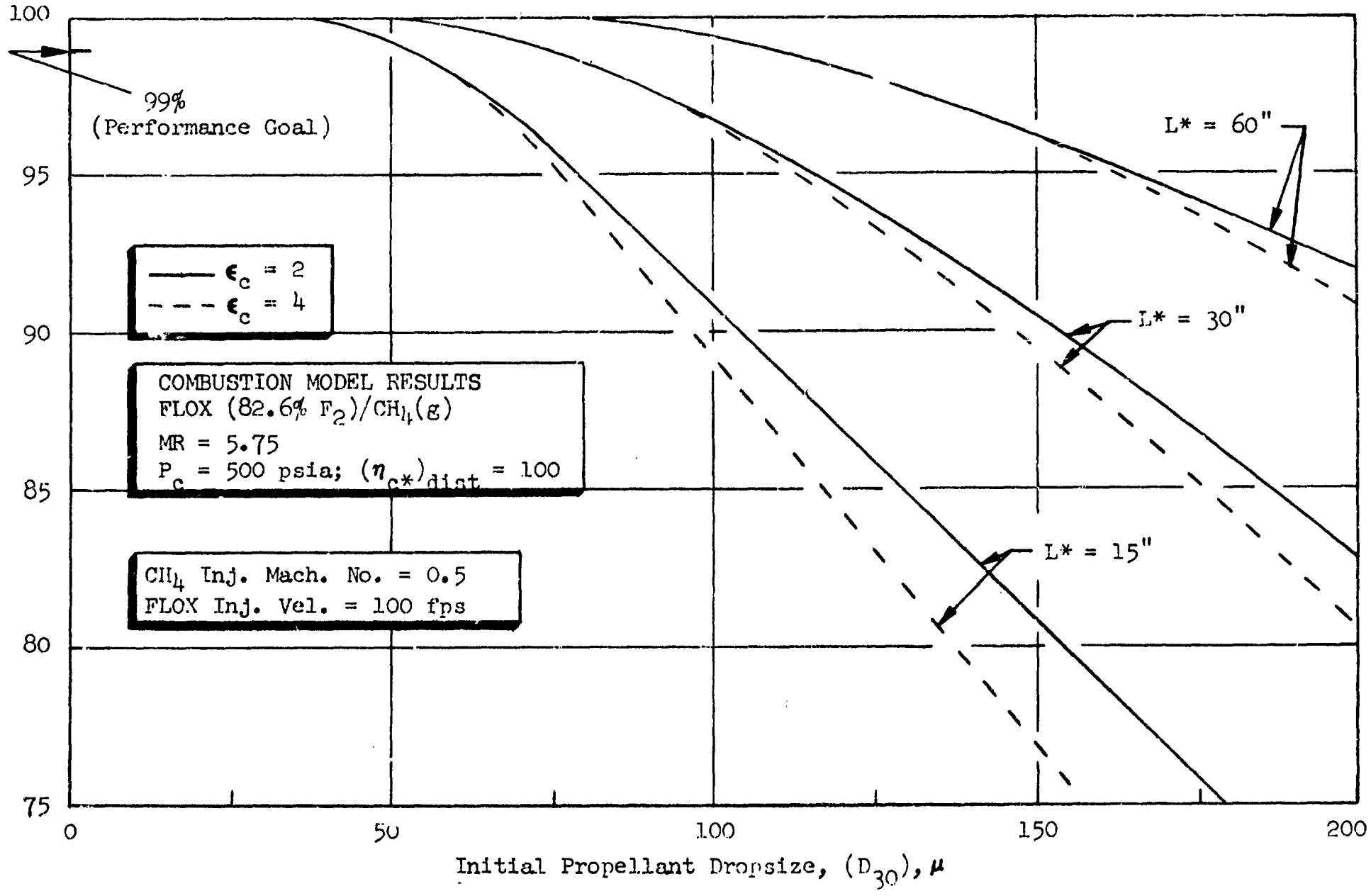

Figure 2. Effect of Propellant Drop Size and Chamber Geometry on c* Efficiency (Due to Vaporization) for FLOX/(CH_4)g

efficiency due to vaporization, $\eta_{c^*,vap}$. Curves of $\eta_{c^*,vap}$ versus drop size are shown for conventionally shaped thrust chambers (i.e., cylindrical with 60-degree conical nozzle approach section) having characteristic lengths of 15, 30, and 60 inches. The solid lines (A_c/A_t = 2) and dashed lines (A_c/A_t = 4) define the effect of contraction ratio at any given L* value.

Figures 2 shows that when propellant drop size is small, the effects of chamber geometry are generally attenuated. Conversely, when initial propellant drop sizes are large, chamber geometry effects become pronounced and c* efficiency becomes much more sensitive to specific geometric features such as chamber length and contraction ratio. For a given initial drop size and chamber L*, increase in vaporization efficiency can be effected by reduction of the contraction area ratio (increase of physical length).

The effect of chamber pressure on c* efficiency due to vaporization is shown in Fig. 3. The curves are for a common mixture ratio (MR = 5.75) and chamber characteristic length, L*, of 30 inches. Curves of $\eta_{c^*,vap}$ versus drop size are shown for chamber pressures of 250, 500, and 750 psia. The solid lines (A_c/A_t = 2) and dashed lines (A_c/A_t = 4) define the effect of contraction ratio at the three chamber pressure values. The effect of chamber pressure on $\eta_{c^*,vap}$ is attenuated when propellant drop size is small, while both pressure and geometry effects become more pronounced with larger drop sizes

The effect of mixture ratio on c* efficiency (due to vaporization) is shown in Fig. 4 in which $\eta_{c^*,vap}$ is shown as a function of drop size for various mixture ratios. The curves are for a chamber pressure of 500 psia and constant thrust chamber geometry (L* = 30 inches, A_c/A_t = 2). The effect of mixture ratio is small when initial drop size is small, and conversely, becomes more pronounced when initial drop sizes are large. The effect of mixture ratio is not monatomic and a specific optimum mixture ratio less than that corresponding to the theoretical optimum of 5.75 is indicated for maximum vaporization efficiency.

An explanation of mixture ratio effects can be aided by reference to Fig. 5 in which $\eta_{c^*,vap}$ is shown as a function of mixture ratio for a nominal drop size of 150 microns. The contributing product terms defined in the Priem model:

$$\eta_{c^*,vap} = \left(\frac{\dot{w}_B}{\dot{w}_I}\right)\left(\frac{c^*_B}{c^*_I}\right) \qquad (2)$$

are shown as dashed curves. The percent burned $\dot{w}_B/\dot{w}_I$ is the ratio of total propellant vaporized and reacted to that initially injected. The c* ratio c^*_B/c^*_I is a coefficient defining the ratio of the theoretical c* at the reacted condition to that corresponding to the initial injection mixture ratio.

3.1.1 Other Variables

The effect of other potentially significant variables were examined to assess their effect on vaporization efficiency for FLOX/CH_4(g). Specific areas investigated included the effect of initial droplet injection velocity, initial vaporization conditions, and specific input variables in the combustion model itself.

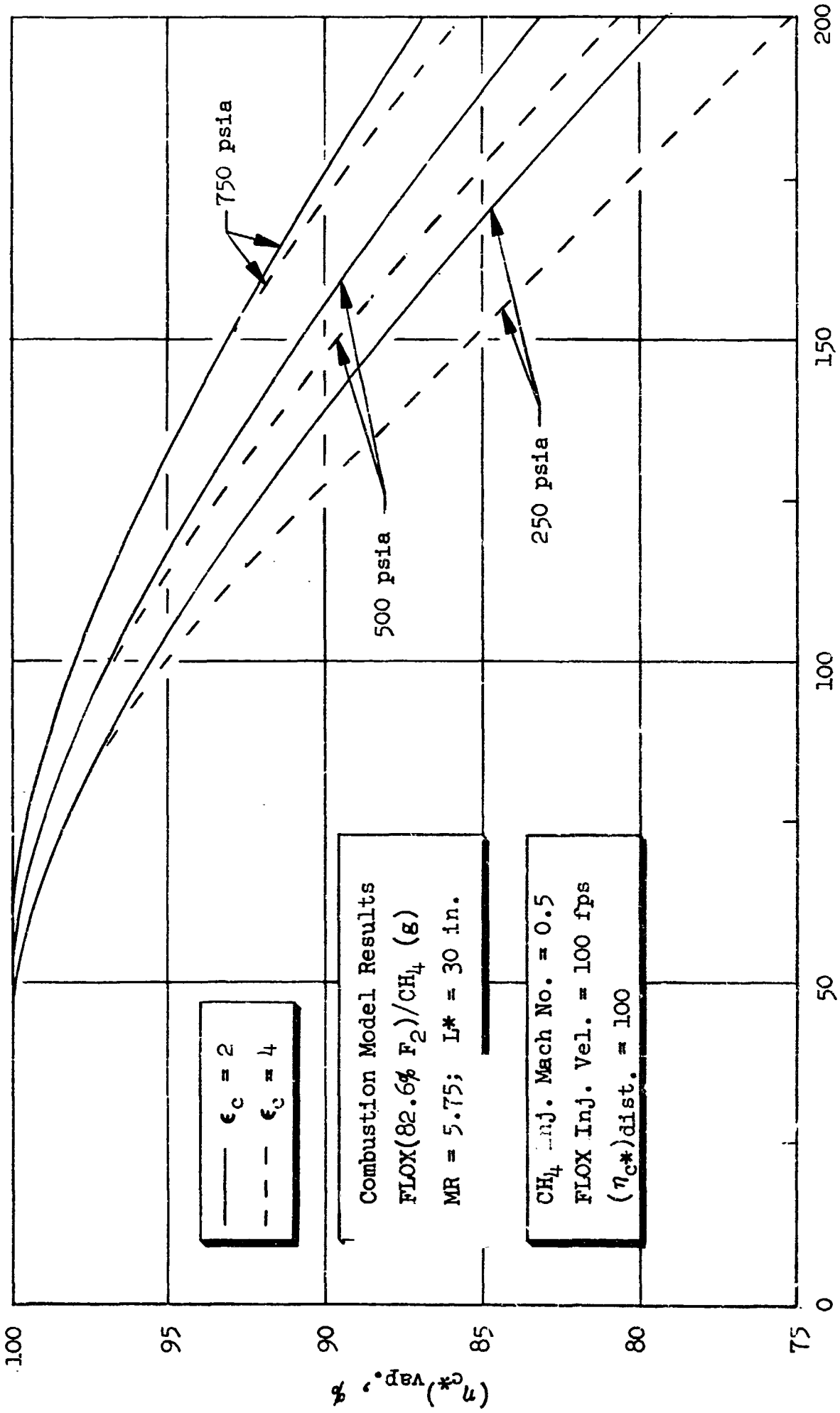

Figure 3. Effects of Initial Propellant Drop Size and Chamber Contraction Ratio on c* Efficiency (Due to Vaporization) for FLOX/CH_4 (g) at Several Chamber Pressures

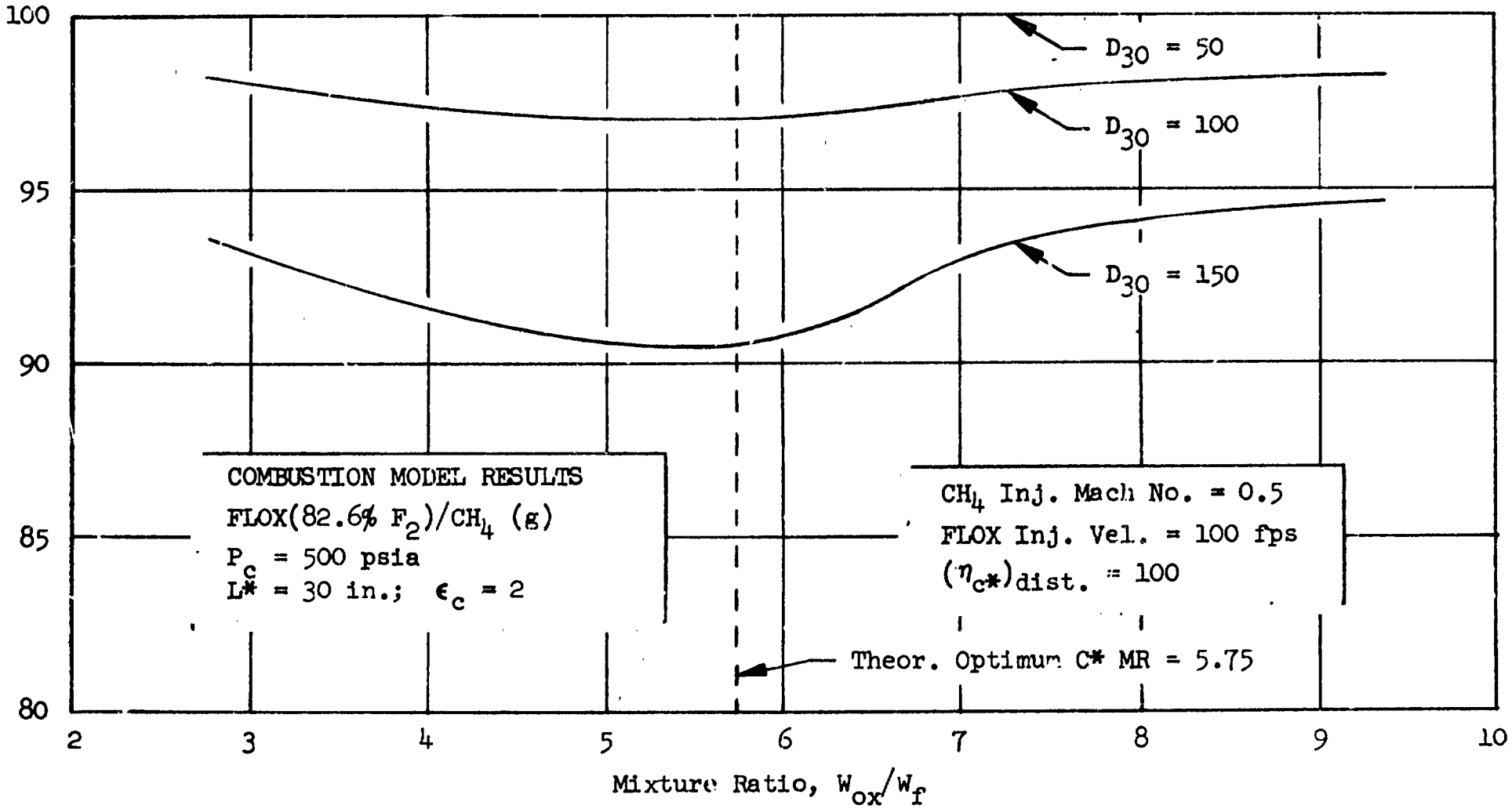

Figure 4. Effects of Mixture Ratio and Initial Propellant Drop Size on c* Efficiency (Due to Vaporization) for FLOX/CH_4(g)

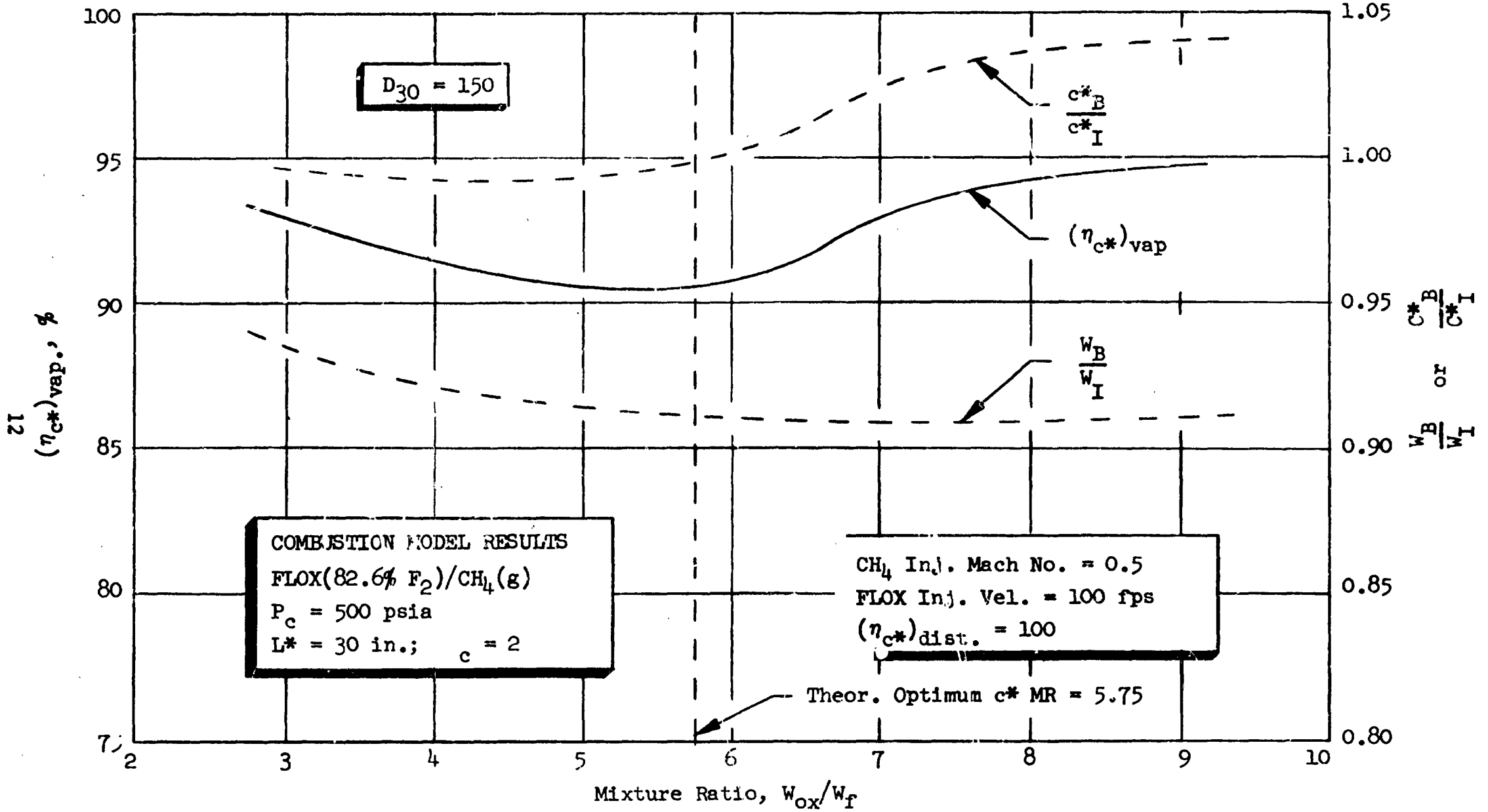

Figure 5. Effect of Mixture Ratio on c* Efficiency (Due to Vaporization), Fraction of Injected Propellants Burned, and the Burned-to-Injector Mixture Ratio

The initial droplet injection velocity was perturbed by a factor of 3 to determine its effect on the resultant propellant vaporization when all other factors (including drop size) are held constant. Generally, propellant vaporization is increased at lower initial injection velocities. This results from a longer residence time and in an increased convective heat transfer coefficient as the drops are gradually accelerated by the combustion gases.

Other parameters investigated were the effect of drop size distribution, physical properties variation with temperature and pressure, inclusion or exclusion of propellant sensible heat capacity and variations of gas and film properties. Again, these variables were of secondary importance and significant only when conditions favored a generally reduced vaporization efficiency (i.e., larger initial drop size and small chamber L^* geometry). This analysis disclosed that chamber geometry and initial propellant drop size were of primary importance, and that other variables were of secondary significance.

3.2 MIXING EFFICIENCY

The effect of nonuniform mass and mixture ratio distribution is considered to be of importance equal to the vaporization process. Regardless of injector type, uniform mixing is a prerequisite for high combustion efficiency. In the absence of uniform mass and mixture ratio distribution, local striated regions of fuel or oxidizer-rich zones will persist throughout the rocket chamber. Because of the short axial dimensions associated with rocket chambers, turbulent mixing and diffusion are relatively ineffective in equilibration of propellant concentration (Ref. 1 through 15). Consequently, the c* potential will be largely dependent on the initial distribution of fuel and oxidizer at the injector end of the chamber. Hence, if by cold-flow techniques the mass and mixture ratio can be determined for local regions within the chamber, the mixing efficiency can be determined by applying simple mass weighted summation techniques.

For this study, the analysis was based on a simplified stream tube model in combination with cold-flow experiments to determine distribution of propellants. The general features of the mixing model permit analytical consideration of an idealized rocket engine composed of N imaginary rocket chambers forming individual, isolated, stream tubes within the main chamber. Each stream tube at its own mass and mixture ratio is allowed to expand isentropically through the chamber and nozzle without heat or mass transfer to adjacent stream tubes. The c* efficiency due to mixing ($\eta_{c^*,mix}$) is determined by summation of individual mass weighted c* contributions of each individual stream tube and comparing the total to that theoretically attainable at the injected mixture ratio.

Correction factors for changes in specific heat ratio as a function of mixture ratio may be applied. However, if the effect of variation on the sonic point for each individual station can be neglected, the mixing c* efficiency can be expressed simply as:

$$\eta_{c^*,mix} = \frac{\sum_{i}^{n} MF_i c^*_i}{c^*_{theo}} \qquad (3)$$

where

MF_i = the mass fraction in the individual stream being considered

c^*_i = theoretical c* corresponding to the mixture ratio of the local stream

c^*_{theo} = theoretical c* corresponding to the overall mixture ratio

The mixing quality can be expressed by an index, E_m, which defines the mass weighted deviation of local mixture ratio from initially injected overall mixture ratio. The index, E_m, was developed by Rupe (Ref. 16) and is shown below.

$$E_m = \left[1 - \sum_i^N MF_i \frac{(R - r_i)}{R} - \sum_i^N MF_i \frac{(R - \bar{r}_i)}{R - 1} \right] 100 \qquad (4)$$

where

E_m = mixing index

MF_i = mass fraction in the stream tube

R = ratio of total oxidizer mass to total oxidizer and fuel mass

r_i = ratio of oxidizer mass to total oxidizer and fuel mass in an individual stream tube for $r_i < R$

$\bar{r}_i$ = ratio of oxidizer mass to total oxidizer and fuel mass in an individual stream tube for $r_i > R$

The foregoing expression for the distribution index is not universal because it is also functionally related to the injected mixture ratio. The c* efficiency due to propellant distribution, $\eta_{c^*,mix}$, is a function of both the distribution index, E_m. and the initially injected mixture ratio. The actual relationship between E_m, MR, and the resultant mixing c* efficiency is shown in Fig. 6, which the mixing c* efficiency, $\eta_{c^*,mix}$, is shown as a function of E_m for various values of mixture ratio for the FLOX/CH_4(g) propellants considered for this study. It should be noted that the basis of constant mixture ratio would be more correctly expressed as bands because even at a constant mixture ratio, $\eta_{c^*,mix}$, is not uniquely related to the E_m index. Analysis and verification experiments indicate, however, that the band width is normally narrow for most injector-produced spray distributions and the actual error introduced by use of single curves is negligible. The curves illustrated in the referenced figure can be used directly to assess the mixing c* efficiency of a given injector for which E_m is known. In practice, however, it is often easier to derive an expression for $\eta_{c^*,mix}$ directly from cold-flow experimental data by utilization of the basic $\eta_{c^*,mix}$ expression of Eq. 3. The more universal expression is, however, much more valuable in that it permits a more generalized approach to performance analysis because it permits $\eta_{c^*,mix}$ determination for any injector in which the same propellants are used. In practical use, the figure permits specific determination of the required injector distribution index E_m for a given target level of mixing efficiency, $\eta_{c^*,mix}$, at any desired operating mixture ratio.

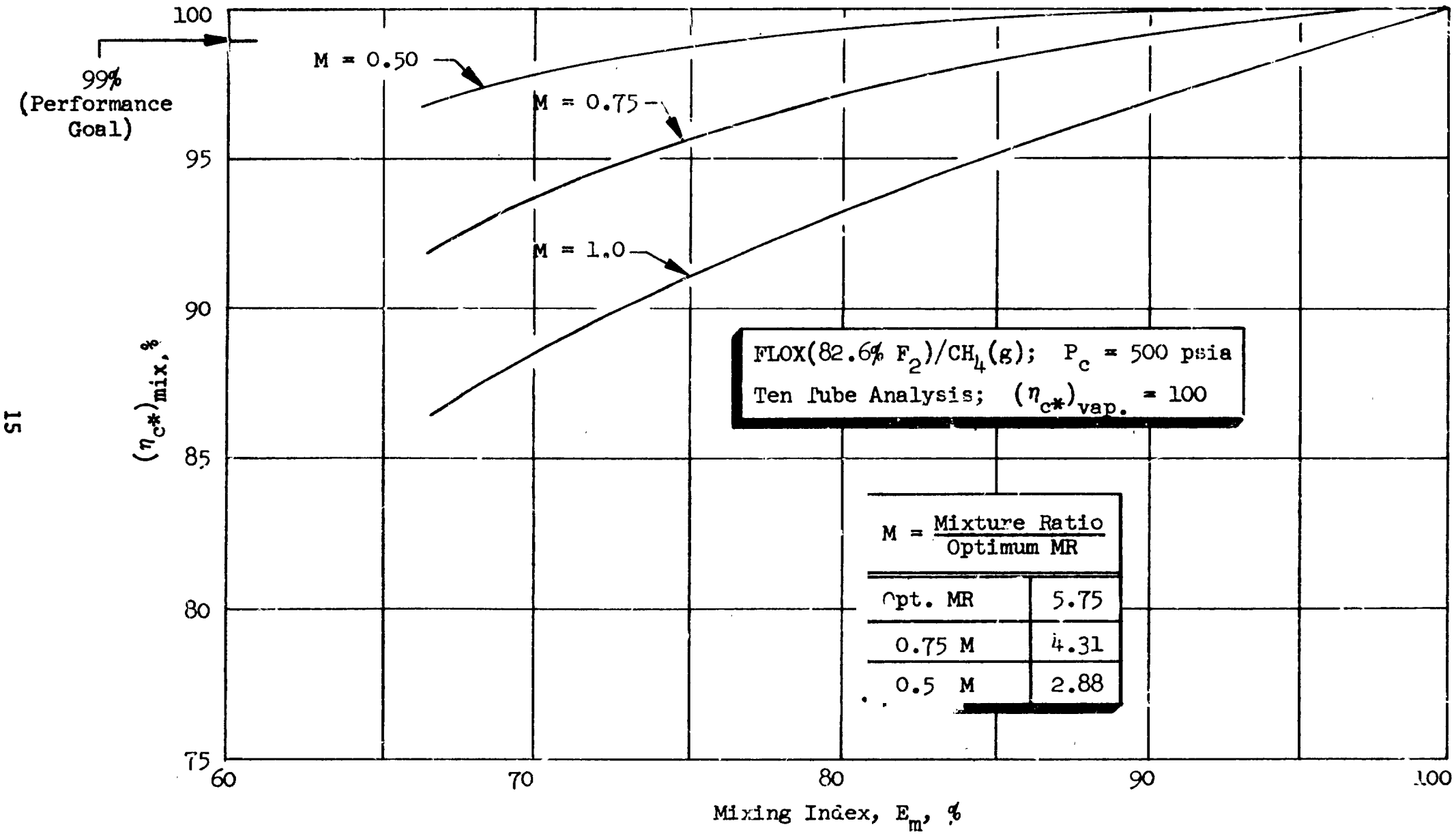

Figure 6. Predicted Effect of Propellant Distribution on Performance for FLOX/CH_4(g) Analytical Results

3.3 SUMMARY OF ANALYTICAL STUDIES

In summary, the combustion model analysis disclosed quite clearly that propellant drop size and chamber geometry were the two most sensitive and important variables affecting propellant vaporization. Chamber pressure was found to have a secondary effect and only becomes important when propellant drop size or chamber geometry favor reduced vaporization efficiency. Mixture ratio effects were found, also, to be of secondary importance; however, analysis indicated that optimum propellant vaporization would normally occur at slightly less than the nominal optimum mixture ratio. Other input parameters were found to be of minor consequence. The most singularly important finding was that volume mean propellant drop sizes of 70 microns or less would be required to attain sufficient vaporization for 99-percent c* efficiency in a nominal 30-in. L* thrust chamber. Analysis of propellant mixing effects indicated that uniform mixture ratio distribution was essential for high c* efficiency. Further, it was shown that the effect of propellant distribution on c* efficiency due to mixing was sensitive to the operating mixture ratio of the injector. For FLOX/CH_4(g) at the nominal mixture ratio of 5.75, it was found that a mixing uniformity index of at least 97 would be required for eventual attainment of 99-percent c* efficiency.

4.0 EXPERIMENTAL APPARATUS

This section describes the experimental hardware which was utilized in the single-element cold-flow and hot-fire studies and in the full scale injector-thrust chamber evaluation. Rationale for the selection of the element design and operating variables which were investigated are presented in a subsequent section (Section 5.0).

4.1 SINGLE-ELEMENT COLD-FLOW INJECTORS

Single-element cold-flow injector models were fabricated of candidate injector "core" elements and "peripheral" zone elements. These models were constructed by designing a basic manifolding system which allowed for the interchanging of "core" and "peripheral" elements. In addition, the basic manifold system was fabricated from Nickel-201 which allowed the same piece of hardware which was cold-flowed to be subsequently hot-fired.

4.1.1 Core Element Injectors

The three "core" element configurations, designated No. 1, 2, and 3, which were chosen for characterization are shown in Fig. 7. Provisions were made to vary the amount of oxidizer post recess from flush (R = 0) to four post diameters (R = 4 D_L) by the insertion of spaces in the single-element models.

All the "core" candidate elements were configured with a diffuser section at the exit of the oxidizer post. The post exit was chamfered at a nominal half-angle of 6 degrees which is below the value at which separation will occur (Ref. 17).

To investigate the effects of swirling the oxidizer jet two types of in-line swirlers were configured. Schematics of the two in-line swirlers are shown in Fig. 8. The swirlers were designed with nominal helix angles of 22-1/2 and 45 degrees and were installed 1.71 inches upstream of the oxidizer post exit. The helical channels in the two swirlers were designed with equivalent flow areas (i.e., the liquid velocity in each channel was equal) so that the radial momentum of the liquid was changed by a factor of 1.85 when the swirler helix angle was changed changed from 22.5 to 45 degrees. Both swirlers were fabricated from Nickel-201 so that they could be utilized in subsequent hot-fire experiments.

4.1.2 Peripheral Element Injectors

Two candidate "peripheral" element configuration were investigated. A baseline configuration was chosen which consisted of a "core" type element with an adjacent boundary layer coolant (BLC) hole. The second peripheral element configuration consisted of the scarfed post with oxidizer jet swirl. Schematics of the candidate peripheral elements along with their respective dimensions are shown in Fig. 9.

The scarfed post with swirl element was designed with a nominal post scarf angle of 22-1/2 degrees as shown in Fig. 9. The method of swirling the oxidizer jet was identical to the method employed for the "core" element with swirl. Note that the gas gaps of the two candidate configurations were equal so that each configuration operated with equivalent gas injection velocities.

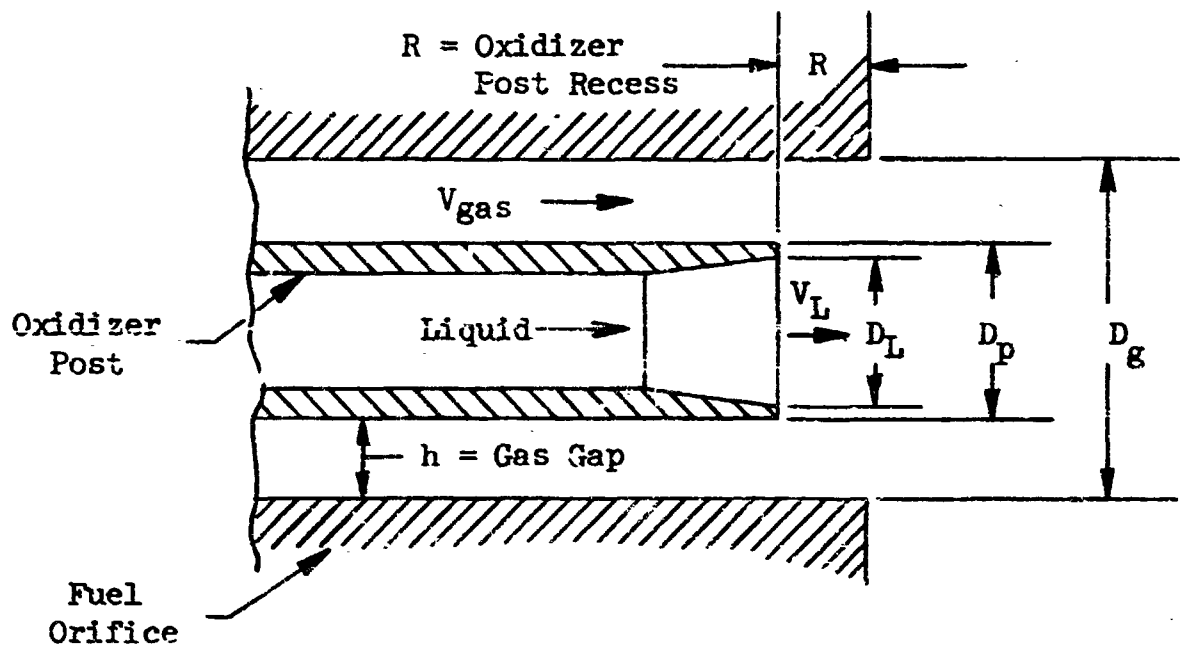

Core Element Configurations (Nominal Dimensions)			
No.	D_L (In.)	D_p (In.)	D_g (In.)
1	0.136	0.146	0.182
2	0.108	0.122	0.166
3	0.070	0.080	0.136

Figure 7. Core Element Configurations

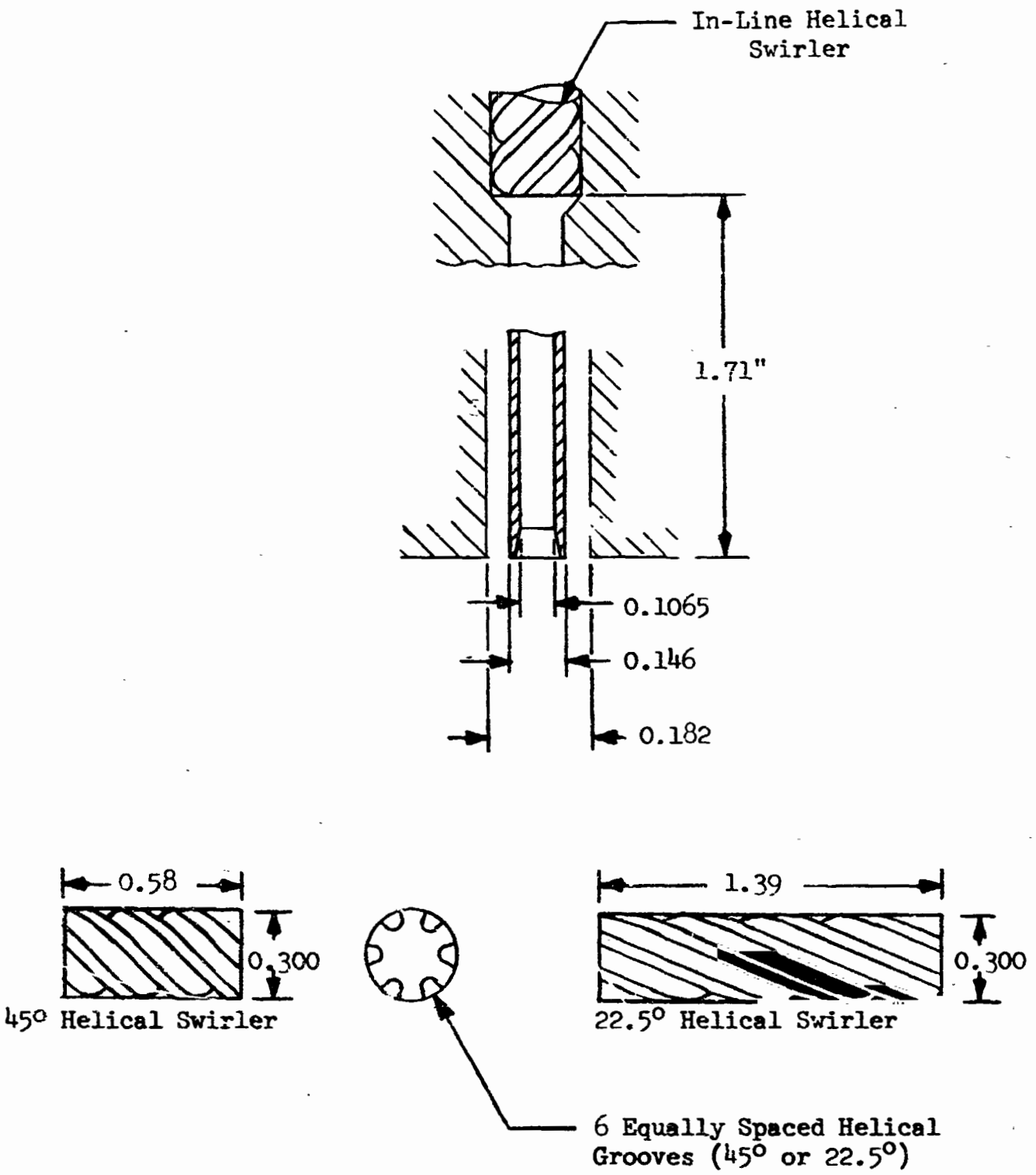

Figure 8. Swirler Configuration

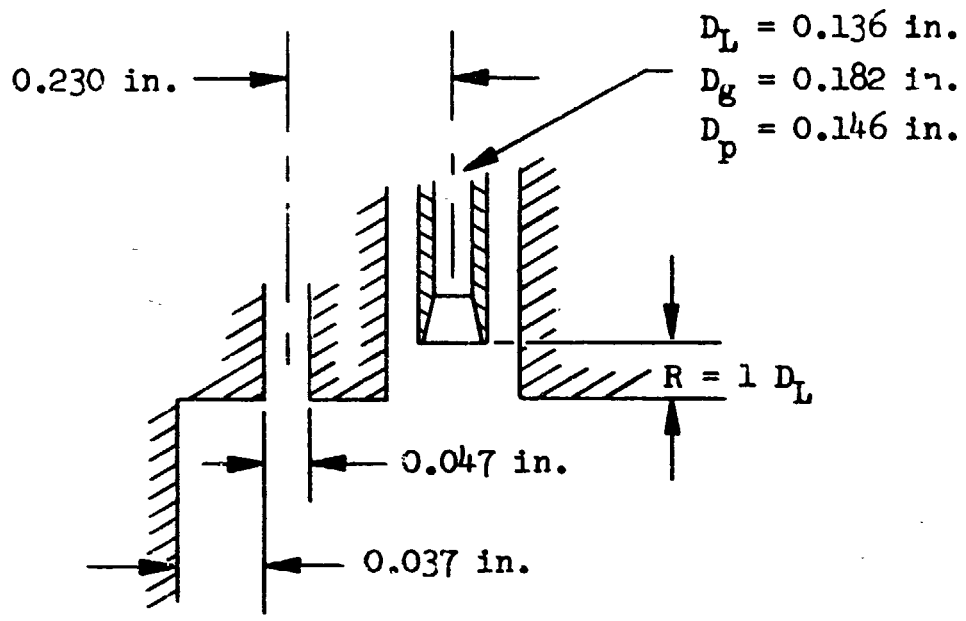

BLC Concept

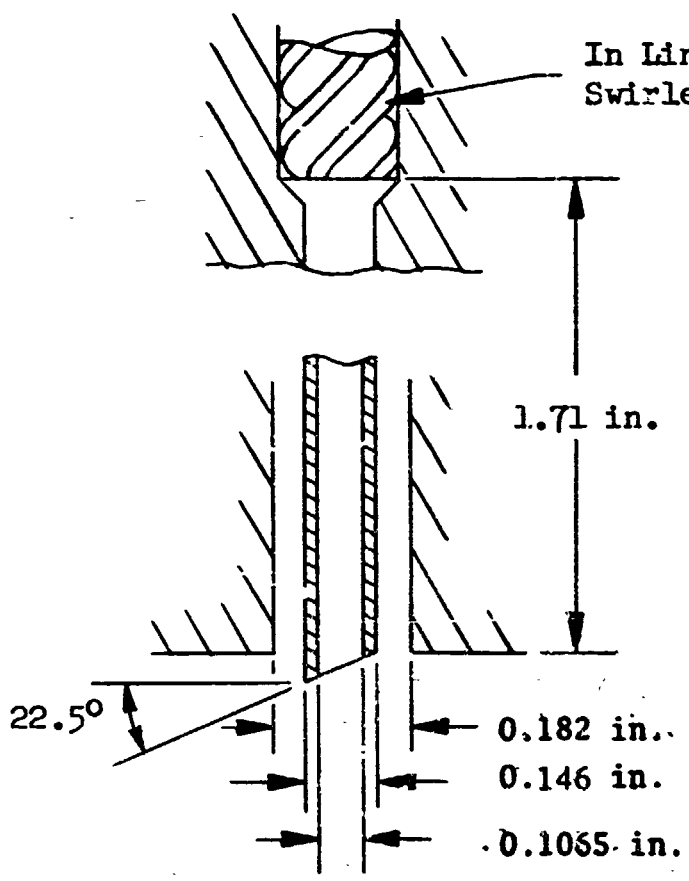

Scarfed Post With Swirl Concept

Figure 9. Peripheral Element Configurations

4.2 SINGLE-ELEMENT HOT-FIRE INJECTORS

Based on the results of the single-element cold-flow studies (see Section 5.0) single-element configurations of "core" and "peripheral" elements were designed for hot-fire evaluation. As mentioned previously, the cold-flow hardware was designed so that only minor modifications were required to hot-fire the cold-flow models. One modification involved the addition of an LN_2 cooling manifold to the injector body to prevent vaporization of the FLOX. This modification was necessary due to the small flowrate (≈0.174 lbm/sec) of FLOX which flowed through a relatively massive piece of hardware.

4.2.1 Core Element Hot-Fire Injector

The "core" element configuration which was selected for hot-fire evaluation is shown schematically in Fig. 10. Rationale for the selection of this configuration is presented in Section 5.0. A photo of the single-element hot-fire injector is shown in Fig. 11. Since cold-flow techniques do not simulate hot-fire effects such as oxidizer post burning, the recess of the FLOX post was designed to be variable. The post recess was varied by the addition of spacers between the oxidizer post body and the fuel orifice assembly. The oxidizer post body was the same hardware which was utilized in the cold-flow investigation with the addition of an LN_2 cooling jacket.

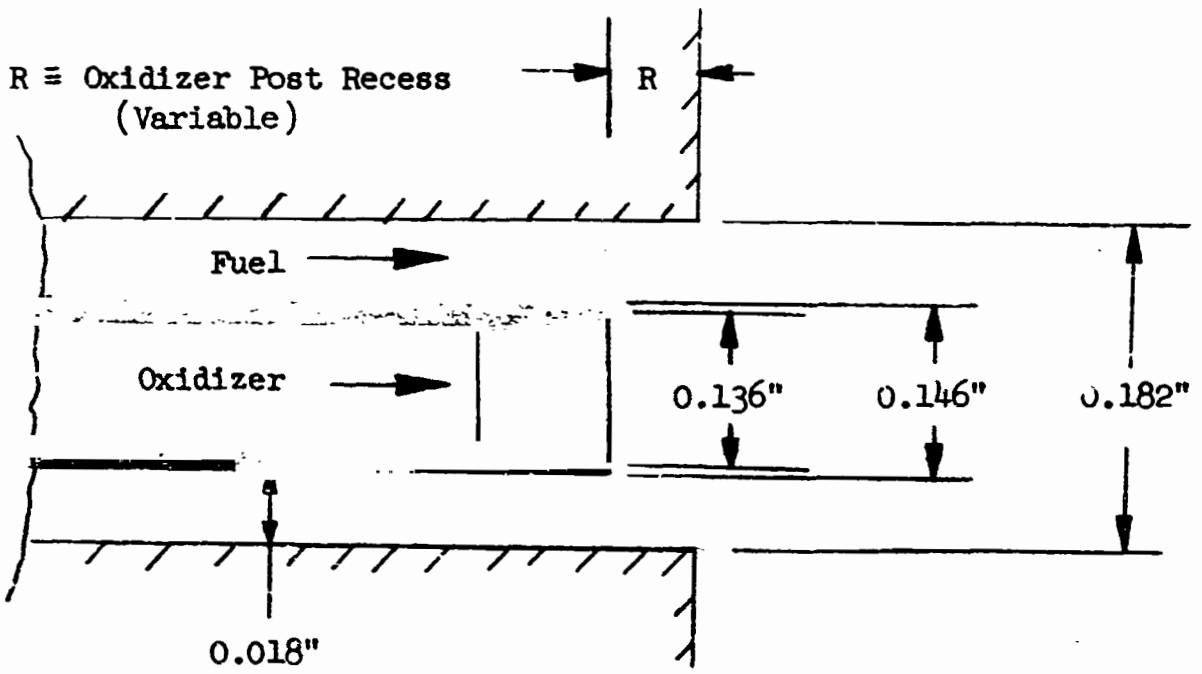

Figure 10. Recessed Post Core Element

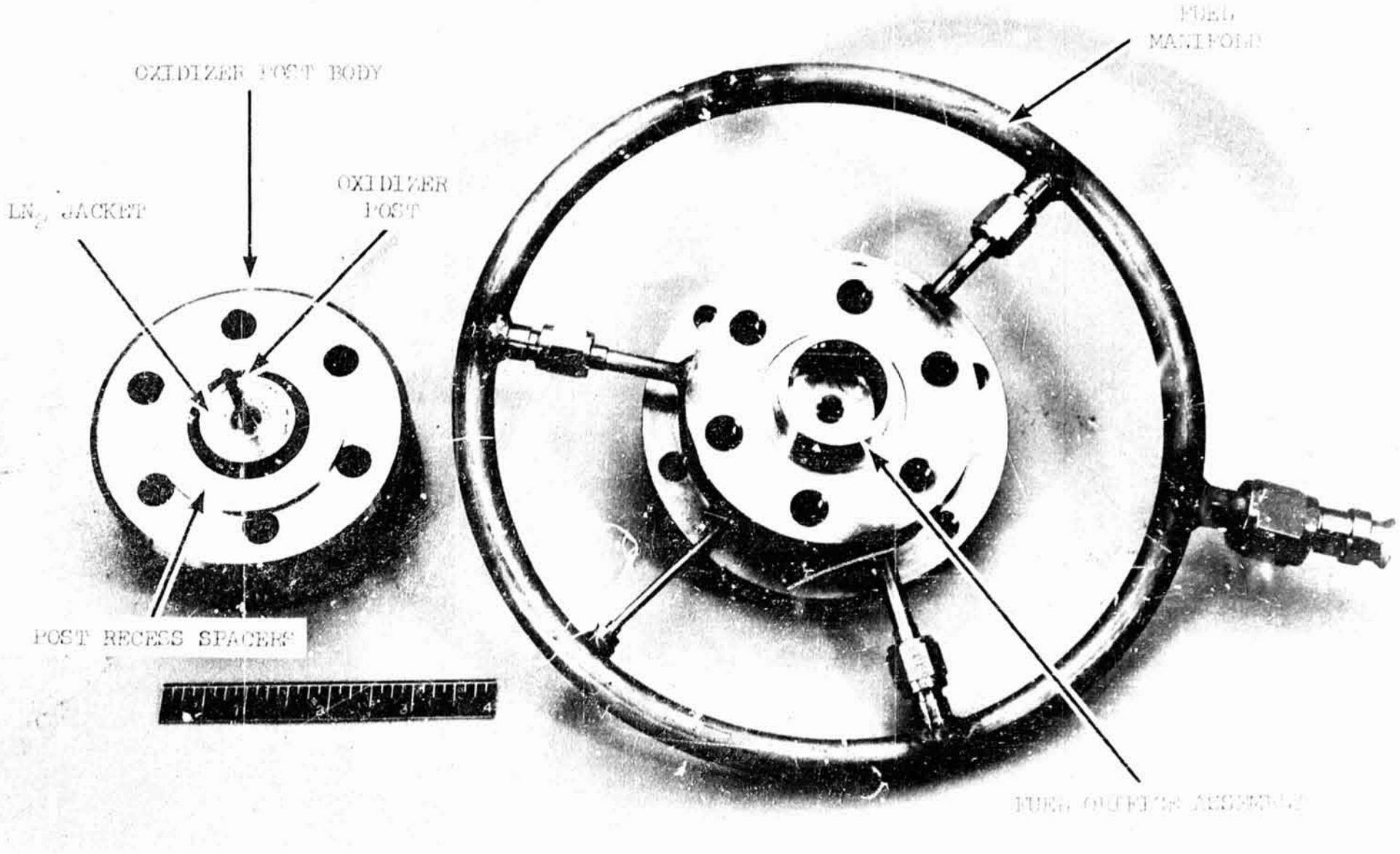

5AA34-2/12/71-S1B

Figure 11. Single-Element Hot-Fire Injector

The injector manifolds were instrumented to provide both fuel and oxidizer pressures and temperatures. No dynamic pressure transducers (Photocons) were installed in the injector due to the small size of the hardware.

4.2.2 Peripheral Element Hot-Fire Injector

The results of the single-element cold-flow studies revealed that both the BLC and the scarfed post with swirl elements were potentially good injector-chamber compatibility elements (see Section 5.0). Thus, both configurations (Fig. 9) were selected for hot-fire evaluation.

The BLC hot-fire injector was configured by adding a 0.047-in. BLC hole to the "core" element injector. The BLC fuel flow was separately manifolded in order to vary the percentage of BLC during the hot-fire evaluation.

The scarfed post with swirl hot-fire element was configured by brazing in a new post into the "core" element oxidizer post body (see Fig. 11). The same in-line swirler which was utilized in the cold-flow studies was employed in the hot-fire experiments.

4.3 SINGLE-ELEMENT HOT-FIRE CHAMBERS

The single-element hot-firing thrust chambers were designed to simulate a single streamtube of a full-scale 3000-pound-thrust chamber. That is, the chamber contraction (ε_c = 3) and chamber L*'s were equal to those of the full scale chamber.

Three chamber L*'s were designed (10, 20, and 40 inches) as shown in Fig. 12. The chamber shells were designed to contain replaceable ATJ graphite liners which were bonded to the stainless steel shell with RTV compound. Each graphite liner contained a convergent-divergent nozzle with a throat diameter of 0.341 inch. The nozzle expansion ratio (5.5) was chosen to provide expansion to 13.8 psia from 500 psia chamber pressure.

Following the curing of the RTV bonding compound, each chamber was instrumented to determine chamber wall heat flux data. This was accomplished by drilling two 3/64-in. thermocouple placement holes at each axial location. Two rows of thermocouples spaced radially 180 degrees apart were installed in each thrust chamber. The placement holes were drilled in order to place the thermocouples 0.150 and 0.300 inch, respectively, from the inner surface of the chamber. To reduce the contract resistance between the thermocouple tip and the bottom of the hole a small amount of powdered graphite was placed at the bottom of each hole prior to insertion of the 10 mil-diameter chromel-alumel thermocouple. The thermocouples were pressure sealed by potting with an epoxy resin.

The performance of the single-element thrust chamber was based on chamber pressure measurements. Thus, three chamber pressure taps were located upstream of the convergent section of the graphite nozzle.

A photo of the single-element hot-fire assembly (L* = 40 in.) mounted on test stand Uncle (Propulsion Research Area) is shown in Fig. 13. The thrust chamber

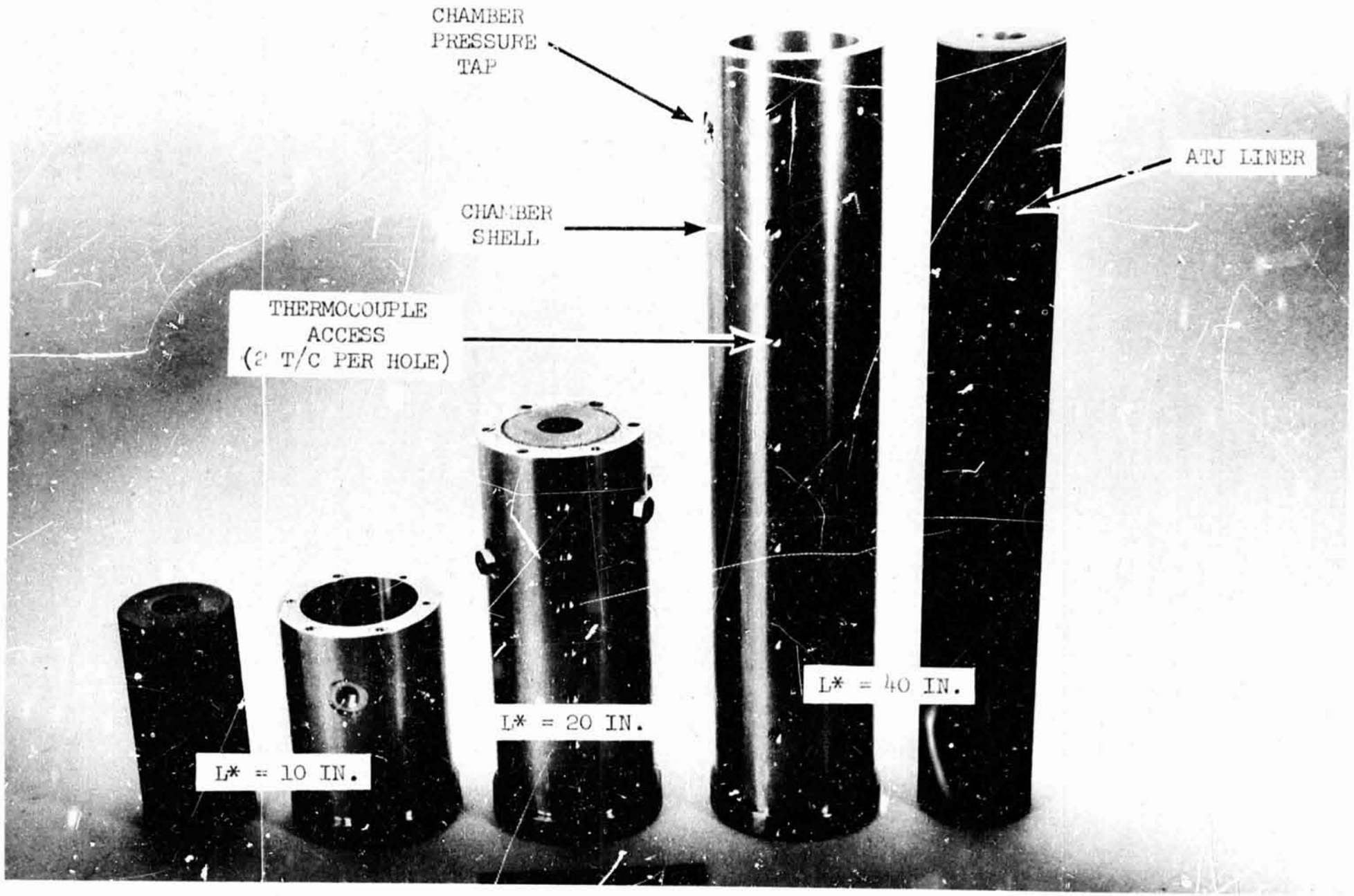

5AA34-2/12/71-S1C

Figure 12. Single-Element Thrust Chamber With Replaceable Graphite Liners

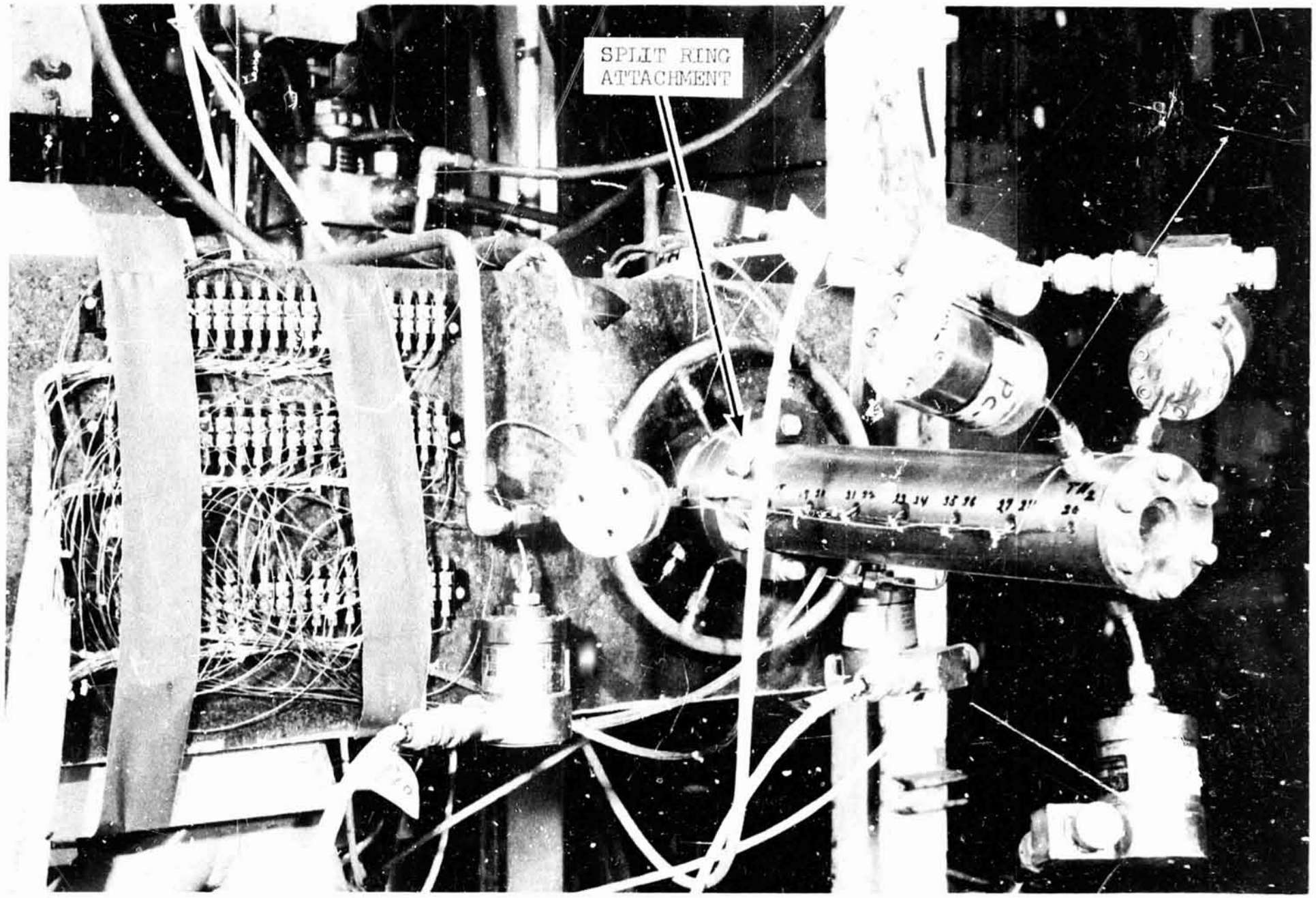

5AA34 3/16/71-S1C

Figure 13. Single-Element Hardware on Test Stand Uncle

shell was attached to the single-element injector by means of a split-ring assembly which allowed the thrust chamber to changed without removing the entire assembly from the test position.

4.4 FULL-SCALE COAXIAL INJECTOR

The full scale coaxial injector hardware was designed to be compatible with the thrust chamber hardware which was utilized in the like-doublet portion of the program (Ref. 4). That is, the diameter of the injector face was configured to match a 3.880-inch-diameter graphite lined thrust chamber.

Based on the results of the single-element cold-flow and hot-firing investigations, the element configuration which was selected for the injector core was identical to the configuration which was utilized in the single-element hot-firing task (Fig. 10) with an oxidizer post recess of 1-1/2 D_L (0.204 inch) Rationale for the selection of this configuration is described in Section 6.0. The "peripheral" zone element which was used consisted of a "core" type element with a showerhead boundary layer coolant (BLC) hole adjacent to each peripheral element. The showerhead BLC holes were separately manifolded from the core methane manifold to permit variation of the amount of BLC during the hot-firing evaluation. As in the single-element hot-fire studies, the BLC holes were designed for an injection velocity equal to the fuel annulus velocity at the 6-percent BLC level* (≈350 ft/sec).

To configure a 3000 lbf (sea level) injector, 43 elements were required. The 43 elements were configured into a face pattern shown schematically in Fig. 14. The face pattern consisted of three circumferential element rings with a single-element in the center of the injector. The radial spacings between rings were equal (0.553 in.) as were the circumferential spacing between elements (0.496 in.). This face pattern allowed for uniform mass flux distribution across the injector face as well as providing for an interpropellant purge cavity (discussed in a later paragraph). Note that the interelement spacing of the injector face pattern is relatively large (≈0.55 in. radially, ≈0.50 in. circumferentially).

The large interelement spacings were required with 70 lbf elements since the injector had to be compatible with the existing 3:1 contraction ratio chamber which was utilized in the like-doublet portion of the program. Use of a lower contraction ratio chamber with the coaxial injector appears feasible. Use of a $\varepsilon_c < 3$ chamber would provide improved vaporization for a given chamber L* (Fig. 2).

The injector assembly consists of three separate subassemblies: (1) the oxidizer flange, (2) the injector body, and (3) the injector face assembly (Fig. 15 and 16). The three were designed so that the injector could be assembled before it was mated with the thrust chamber assembly. Additional, important design guidelines for the injector are summarized below:

1. Element placement on the face was designed to provide a uniform propellant distribution.

*BLC percentage level is defined a percent of total injector fuel flow.

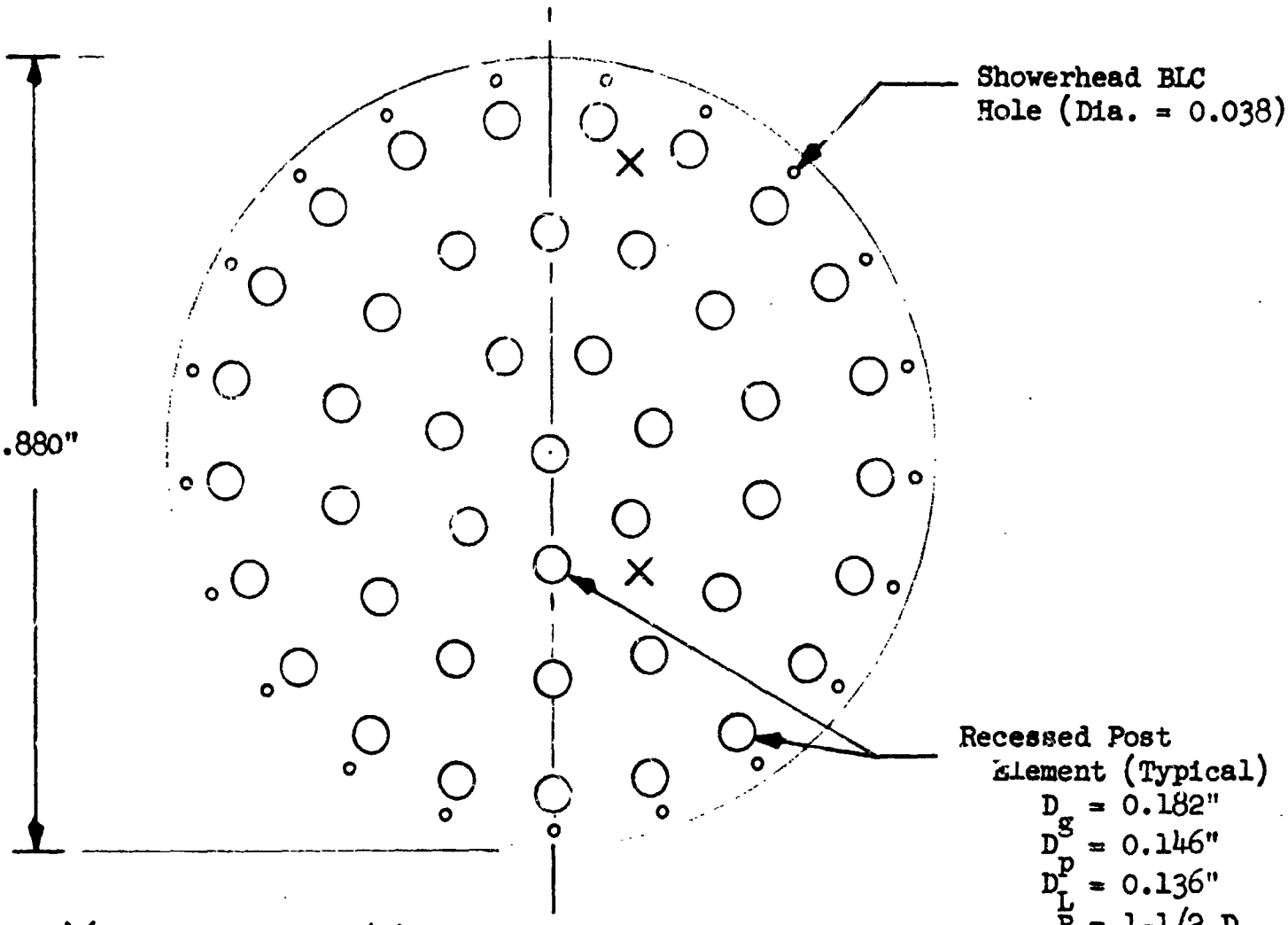

LOCATION

Ring	Radial	Circumferential	No.	
	-	-	1	
1	0.553"	0.496"	7	
2	1.106"	0.496"	14	$\sum$=43 Elements
3	1.659"	0.496"	21	
BLC Holes	1.819"	0.549"	21	

Figure 14. Face Pattern of Full-Scale Injector

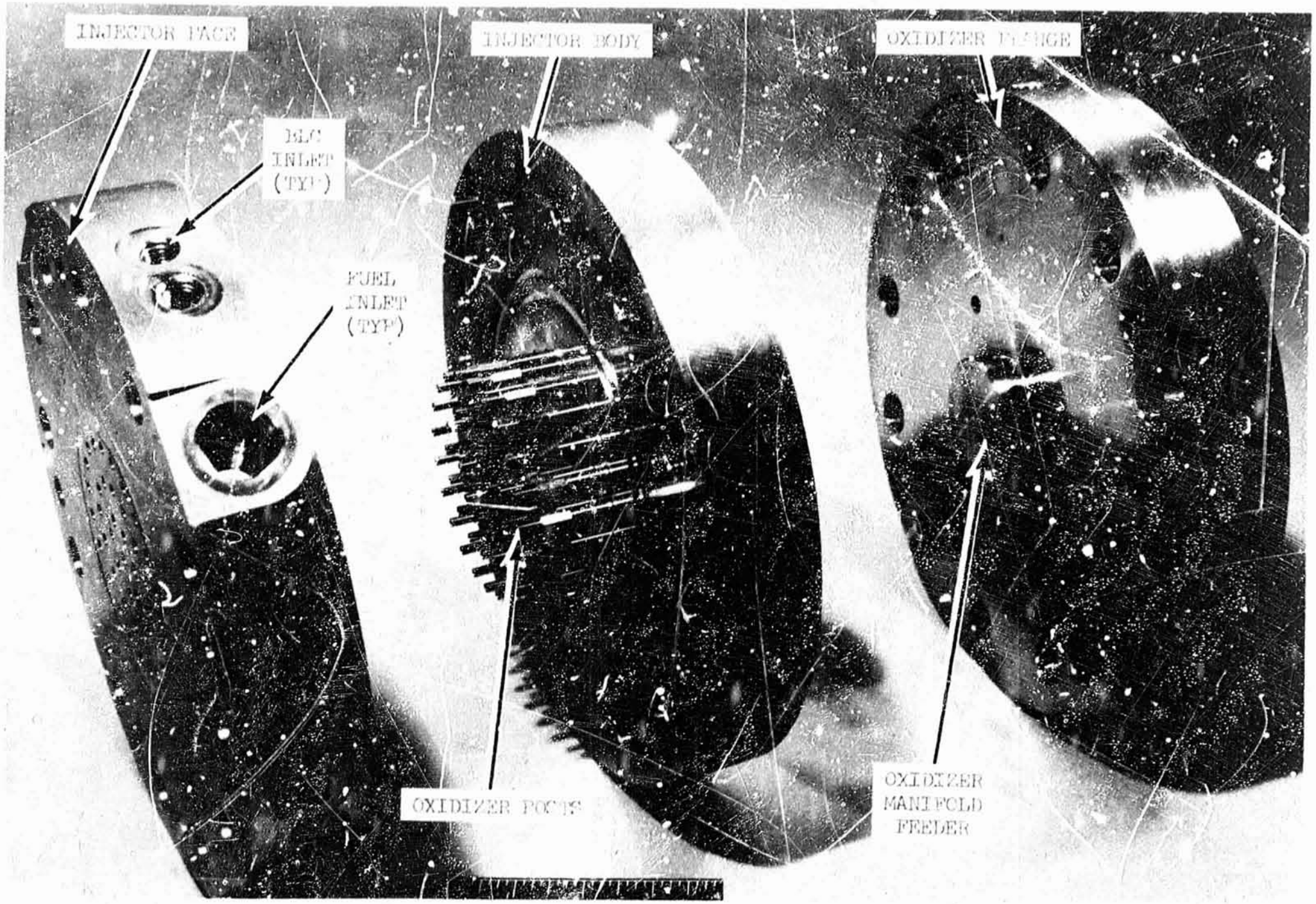

5AA34-9/7/71-S1L

Figure 15. Photograph of Full-Scale Injector Subassemblies

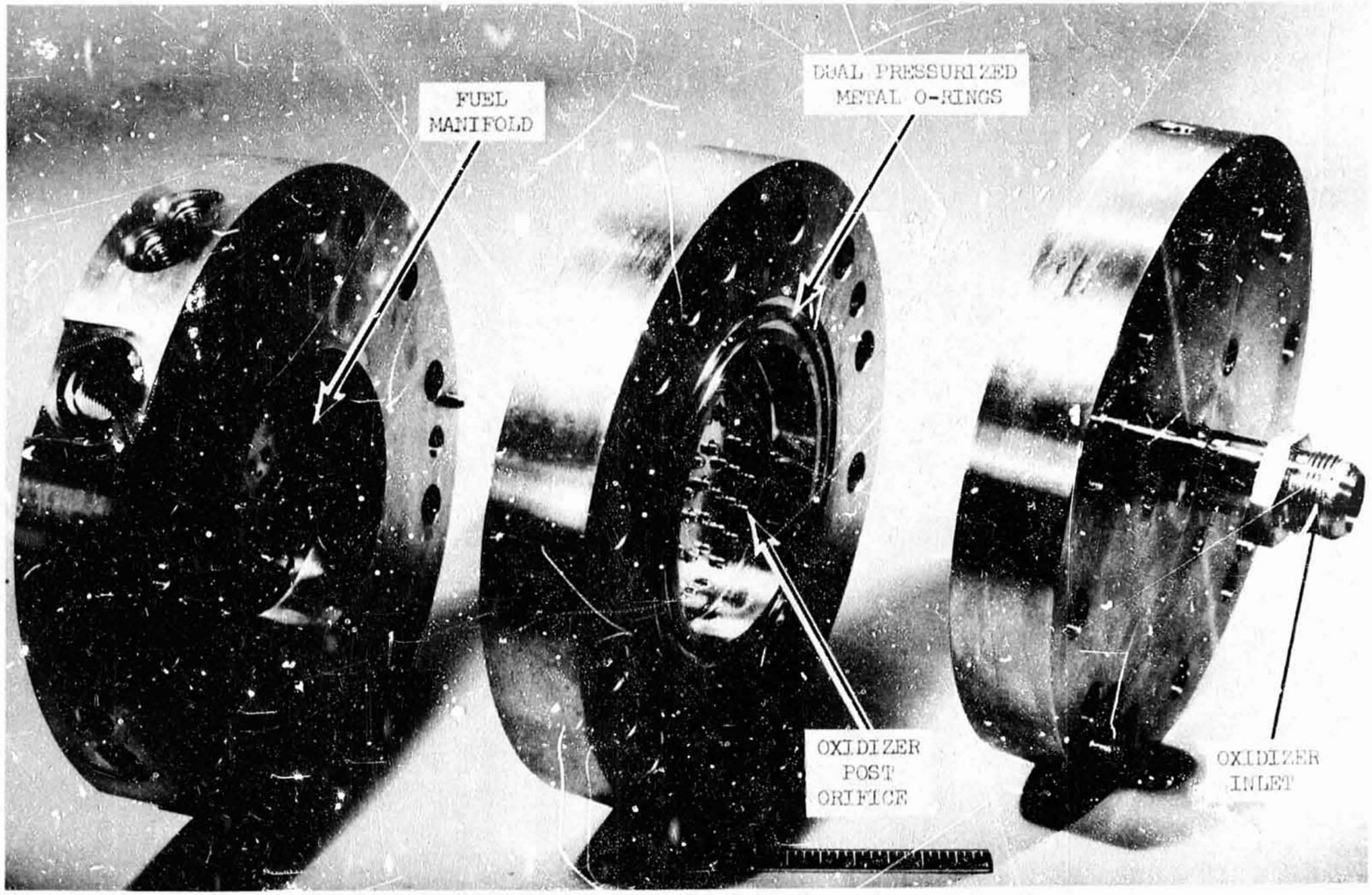

SAA34-9/7/71-S1J

Figure 16. Photograph of Full-Scale Injector Subassemblies

2. Oxidizer manifold/feeder passages were sized so that velocities were less than 15 ft/sec at the design operating conditions and passage entrances were chamfered or rounded as much as possible to avoid sharp edges. Fuel manifold/feeder velocities were less than 90 ft/sec at the design condition.

3. Fuel (CH_4) annulus length/height ratio was approximately 15. Velocity of the fuel in the annuli was nominally 350 ft/sec at the design condition.

4. The FLOX posts contain integral guide surfaces to maintain oxidizer post/fuel annulus concentricity and prevent possible oxidizer post vibration. The end of the guide surfaces were approximately 0.362 in. (≈20 gas gap heights) from the end of the FLOX post. The FLOX posts contained head-end orifices which were designed for an oxidizer post ΔP of ≈120 psi at the design condition. The diffused FLOX injection velocity was 19.1 ft/sec at the design condition.

The injector face and injector body were fabricated from Nickel-201. The individual FLOX posts were fabricated from stock seamless Nickel-200 tubing. The oxidizer flange assembly was fabricated from 347 CRES.

Sealing of the three separate assemblies was accomplished with double pressurized metal O-rings. Each seal ring contained a purge bleed which was pressurized to a pressure higher than the adjacent manifold pressure (either fuel or oxidizer). Pressurizing the bleed cavity not only energizes the metal O-rings but prevented leakage from within the injector manifolds.

The FLOX posts and orifice caps were brazed into the injector body assembly using Nicoral braze alloy. The body was designed so that each FLOX post passed through an interpropellant purge cavity as shown in Fig. 17. During a firing, this purge cavity was pressurized to a pressure greater than either the methane or FLOX manifold pressure. Thus, in the event of a braze joint failure during a run, the purge cavity would prevent contact between the fuel and oxidizer.

The injector subassemblies were pressure checked at appropriate times during fabrication to ensure the integrity of all welds and braze joints. In addition, the assembled injector was helium leak checked prior to each day of hot-fire testing.

To determine injector face heat flux levels, two thermocouples were installed in the injector face. The thermocouples were placed so that one was within the core region of the injector and the other in the peripheral zone (Fig. 14). The 10-mil-diameter Chromel-Alumel thermocouples were mounted by placing them in holes bored from the back side of the injector face. The holes were accurately counter bored to within 0.030 in. of the injector face.

The injector was instrumented to determine the following injection parameters:

1. CH_4 manifold static pressure (Taber 0 to 2000 psi transducer)

2. CH_4 manifold temperature (Chromel-Alumel thermocouple)

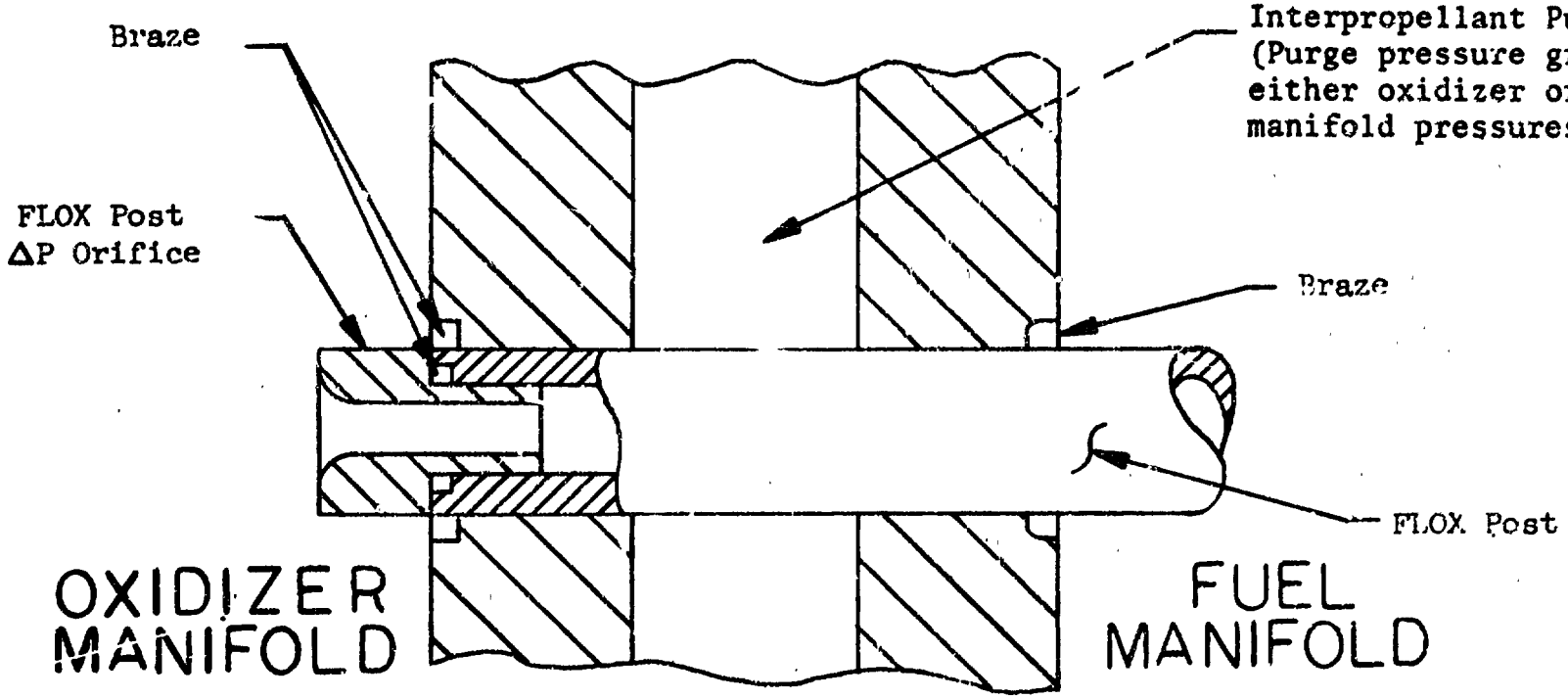

Figure 17. Schematic of Interpropellant Purge Cavity

3. CH_4 manifold dynamic pressure (Photocon model 307 transducer)

4. FLOX manifold static pressure (Taber 0 to 2000 psi transducer)

5. FLOX manifold temperature (sheathed Iron-Constantan thermocouple)

6. FLOX manifold dynamic pressure (Photocon model 307 transducer)

7. BLC manifold pressure (Taber 0 to 2000 psi transducer)

4.5 FULL-SCALE THRUST CHAMBER

The full-scale thrust chamber which was utilized for hot-fire evaluation was designed and fabricated in the like-doublet injector portion of the subject program (Ref. 4). Presented herein are the applicable design principles, the design approach, and the results of analysis.

The thrust assembly consisted of multiple cylindrical chamber sections with an attached conventional convergent-divergent nozzle. This design was selected to permit maximum use of available hardware while studying the effects of chamber L* on performance in the like-doublet portion of the program. Since the primary objective of the program was injector development and not thrust chamber design, a passively cooled ATJ graphite lined chamber configuration was chosen. This approach minimized thrust chamber cost while still providing a means of determining circumferential and axial chamber/nozzle heat flux profiles.

Dimensions of the thrust chamber assembly were established with the aid of the following system requirements, results from the analytical performance study (Section 3.0), and injector design consideration.

SYSTEM REQUIREMENTS

Propellants:	FLOX (82.6-percent F_2)/$CH_{4(g)}$
Nominal Operating Conditions:	P_c = 500 psia
	MR = 5.2 to 5.75
	Sea-Level Thrust = 3000 lbf with an Optimum Sea-Level Expansion Nozzle
Performance Level	99-percent c* Efficiency (shifting equilibrium)

The above requirements were employed to define pertinent dimensions (throat diameter, expansion ratio, etc.) of the thrust chamber assembly. The results of the analytical performance studies and injector design considerations were utilized in defining the chamber contraction ratio and characteristic chamber length.

Nozzle design details such as convergence angle, radius of curvature of the throat-to-throat radius ratio, etc., were similar to those commonly used on previous Rocketdyne research programs (Ref. 7 and 18). The selected nozzle parameters are listed below for the thrust chamber assembly:

Nozzle Throat Area, $in.^2$ = 3.96

Nozzle Throat Diameter, $in.^2$ = 2.245

Nozzle Expansion Ratio = 5.55 (optimum sea-level expansion at P_c = 500 psia and MR = 5.75)

Nozzle Convergent Angle, degrees = 30

Exit Nozzle (cone), degrees = 15

$$\frac{R_c}{R_t} = \frac{\text{radius of curvature of nozzle throat}}{\text{throat radius}} = 2.0$$

$$\text{Contraction Ratio} = \frac{A_c}{A_t} = \frac{\text{chamber cross-sectional area}}{\text{throat area}} = 3.0$$

Chamber Diameter, inches = 3.888

Chamber L*, inches = 10, 20, 30, and 40

In the analytical study, performance calculations were made using the vaporization rate and distribution-limited computer programs. Since distribution-limited c* efficiency is not a direct function of chamber geometry, only the vaporization-limited c* efficiency portion of the analytical performance study was considered in selection of the thrust chamber design.

The two most important variables affecting the vaporization-limited c* efficiency are propellant drop size and combustion chamber geometry. The effect of these two variables on $(\eta_{c^*})_{vap}$ was shown parametrically in Fig. 2 (Section 2.0) for FLOX (82.6-percent F_2)/CH_4(g).

As shown in Fig. 2, when propellant drop size is small, the effect of chamber geometry are generally attenuated. Conversely, when initial propellant drop sizes are large, chamber geometry effects become more pronounced. For a given initial drop size and chamber L*, vaporization-limited c* efficiency can be increased by reduction of the contraction area ratio (corresponding to an increase in physical chamber length). This (contraction ratio) effect is negligible at the high performance level (η_{c^*} > 95-percent); however, it becomes significant when $(\eta_{c^*})_{vap}$ drops below 95-percent. Note that the distribution-limited c* efficiency is assumed to be 100-percent.

Based on the above analytical performance study results, a 2:1 contraction ratio would have been selected for the basic thrust chamber assemblies. Injector design considerations, however, favored the use of a higher contraction ratio chamber for the like-double injector. A chamber contraction ratio greater than 2:1 was required to permit use of an injector with sufficient elements for good atomization and injector-chamber compatibility. Element feeding problems severely limit the number of elements that could have been used in 2:1 contraction ratio chamber/injector (like-doublet). Thus, a 3:1 contraction ratio chamber was chosen for the chamber assembly.

By the addition of cylindrical sections, chamber L* was variable over the 10- to 40-in. range. In addition, the chamber L* and contraction ratio were similar to those commonly employed in related programs (Ref. 22), thus permitting direct comparisons to be made between program results.

The cylindrical chamber/nozzle sections consisted of a stainless-steel shell (or housing) with an ATJ graphite liner. The steel shells were made from CRES 321 pipe and had welded flanges. A liner thickness of 1 in. was sufficient to permit test durations suitable for definition of performance and transient chamber/nozzle heat transfer characteristics. Chamber construction was similar to that successfully used in Contract NAS7-304 (Chamber Technology for Space Storable Propellants; Ref. 18).

The nozzle convergence angle (30 degrees) and exit configuration (15-degree cone) are similar to those commonly used in numerous research programs at Rocketdyne (Ref. 7 and 18). A radius of curvature of the nozzle throat-to-throat radius ratio (R_c/R_t) of 2.0 was chosen because the nozzle discharge coefficient for this specific configuration is well defined. A known nozzle discharge coefficient is essential for a valid definition of performance (based on chamber pressure measurement).

For calculation of a "valid" performance value (based on chamber pressure measurement), care must be taken to ensure measurement of a "valid" static chamber pressure near the start of nozzle convergence. Experience gained on related programs at Rocketdyne (Ref. 18 and 20) indicate that an increase in static chamber pressure can occur near the start of convergence. This increase in pressure appears to be caused by subsonic deceleration effects associated with the turning of the combustion gases prior to acceleration in the nozzle. The magnitude of this increase is dependent on the geometric configuration of the nozzle. Measurement of the static pressure must be taken sufficiently upstream of the start of convergence so that its value is not affected by the subsonic decelerating effects discussed above. Furthermore, chamber pressure must be measured where combustion is nearly complete.

To ensure that the proper static chamber pressure measurement was employed for calculation of performance, the hot-fire static pressure profile along the wall of the nozzle section was determined. Two rows of pressure taps 180 degrees apart are located 0.50 and 1.25 in. from the nozzle assembly inlet. The start of nozzle convergence was 1.462 in. upstream of the plane of minimum nozzle area.

The nozzle was designed with an optimum sea level expansion ratio (5.55) at the nominal design operating conditions (MR = 5.75; P_c = 500 psia). Nozzle exit base pressure was measured by means of pressure taps placed in the nozzle retainer ring to provide nozzle base pressure information for calculation of performance based on thrust measurements.

Thermocouples were installed in the ATJ graphite chamber liner for the determination of chamber wall heat flux data. The method of thermocouple placement was identical to that used to instrument the single-element thrust chambers. In the full-scale chamber, thermocouples also were installed in the nozzle section to determine nozzle heat flux levels. However, in the convergent and throat areas of the nozzle the thermocouple tips were installed 0.250 in. from the inner surface as compared to 0.180 in. in the cylindrical portion of the chamber. This increased thermocouple depth was based on higher anticipated heat flux levels in the nozzle section.

5.0 SINGLE-ELEMENT COLD-FLOW RESULTS

This section describes the results of the cold-flow studies (mixing and atomization) which were conducted with the candidate "core" and "peripheral" elements. Preceeding the experimental results the rationale for the selection of the test variables and design configurations are presented.

5.1 SELECTION OF EXPERIMENTAL VARIABLES

Results from a previous Rocketdyne technology program (Ref. 21) indicated that for gas/liquid coaxial injectors the following physical parameters influenced the resulting mixing and atomization characteristics: (1) the injection velocity of the gas (Vg), (2) the injection velocity of the liquid (V_L), and (3) the density of the gas phase (ρ_g). For a specific element, the aforementioned variables are a function of the flowrates of fuel and oxidizer through the element as well as the combustion pressure. Experimentally, the variables can be changed in several ways. For instance, the liquid injection velocity, V_L, can be varied by changing the liquid flow area, the flowrate of liquid, or the density of the liquid phase. However, for a given propellant combination, once a thrust-per-element value is chosen, the only variable that can be changed by the injector design is the liquid flow area (i.e., D_L). Similar arguments can be given for the gas injection velocity. Thus, a thrust-per-element value was chosen and the variables V_g and V_L were systematically varied by changing the geometric variables of the element (i.e., D_L and h; see Fig. 7). In addition, the flow-per-element was varied to determine thrust level effects.

The referenced study also indicated that oxidizer post recess and oxidizer jet swirl significantly affect element performance. Thus, these variables also were chosen for investigation.

The nominal thrust level of the circular coaxial element which was chosen for characterization was 70 lbf (FLOX/CH_4(g), P_c = 500 psia) at optimum sea level expansion. This size of element had previously been employed in thrust chamber technology programs (Ref. 21) and, at the inception of the program, was considered to be a candidate element thrust level for the FLOX/CH_4(g) breadboard engine. The nominal design values selected for the element operating conditions for the FLOX/CH_4(g) propellant system were as follows:

P_c = 500 psia (ρ_{fuel} = 1.45 lbm/ft^3)
MR = 5.25 to 5.75
Fuel Temperature = 530 R
FLOX Density = 89 lbm/ft^3

In cold-flow simulation of these hot-fire conditions, it was possible to model all of the above-mentioned variables (i.e., ρ_{fuel}, V_{gas}, etc.) except the density of oxidizer. Water (ρ = 62.4 lbm/ft^3) was employed as oxidizer simulant in the mixing experiments and Shell-270 wax (ρ = 47.1 lbm/ft^3) was used as oxidizer simulant in the atomization experiments. Thus, for a given liquid flowrate, liquid injection velocities in the mixing, atomization, and hot-fire experiments were not equivalent.

To simulate the dynamic conditions of a hot-fire gas/liquid propellant system, both mixing and atomization experiments were conducted in pressurized environments with single-element injector models. Conducting the experiments in a pressurized environment allowed for the exact modeling of the hot-fire gas-phase density, which previously had not been possible with ambient pressure experiments. Descriptions of the pressurized mixing and atomization facilities are presented in Appendixes B and C, respectively.

5.1.1 Core Element Injectors

The core element concept which was chosen for characterization is shown in Fig. 7. Shown in Table II is the range of the pertinent variables which were investigated in the cold-flow effort.

TABLE II. RANGE OF COLD-FLOW VARIABLES

Parameter	Symbol	Range
Liquid Jet Diameter (oxidizer)	D_L	0.070, 0.108, 0.136 in.
Gas Gap Height (fuel)	h	$0.005 \leq h \leq 0.041$ in.
Oxidizer Post Recess	R	$0 \leq R \leq 4\ D_L$
Gas Velocity in Annulus (fuel)	V_g	$100 \leq V_g \leq 630$ ft/sec
Diffused Liquid Velocity at Post Tip (oxidizer)	V_L	$5 \leq V_L \leq 100$ ft/sec

To investigate the effects of the liquid (oxidizer) injection velocity, three oxidizer post sizes were configured, and their respective dimensions also are shown in Fig. 7. To investigate the effects of the injected fuel velocity, the annulus gas gap (h) was changed by varying the diameter of the fuel orifice. Provisions were made to vary the amount of the oxidizer post recess from flush (R = 0) to four post diameters (R = 4 D_L) by the insertion of spacers in the models.

All the "core" candidate elements were configured with a diffuser section at the exit of the oxidizer post. The diffuser section was incorporated in the design since available data indicated that increasing the relative velocity between the gas and liquid streams (V_g-V_L) was conducive to improving mixing and atomization performance (Ref. 21). In addition, the diffuser section not only lowers the liquid injection velocity but imparts a finite amount of radial momentum to the liquid jet.

5.1.2 Peripheral Element Injectors

The two candidate "peripheral" element configurations consisted of a baseline BLC element and a scarfed post with swirl element as shown in Fig. 9.

The BLC configuration was designed to provide coolant flowrates based on typical Rocketdyne J-2 engine data. Accordingly, the element was designed to operate with approximately 6 to 10 percent of the total fuel flow as BLC*. At the 6-percent BLC level, the injection velocity of the BLC gas was approximately equal to the gas velocity in the fuel orifice annulus.

The scarfed post with swirl element was designed with a post scarf angle of 22-1/2 degrees. That value of post scarf angle had been employed in similar FLOX/CH_4 injector programs (Ref. 22).

5.2 CORE ELEMENT MIXING RESULTS

Parametric mixing experiments were conducted with candidate core elements to determine the effects of gas velocity, liquid velocity, throttling (gas density and flowrate), element mixture ratio, oxidizer post recess, and oxidizer jet swirl on the mixing characteristics of coaxial elements. Additional tests with increased flow per element (i.e., thrust/element) were performed. Analogous atomization experiments will be discussed in subsequent paragraphs.

The experiments were designed so that the effects of gas and liquid velocity could be assessed independently of the other test variables. As an example, to determine the effects of liquid injection velocity, the diameter of the oxidizer jet (D_L) was varied along with the diameter of the gas orifice (D_g) to maintain the gas velocity constant with constant total propellant flowrate and mixture ratio. However, it should be noted that, in the throttling experiments, the parameter V_L cannot be held constant when the experiments are conducted with a fixed piece of hardware. Similarly, for the mixture ratio experiments, V_g and V_L vary for tests conducted with a constant total element flowrate.

5.2.1 Selection of Mixing Measurement Plane

To select a common measurement plane for the mixing experiments, tests were conducted with the No. 1 element (Fig. 7) configuration wherein mixing levels were determined at two separate distances from the injector face. Figure 18 presents the results of these experiments which show that, for this element configuration, mixing proceeds rapidly within the first 2 inches of mixing length. Mixing appears to be nearly complete at the 5-inch collection distance.

A common measurement plane of 5 inches was selected for subsequent experiments based on the data of Fig. 18 and the consideration of spacial resolution. For a nominal 70-lbf element, the diameter of the spray field at the 2-in. measurement plane was on the order of 0.75 in. whereas, at the 5-in. plane, the spray field width was approximately 1.5 in. in diameter. Thus, measuring at 5 in. allowed the spray field to be studied in greater detail than would have been possible at the 2-in. measurement plane. All of the single-element mixing experiments were conducted in a chamber which was 3.0 in. in diameter.

*BLC percentage is defined as percent if total engine fuel flow.

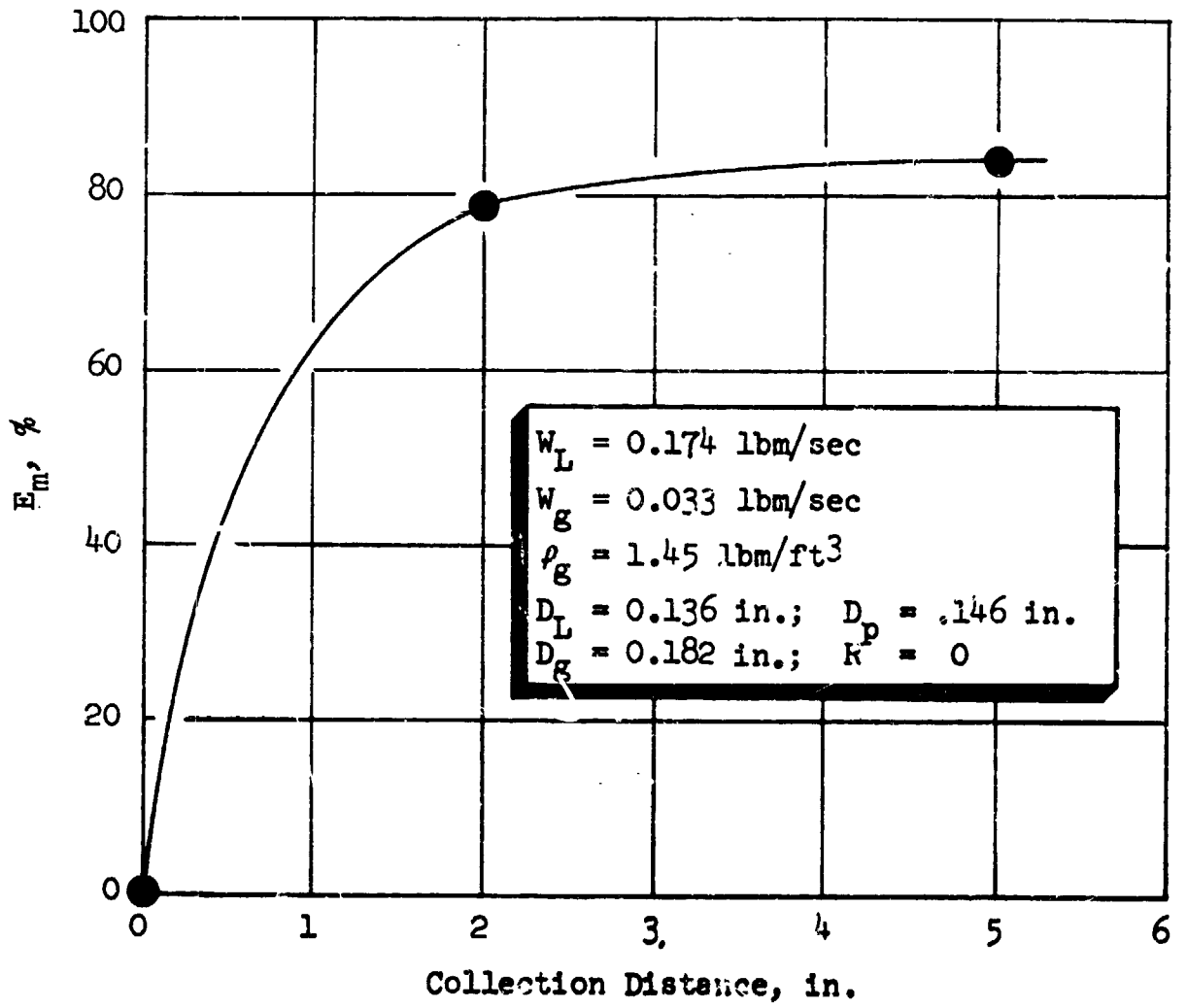

Figure 18. Mixing Efficiency as a Function of Collection Distance

5.2.2 Core Element Parametric Mixing Results

To determine the independent effects of gas velocity, the gas annulus thickness ("gas gap") of the No. 1 element configuration (D_L = 0.136 in., D_g = 0.182 in.) was varied from 0.005 to 0.041 in., keeping the oxidizer post diameter constant (D_p = 0.146 in.). The mixing tests were performed for ρ_g = 1.45 lbm/ft^3, MR = 5.25, and for flush and recessed oxidizer post. Total element mass flow, $\dot{w}_g + \dot{w}_L$, was also maintained constant. Figure 19 presents the results of the mixing experiments which are plotted as E_m versus gas gap velocity. As indicated, the mixing factor, E_m, was found to increase as the gas gap velocity was increased from 134 to 630 ft/sec. Shown at each point are corresponding values for FLOX/CH_4 mixing limited c* efficiency, $\eta_{c^*,mix}$.

The effects of oxidizer injection velocity on mixing were investigated by changing the exit diameter of the oxidizer post (see the three element configurations of Fig. 7). All experiments were performed with a constant mixture ratio and total propellant flowrate ($\dot{w}_L$ = 0.174 lbm/sec, $\dot{w}_g$ = 0.033 lbm/sec). The gas annulus for each oxidizer post configuration was designed to maintain the gas gap velocity constant (V_g = 350 ft/sec). The measured mixing efficiency is shown in Fig. 20 as a function of oxidizer velocity for different values of FLOX post recess. For a flush oxidizer post, the mixing efficiency was relatively constant for the range of liquid velocities which were investigated. At a post recess of 1 D_L, however, the mixing efficiency showed a decidedly downward trend as the oxidizer velocity was increased.

The throttling characteristics of the No. 1 element configuration (D_L = 0.136 in.) are presented in Fig. 21. The experiments were performed for a constant mixture ratio and the total propellant flowrate was maintained proportional to the simulated gas phase density (i.e., the tests simulated throttling a hot-fire injector at constant mixture ratio). Results are presented for both a flush and recessed oxidizer post for a 5.6:1 throttling range. The data show a significant decrease in mixing limited performance as the element was throttled (i.e., ρ_g and flowrate decrease) for both the flush and recessed post. Note, however, the high mixing performance (E_m = 95.6%) of the recessed element at the design condition (ρ_g = 1.45 lbm/ft^3, MR = 5.25). For the FLOX/CH_4(g) propellant system at 500 psia, that value of E_m corresponds to $\eta_{c^*,mix}$ = 99.6%.

Figure 22 presents additional throttling data which were obtained employing elements with different post sizes (D_L = 0.136, 0.108, 0.070 in.). The data were obtained for a nominal oxidizer post recess of approximately one liquid orifice diameter. As indicated, for all three configurations, the mixing efficiency significantly decreased as the elements were throttled. Note that the mixing of the largest (D_L = 0.136 in.) element, i.e., the one with the lowest liquid velocity, was significantly superior to the other two configurations over the entire throttle range.

The independent effects of element injected mixture ratio were determined utilizing the No. 1 (D_L = 0.136 in.) element configuration. Figure 23 presents the results of the mixing experiments for two values of post recess. For a flush oxidizer post, decreasing mixture ratio resulted in increased mixing efficiency. At

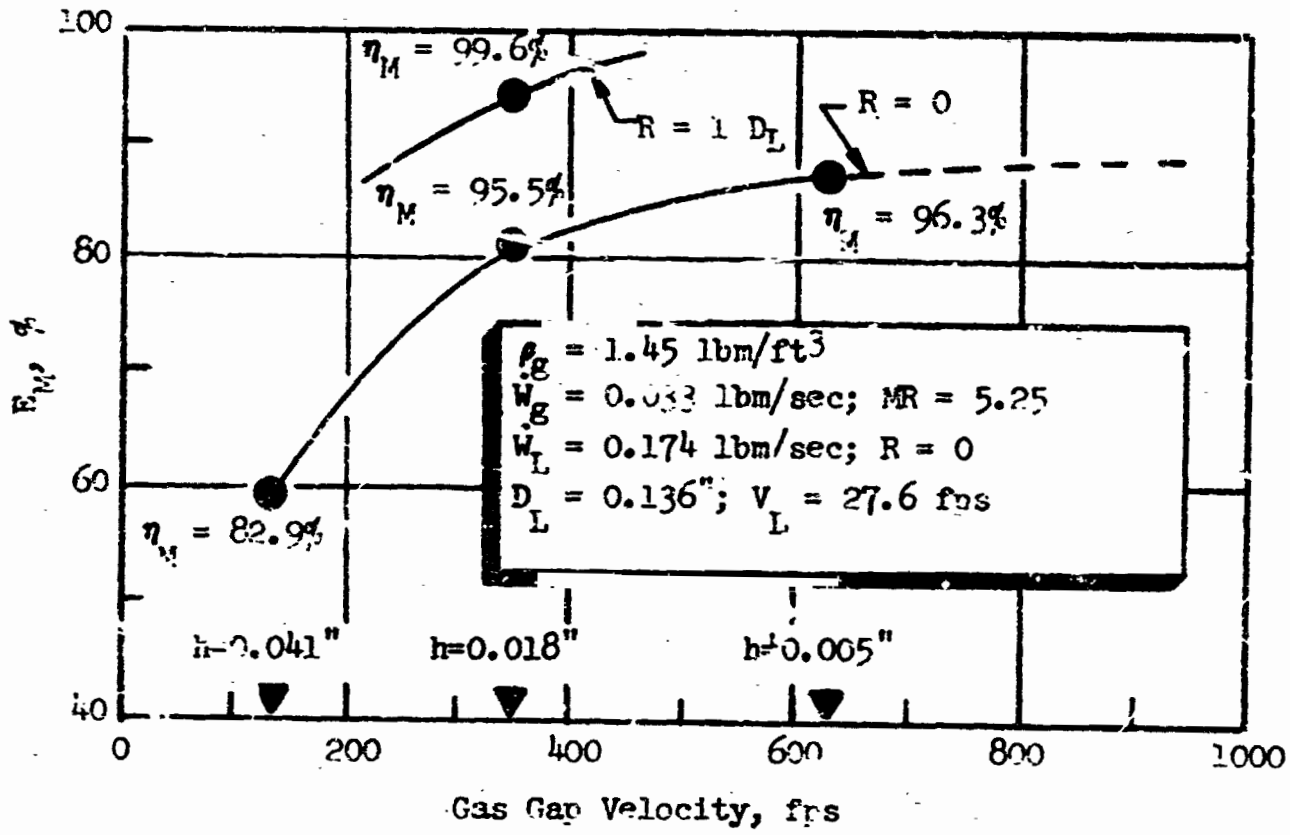

Figure 19. Effects of Gas Gap Velocity Changes as a Result of Variations in the Gap Height

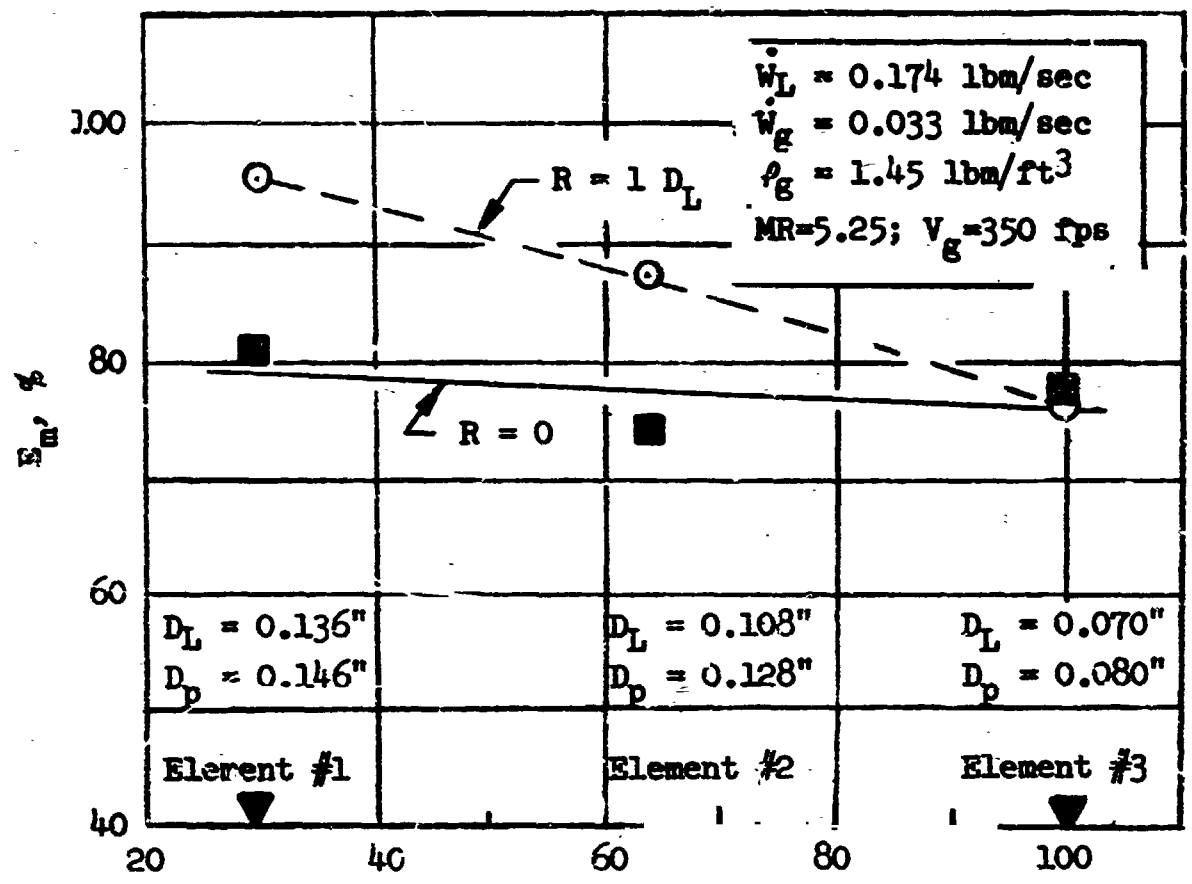

Figure 20. Effect of Liquid Injection Velocity Varied by Changing the Liquid Orifice Size

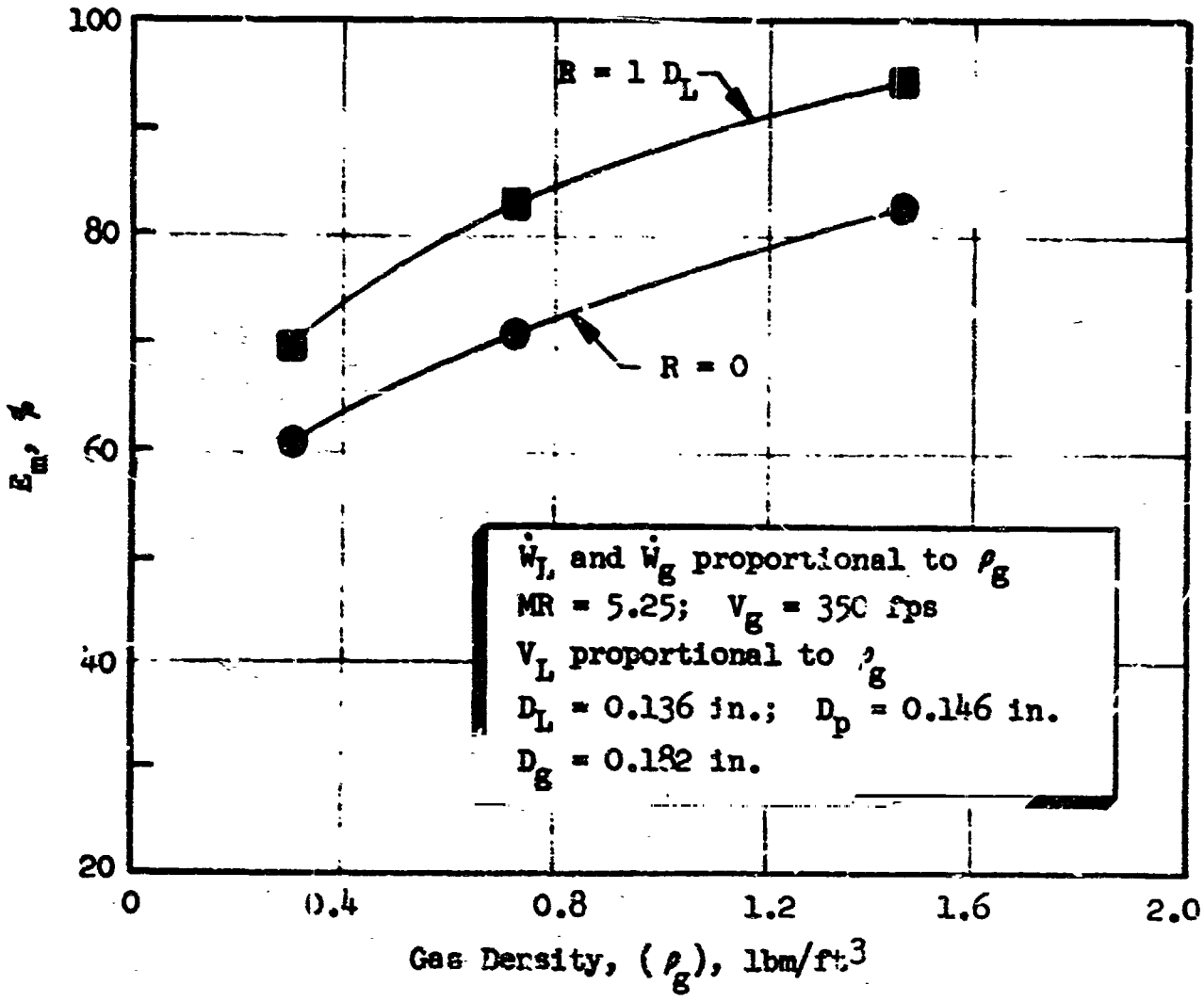

Figure 21. Throttling Characteristics of Coaxial Element With Flush and Recessed Oxidizer Posts

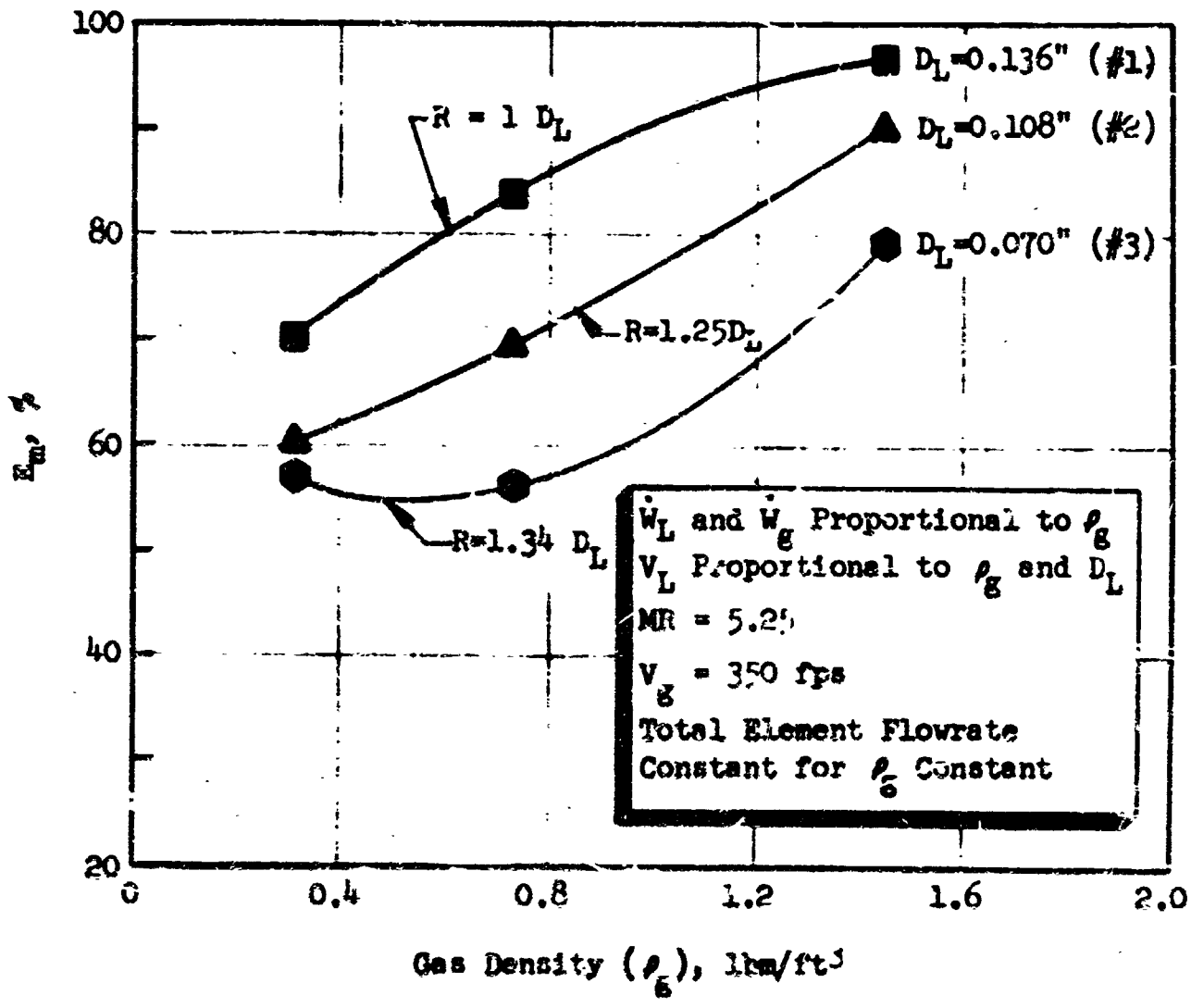

Figure 22. Throttling Characteristics for Coaxial Elements With Various Size Liquid Orifices (D_L)

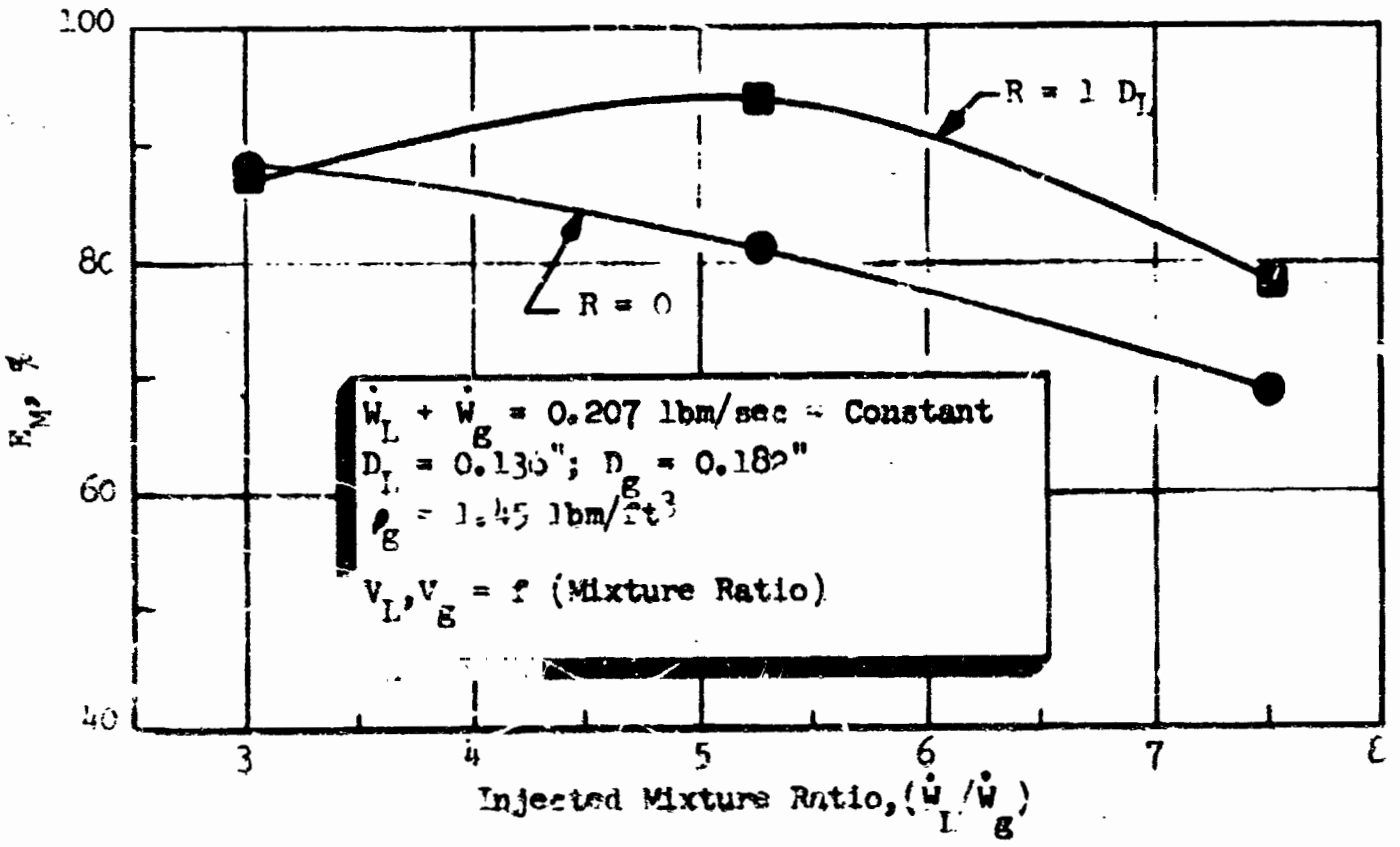

Figure 23. Effects of Injected Mixture Ratio With and Without Post Recess

a post recess of 1 D_L, an optimum point at approximately the design FLOX/CH_4 mixture ratio was found. These results indicate that, from a mixing standpoint, recessing the oxidizer post may not be beneficial for low element mixture ratios (MR < 4).

The independent effects of FLOX post recess were determined for a gas phase density of 1.45 lbm/ft^3 and MR = 5.25 (and fixed total flow). Figure 24 presents the mixing test results for the three element configurations. As indicated in the figure, a distinct optimum for the D_L = 0.136 in. configuration was found for a recess of approximately 1 liquid jet diameter. Increasing the post recess from 2 to 4 D_L resulted in essentially the same mixing performance. The D_L = 0.108-in. configuration exhibited an apparently similar trend, but oxidizer post recess did not affect the D_L = 0.070-in. configuration mixing efficiency over the range investigated. These results demonstrate that geometric scaling of oxidizer posts may result in substantially changing the influence of post recess on the element mixing efficiency. Note, however, that for a post recess of approximately 1 D_L, mixing performance decreased as the oxidizer post size was decreased (i.e., V_L increased; see Fig. 20).

One mixing test was conducted with the No. 1 element to determine the effects of swirling the oxidizer jet. The test was conducted at R = O with the 45-degree in-line helical swirler (Fig. 8). The test was at the nominal design condition (ρ_g = 1.45 lbm ft^3 $\dot{w}_{tot}$ = lbm/sec and MR = 5.25) which resulted in an E_m = 90.8 percent as compared to a mixing level of E_m = 83 percent when the oxidizer jet was not swirled.

Two mixing tests were conducted to determine the effects of increasing the nominal design flowrate (i.e., increasing the thrust/element) of the No. 1 element at R = O. Figure 25 presents the results of these tests which show that the mixing level decreased as flowrate per element was increased. These data were utilized together with throttling data to construct a map of the mixing characteristics of the No. 1 element as a function of total element flowrate, gas velocity, and gas-phase density (see Section 7.0).

Additional post recess tests were conducted with the No. 1 element employing increased total element flowrates. Figure 26 presents the results of these tests for the nominal design condition (P_c = 500 psia, MR = 5.25) at a thrust-per-element level of 14 lbf. Note that both the gas and liquid velocities were twice those employed in the post recess series of Fig. 24. At higher thrust-per-element levels, an optimum recess value was not obtained for recess depths up to 2 D_L. However, recessing the oxidizer post was beneficial to mixing and and optimum point could occur for some recess greater than 2 D_L. These data and those of Fig. 24 clearly indicate that post recess mixing effects are a complex function of element geometry as well as element operating conditions.

5.2.3 Core Element Mass Flux Profiles

The influence of design and operating parameters on mixing quality, E_m, may be physically understood by examining the local gas and liquid mass flux distributions. Figure 27 presents the "normalized" $(MMF_i = \dot{w}_i/A_i)_{local}/\dot{w}_{i,tot}$, i = gas or

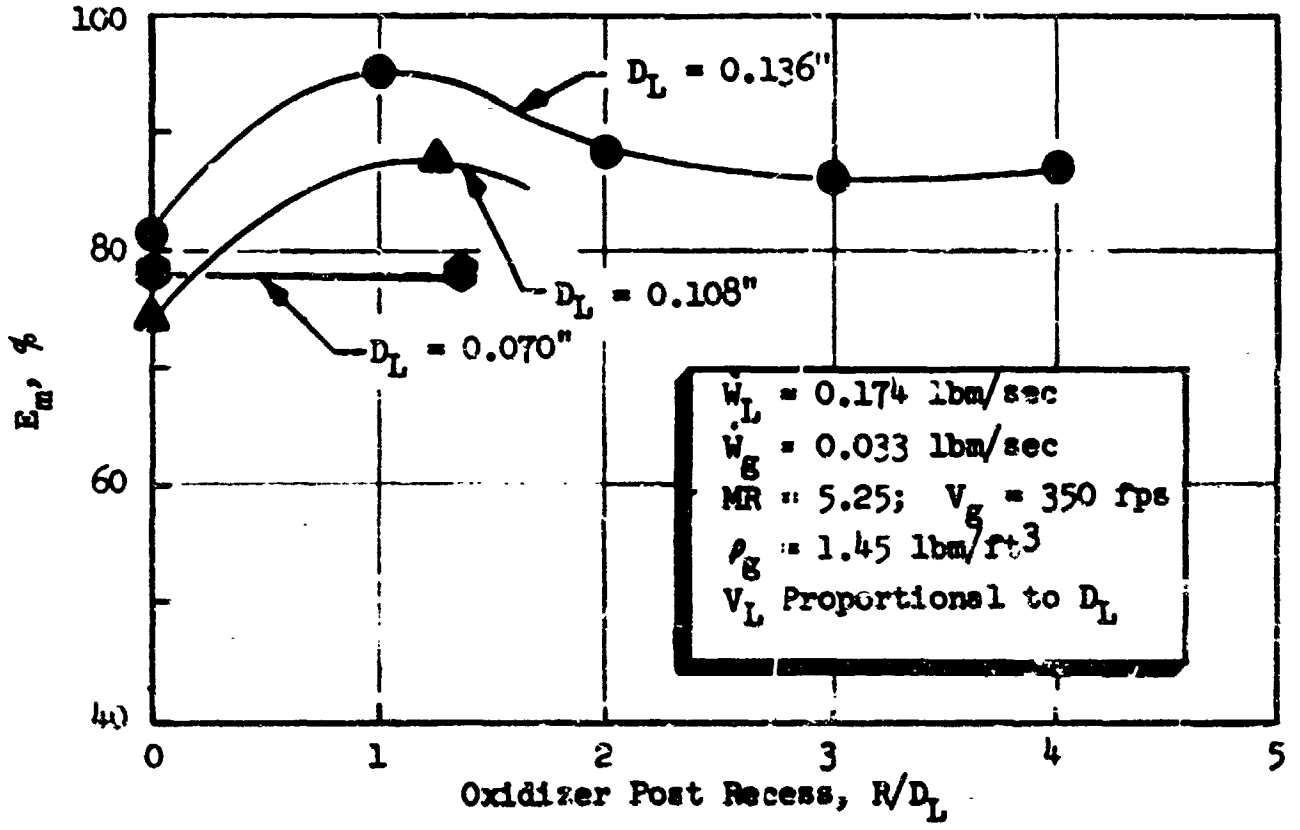

Figure 24. Effects of Oxidizer Post Recess for Various Size Liquid Orifices (D_L)

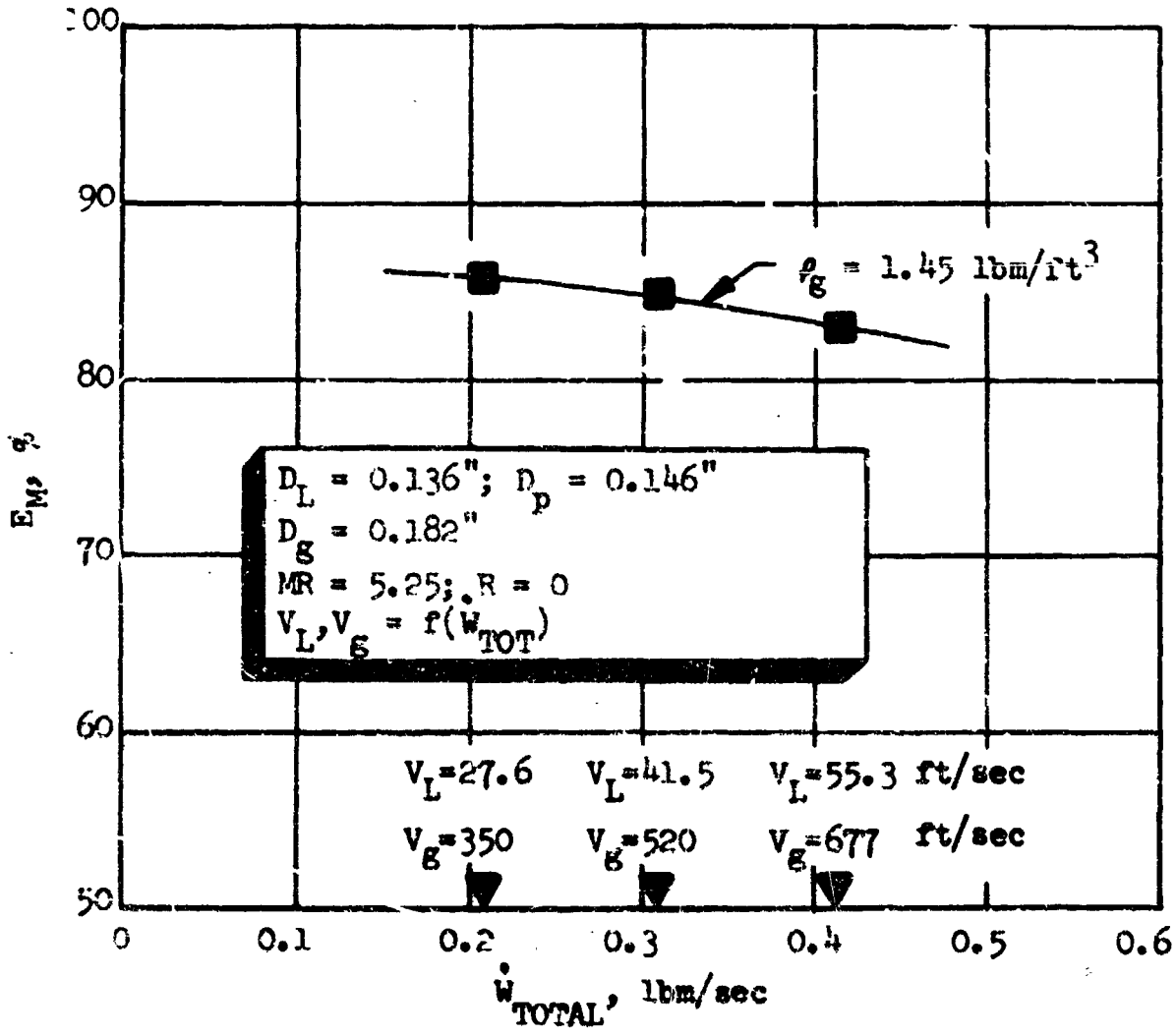

Figure 25. Mixing Effects of Flowrate-Per-Element With Fixed Element Geometry

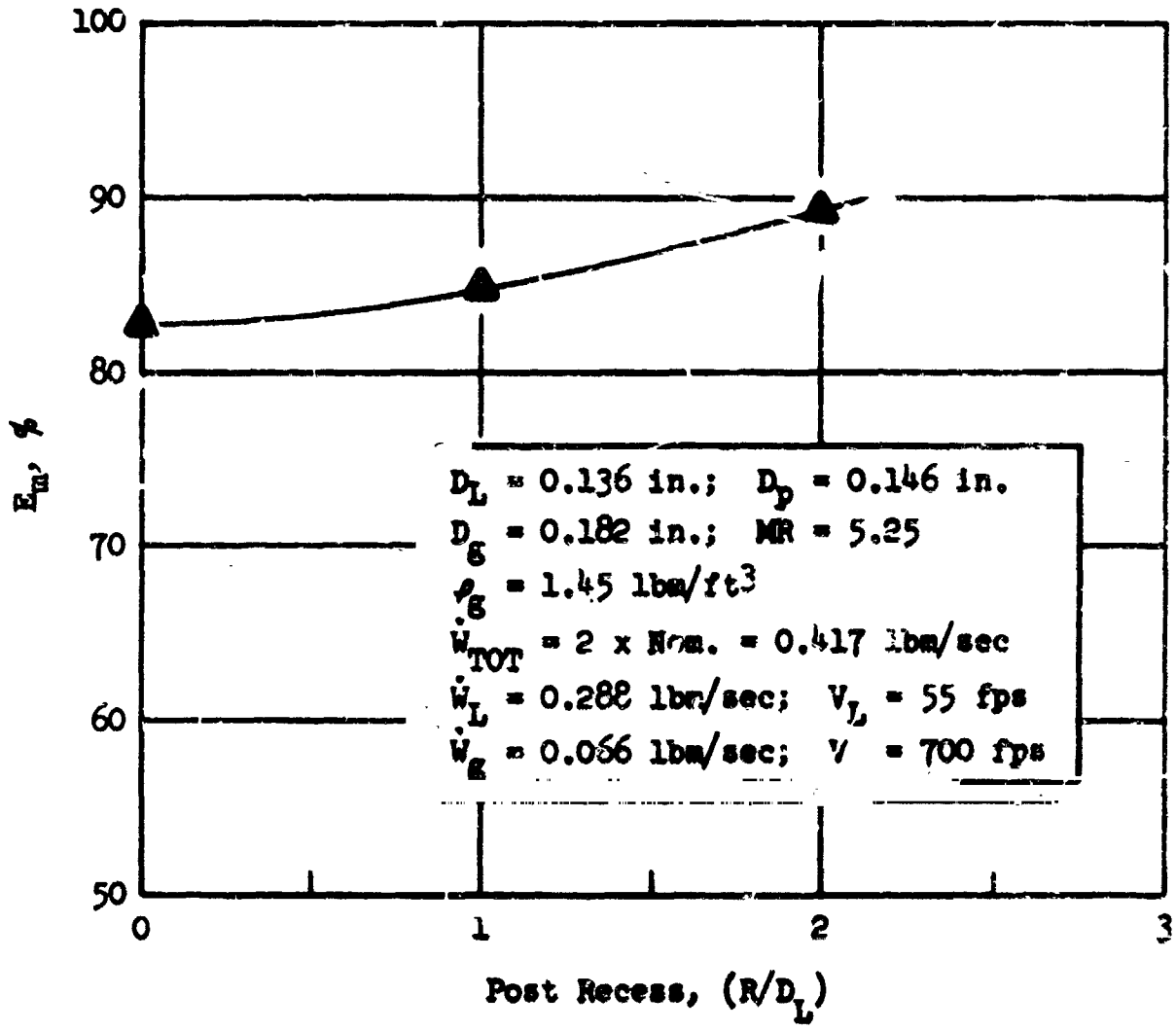

Figure 26. Mixing Effect of Oxidizer Post Recess for No. 1 Element at a Thrust Level of 140 lbf

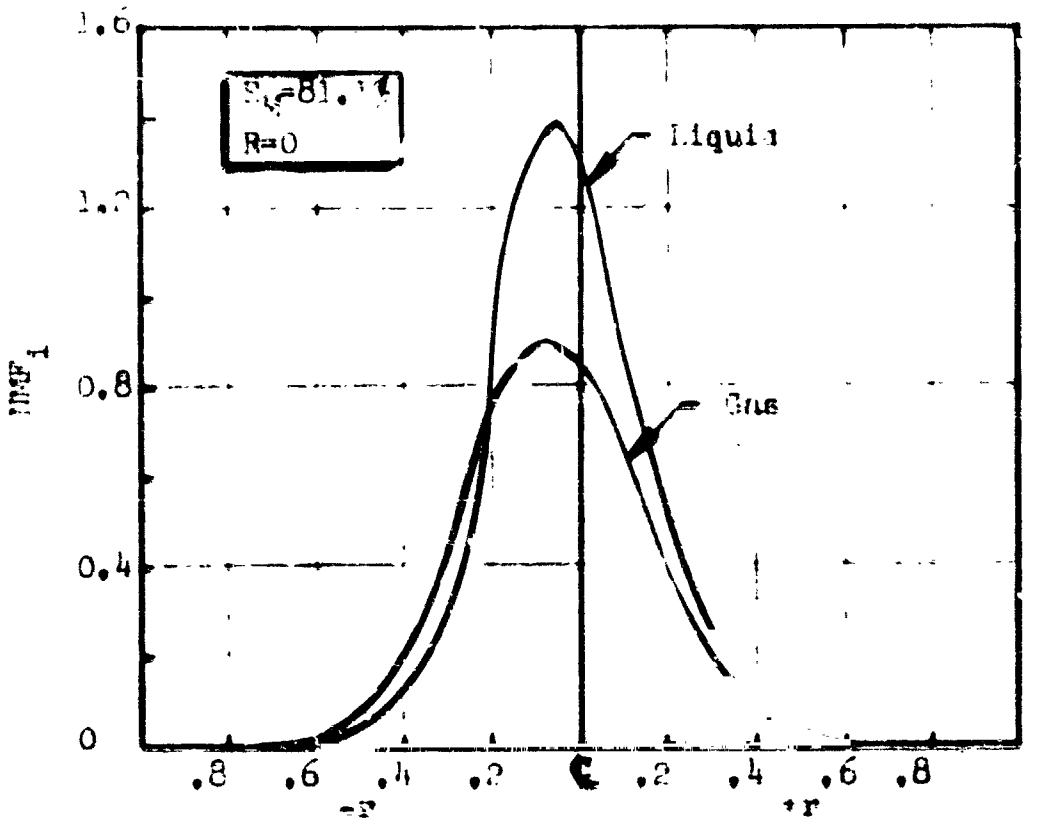

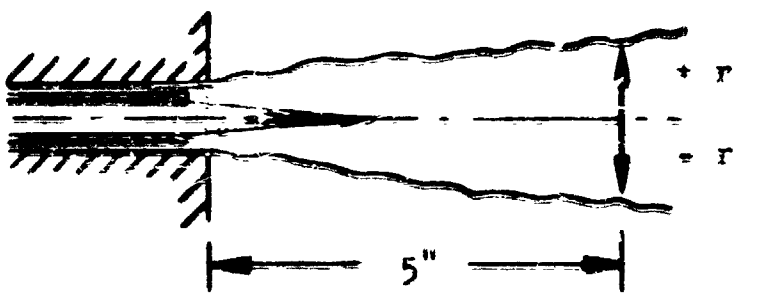

D_L = 0.136"
D_T = 0.136"
D_g = 0.180"
$\dot{w}_L$ = 0.174 lbm/sec
$\dot{w}_g$ = 0.033 lbm/sec
ρ_g = 1.45 lbm/ft^3

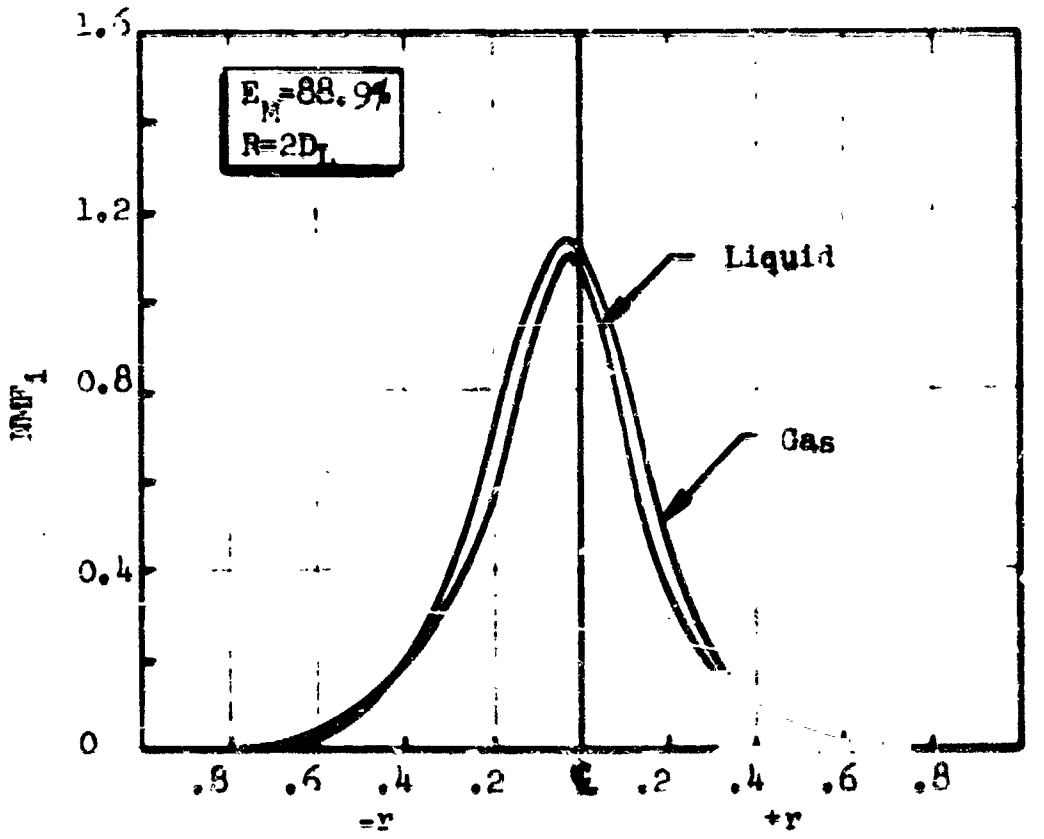

Figure 27. Gas and Liquid Mass Flux Profiles

liquid) gas and liquid mass fluxes for the series of experiments which utilized the No. 1 element configuration to determine the effect of oxidizer post recess. Note that the mass flux is "normalized" only with respect to total propellant flowrate and not with respect to area.

Plotting the "normalized" mass fluxes allows for a visual determination of the uniformity of the sprayfield. That is, if local values for the "normalized" liquid and gas mass flux coincide, then, at that point, the local mixture ratio is equal to injected mixture ratio. If the liquid values are higher than the gas, then the local mixture ratio is greater than the injected mixture ratio, and vice versa. For complete mixing (i.e., E_m = 100 percent) the curves would coincide both spacially and in magnitude.

Figure 27 presents "normalized" mass flux data for two values of oxidizer post recess (R = 0, and 2 D_L). At the condition of zero post recess, note that near the centerline of the spray field the local mixture ratios are higher than the injected mixture ratio. In one outer zone of the spray field (-r > 0.2 in.) the mixture ratios are less than the injected mixture ratios. The net result of the combination of the profiles is a degradation in the mixing quality of the spray field (i.e., E_m = 81.1 percent). When the oxidizer post was recessed to a value of 2 D_L, the flux profiles more nearly coincide throughout the sprayfield. Thus, high mixing quality (E_m = 88.9) was obtained.

Figure 28 presents "normalized" mass flux profiles for the No. 1 core element with the 45-degree in-line helical swirler. Data for the same element without oxidizer swirl are shown for comparison. It is evident that by swirling the liquid jet, the coring (i.e., high liquid mass flux near the centerline of the element) of the liquid jet was reduced significantly. The net result in decreasing the coring of the liquid jet was an improvement in the mixing performance (i.e., E_m increased from 83 to 90.8 percent).

Examination of cold-flow data, as shown in Fig. 27 and 28, provides the experimentor not only with information in regard to the mixing characteristics of the element but, also, information in regard to the mass flux and mixture ratio characteristics. By examination of mass and mixture ratio profiles in the outer zones of the spray field, the relative chamber wall heat transfer characteristics of elements can be assessed. These data are useful for the selection of injector peripheral elements for enhanced injector/chamber compatibility, as will be discussed in a subsequent section.

5.2.4 Correlation of Core Element Mixing Data

The mixing results presented in Fig. 19 through 24 were analyzed to determine if a single parameter could be found to correlate the results in terms of pertinent variables. The correlating parameter was formulated by considering the dynamic and operating variables that could be expected to control the stripping of the liquid jet by the high-velocity gas annulus. The variables included the kinetic energy of the high-velocity gas ($\rho_g V_g^2$), an operating variable proportional to the residence time of the liquid jet (V_l), the density of the gas phase (ρ_g), and the ratio of liquid mass to gas mass (MR). These variables were formulated into a

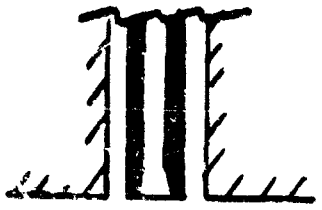

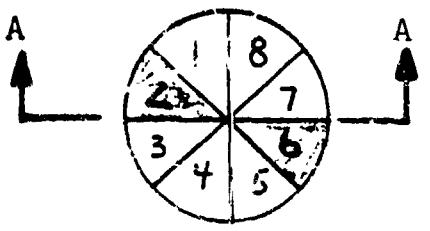

LIQUID

GAS

CORE ELEMENT

Sector 2

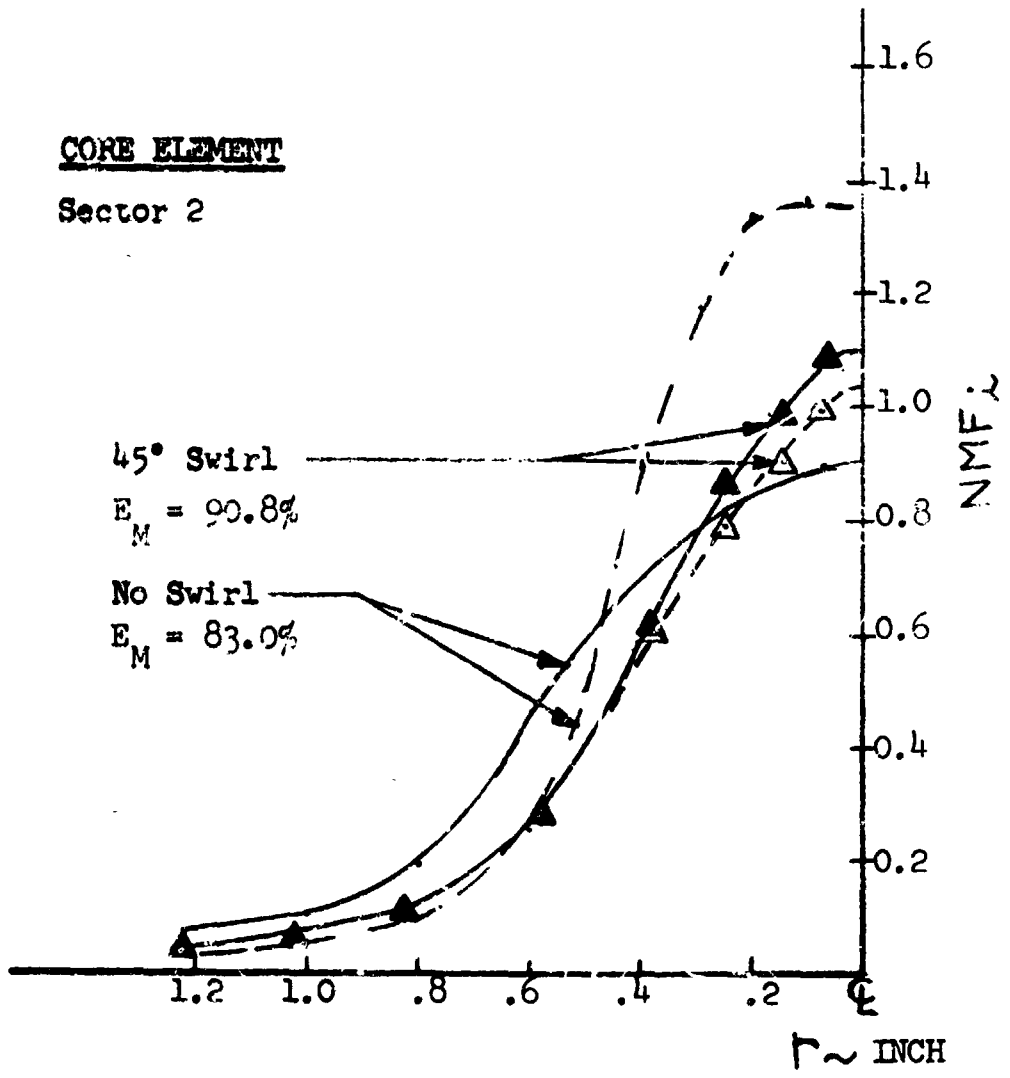

$\dot{W}_L$ = 0.174 lbm/sec

$\dot{W}_g$ = 0.033 lbm/sec

ρ_g = 1.45 lbm/ft^3

MR = 5.25

R = 0

Figure 28. Effect of Oxidizer Jet Swirl

single parameter by considering the qualitative trends of the data. Figure 29 presents a correlation of the mixing data (E_m) with the parameter $(\rho_g V_g)^2/(MR \cdot V_L)$. As indicated in the figure, the parameter provides a reasonable correlation of the mixing data.

Note that separate curves are necessary for different post recess (R = 0, R = 1 D_L). For almost all values of $(\rho_g V_g)^2/(MR \cdot V_L)$, the recessed post gave better mixing, but the difference becomes nil for values above about 6000 lbm^2/ft^5-sec.

5.2.5 Cold-Flow Mixing Data

Summarized in Table III are pertinent data measured and calculated from the single-element cold-flow mixing experiments. Sufficient data are supplied for the calculation if the element operating conditions (i.e., V_g, V_L, ρg, etc). Also shown is the element configuration for each test.

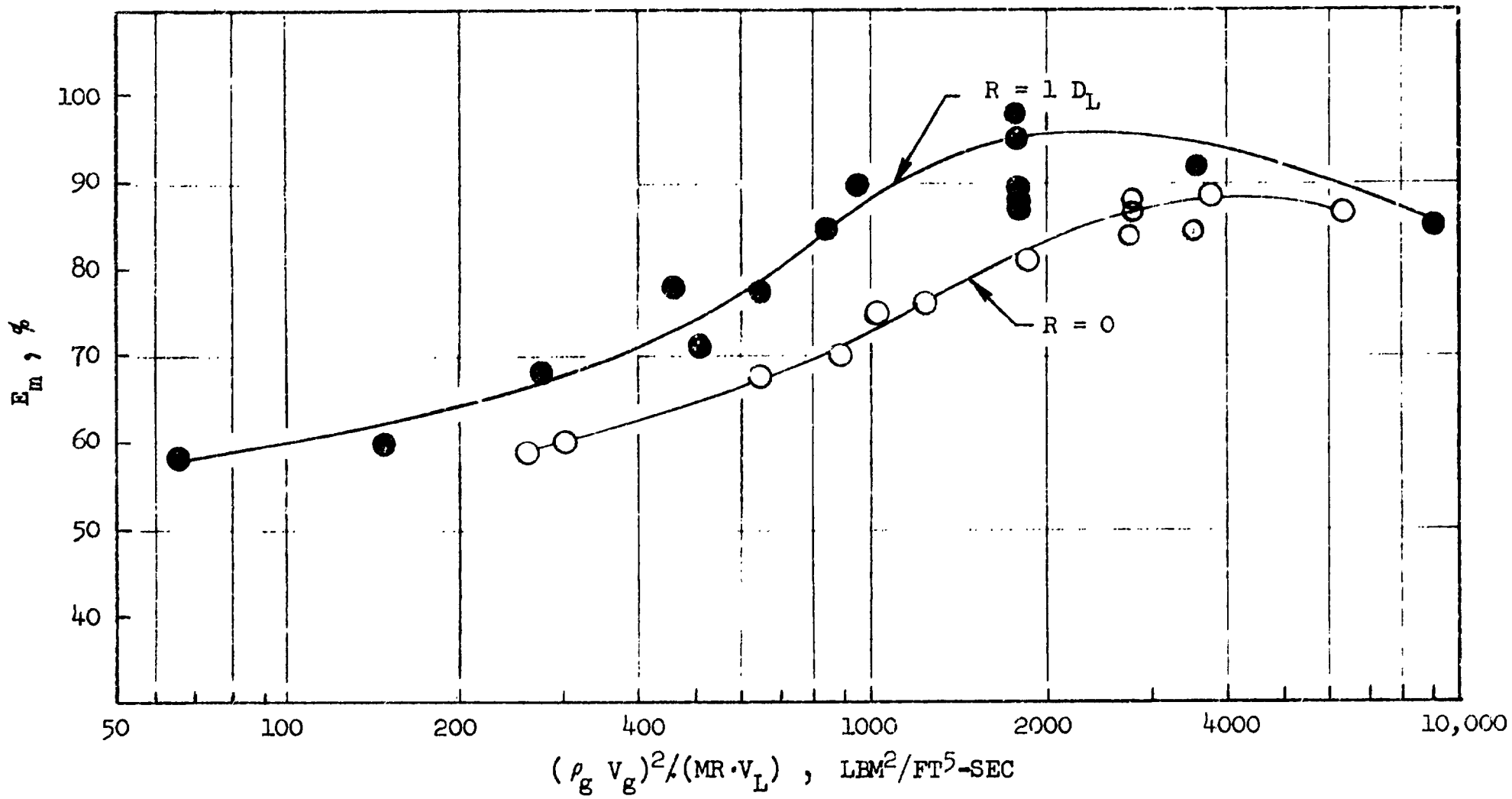

Figure 29. Correlation of Core Element Cold-Flow Mixing Data

TABLE III. GAS/LIQUID MIXING DATA
(Simulants: Fuel-Air, Oxidizer-Water; ρ = 62.4 lbm/ft^3)

Run No.	$\dot{W}_{Liq}$ (lbm/sec)	$\dot{W}_{Gas}$ (lbm/sec)	Pressure (psig)	Gas Injection Temperature (°R)	E_M (%)	D_L (In.)	D_p (In.)	D_G (In.)	R (In.)	Comments
006	.1740	.0333	265	510	81.09	.136	.146	.182	0	All measurements at 5" from injector face unless noted.
007	.1543	.0524	265	495	88.54					
008	.1745	.0333	129	484	75.44					
009	.0250	.0080	32	499	76.56					
010	.0301	.0056	32	509	59.57					
011	.1740	.0333	121	481	87.57					
012	.1740	.0333	265	510	59.11			.228		
013	.1740	.0333	265	486	87.91			.166		
014	.1740	.0331	265	514	95.64			.182	.136	
015	.1740	.0331	265	515	88.91				.272	
016	.1740	.0332	265	512	86.14				.408	
017	.1740	.0334	265	507	87.63				.544	
018	.0879	.0163	121	528	32.36				.136	
019	.0301	.0055	32	534	69.33					
020	.1543	.0522	265	496	87.71					
021	.1830	.0244	265	515	77.74					
022	.1830	.0243	265	516	68.20				0	
023	.1740	.0327	265	523	78.99	.070	.080	.136		
024	.1740	.0329	265	516	78.01				.094	
025	[illegible]	[illegible]	121	526	56.31					
026	.0301	.0053	32	573	57.70					
027	.1740	.0326	265	525	74.81	.108	.122	.166	0	

TABLE III. (Concluded)

Run No.	$\dot{W}_{Liq}$ (lbm/sec)	$\dot{W}_{Gas}$ (lbm/sec)	Pressure (psig)	Gas Injection Temperature (°R)	E_M (%)	D_L (In.)	D_p (In.)	D_G (In.)	R (In.)	Comments
028	.1740	.0319	265	551	88.98	.108	.122	.166	.136	
029	.0875	.0159	121	557	68.95	↓	↓	↓	↓	
030	.0301	.0054	32	566	59.88					
031	.1740	.0333	265	538	82.48	.136	.146	.182	45	Data questionable due to hardware damage during assembly
032	.1740	.0331	265	540	---	↓	↓		↓	
033	.1740	.0333	265	541	83.40				22.5	
034	.1741	.0333	265	533	85.19					
035	.1740	.0333	265	533	69.98	↓	↓			
036	.1740	.0333	265	530	69.04	.106	.146			
037	.1740		265	543	---	↓	↓			
038	.1740	.0333	265	533	74.45					22.5° Swirler
039	.1740	.0333	265	540	80.78				Scarfed	45° "
040	.1741	.0333	265	532	85.40				Post	45° " .2" Distance
041	.1740	.0333	265	535	80.69				↓	22.5° " .2" Distance
042	.3480	.0666	265	535	82.79	.136			0	
043	.2610	.0499	265	525	84.91	↓			↓	
044	.1740	.0333	265	525	85.77					
045	.2610	---	147	535	---					
046	.3480	.0666	265	540	84.79				.136	
047	.3480	.0666	265	540	89.78				.272	
048	.1740	.0333	265	555	83.35				0	
049	.1740	.0333	265	525	88.93					
050	.1740	.0333	265	545	78.87					
051	.174	.0333	265	534	90.35					
052	.174	.0333	265	535	91.13					
053	.174	.0333	265	540	77.63					$\dot{W}_{Liq}$ = 0.035 lbm/sec
054	.174	.0333	265	544	75.59					$\dot{W}_{Gas}$ = 0.010 lbm/sec
055	.174	.0333	265	525	86.83	↓	↓	↓	↓	Liq/Gas Injector

5.3 CORE ELEMENT ATOMIZATION RESULTS

Parametric atomization studies analogous to the mixing experiments were conducted employing the three element configurations (see Fig. 7). In all cases, the cold-flow models utilized in the mixing experiments were also utilized in the atomization experiments. All experiments were conducted in the pressurized atomization facility employing molten wax and gaseous nitrogen as nonreactive propellant simulants (see Appendix C).

The independent effects of gas velocity were investigated for the D_L = 0.136-in. element by varying the "gas gap" from 0.041-inch to 0.005-inch. Simulated conditions were ρ_g = 1.45 lbm/ft^3 and MR = 5.25 and W_{Tot} = 0.207 lbm/sec for a flush oxidizer post. As shown in Fig. 30, increasing the gas velocity (by changing the gas gap) from 134 to 350 ft/sec resulted in a significant decrease in the mean drop size. Further increases in the gas velocity to 630 ft/sec did not significantly change the drop size.

The effect of increasing the oxidizer velocity by means of reducing the oxidizer post diameter is presented in Fig. 31. As in the mixing experiments, liquid jet diameters of 0.136 in. 0.108 in., and 0.070 in. were employed. For both a flush and recessed oxidizer post, the data indicate a linear drop size relationship with the oxidizer velocity. Apparently, over the range tested, reduction of the jet diameter continually reduced the resultant drop sizes in spite of the attendant increase in injection velocity.

The throttling characteristics of the three element configuration are presented in Fig. 32 for both recessed and flush post configurations. The experiments were performed at MR = 5.25 and the total propellant flowrate was maintained proportional to the simulated gas-phase density, as would be the case under hot-firing conditions. As indicated, for the D_L = 0.136 and 0.108-in. configurations, the mean drop size decreased as the element was throttled. For the D_L = 0.070-in. element, throttling did not significantly affect the resultant mean drop size.

The effects of the injected mixture ratio were investigated with the D_L = 0.136 in. element for both a flush and recessed oxidizer post configuration. Figure 33 presents the results for mixture ratios from 3 to 7.5. Decreasing the injected mixture ratio resulted in decreased drop sizes for both the flush and recessed configurations.

The independent effects of FLOX post recess were determined for the design point of ρ_g = 1.45 lbm/ft^3, MR = 2.25 and w_{tot} = 0.207 lbm/sec. Figure 34 presents the results of the atomization experiments for several element geometries. The solid curves in Fig. 34 are the results for elements with liquid jet diameters of 0.136, 0.108, and 0.070 in. All of these elements were designed with a 6-degree chamfer (diffuser section) at the exit of the oxidizer post. As indicated for these elements, the effect of post recess was a constant or even an increasing drop size as the post was recessed to practical depths (recess/D_L 2.5).

These data are not in accord with previously reported coaxial element atomization data, which indicates a significant decrease in drop size as the oxidizer post is

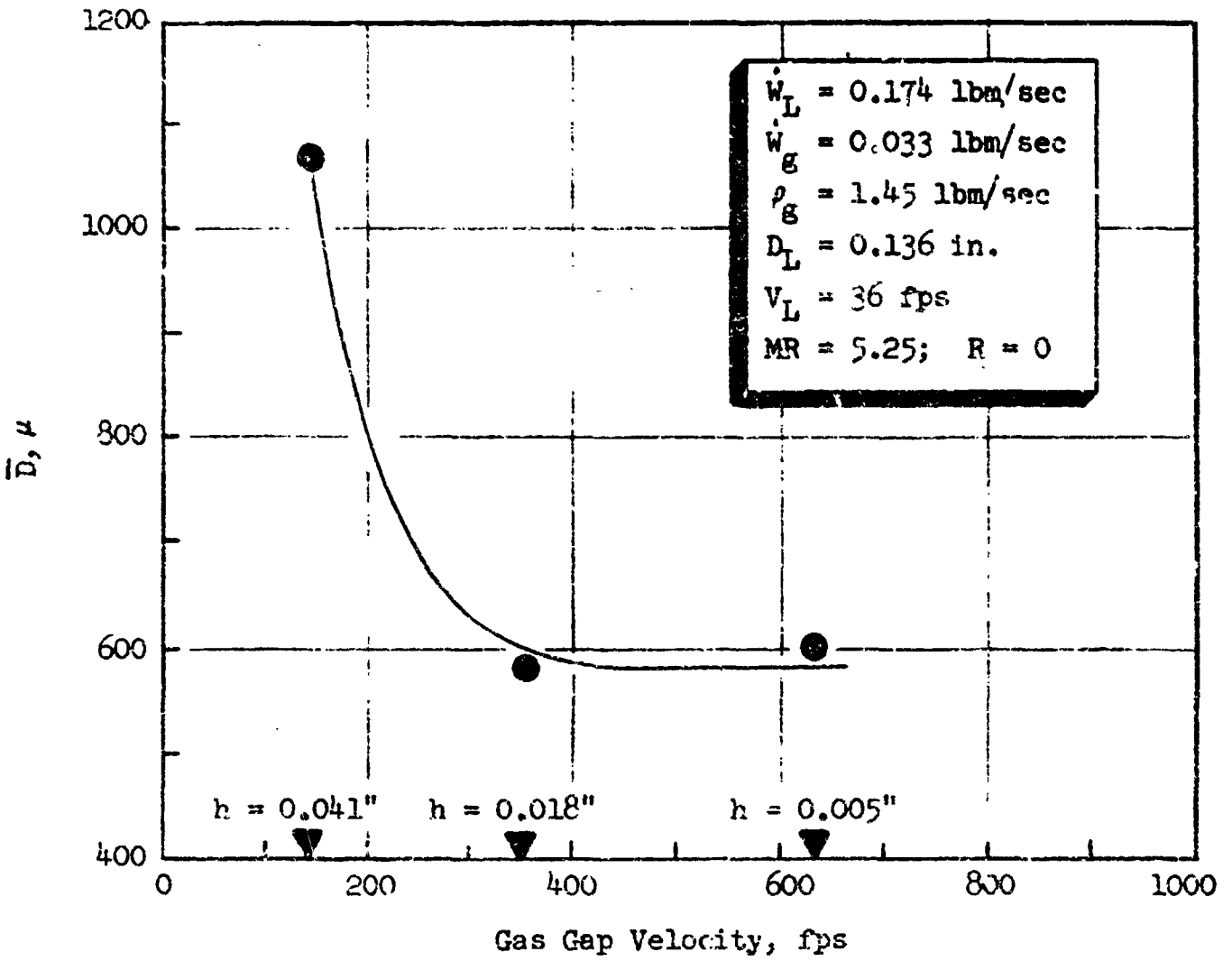

Figure 30. Atomization Effects of Gas Gap Velocity Changes as a Result of Variations in the Gas Gap Height

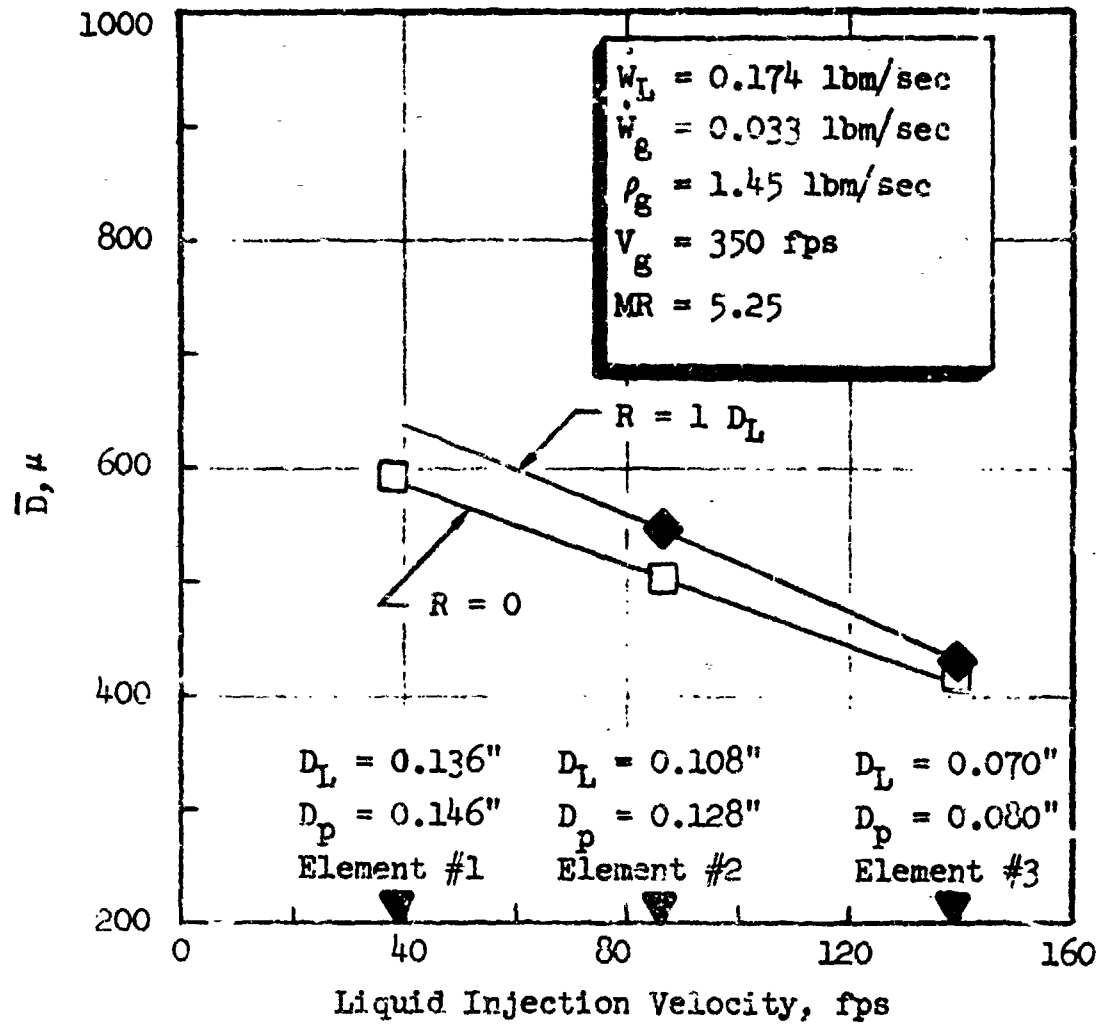

Figure 31. Effect of Liquid Injection Velocity Varied by Changing the Liquid Orifice Size

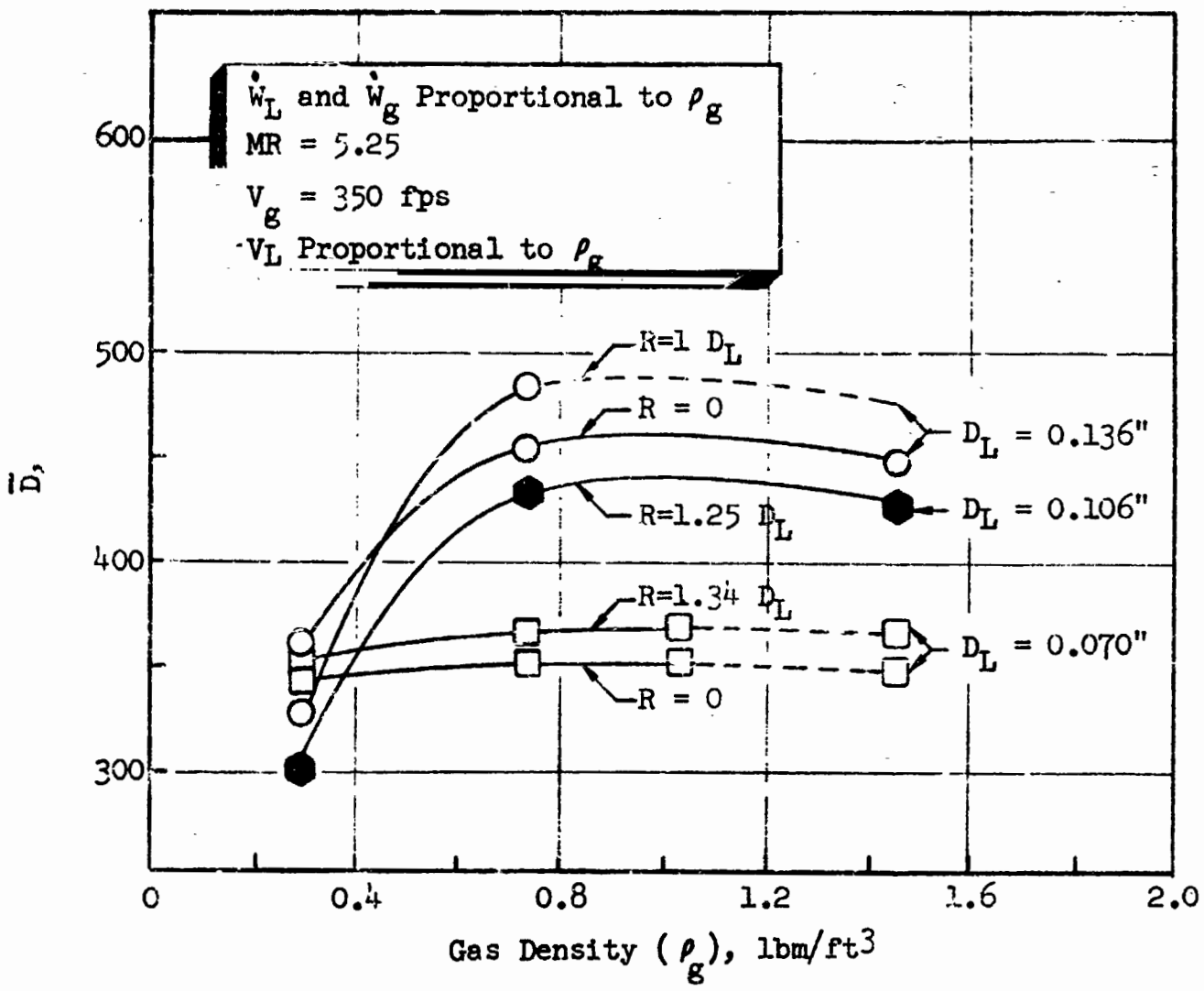

Figure 32. Throttling Characteristics for Flush and Recessed Oxidizer Posts With Different Size Liquid Orifices (D_L)

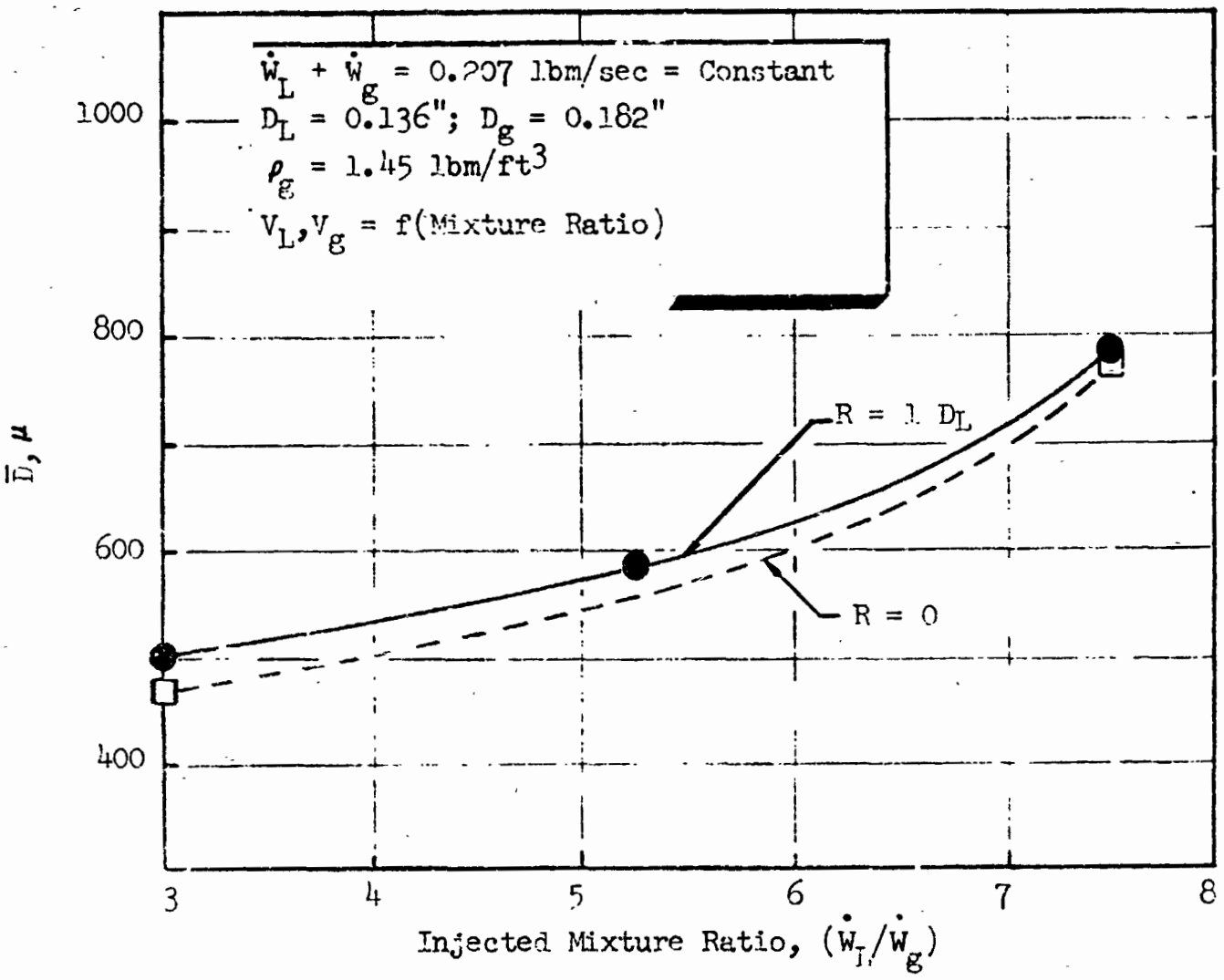

Figure 33. Effect of Injected Mixture Ratio With and Without Post Recess

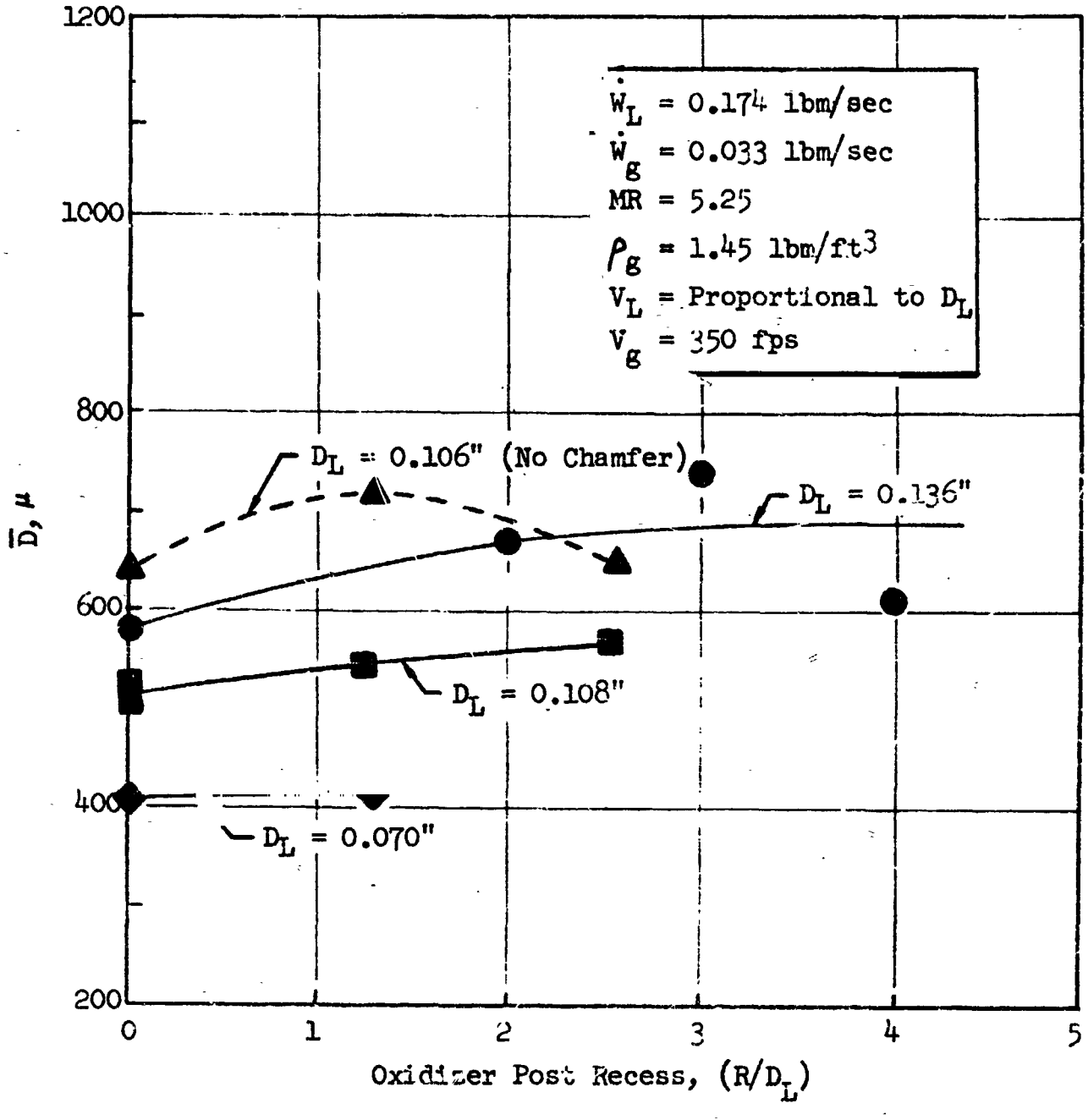

Figure 34. Effect of Oxidizer Post Recess for Various Sized Liquid Orifices

recessed (Ref. 21). However, the referenced study investigated large thrust/element injectors (≈2000 lbf) and the elements which were employed did not have a chamfer at the exit of the oxidizer post.

To determine whether or not the post exit chamfer was the reason for the discrepancy between the data, an element was fabricated which was identical to the D_L = 0.136 in. element except that the post chamfer was eliminated. As indicated in Fig. 34 (dashed line), this element produced drop sizes which were slightly larger than the D_L = 0.136-in. element and significantly larger than the D_L = 0.108-in. configuration. Recessing the nonchamfered oxidizer post again did not result in decreased drop sizes. Note also that the experiment with the D_L = 0.108-in. configuration of zero post recess was repeated and the results were 500 and 527 microns, respectively. Thus, it appears that large thrust-per-element coaxial injectors are more sensitive to oxidizer post recess than small-thrust-per element coaxial injectors.

To determine the effects on atomization of swirling the oxidizer jet, a test with the 45-degree in-line swirler was performed at the design condition with the No. 1 core element at zero recess. The test resulted in a $\overline{D}$ of 590 microns as compared to 580 microns when the jet was not swirled. Thus, swirling the liquid jet had little effect on the mean drop size for the element configuration of this study. However, significant swirling effects have been observed for large-thrust-per-element injectors (Ref. 21) whenever the gas gaps were large (h≈0.2 in.).

Two atomization tests were conducted to determine the effects of increasing the nominal flowrate (i.e., increasing the thrust/element) of the No. 1 element at R = 0. Figure 35 presents the results of those tests which show $\overline{D}$ decreasing with increased flowrate. As in the mixing tests, these data were utilized to construct a map of the atomization characteristics of the No. 1 element as a function of flowrate, gas velocity, and gas-phase density.

Atomization tests analogous to mixing tests conducted with the No. 1 element at a thrust level of 140 lbf were conducted for post recess depths up to 3 D_L. Figure 36 presents these results which show that post recess did not significantly effect drop size. Those data are in accord with the data of Fig. 34 which were conducted for a thrust level of 70 lbf.

3.3.1 Drop Size Distribution Correlation

Figure 37 presents normalized drop size distribution data from several of the pressurized atomization experiments. Also shown in the figure is the normalized Rosin - Rammler drop size distribution function (Ref. 23). Note the excellent agreement with the coaxial injector data for values of $D/\overline{D} > 1.0$. Use of realistic drop size distribution functions for $D/\overline{D} > 1.0$ in combustion model programs is critical because these drop size ranges significantly influence the predicated $\eta_{c^*,vap}$.

The mass median drop size, $\overline{D}$, for a spray sample which conforms to the Rosin-Rammler distribution function may be converted to an equivalent volume mean drop size by the equation (Ref. 23):

$$D_{30} = 0.455\ \overline{D} \qquad (5)$$

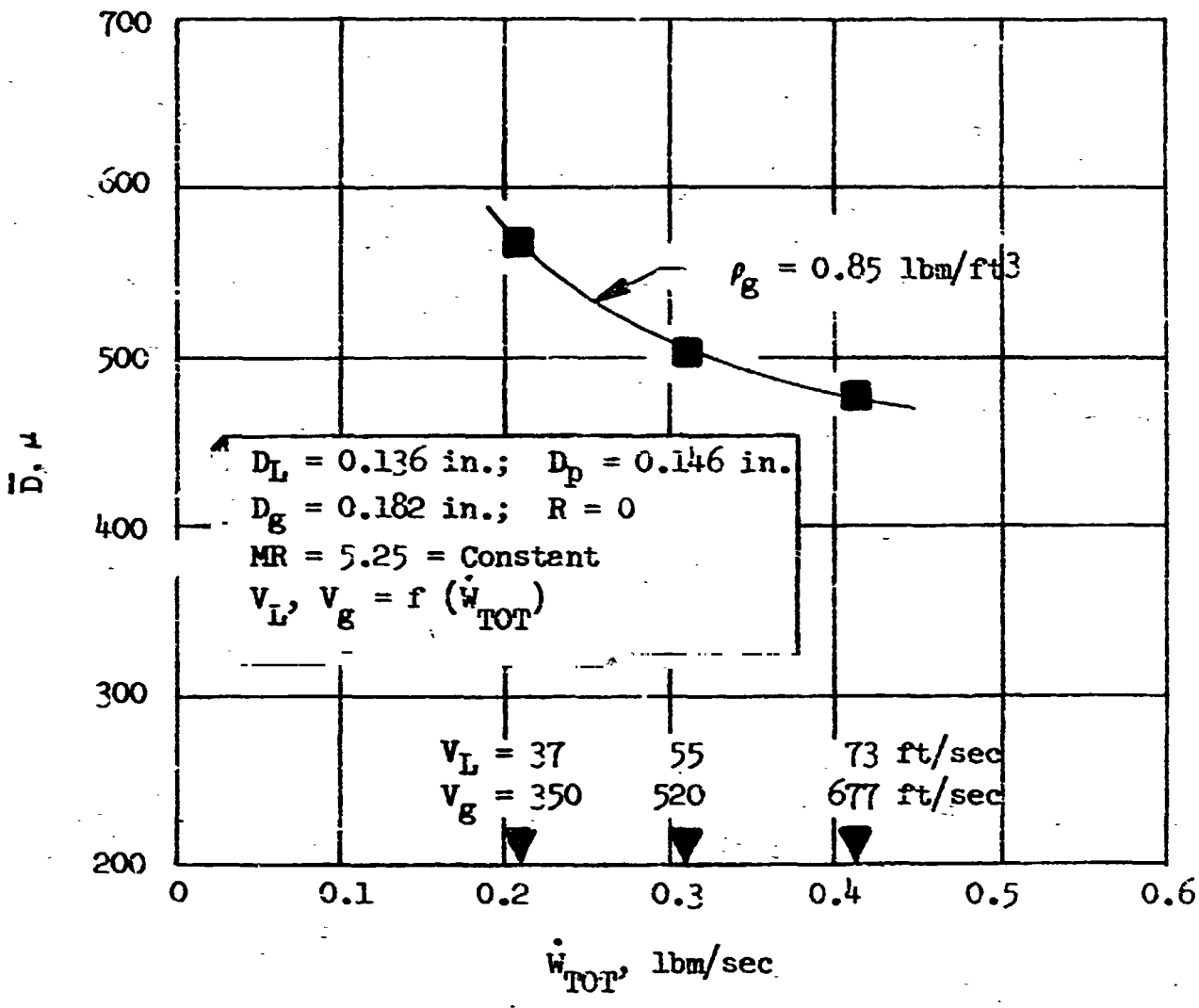

Figure 35. Atomization Effect of Flow-Per-Element With Fixed Element Geometry

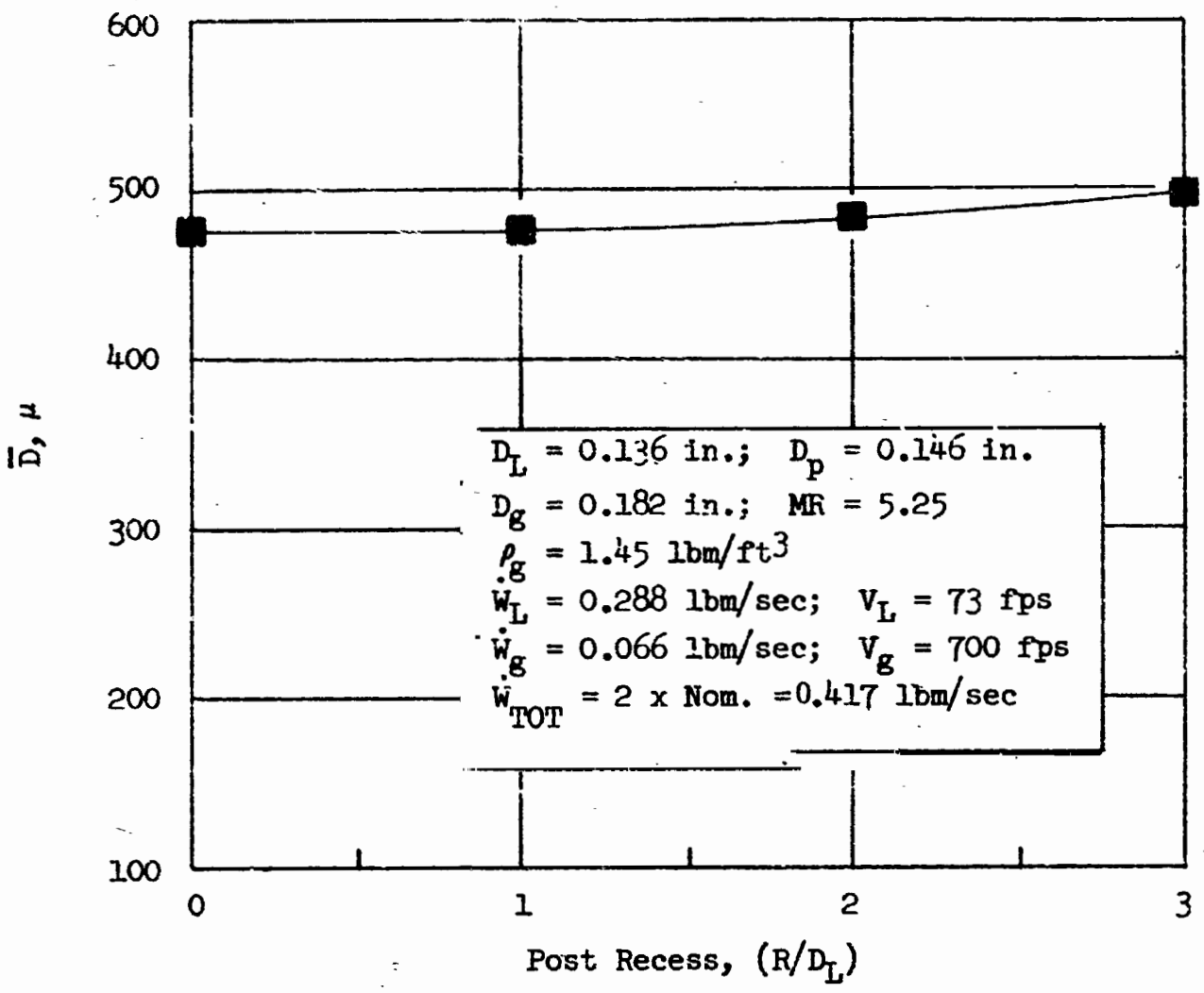

Figure 36. Atomization Effects of Oxidizer Post Recess for No. 1 Element for Thrust Level of 140 lbf

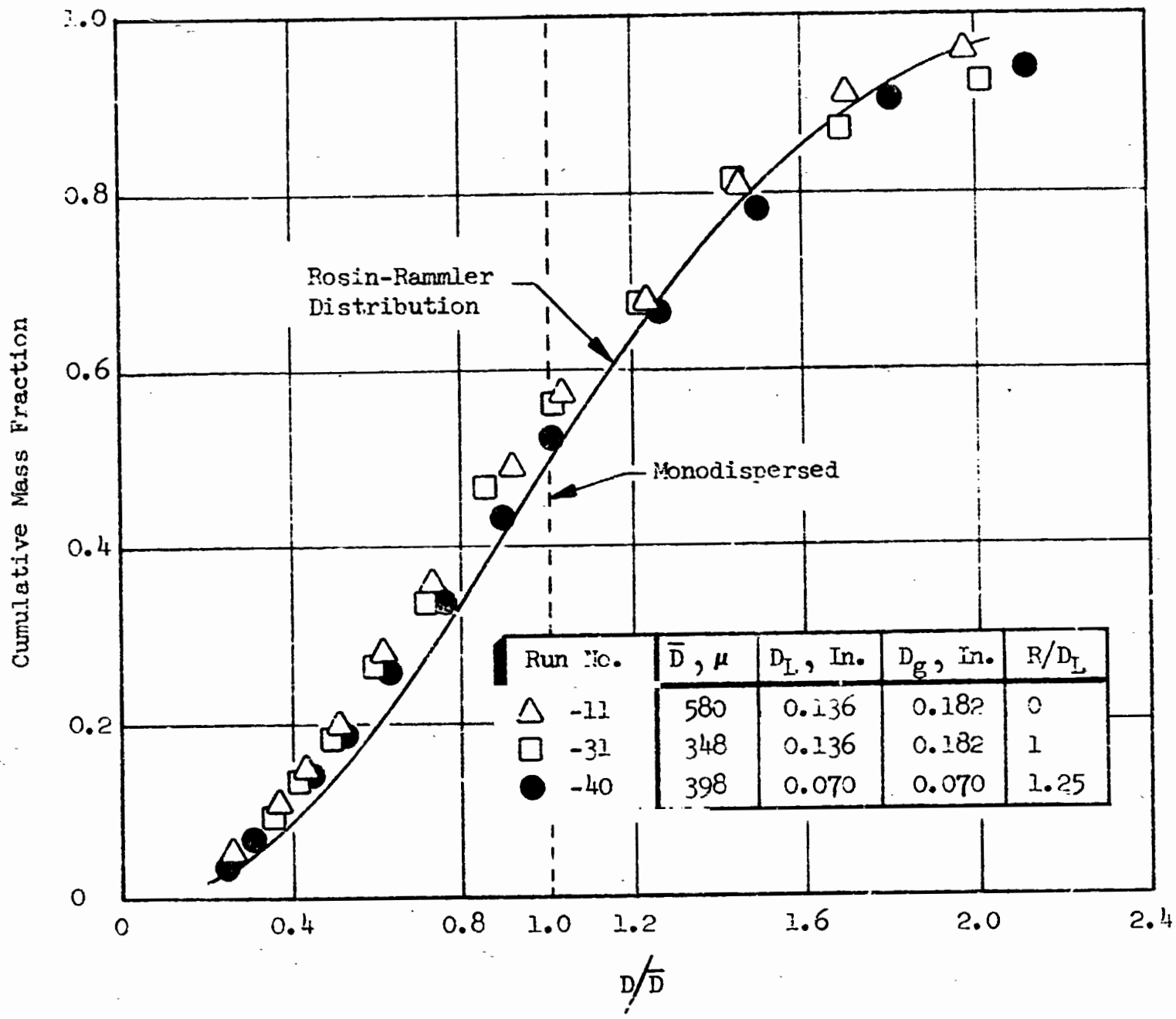

Figure 37. Core-Element Normalized Drop Size Distribution Data

where

D_{30} = volume mean drop size

$\overline{D}$ = mass median drop size

5.3.2 Correlation of Core Element Atomization Data

An attempt was made to correlate the atomization data presented in Fig. 30 through 36 utilizing the parameter $(\rho_g V_g)^2/MR\ V_L)$ which correlated the mixing data (see Fig. 29). However, no reasonable correlation was obtained. The most successful correlation of the atomization data was obtained by replacing the numerator of the mixing correlation parameter by a term proportional to the shear rate at the gas-liquid interface (i.e., V_g-V_L). In addition, it can be assumed that the resultant mean drop size will be some fraction of the oxidizer jet diameter. Thus, the resultant mean drop sizes were nondimensionalized by D_L. Figure 38 presents the parameter $\overline{D}/D_L$ as a function of $(V_g-V_L)/V_L\ MR)$. As indicated in the figure, the parameters provide a reasonable correlation of the atomization data.

5.3.3 Single-Element Atomization Data

Summarized in Table IV are pertinent data measured and calculated from the single-element atomization experiments. Sufficient data are supplied for the calculation of the element operating conditions (i.e., V_g, V_L, ρ_g, etc.). Also shown is the element configuration for each test.

5.4 PERIPHERAL ELEMENT MIXING RESULTS

Mixing experiments were conducted with the candidate peripheral elements to assess their potential chamber wall heat flux characteristics. In addition to the determination of their mixing performance, an area of primary concern was the resulting wall zone mass and mixture ratio distributions of the elements.

5.4.1 BLC Peripheral Element

Two mixing experiments were conducted with the BLC element (see Fig. 9) to determine the effects of the amount of BLC flow. The mixing performances and pertinent data are tabulated below:

$\dot{w}_{liq}$, lbm/sec	$\dot{w}_{gas,\ element}$, lbm/sec	$\dot{w}_{gas,\ BLC}$, lbm/sec	$MR_{element}$	$MR_{overall}$	E_M, %
0.174	0.033	0.006	5.27	4.47	77.6
0.174	0.033	0.010	5.27	4.05	75.6

From the above data, increasing the amount of BLC flow resulted in lower (≈2 percent mixing levels. However, no significant qualitative differences were noted between the resulting mass and mixture ratio distributions.

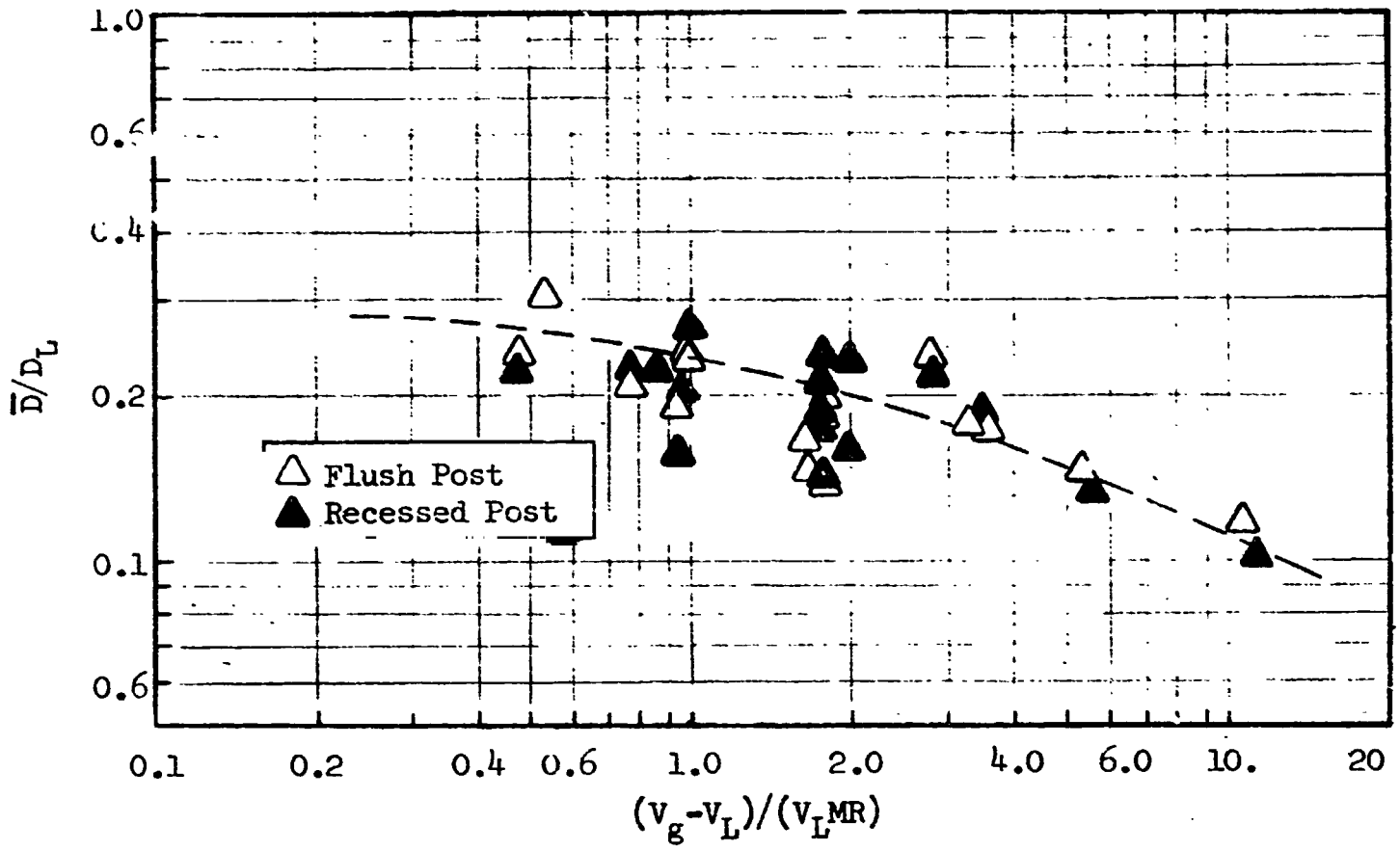

Figure 38. Correlation of Cold-Flow Atomization Data

TABLE IV. ATOMIZATION DATA

(Simulants: Fuel--GN_2, Oxidizer--Shell-270 Wax; ρ = 47.1 lbm/ft^3)

Run No.	$\dot{W}_{Liq}$ (lbm/sec)	$\dot{W}_{Gas}$ (lbm/sec)	Pressure (psig)	Gas Injection Temperature (°R)	$\bar{D}$ (μ)	D_L (In.)	D_p (In.)	D_g (In.)	R (In.)	Comments
005	.0710	.0167	190	674	550	.136	.146	.182	0	
006	.0810	.0131	172	669	595					
007	.0730	.0254	175	678	260					
008	.0660	.0253	175	666	265					
010	.0730	.0253	180	672	278					
011	.1740	.0334	362	679	580					
012	.1540	.0524	360	658	500					
013	.0710	.0257	175	670	320					
014	.0252	.0081	49	669	280					
015	.0290	.0054	48	680	410					
016	.1570	.0525	170	609	282					
017	.1730	.0329	170	660	472					
018	.1740	.0319	257	681	678					
019	Flowmeter Problems									
020										
021	.1570	.0522	270	649	420					
025	.1740	.0337	355	678	1070	.136	.146	.228		
026	.1740	.0334	355	652	600			.166		
027	.1740	.0333	355	679	855			.182	.136	
028	.1540	.0525	355	669	470					
029	.1830	.0242	355	693	780					
030	.0875	.0164	169	681	648					
031	.0284	.0055	48	682	348					
032	.1740	.0333	355	689	650				.272	
033	.1740	.0332	355	690	742				.408	
034	.1740	.0332	355	682	615				.544	
035	Flowmeter Problems				785					
036	.0875	.0163	169	690	595					
037	.0875	.0163	169	691	390	.070	.080	.136		
038	.1310	.0248	260	684	415				0	
039	.0284	.0055	48	685	413				0	

TABLE IV. (Concluded)

Run No.	$\dot{W}_{Liq}$ (lbm/sec)	$\dot{W}_{Gas}$ (lbm/sec)	Pressure (psig)	Gas Injection Temperature (°R)	$\bar{D}$ (μ)	D_L (In.)	D_p (In.)	D_g (In.)	R (In.)	Comments
040	.1310	.0246	260	688	398	.070	.080	.136	.094	
041	.0875	.0163	169	684	405	↓	↓	↓	↓	
042	.0284	.0055	48	681	390	↓	↓	↓	↓	
043	.1740	.0334	355	693	500	.112	.122	.166	0	
044	.1740	.0334	385	697	255	↓	↓	↓	.136	
045	.1740	.0334	169	700	645	↓	↓	↓	↓	
046	.0284	.0055	48	685	297	↓	↓	↓	↓	
047	.1740	.0334	355	675	638	.106	.146	.182	0	
048	.1740	.0334	355	675	722	↓	↓	↓	.136	
049	.1740	.0334	355	670	235	↓	↓	↓	.272	
050	.1740	.0334	355	684	535	.112	.122	.166	.136	
051	.1740	.0334	169	685	543	↓	↓	↓	↓	
052	.1740	.0334	355	665	564	↓	↓	↓	.272	
053	.1740	.0334	355	670	527	↓	↓	↓	0	
054	.1740	.0334	355	670	642	.106	.146	.182	.272	
055	.1740	.0334	355	680	685	↓	↓	↓	0	
056	.1740	.0334	355	680	642	↓	↓	↓	.136	
057	Flowmeter Problems					↓	↓	↓	↓	
058	.0157	.0030	0	655	—	↓	↓	↓	↓	
059	.3480	.0666	355	635	475	.136	.146	.182	0	
060	.2610	.0500	355	646	500	↓	↓	↓	↓	
061	.2610	.0500	202	643	355	↓	↓	↓	↓	
062	.1740	.0333	355	642	590	↓	↓	↓	↓	45° In-Line Swirler
063	.3480	.0666	355	640	475	↓	↓	↓	.136	
064	.3480	.0666	355	633	485	↓	↓	↓	.272	
065	.3480	.0666	355	635	495	↓	↓	↓	.408	

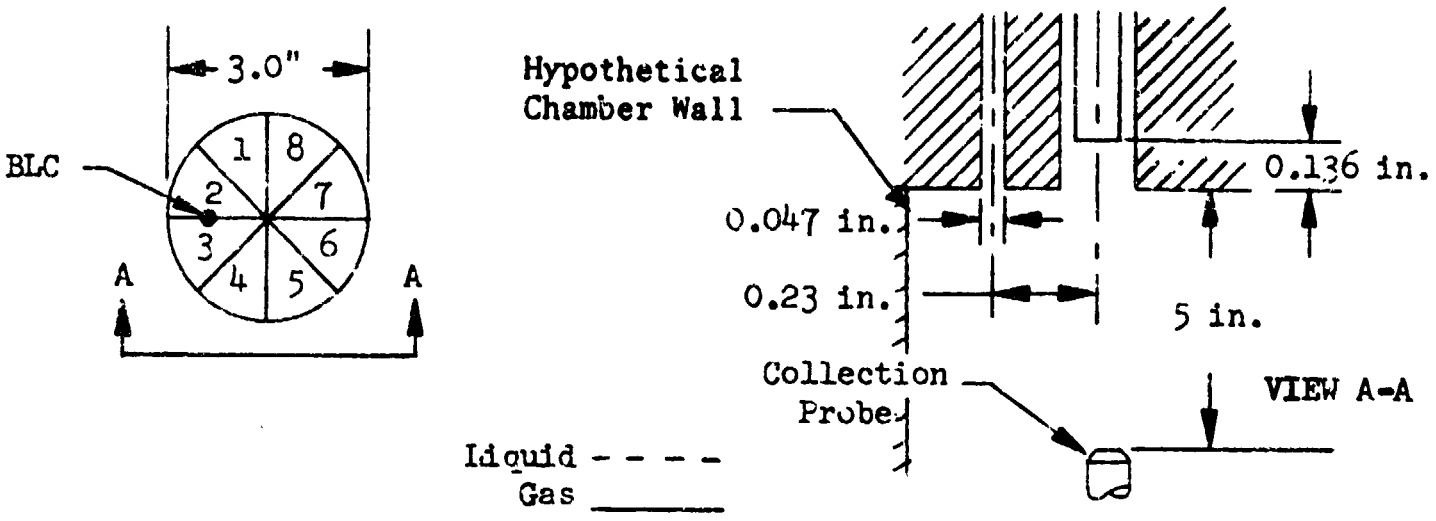

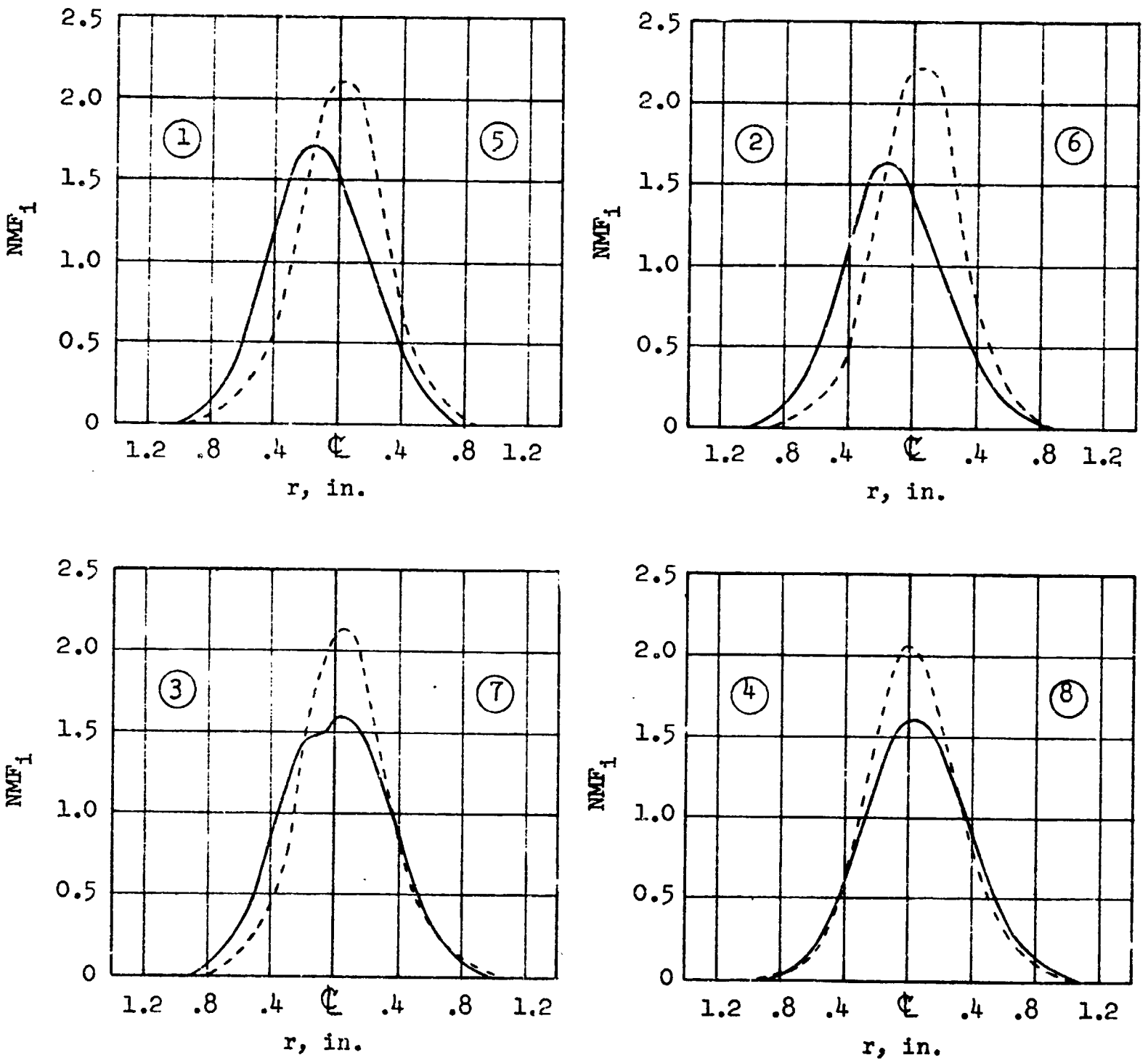

Figure 39. Mass Flux Profiles Measured at the 5-in. Station for the BLC Element

The mass flux profiles resulting from the experiment with w_{BLC} = 0.006 lbm/sec are shown in Fig. 39. The data are for a collection distance of 5 in. from the injector face. Note that in the region immediately downstream (adjacent to the hypothetical chamber wall) of the BLC hole (sectors 2 and 3), that a region of low mixture ratio but high mass flux was produced. In regions furthest away from the hypothetical wall, low mass flux levels were obtained, but the local mixture ratios were high (MR > 5.25). Thus, the intended mixture ratio bias was achieved.

5.4.2 Scarfed Post Element

Mixing tests were conducted with the element configuration shown in Fig. 9 with the two in-line helical swirlers. Since the scarfed post design is intended to move mass away from a chamber wall, tests were made at two planes to determine the wall zone mass and mixture ratios profiles as a function of distance from the injector face.

The element mixing performance, E_m, is presented in Fig. 40 as a function of distance from the injector for both in-line helical swirlers. The mixing level at the injector face was assumed to be zero. From an overview of the figure, it is clear that whatever mixing is accomplished occurs within 2 inches of the injector face. For comparison, mixing levels for an equivalent "core element" configuration with zero oxidizer post recess and the BLC element are also shown in Fig. 40. At the 5-in. measurement plane, the mixing quality of the scarfed post with the 45-degree swirler was only slightly below that of the core element, but that of the element with a 22.5-degree swirler fell substantially lower. Mixing levels of the two peripheral elements are nearly equivalent at the 5-in. measurement plane.

Figure 41 presents "normalized" mass flux profile data for the scarfed post with 45-degree swirler at the 2-in. measurement plane. For convenience of discussion, a hypothetical chamber wall is drawn adjacent to sectors 2 and 3. At the 2-in. measurement plane, the gas and liquid mass fluxes are almost symmetrical with respect to the centerline of the element, and very little displacement is still in evidence.

Figure 42 presents the "normalized" mass flux profiles as measured at the 5-in. station. By this distance, the center of mass has clearly been displaced from the centerline of the element. As expected, the gas and liquid mass are concentrated in sectors 5 through 8. Note, however, while the element successfully displaces mass from the hypothetical chamber wall, the local mixture ratio adjacent to the wall is higher than the injected mixture ratio.

For comparison, Fig. 43 presents normalized mass flux data for both the scarfed post and BLC configurations with w_{BLC} = 0.006 lbm/sec. The data are plotted for the hypothetical wall region of interest (sectors 2 and 3). Examination of the cold-flow data shows that both configurations possess characteristics which could provide enhanced injector/chamber compatibility. The flux profiles for the scarfed post with swirl show that the element displaces mass away from the wall region, but the local wall mixture ratios are higher than the injected mixture ratios. That is, near the wall, local values of "normalized" liquid mass flux are higher

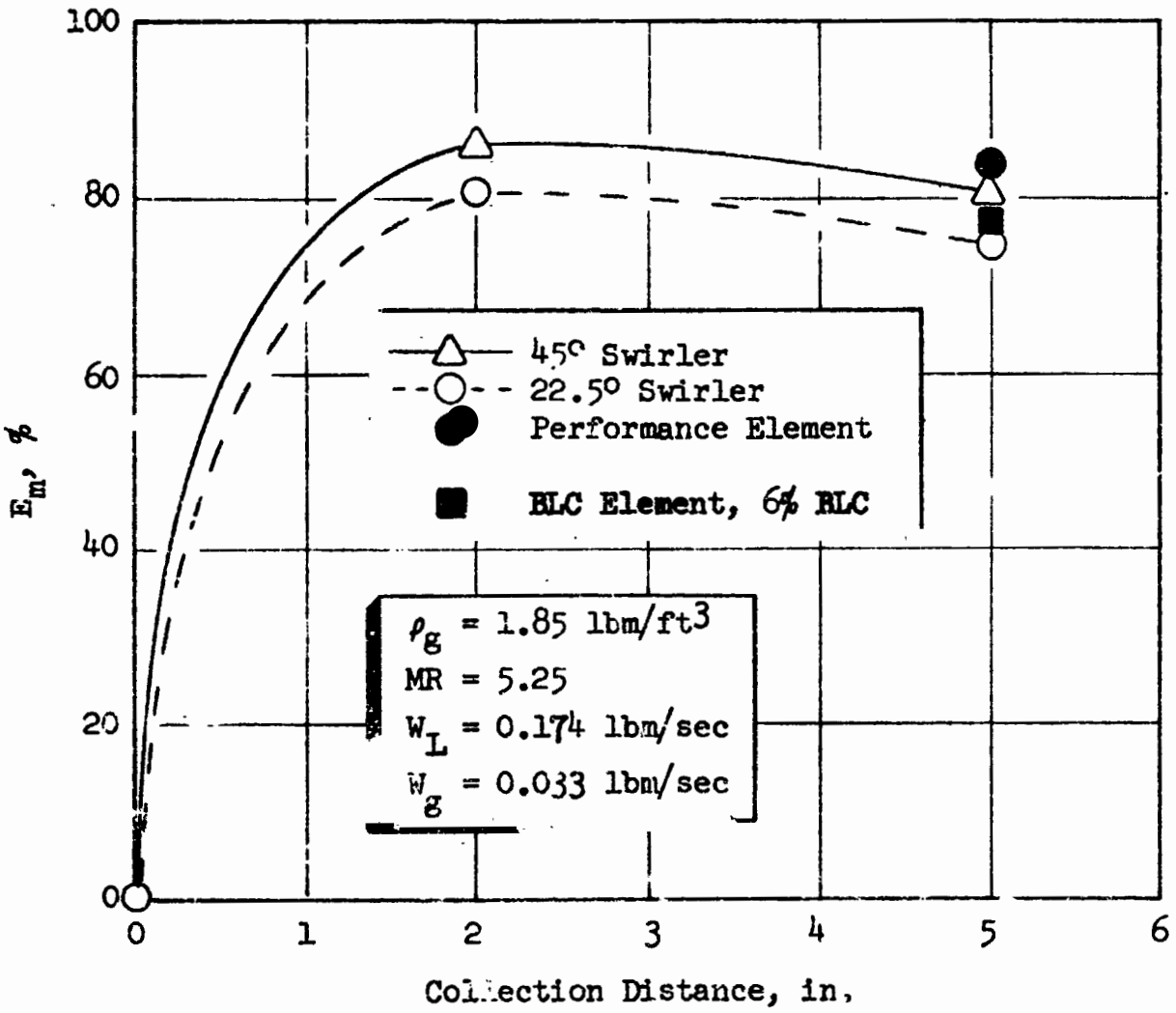

Figure 40. Mixing Performance of Scarfed Post With Swirler Configuration and BLC Element

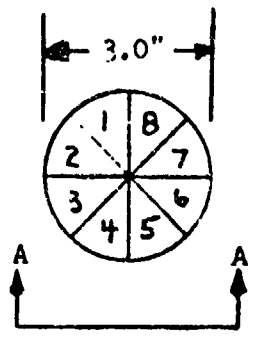

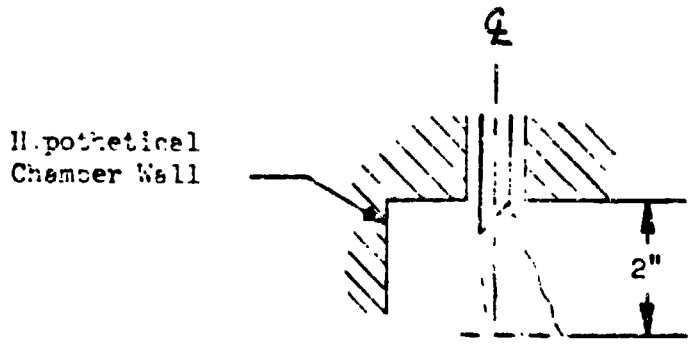

View A-A

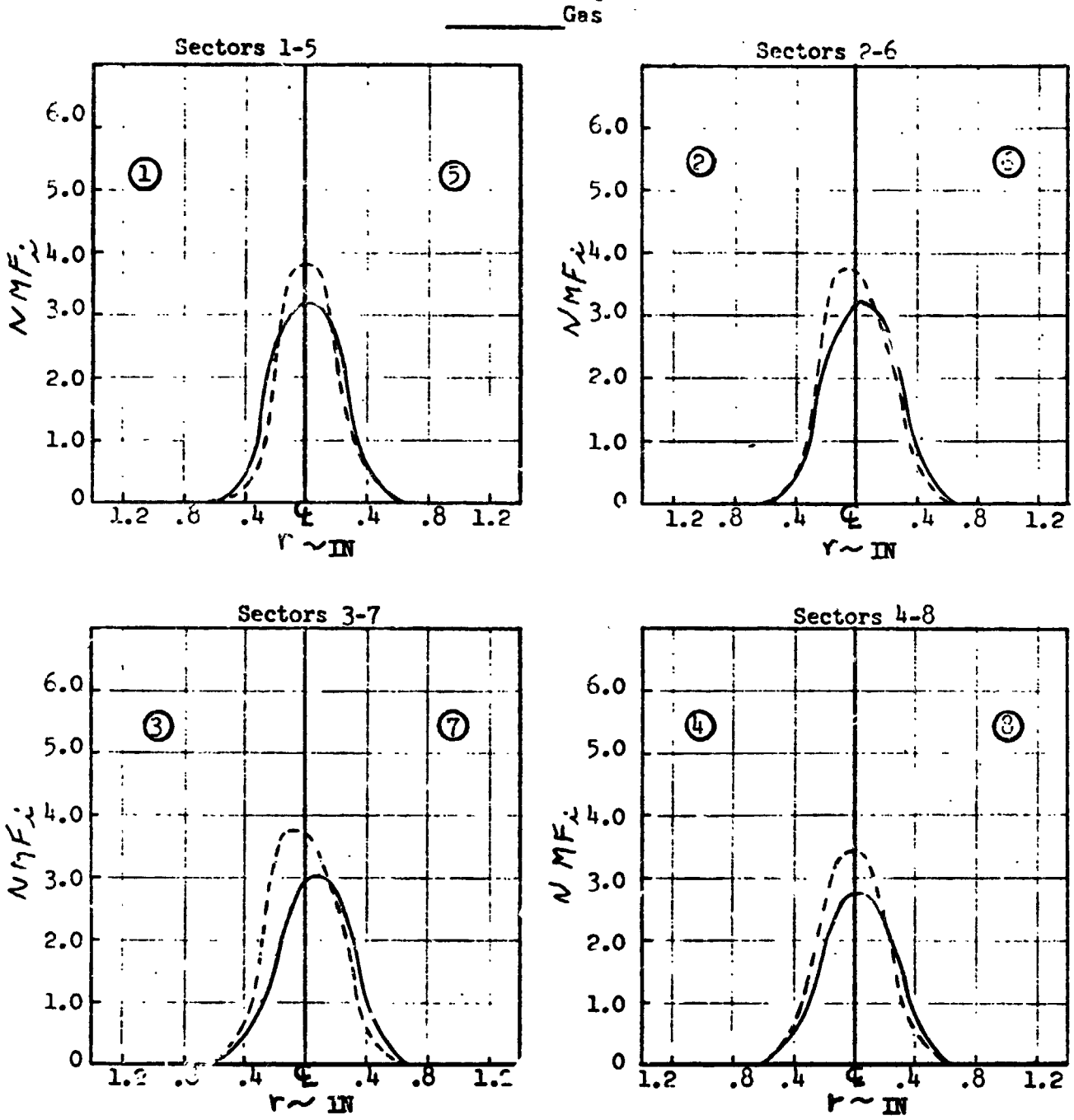

Figure 41. Mass Flux Profiles Measured at 2-In. Station (45-degree Helical Swirler, E_m = 86%)

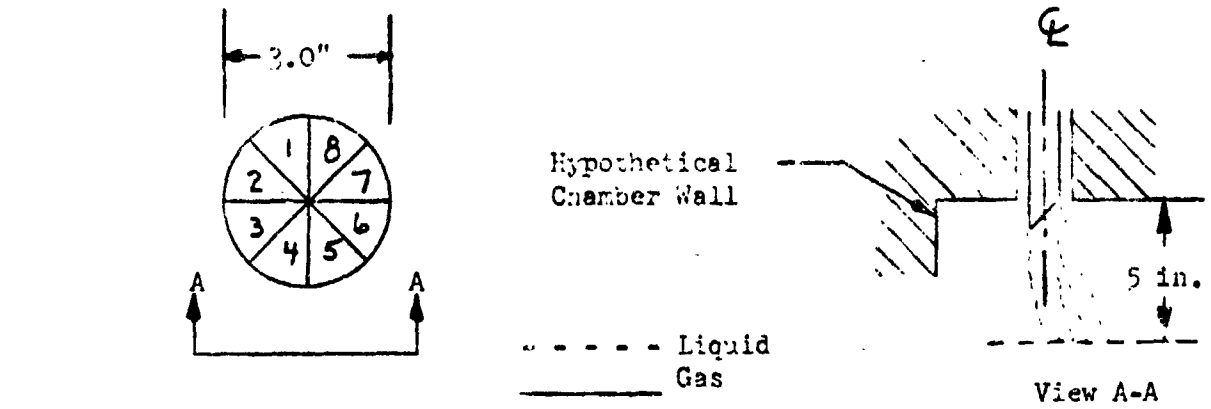

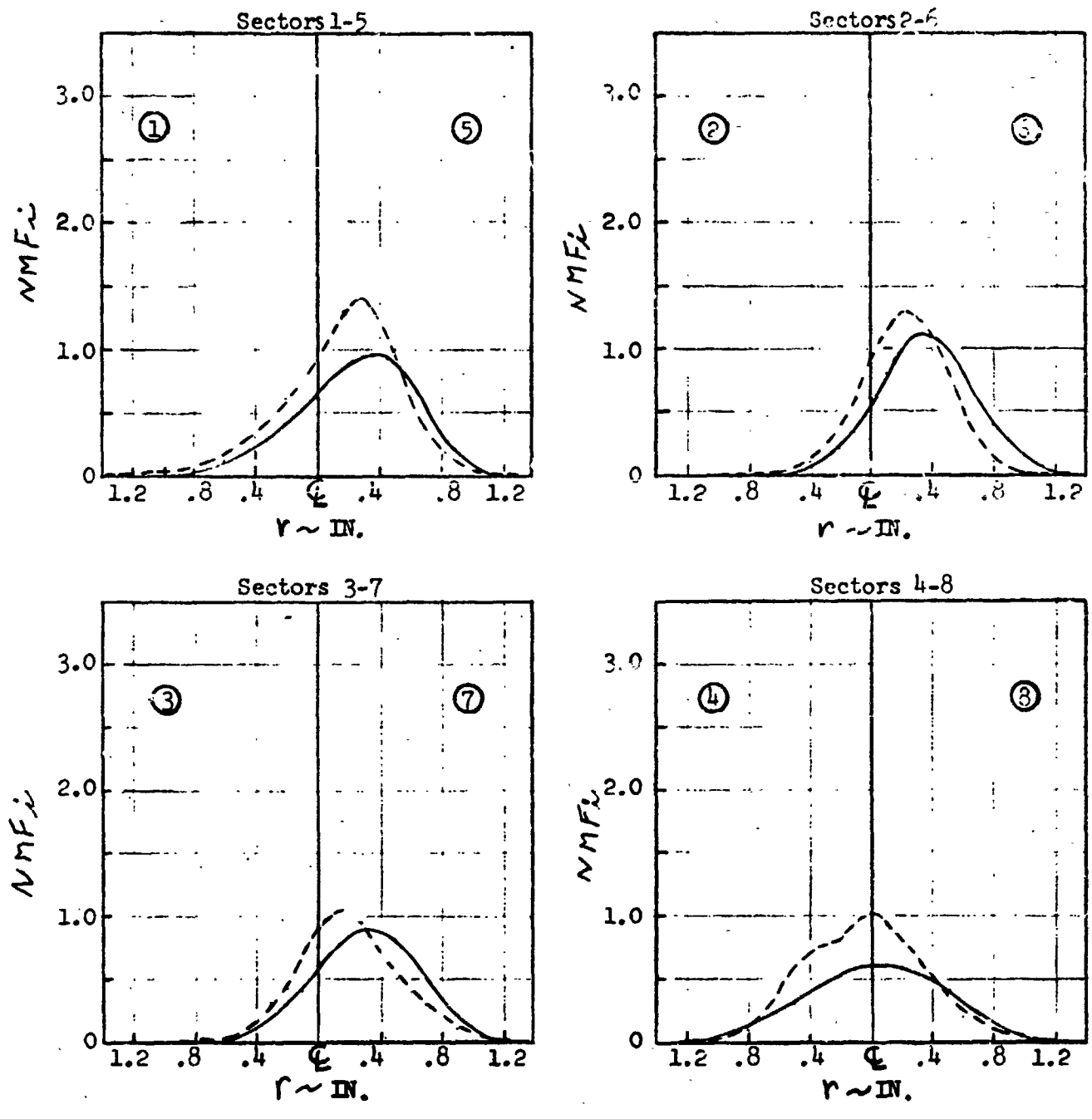

Figure 42. Mass Flux Profiles Measured at 5-In. Station (45-degree Helical Swirler, E_m = 80.5%)

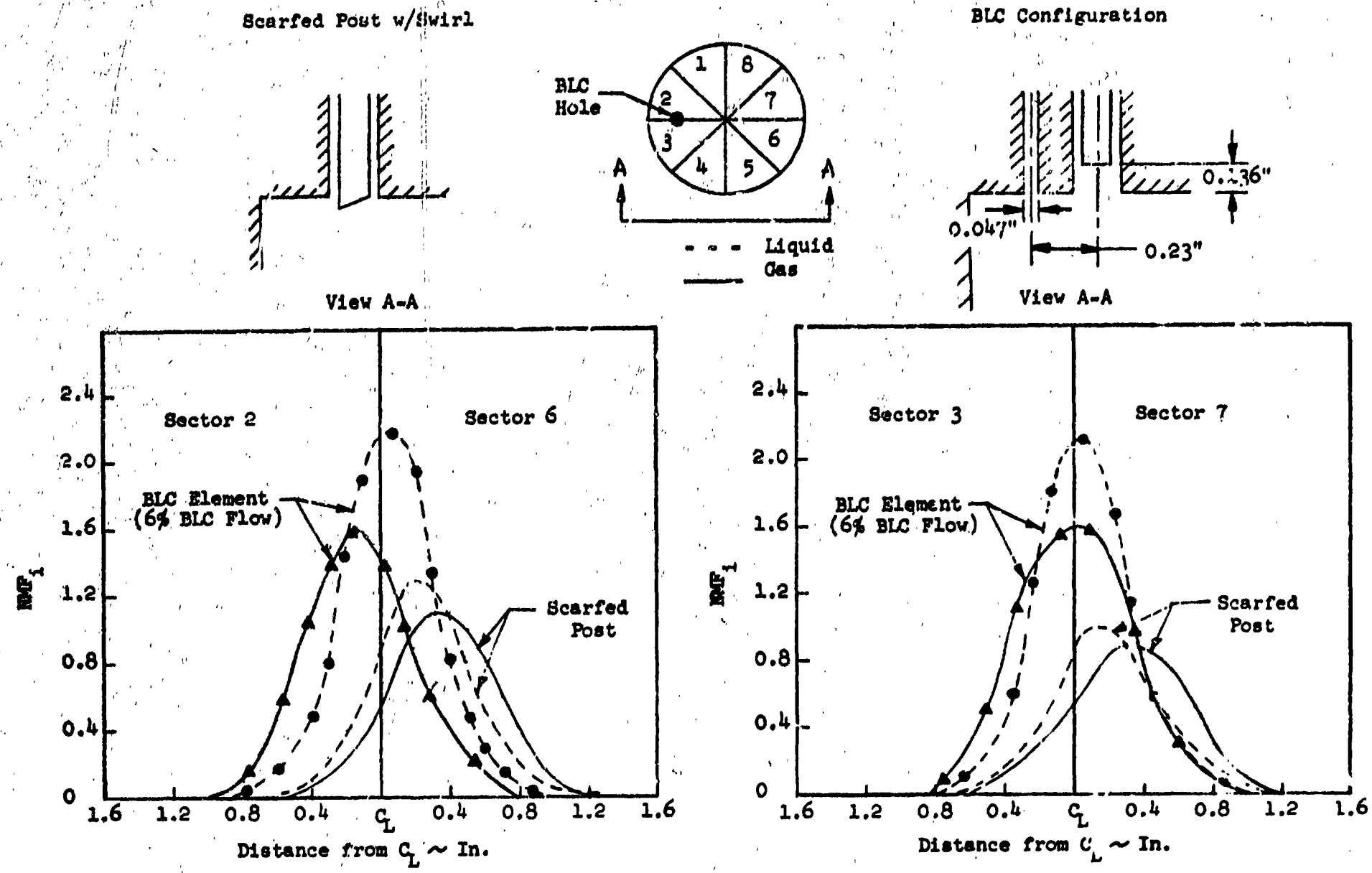

Figure 43. Comparison of Scarfed Post and BLC Element Configurations

than gas mass flux. The flux profiles for the BLC tests show that liquid distribution is not affected by the showerhead BLC flow. However, the displacement of the gas distribution from the centerline of the element is evident. The resulting BLC element flow field is characterized by a low wall region mixture ratio, but with relatively increased mass flux near the wall.

The relative merits of each configuration as a peripheral element were investigated with single-element hot firings (Section 6.0). These data show the relative merits of low wall mixture ratio versus low wall mass flux.

5.5 PERIPHERAL ELEMENT ATOMIZATION RESULTS

Extensive atomization testing of the candidate peripheral elements was not performed. In the case of the BLC element, an analysis of the free-jet flow field indicated that, due to the diffusion of the small (0.047 in.) BLC jet, little excess gas velocity would be available for interaction with the adjacent element flow field. Consequently, the BLC element can be expected to yield drop sizes of approximately the same size as the basic recessed core element without the adjacent BLC hole.

To assess the effects of swirling the liquid jet, an atomization test was run using the No. 1 core element (nonscarfed) with zero recess and with a 45-degree helical swirler. The test resulted in a $\overline{D}$ of 590 microns as compared to 580 microns (nonscarfed) when the jet was not swirled. Thus, swirling the liquid jet had little effect on the mean drop size for this size element. Significant influence of swirl has been observed on atomization for large-thrust-per-element injectors whenever the gas gaps were large, e.g., L≈0.2 in. (Ref. 24).

5.6 EVALUATION OF MIXING AND ATOMIZATION CHARACTERISTICS

From an overview of the mixing and atomization data presented in this section, it is apparent that parameters that enhance mixing performance do not necessarily provide good atomization characteristics. For example, reference to Fig. 24 shows that for the No. 1 element, as the oxidizer post recess was increased from 0 to 1 D_L, the mixing level, E_M, increased from 81 to 95-percent (i.e., $\eta_{C^*,mix}$ increased). However, analogous atomization data (Fig. 34) shows that the mass medium drop size also increased from 580 to 630 microns (i.e., $\eta_{C^*,vap}$ decreased). Consequently, tradeoff studies must be made to optimize element performance both with respect to element geometry as well as element operating conditions. Thus, in order to select a "core" element configuration for single-element hot-fire evaluation, a tradeoff study of the three "core" configurations was made with the intent of maximizing performance both at design and throttled conditions. The results of that study are presented in a subsequent section (Section 6.0).

The results of the cold-flow studies with the "peripheral" element configurations showed that the mixing levels of the scarfed post and BLC elements were nearly equivalent (Fig. 40). However, examination of the resulting wall zone mass and mixture ratio characteristics of the two elements shows significant differences (Fig. 43). That is, the BLC element provides a low mixture ratio, high mass flux wall region, whereas the scarfed post elements provides a high mixture ratio, low mass flux wall region. The relative effects of each characteristic were assessed in the single-element hot-fire studies.

6.0 SINGLE-ELEMENT HOT-FIRE RESULTS

The purpose of the single-element hot-fire task was twofold: (1) verification of the cold-flow simulation techniques, and (2) investigation of the effects of combustion which cannot be simulated in cold-flow experiments.

Since the influence of combustion within a recessed cup* was expected to be the most difficult combustion effect to simulate in cold flow, post recess was chosen to be a variable in the "core" single-element hot-fire studies. Combustion within the cup region can significantly change the atomization and mixing characteristics of the element due to generation of combustion gases within the confined cup region can lead to oxidizer post burning. An additional variable, chamber L*, was changed in order to verify the mixing levels which were determined in the cold-flow studies.

6.1 SELECTION OF SINGLE-ELEMENT HOT-FIRE ELEMENTS

The cold-flow data presented in Section 5.0 defined independent effects of element design and operating conditions on the mixing and atomization processes. Based on these cold-flow studies, element configurations were selected for further hot-fire evaluation.

6.1.1 Core Hot-Fire Element

To select a core element for hot-fire evaluation, the cold-flow data of the three candidate (see Fig. 7) core elements were analyzed for predicted performance levels both at the design and throttled conditions. Table V presents the results of this analysis for chamber pressures of 500 and 250 psia. For this analysis, a baseline recess value of 1 D_L was chosen. This value of post recess had been used in similar FLOX/CH_4 programs without experiencing post burning problems (Ref. 19).

In the analysis, the wax drop sizes ($\bar{D}$) were corrected for the difference in physical properties of wax and FLOX using the empirical relations of Ingebo, Ref. 24 (see Section 7.0). The resulting predicted FLOX drop size was utilized to predicted $\eta_{c^*,\ vap}$ by employing the analysis of Section 3.0. The mixing limited c* efficiency, $\eta_{c^*,\ mix}$, was obtained directly from the cold flow mixing data.

Examination of Table V shows that at the design condition (P_c = 500 psia) decreasing the liquid jet diameter (D_L) resulted in decreasing the mixing performance (E_m decreased, $\eta_{c^*,\ mix}$ decreased). However, the resultant mean drop size also decreased with decreasing D_L ($\bar{D}$ decreased, $\eta_{c^*,vap}$ increased). The net result of the product of the mixing-limited and vaporization-limited efficiencies at the design condition is that the predicted performance level of the No. 1 element is approximately 1 and 3 percent higher than the No. 2 and 3 element, respectively. At the throttled condition (P_c = 250 psia) the predicted performance level of the No. 1 element (D_L = 0.136-in., D_g = 0.182-in.) is clearly superior to that of the

*The cup region of a recessed post injector is defined as the cylindrical volume between the exit of the oxidizer post and the exit plane of the gas orifice.

TABLE V. SUMMARY OF PREDICTED CORE ELEMENT PERFORMANCE

Hot-Fire Condition	D_L, inch	Recess (R/D_L)	E_m, percent	$\eta_{c^*,mix}$ percent	$\overline{D}_{WAX}$, microns	$\overline{D}_{FLOX}$, microns	$L^* = 40$ $E_c = 3:1$ $\eta_{c^*,vap}$ percent	Predicted Performance $\eta_{c^*} = \eta_{c^*,mix} \times \eta_{c^*,vap}$ percent
500 psia	0.136	1	95.6	99.9	630	248	97.5	97.2
MR = 5.25	0.108	1	87	97.6	550	217	98.5	96.0
V_g = 350 ft/sec	0.070	1	78	94	425	168	99.8	93.9
250 psia	0.136	1	83	96.4	630	248	97.5	94.0
MR = 5.25	0.108	1	68.5	87.2	560	220	98.5	86.0
V_g = 350 ft/sec	0.070	1	56	77.4	405	160	99.9	77.3

No. 2 and 3 elements. This, in addition to consideration of the relative ease of fabrication, led to selection of the (larger) No. 1 element for further hot-fire study.

Choice of a gas annulus gap thickness for the No. 1 element was based both on performance and fabrication considerations. Figure 19 shows that decreasing the gas gap below the 0.018-in. value element at R = 0 could further raise E_m. However, at R = 1 D_L mixing performance ($\eta_{c^*,mix}$) was already 99.6 percent with a 0.018-in. gap. Analogous atomization data (Fig. 30) shows that decreasing the gas gap below 0.018 in. (i.e., increasing V_g) results in nearly equivalent drop sizes. Thus, no significant performance improvement was predicted by further decreasing the gas gap (i.e., increasing V_g).

Consideration of the fabrication of multielement hot-fire injectors dictates that extremely small gas gaps ($\simeq$0.005 to 0.010-in.) will result in increased fabrication cost due to the problem of maintaining oxidizer post/gas annulus concentricity. Thus, a gas gap of 0.018 in. was chosen for the hot-fire core element studies (see Fig. 10).

6.1.2 Peripheral Hot-Fire Elements

The results of the single-element cold-flow studies with the peripheral element candidates revealed the two element types possessed different characteristics either of which could provide enhanced injector/chamber compatibility. Thus, both the BLC element and the scarfed post with swirl elements were selected for single-element hot-fire evaluation. For the scarfed post element, the 45-degree in-line helical swirler was selected instead of the 22-1/2-degree swirler based on higher mixing level performance (see Fig. 40).

6.2 CORE ELEMENT HOT-FIRE RESULTS

Initial parametric hot-fire experiments were conducted with the core element to assess the effects of oxidizer post recess and chamber L*. All firings were conduct d in graphite lined chambers (see Section 4.0) which were instrumented in order to determine chamber wall heat flux. A summary of the single-element hot-fire data is presented in Table VI (both core and peripheral element results).

Figure 44 presents c* efficiency data for three values of post recess (0, 0.5, and 1.0 D_L) and chamber L* (10, 20, and 40 inches). The data are based on chamber pressure measurements which were corrected for heat loss based on measured wall $\dot{q}/A$ data. As expected, performance for all tests increased with increasing L*.

A further series of tests were conducted to determine the effects of FLOX post recess on performance in a 40-inch L* chamber. Figure 45 presents the resultant performance (η_{c^*}) data for FLOX post recess values up to 2 D_L. Note that the results of the hot-firing post recess series are in essential agreement with the cold flow data (Section 5.0, Fig. 24 and 34) which indicated little change in element performance with increased post recess depths. That is, the cold flow data predict nearly constant $\eta_{c^*,mix}$ and $\eta_{c^*,vap}$ as a function of post recess.

FOLDOUT FRAME 1

TABLE VI. SUMMARY OF SINGLE-ELEMENT HOT-FIRE D

Run No.	Chamber L* (In.)	Throat Area ($In.^2$)	Post Recess (In.)	$\dot{W}_{Oxidizer}$ (lbm/sec)	$\dot{W}_{Fuel}$ (lbm/sec)	Stagnation Chamber Pressure (psia)	Fu
1	20	0.0960	0	0.170	0.034	--	
2	20	0.0960	0	--	--	--	
3	20	0.0970	0	0.169	0.035	391	
4	20	0.1020	0	0.167	0.035	312	
5	20	0.1162	0	0.165	0.036	301	
6	20	0.1258	0	0.183	0.026	256	
7-10	Calibration of cavitating venturi						
11	10	0.0985	0	0.172	0.035	280	
12	40	0.1000	0	0.173	0.035	--	
13	40	--	0	0.184	0.035	--	
14	10	0.1070	0.068	0.199	0.036	319	
15	20	0.1360	0.068	0.230	0.041	357	
16	40	0.1200	0.068	0.228	0.041	436	
17	10	0.1220	0.136	0.212	0.037	324	
18	20	0.1455	0.136	0.172	0.030	245	
19	40	0.1230	0.136	0.237	0.041	--	
20	40	0.09561	0.068	0.184	0.034	469	
21	40	0.09589	0.136	0.183	0.030	452	
22	40	0.09534	0.136	0.183	0.031	465	
23	40	0.09616	0.204	0.187	0.035	448	
24	40	0.09616	0.272	0.187	0.034	453	
25	40	0.09920	0.408	0.184	0.033	--	
26	40	0.09782	0	0.181	0.034	404	
27	40	0.09782	0	0.160	0.053	320	
28	40	0.1054	0	0.196	0.037	--	

*Corrected for chamber heat loss only.
**Corrected for Rayleigh loss, L* = 10"

FOLDOUT FRAME 2

NT HOT-FIRE DATA

tion ressure ₂)	Fuel Injection Temperature (°F)	η_{c*}, P_c * (%)	Comments
	--	--	1 sec check-out test
	--	--	Failure of FLOX supply line
	-136.1	--	1 sec checkout tests
	12.7	--	
	19.6	81.7	
	8.2	74.5	High MR test
	3.9	58.3**	
	4.7	--	Transducer problems
	25.6	--	Nozzle failure
	14.9	63.0**	
	13.2	82.9	
	2.1	90.8	
	33.7	69.1**	
	39.1	81.7	
	31.3	--	Transducer problems
	128.6	96.8	Heated CH_4 test
	18.5	92.4	$\dot{W}_{BLC}$ = 0.00741 lbm/sec
	-20.1	93.7	$\dot{W}_{BLC}$ = 0.01095 lbm/sec
	13.8	91.3	
	27.2	92.3	
	26.7	--	Transducer failure
	-49.1	85.5	Scarfed post w/swirl, MR = 5.28
	-11.1	72.2	Scarfed post w/swirl, MR = 3.02
	-7.2	--	Nozzle failure

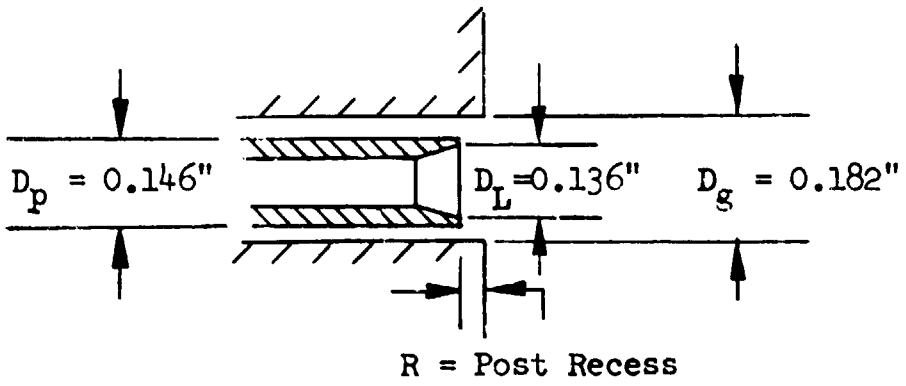

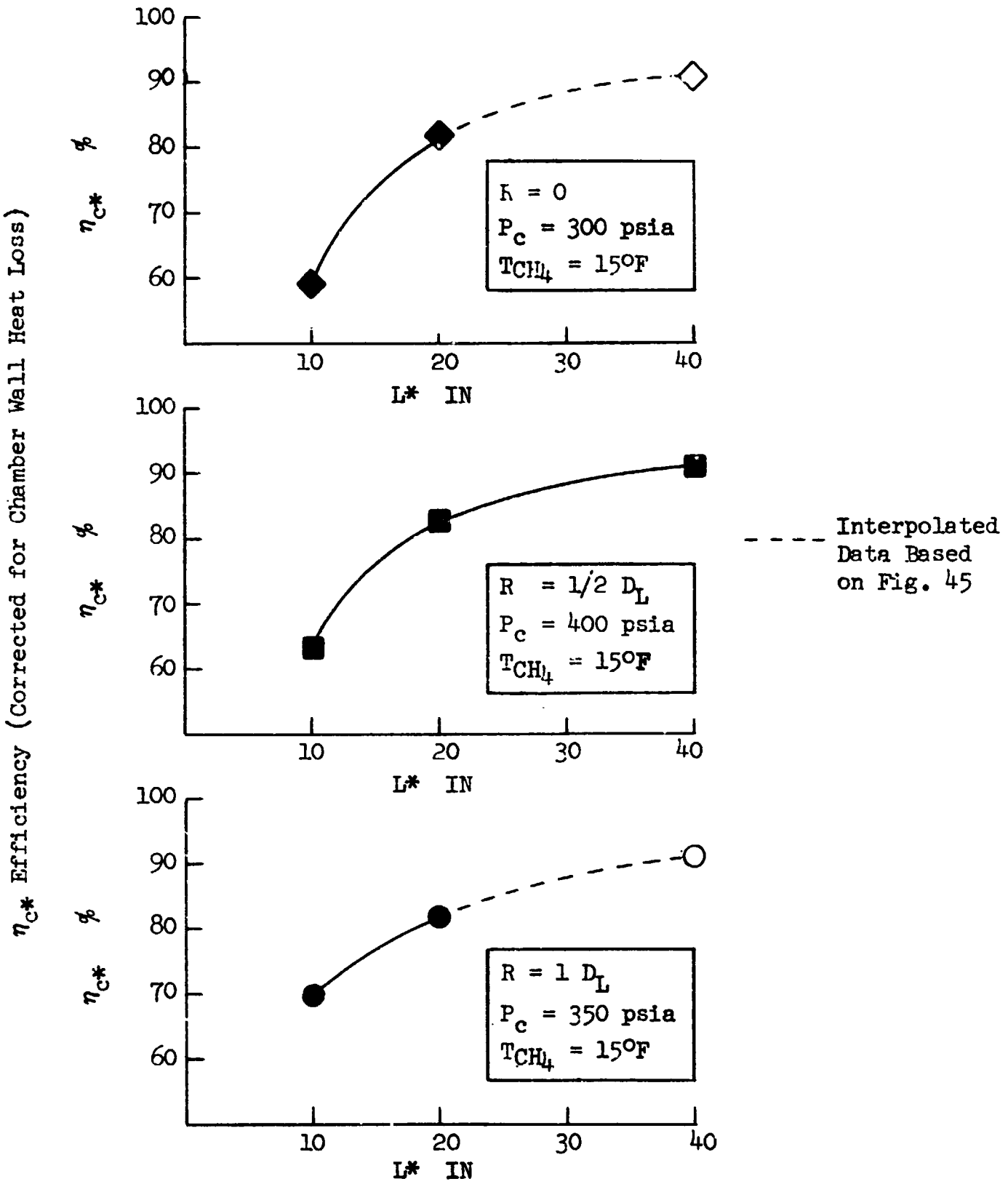

Figure 44. Single-Element Hot-Fire Data

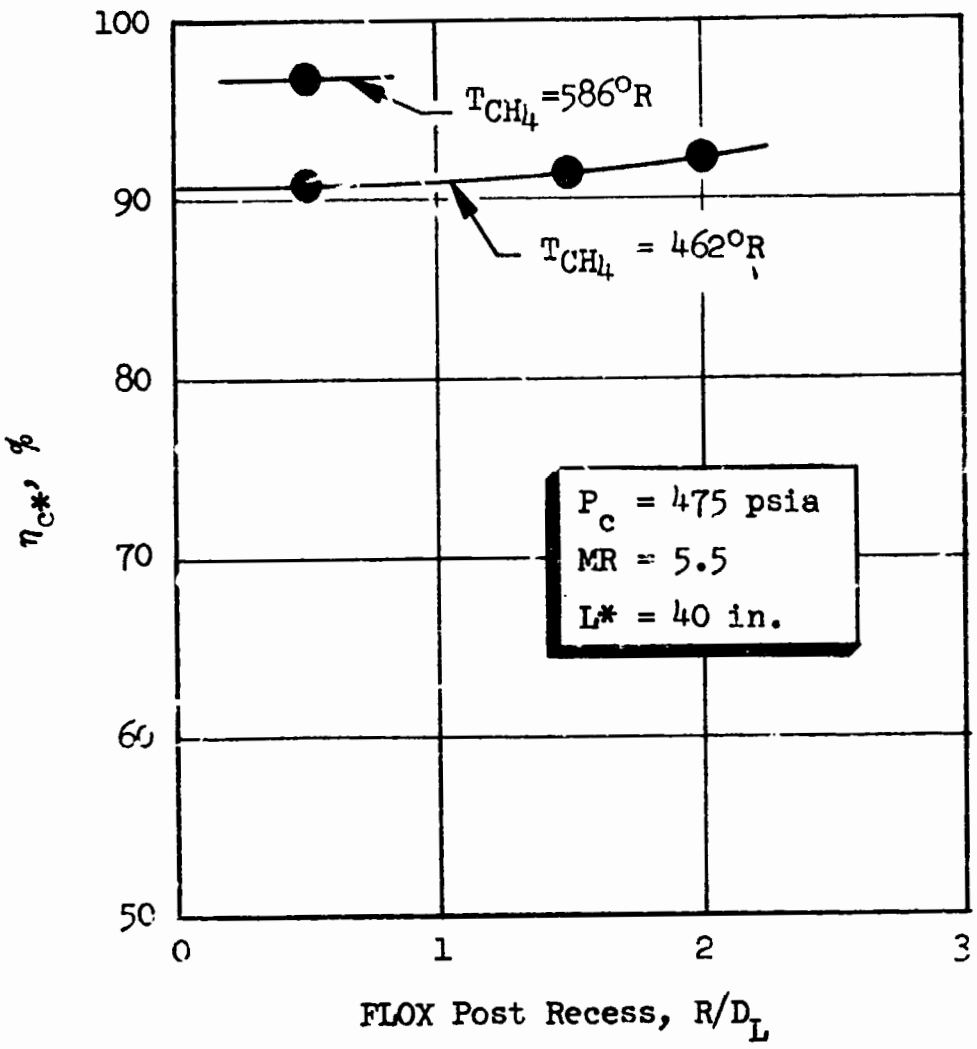

Figure 45. Hot-Fire Results of FLOX Post Recess Tests

A firing with R = 3 D_L was made, but due to the failure of a pressure transducer during the firing reliable performance data were not obtained. However, no injector hardware burning (neither oxidizer post nor injector face) was experienced. Note that the methane injection temperature for all the data of Fig. 44 and 45 was low ($\approx$15 F) due to the cooling of the ambient temperature methane by the LN_2 chilled injector hardware. The low methane injection temperature resulted in gas phase densities higher than the target value (ρ_g = 1.45 lbm/ft^3) with an attendant decrease in the gas gap velocity.

Examination of the data of Fig. 44 and 45 show that the highest performance level ($\approx$92 percent) was short of the program performance goal of η_{c*} = 99 percent.

Analysis of the cold-flow mixing and atomization data indicated that element performance would be improved if the methane were heated above ambient temperature. For a given chamber pressure, heating the methane above ambient temperature results in decreased gas phase density with an attendant increase in the gas gap velocity. The analysis predicted increased performance levels due to a reduction in the mean drop size.

To substantiate the cold-flow data and analysis, a test at R = 1/2 D_L was conducted with methane heated to 586 R (injected stagnation temperature). Element performance increased from 90.8 to 96.8 percent when the methane temperature was increased from 462 to 586 R. These data also are shown in Fig. 45.

6.2.1 Single-Element Chamber Heat Flux

Figure 46 presents typical measured chamber wall heat flux profiles measured during the short duration ($\approx$3.5 seconds) parametric hot-firing series. The data are for an oxidizer post recess of 1/2 D_L for the 10, 20, and 40-inch L* chamber, respectively. No apparent dependency of chamber wall heat flux on post recess was evident. Note that for all three chamber L*'s, heat flux levels near the injector face are very low ($\approx$0.5 Btu/in.^{2}-sec). This heat flux data near the injector face was utilized to provide guidelines for the selection of a full-scale injector in the later phases of the program.

6.2.2 Single-Element Cup ΔP

The test series which was used to assess the performance effects of recessing the FLOX post at constant L* (Fig. 45) provided information in regard to combustion effects within the cup region of the element. Figure 47 presents cup pressure drop data for both hot-fire and cold-flow (i.e., nonburning) experiments with the No. 1 element configuration. Plotting the parameter $\rho\Delta P$ allows comparison of the data from cold-flow and hot-fire experiments which were conducted at slightly different gas-phase densities, but at the same mass flowrate ($\dot{w}_g \simeq 0.033$ lbm/sec). Examination of Fig. 47 shows a rapid divergence of cup pressure drop between hot-fire and cold-flow for post recess values greater than 1-1/2 D_L. These data indicate for post recess depths greater than 1-1/2 D_L that combustion occurred within the cup.

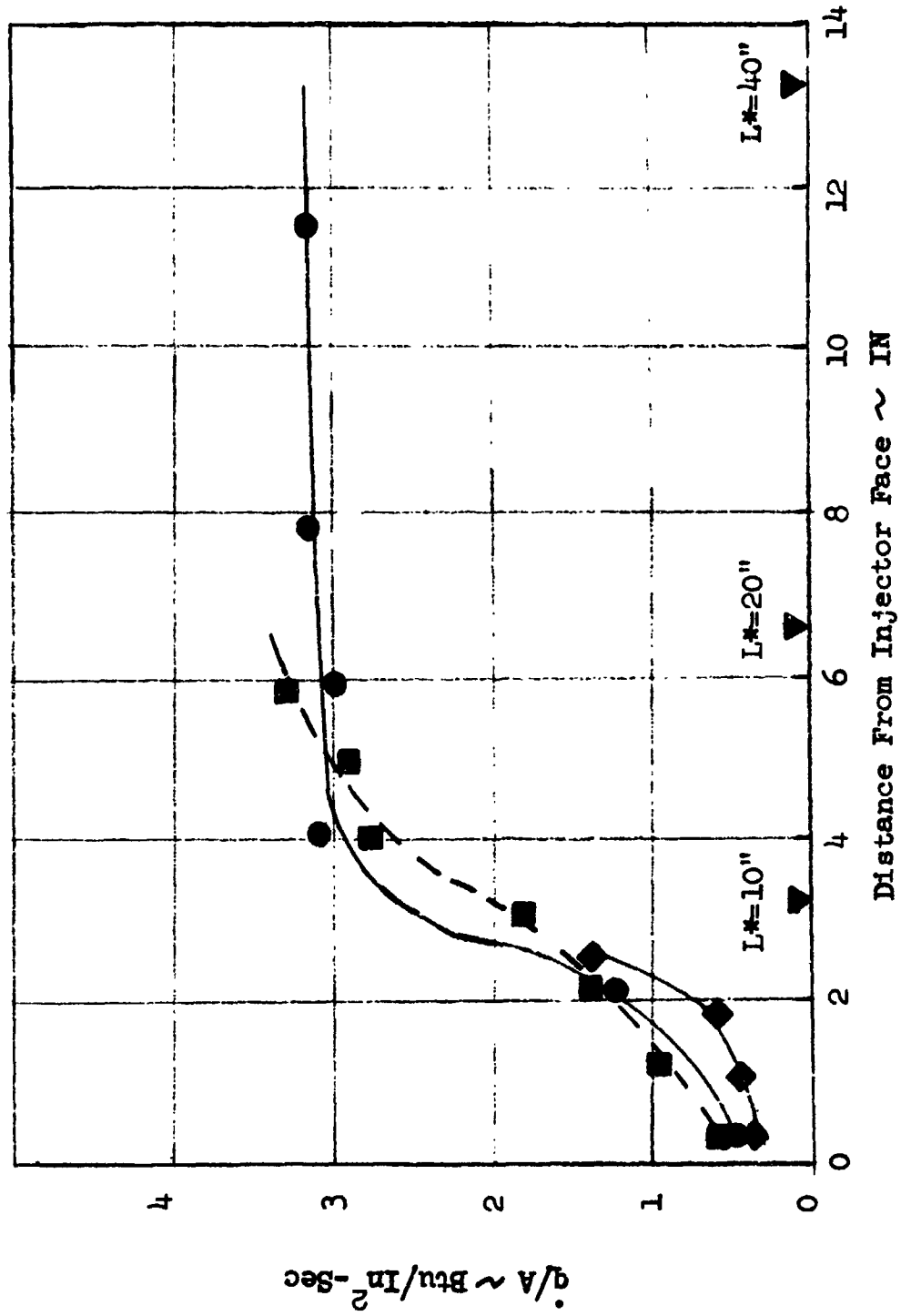

Figure 46. Single-Element Chamber Wall Heat Flux Data

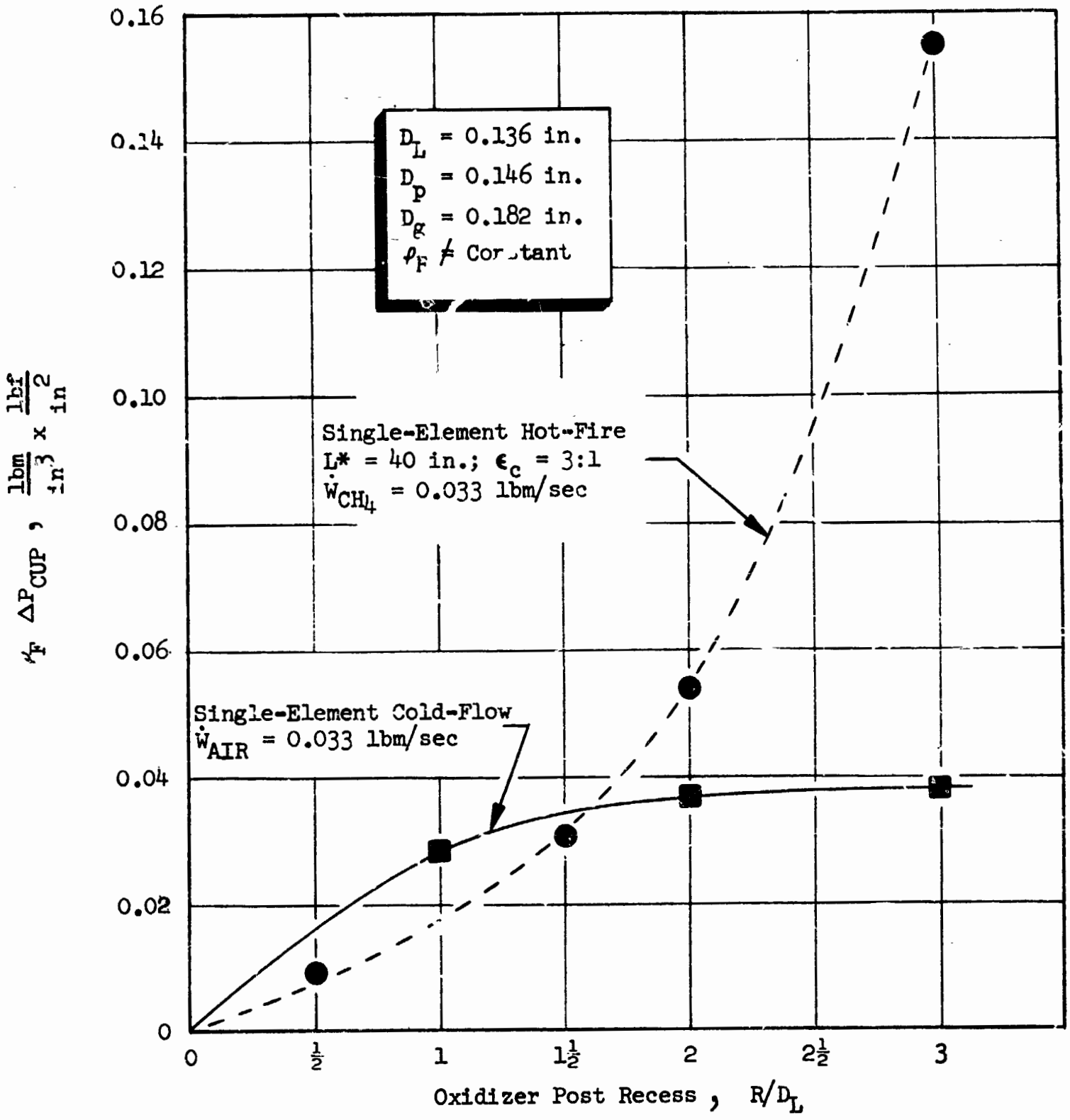

Figure 47. Hot-Fire and Cold-Flow (Mixing) Cup Pressure Drop as a Function of Post Recess

6.3 PERIPHERAL ELEMENT HOT-FIRE RESULTS

6.3.1 Peripheral Element Performance

The two candidate peripheral elements were hot-fired to determine their performance levels and chamber wall heat flux characteristics. Table VII presents a comparison of the performance levels of the BLC and scarfed post peripheral (see Fig. 9) element configurations. In comparing the two peripheral element configurations from a performance standpoint, it is evident that the recessed post ($R/D_L = 1$) with BLC is superior for all the conditions which were tested. One test was made with the scarfed post element to determine the effects of lowering the injected mixture ratio. As shown in Table VII, lowering the mixture ratio resulted in a significant decrease in the performance level.

TABLE VII. COMPARISON OF PERIPHERAL ELEMENT HOT-FIRE PERFORMANCE ($T_{CH_4} \approx 470$ R)

Configuration	$MR_{overall}$	$MR_{element}$	P_c, psia	$\dot{w}_{BLC}$	$\eta_{c^*,meas.,\%}$
Recessed Post With 6.8% BLC* ($R/D_L = 1$)	4.86	6.03	441	0.0074	92.4
Recessed Post With 10% BLC ($R/D_L = 1$)	4.39	5.96	454	0.01095	93.8
Scarfed Post With Swirl	5.28	5.28	418	-	85.5
Scarfed Post With Swirl	3.02	3.02	454	-	72.2

*BLC percentage is defined as a percent of total fuel flow for a 3000-lbf FLOX/CH_4(g) engine at 500 psia assuming that one third of injector elements are located in the peripheral zone.

6.3.2 Peripheral Element Chamber Heat Flux

The single-element graphite chambers ($L^* = 40$ in.) were instrumented with thermocouples to obtain axial heat flux data at two circumferential locations (180 degrees apart) in the chamber. One of these rows of thermocouples was oriented to be in line with the 0.047-in. BLC hole for that element type, and in the low mass flux region for the scarfed element type.

Figure 48 presents measured heat flux levels for tests conducted with the BLC configuration at 6.8 and 10-percent BLC flow. Shown in the plot are typical data for the chamber region which was 180 degrees away from the BLC hole. Comparison of the

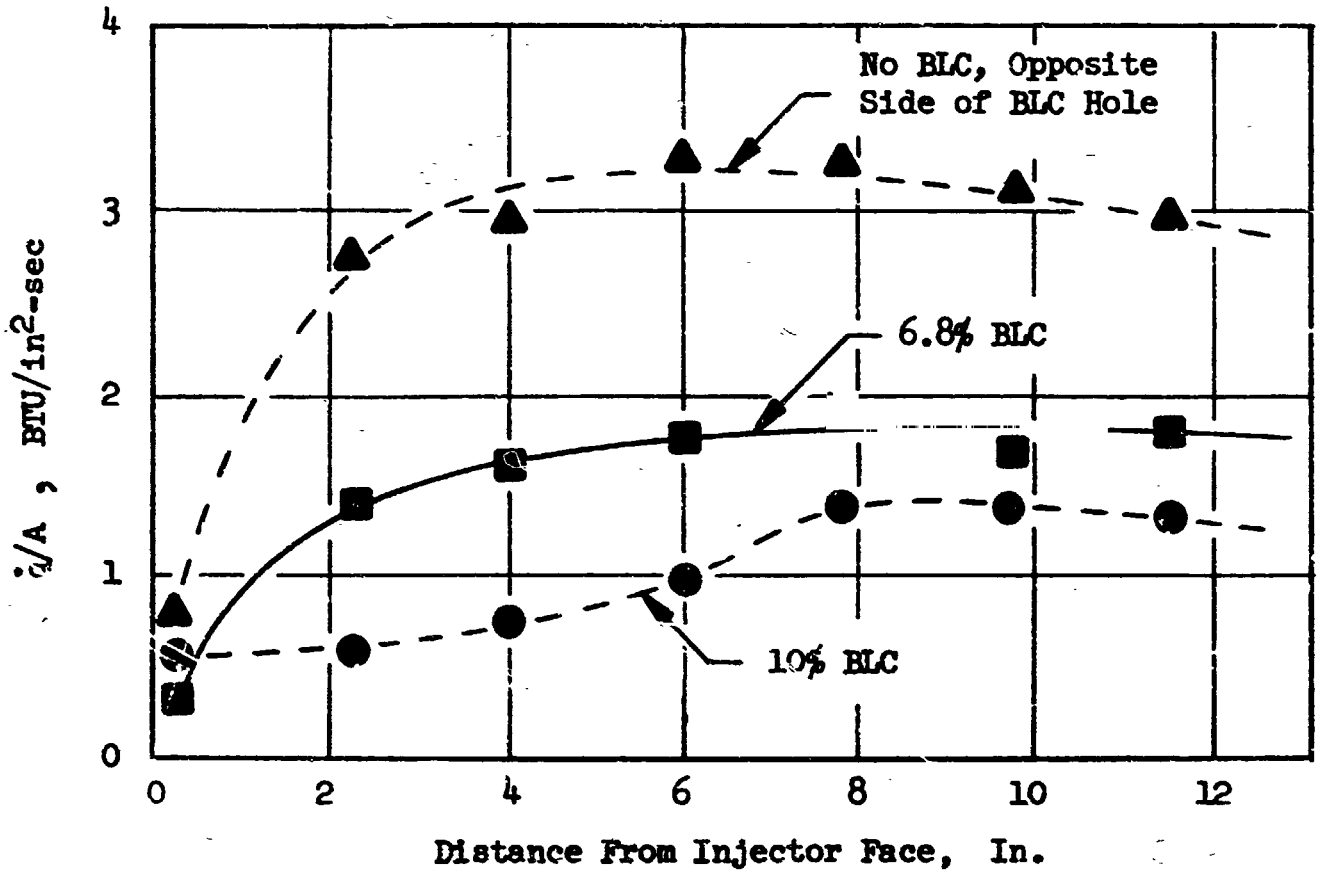

Figure 48. Chamber Heat Flux Profiles From Single-Element BLC Hot-Fire Tests

heat flux levels seen along the two sides of the chamber provided a direct measure of the intended bias of heat flux away from one side of the element. As expected, significant lower heat fluxes were measured in the BLC region.

Figure 49 presents chamber wall heat flux data for the scarfed post with swirl element at a mixture ratio of 5.28. Also shown on the figure (for comparison) are heat flux data from a "performance" element (R = 1 D_L, MR = 5.5). As indicated, local heat flux levels in the low mass flux wall region were reduced approximately 30 percent from "performance" element heat flux levels, whereas, at the opposite side of the chamber, heat fluxes corresponded closely with those produced by the "core" element.

For another comparison, heat flux data for the scarfed post with swirl and the BLC peripheral element data are shown together in Fig. 50. Even at the 6.8-percent BLC level, wall heat flux levels are lower (≈10 percent) than those obtained with the scarfed post with swirl element. This is true in spite of the fact that the performance levels (see Table VII) are significantly higher with the BLC configuration.

The results of the single-element hot-firing data can be physically interpreted in light of the mass flux profiles from the cold-flow experiments. Figure 43 presented (normalized) cold-flow mass flux data for the scarfed post and BLC elements. The flux profiles for the scarfed post element show that the element displaces mass from the wall region but the local wall mixture ratios are higher than the injected mixture ratios. The flux profiles for the BLC tests show that liquid distribution is not affected by the showerhead BLC flow. However, the displacement of the gas distribution from the centerline of the element is evident. The resulting characteristics of the BLC flow field include a low wall region mixture ratio, but no reduction in mass fluxes near the wall. From the results of hot-firing experiments, it appears that the low mixture ratios produced by the BLC element were more effective in reducing wall heat fluxes than were the reduced wall mass flux generated by the scarfed post with swirl element. This result, in addition to the higher performance of the BLC configuration, clearly makes that element a superior peripheral candidate.

L* = 40 In.

MR = 5.28

P_c = 418 psia

● ~ Chamber Region of High Mass Flux

■ ~ Chamber Regic.. of Low Mass Flux

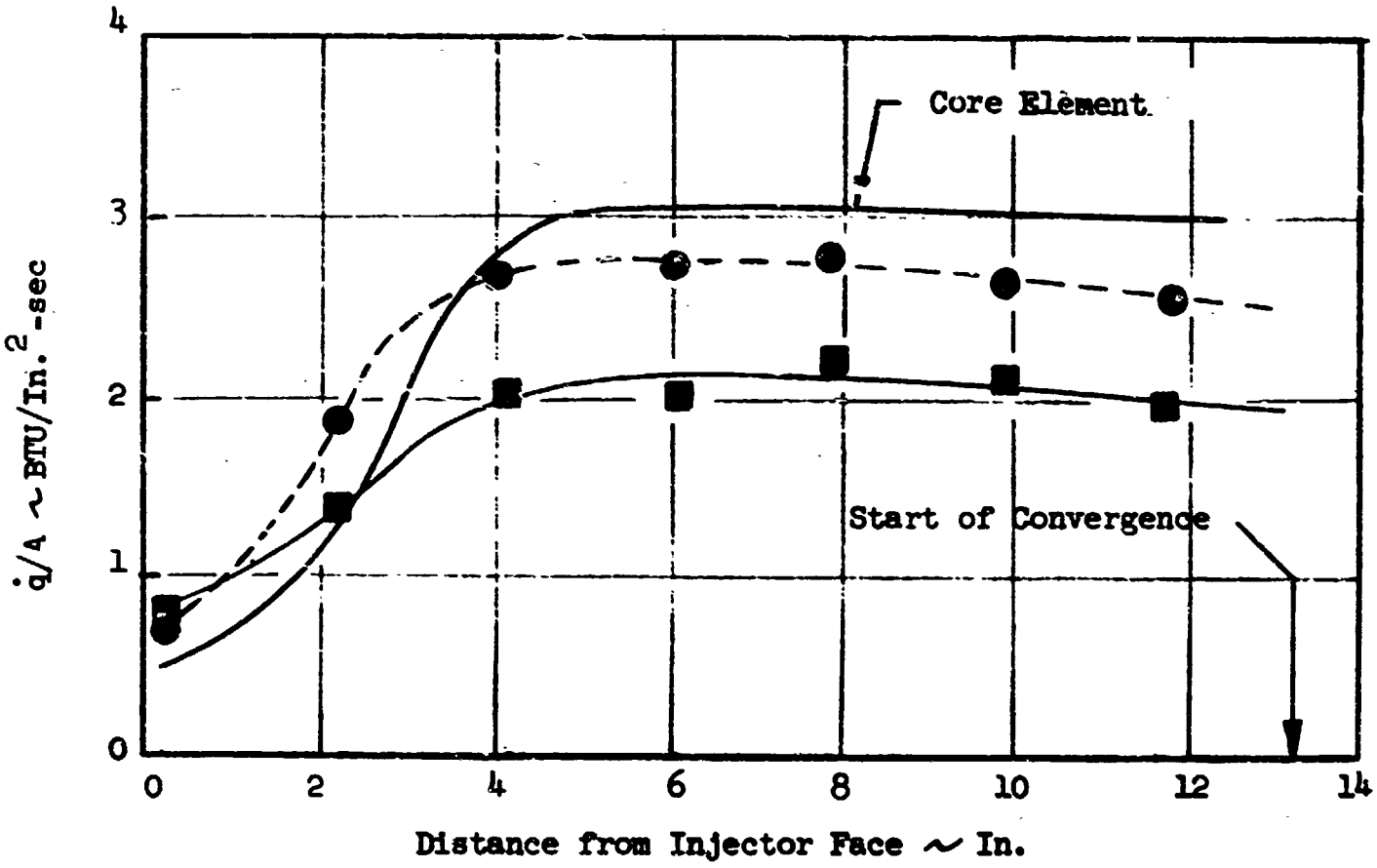

Figure 49. Heat Flux Data from Scarfed Post With Stirl Element

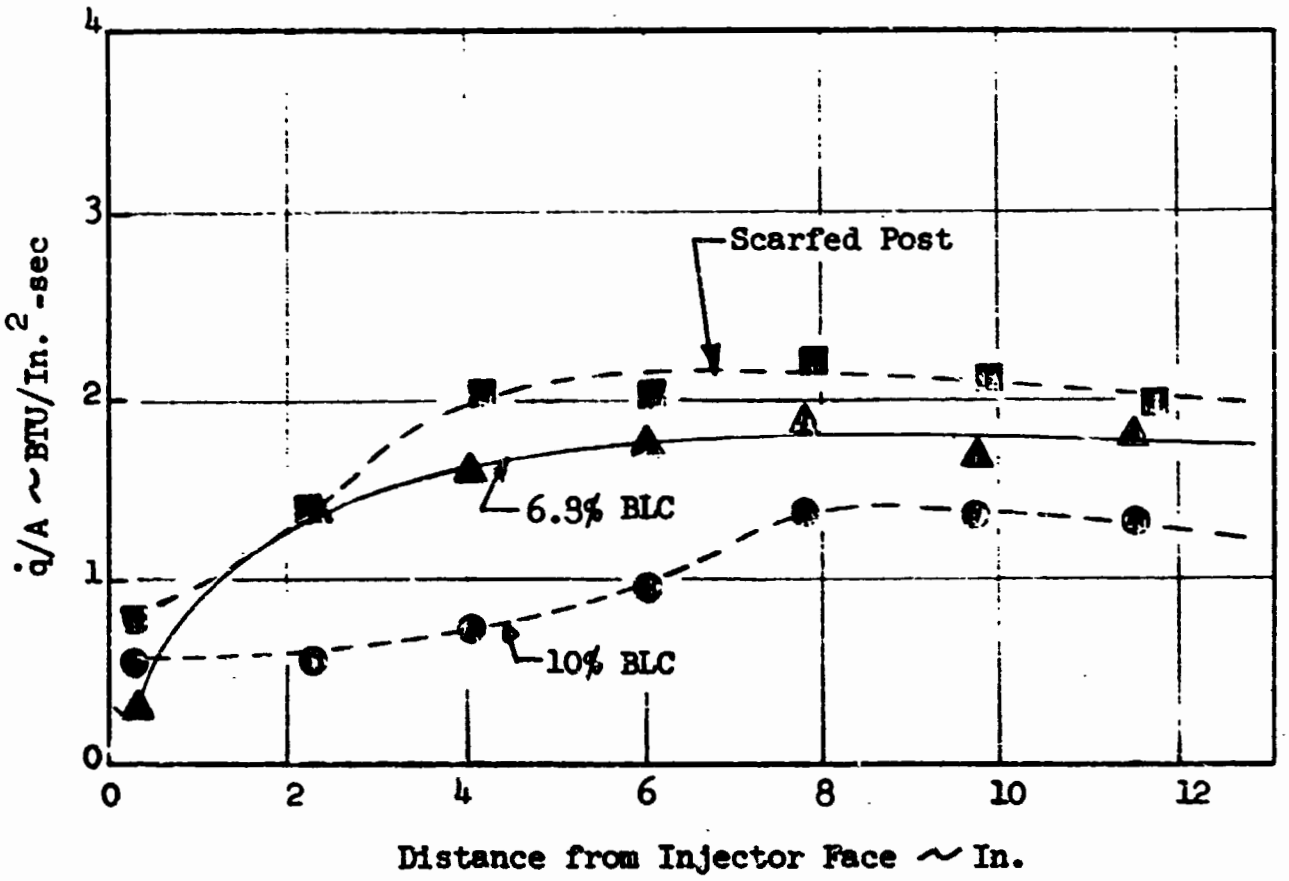

Figure 50. Comparison of Scarfed Post and BLC Heat Flux Levels

7.0 CORRELATION OF SINGLE-ELEMENT COLD-FLOW/HOT-FIRE DATA

The cold-flow data (atomization and mixing) of Section 5.0 and the single-element hot-fire data of Section 6.0 were analyzed to determine if the cold-flow data could successfully predict the parametric variations investigated in the single-element hot-firing series. That is, chamber L* was varied keeping post recess constant to infer hot-fire mixing levels. Also, FLOX post recess and percent BLC flow were varied to assess their relative effects on performance.

7.1 CORRELATION OF CORE ELEMENT PERFORMANCE DATA

Since the individual single-element hot-fire operating conditions did not precisely match the cold-flow conditions (i.e., ρ_g, V_g, $\dot{w}_{TOT}$) the cold-flow data were plotted in a form convenient for interpolation to the hot-fire conditions. Figure 51 presents a composite plot of the D_L = 0.136 in., D_g = 0.182 in., R = O mixing data (E_m) as a function of the total propellant flowrate. Figure 52 presents a similar plot of the atomization data ($\bar{D}_{wax}$) for the element. Utilizing these two curves it was possible to predict element E_m and $\bar{D}_{wax}$ for a specific hot-fire condition.

In correlating the hot-fire experiments where the post recess was not equal to zero, appropriate corrections were made to the data of Fig. 51 and 52. These correction factors were derived from cold-flow mixing and atomization data which showed the independent effects of oxidizer post recess (see Fig. 24 and 34). That is, the predicted E_m values of Fig. 51 were adjusted for R > 0 and the predicted D values of Fig. 52 were increased slightly for R > 0.

To predict a mean FLOX drop size for the hot-fire system the mean drop size data ($\bar{D}_{wax}$) of Fig. 52 were corrected for the difference in physical properties of Shell-270 wax and FLOX.

The values employed for the respective physical properties of 82.6% FLOX and Shell-270 wax are shown in Table VIII.

TABLE VIII. PHYSICAL PROPERTIES OF FLOX AND WAX

Property	82.6% FLOX*	Shell-270 Wax**
Viscosity (μ), centipose	0.23	4.0
Surface Tension (σ), dyne/cm	13.8	17.5
Density (ρ), lbm/ft^3	89	47.1

*Interpolated data taken from NASA SP-3037, "Handling and Use of Fluorine-Oxygen Mixtures in Rocket Systems"
**Dannenbrink, R. W., Shell Chemical Co., Private Communication, Telecon to L. Zajac, Advanced Programs, Rocketdyne

As indicated, Shell-270 wax simulates reasonably well the surface tension of FLOX but differs in density and absolute viscosity.

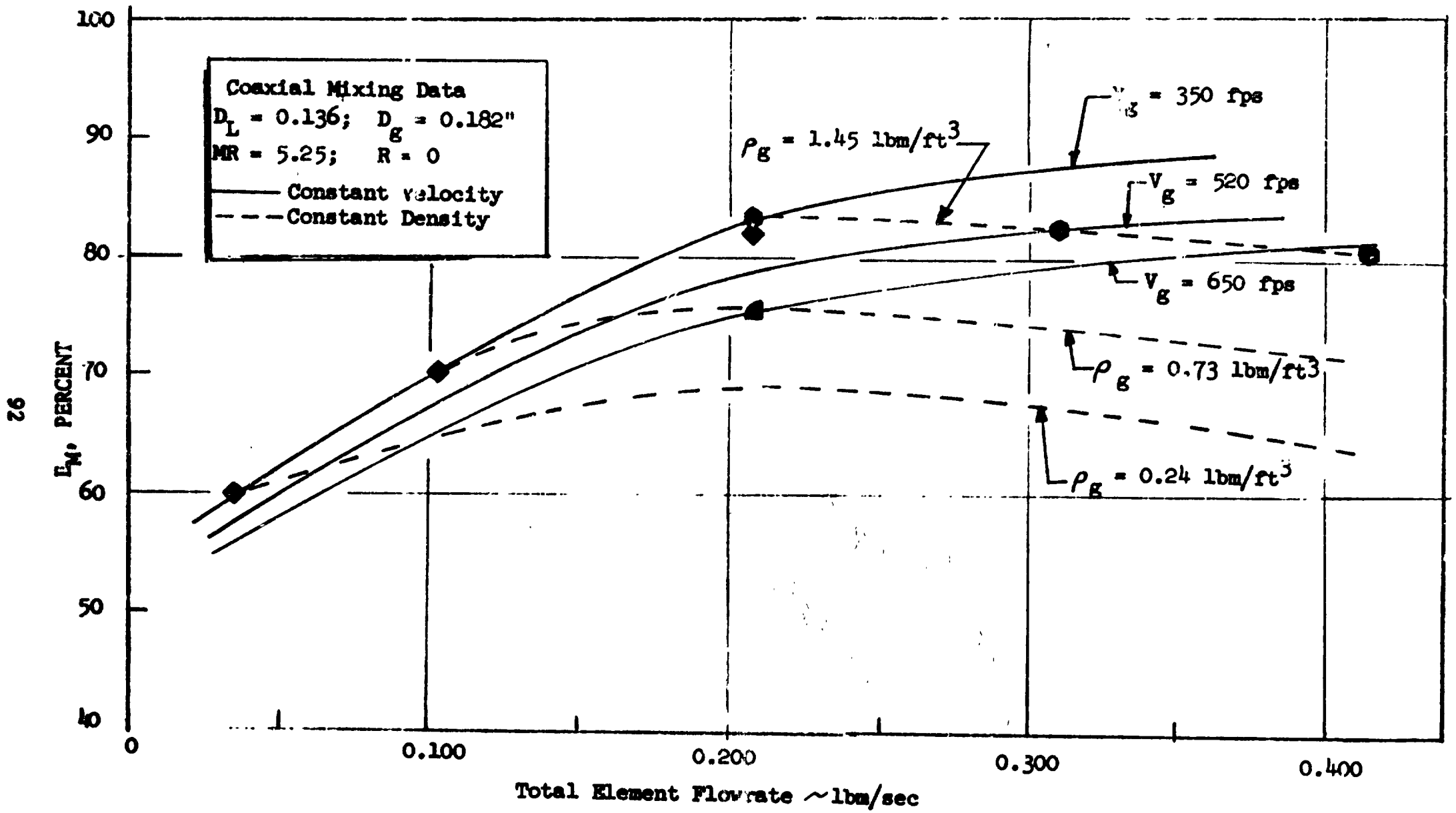

Figure 51. Single-Element Mixing Data

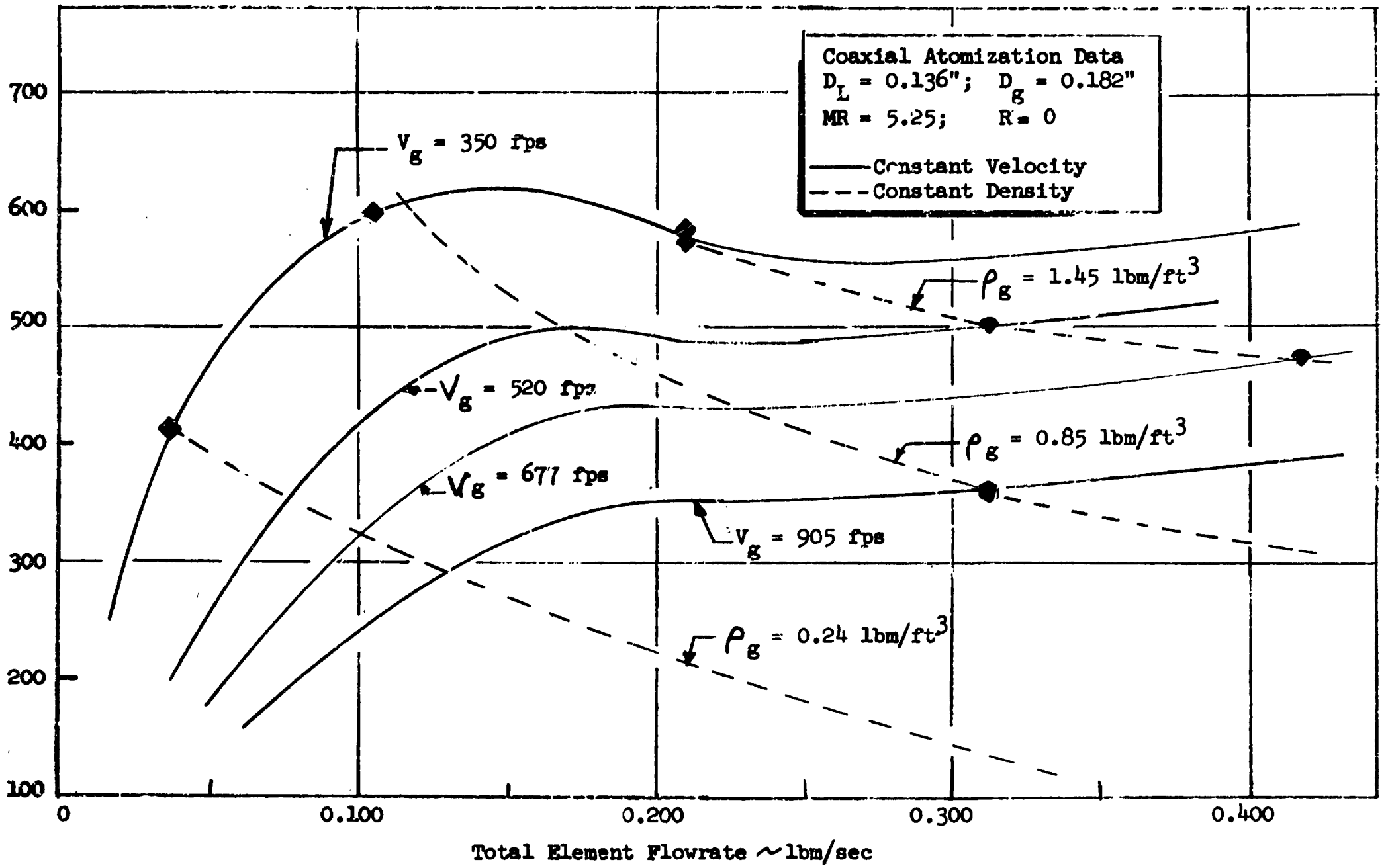

Figure 52. Single-Element Atomization Data

The correction factor which was employed was based on the work of Ingebo (Ref. 24); i.e.,

$$\bar{D}_{FLOX} = \left[\frac{\mu FLOX}{\mu WAX} \quad \frac{\sigma FLOX}{\sigma WAX} \quad \frac{\rho WAX}{\rho FLOX}\right]^{1/4} \bar{D}_{WAX} \tag{6}$$

$$= 0.394\ \bar{D}_{WAX}$$

The predicted vaporization efficiencies ($\eta_{c^*,vap}$) were then determined employing the corrected atomization data of Fig. 52 and the results of the vaporization limited combustion model (K-PRIME). Figure 53 presents combustion model results for the three single-element hot-firing chambers (L* = 10, 20, and 40 inches, ε_c = 3:1). For initial conditions it was assumed that the initial spray velocity was 100 ft/sec and 10 percent of the FLOX had vaporized 1 in. from the injector face.

The predicted mixing efficiencies ($\eta_{c^*\ mix}$) were determined employing the mixing data E_m of Fig. 51 (corrected for R ≠ 0) and the curve of Fig. 54 which presents the relationship of E_m and $\eta_{c^*,mix}$ for the FLOX/CH_4(g) propellant combination. The overall predicted c* for efficiency was calculated by:

$$\eta_{c^*} = \eta_{c^*,mix} \times \eta_{c^*,vap} \tag{7}$$

Figure 55 presents the comparison of the cold-flow/hot-fire results for the test series where chamber L* was varied to infer a hot-firing mixing performance. The measured c* efficiency data for the 10-in. L* experiments were lowered by 5 percent to correct for the Rayleigh pressure losses which occur in the nozzle portion of short L* chambers (due to combustion within the nozzle). The 5 percent correction factor was based on measured chamber pressure profile data which were generated in NAS3-11199(20). This correction is necessary only when measured c* is based on chamber pressure rather than thrust. Shown in Fig. 55 are the predicted cold-flow mixing levels for each of the test series (R = 0, 1/2, and 1 D_L with changing L*). Extrapolation of the hot-fire data to L* values (L* >> 40 in.) where the performance loss due to vaporization (i.e., $\eta_{c^*,vap}$ = 100%) would be insignificant shows that within the precision of the data that the cold-flow and hot-fire mixing levels are essentially in agreement.

Figure 56 presents the results of the data correlation analysis for the test series where FLOX post recess was changed keeping chamber L* constant. Figure 56 presents the results of the analysis in a manner which illustrates the ability of the cold-flow data to predict the parametric variations of the hot-fire results. The data are plotted as change in c* efficiency ($\Delta\eta_{c^*}$) from the efficiency which was determined (in either hot-fire or cold-flow tests) from a nominal condition (R = 0, L* = 40 in.). As indicated, the cold-flow data successfully predict the results of the hot-fire tests in that performance was not a strong function of post recess.

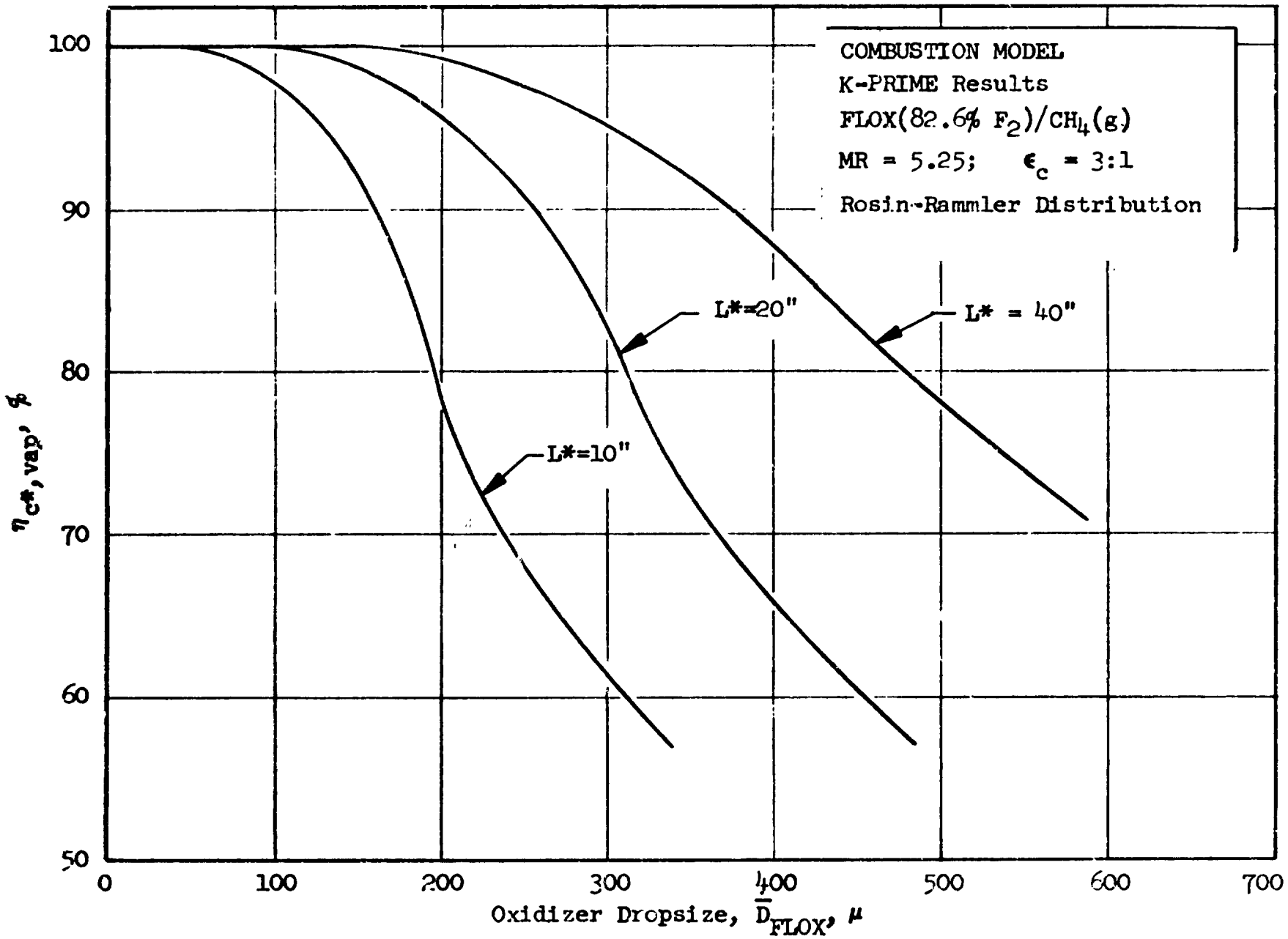

Figure 53. Combustion Model Results

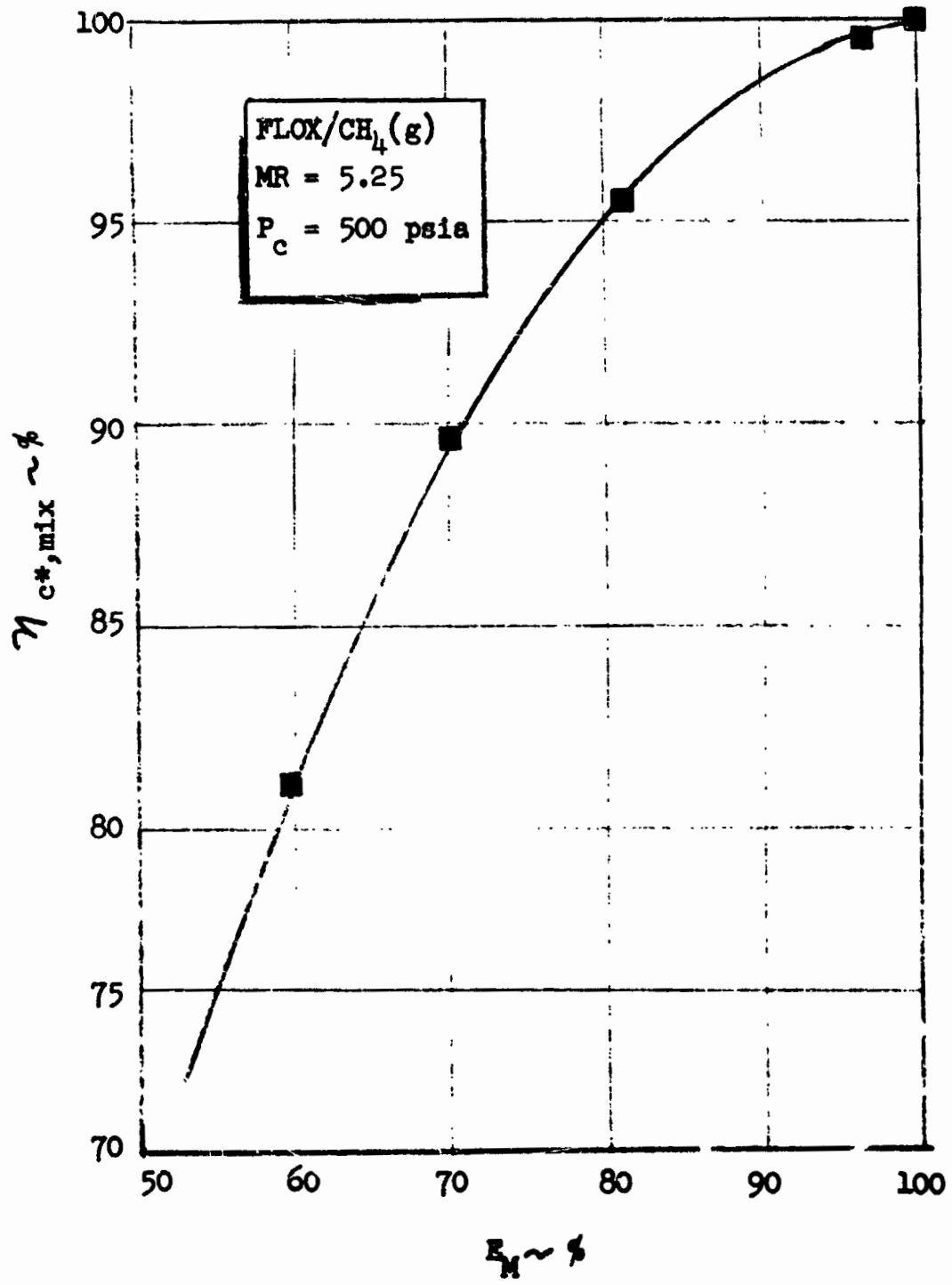

Figure 54. Relationship Between $\eta_{c^*,mix}$ and E_M

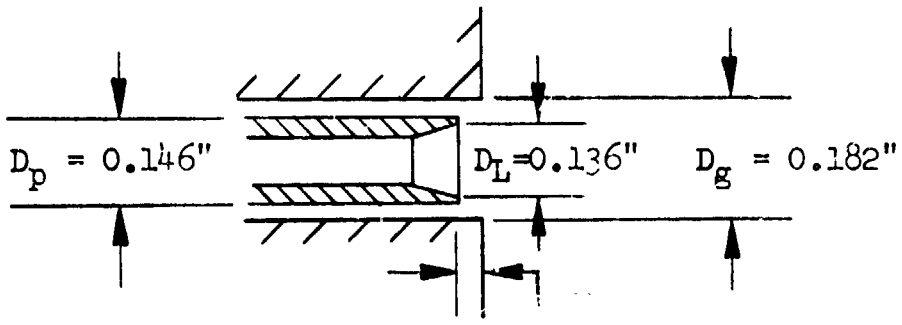

R = Post Recess

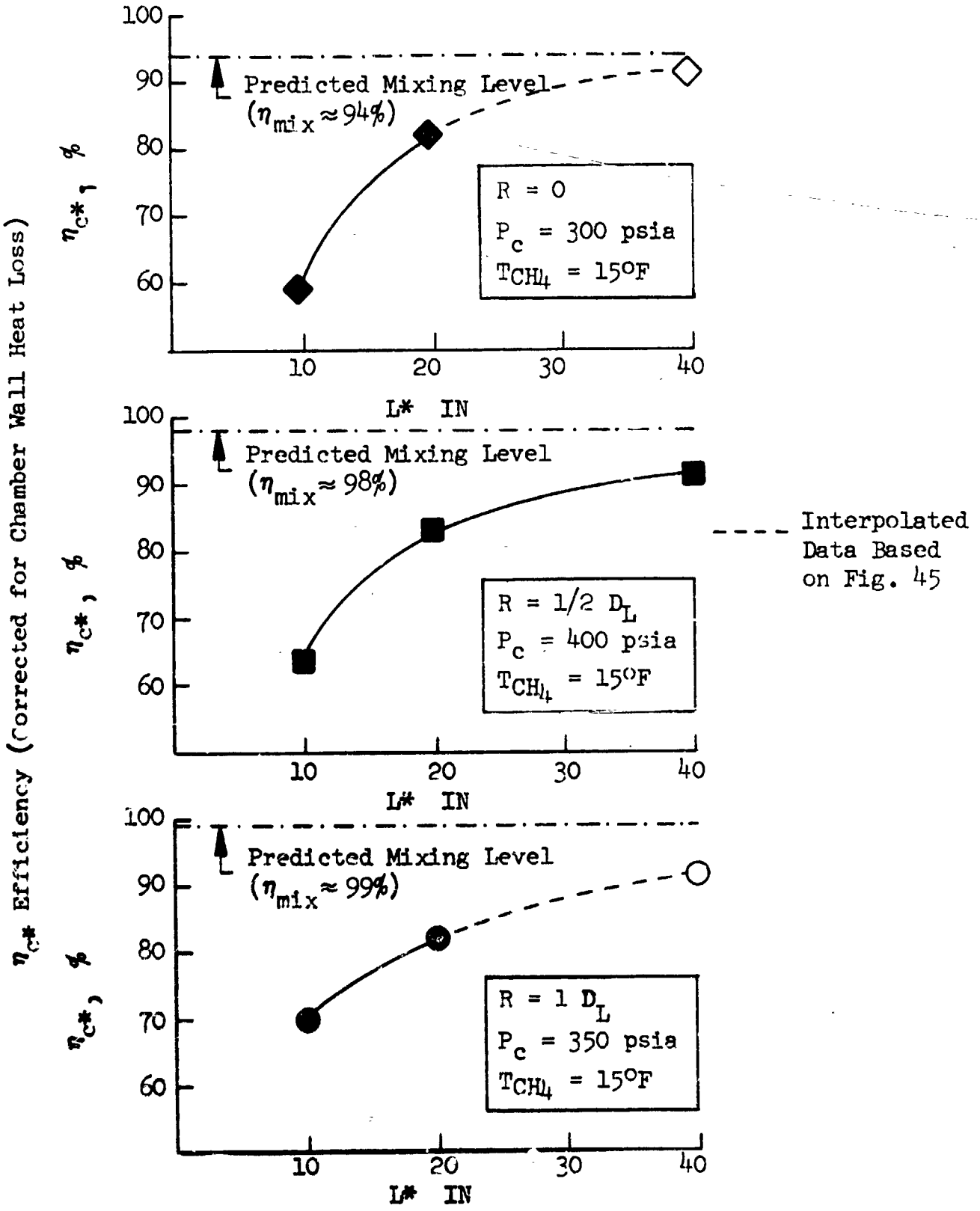

Figure 55. Cold-Flow/Hot-Fire Correlation of Chamber L* and Post Recess Hot-Fire Results

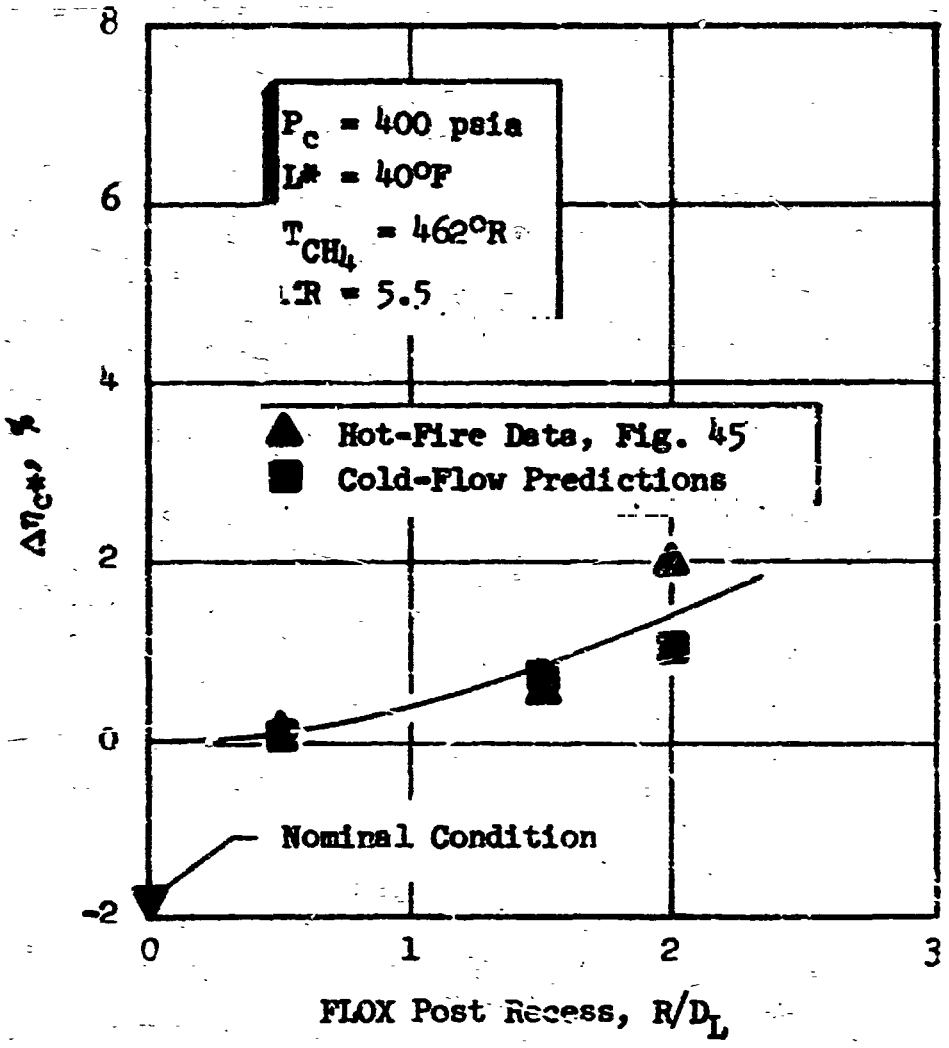

Figure 56. Hot-Fire/Cold-Flow Correlation of FLOX Post Recess Series

7.2 CORRELATIONS OF PERIPHERAL ELEMENT PERFORMANCE DATA

The results of the peripheral element hot-firing tests were correlated with available cold-flow data. For the BLC element, mixing levels were determined by interpolating (as a function of $\dot{w}_{BLC}$) the data presented in Section 5.0. Predicted mean drop size was based on the results of the core element studies at a recess value of 1 D_L. The scarfed post element mixing levels were taken from Fig. 40 and the mean wax drop size was taken as 590μ. That drop size was the result of an atomization test which employed a 45-degree in-line helical swirler but for which the post tip was not scarfed.

Figure 57 presents the results of the correlation analysis for the test series in which the performance effect of percent BLC flow are determined. As in Fig. 56, the results are presented as relative change in performance, $\Delta\eta_{c^*}$, from a nominal condition (BLC = 6.7%, R = 1 D_L). The cold-flow data are essentially in agreement with the hot-fire results which showed performance is not a strong function of BLC flowrate.

Extensive data were not available to correlate the performance levels of the scarfed post with swirl element. At an injected mixture ratio of 5.28, the cold-flow data predicted η_{c^*} = 88.3 percent compared to η_{c^*} = 85.8 percent as measured in the hot-fire test.

7.3 CORRELATION OF PERIPHERAL ELEMENT HEAT FLUX DATA

The results (see Fig. 50) from the single-element hot-firing tests showed that reducing chamber wall zone mixture ratio was more effective in reducing heat flux levels than reducing wall zone mass flux levels. Thus, local wall zone mixture ratios of the peripheral and core elements were correlated with measured wall heat flux rates. Local wall zone mixture ratios for the peripheral elements were determined by integrating the mass flux profiles shown in Fig. 43. Only the profiles from Sectors 2 and 3 were integrated since those regions comprise the wall region in the single-element chamber. For the "core" element, wall zone mixture ratio was taken as the injected mixture ratio since at the test conditions mixing levels were approximately 98 percent.

Figure 58 presents the results of the correlation analysis plotted as average chamber wall heat flux as a function of wall zone mixture ratio. Average chamber wall heat fluxes were determined by integrating the heat flux profiles of Fig. 49 and 50 from the injector to the start of nozzle convergence. The average chamber wall heat flux was found to decrease with wall zone mixture ratio. In addition, Fig. 58 shows that employing "peripheral" elements instead of "core" elements in the wall zone of an injector can result in significant reductions in chamber heat flux levels.

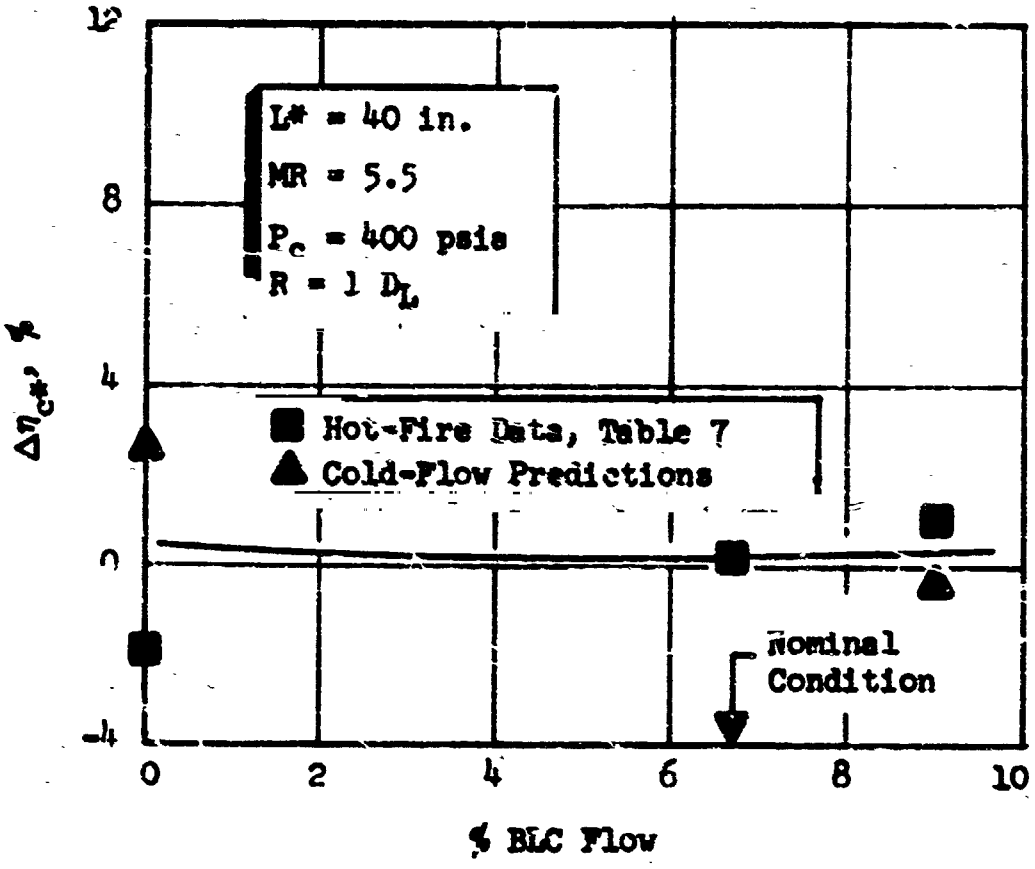

Figure 57. Cold-Flow/Hot-Fire Correlation of BLC Peripheral Element Performance Data

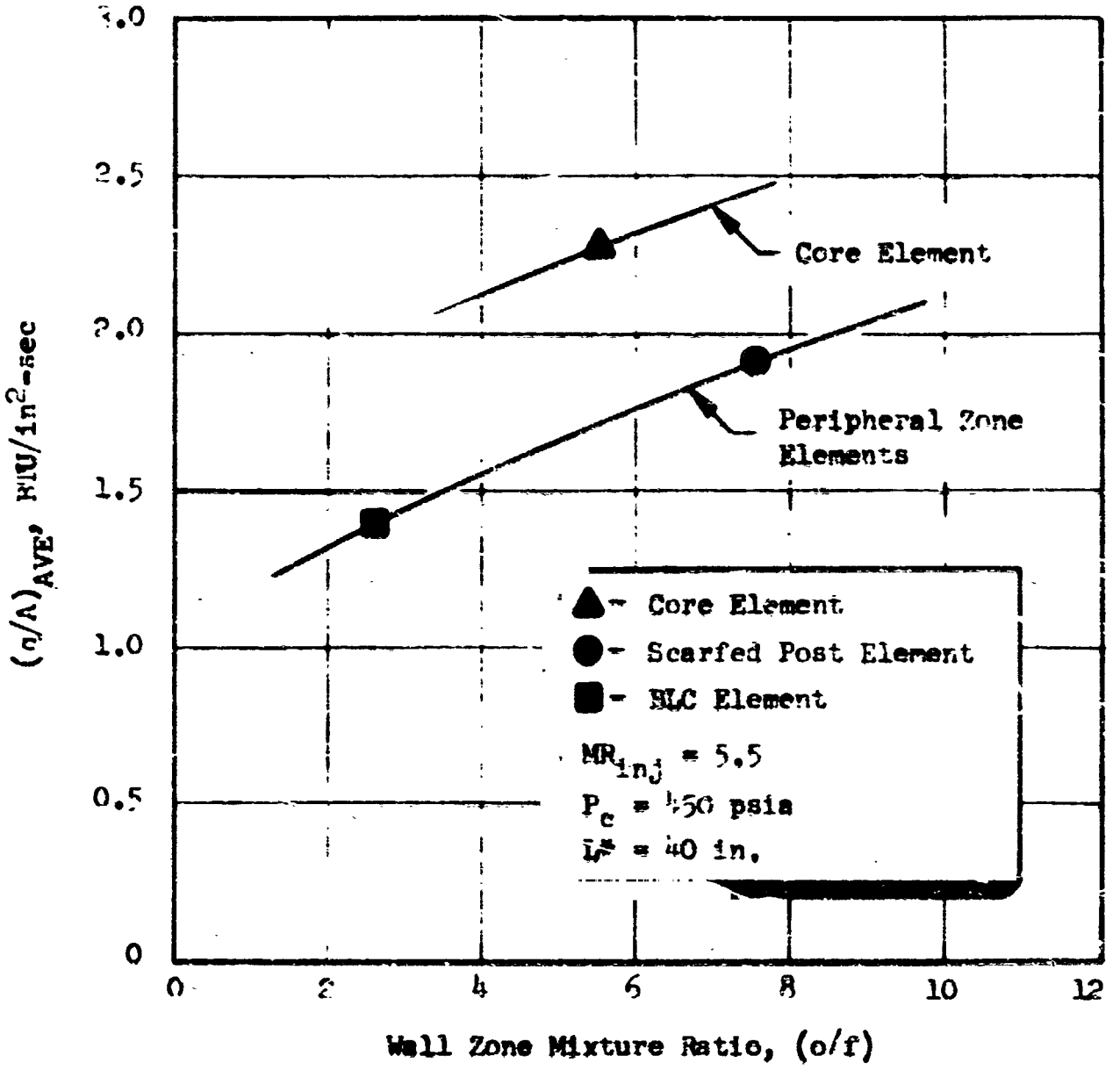

Figure 58. Correlation of Cold-Flow Wall Mixture Ratios With Hot-Fire Average Heat Flux Levels (Injector Face to Start of Nozzle Convergence)

PRECEDING PAGE BLANK NOT FILMED

8.0 FULL-SCALE INJECTOR EVALUATION

This section presents the design rationale, cold-flow evaluation, and the results of the hot-fire testing of the 3000-lbf full-scale coaxial injector. The design of the full-scale injector was unique in the fact that it was based directly upon guidelines established from analysis of cold-flow and single-element hot-fire data. Heretofore, these data have not been available for the design of high-pressure space storable rocket motors.

8.1 INJECTOR DESIGN RATIONALE

The single-element, cold-flow studies were employed to configure a core element for single-element, hot-fire evaluation. As shown in Table V, the cold-flow studies showed that the performance of the No. 1 element was ≈1 to 3 percent higher than the No. 2 and 3 elements at the design condition. However, under throttled conditions, the No. 1 element clearly was superior.

Agreement with parametric variations was obtained between the single-element, cold-flow results and hot-fire performance data (see Section 7.0). As shown in the hot-fire studies, recessing the FLOX post did enhance performance, but the effect was quantitatively small (see Fig. 45). A significant result of the single-element, hot-fire testing was that no injector burning was encountered, even at post recess depths up to 3 D_L.

Based on the results of the cold-flow investigation, which showed the superior throttling characteristics of the No. 1 element, along with the supporting single-element, hot-fire data, the No. 1 element (D_L = 0.136 in., D_p = 0.146 in., D_g = 0.182 in.) was chosen for the full-scale core element. A FLOX post recess depth of 1-1/2 D_L (0.204 in.) was chosen based on the data of Fig. 44 an 47. Recessing the posts to depths greater than 1-1/2 D_L would have resulted in slight performance improvements (Fig. 44), but would have increased the risk of injector burning due to cup burning effects (Fig. 47).

The chamber wall heat flux measurements which were made during the single-element, hot-fire series indicated very low heat fluxes near the injector face (Fig. 44, 48, and 49). Based on these data, an analysis of the temperature distribution in the injector face indicated that cooling of the face would not be required. Prior to this program, high-pressure FLOX/CH_4(g) programs had employed some method of injector face cooling, i.e., Rigimesh, etc. (Ref. 22). Elimination of the injector face cooling requirements reduced significantly the complexity and fabrication cost of the full-scale injector. A description of the fabrication details of the injector was presented in Section 4.0.

The single-element, hot-fire studies conducted with the two peripheral element candidates (BLC and scarfed post) revealed that significantly higher performances were available with the BLC configuration (Table VII). In addition, lower chamber wall heat flux levels were obtained with the BLC configuration (Fig. 50). Consequently, the BLC element was clearly the superior peripheral element candidate and was chosen for the full-scale injector. For this element, a recess value of

1-1/2 D_L (0.204 in.) was chosen so that all oxidizer posts would be recessed uniformly. A BLC hole diameter of 0.038 in. was chosen to provide a BLC injection velocity equal to the element gas gap velocity at the 6-percent BLC level. Note that 21 of the 43 injector elements are located in the peripheral zone of the injector (Fig. 14). Thus, approximately 50 percent of the injector mass flow was concentrated in the peripheral zone. In addition, the BLC holes were separately manifolded so that the percentage of BLC could be varied during the hot-fire evaluation.

8.2 FULL-SCALE INJECTOR COLD-FLOW RESULTS

Cold-flow mixing tests with the full-scale injector were performed in the pressurized gas/liquid mixing facility. In these tests, a pressurized chamber was employed which was equal in diameter to the hot-fire chamber (3.880 in.), and all measurements were made 5 inches from the injector face as in the single-element mixing experiments. These tests were conducted to determine effects on mixing of overall injected mixture ratio, pressure throttling, and percentage of BLC flowrate. The results of these experiments are presented in Fig. 59 (shaded symbols). Also shown for comparison are results of analogous tests which were conducted with single-element models.

The top portion of Fig. 59 presents results for experiments with no BLC flow. As indicated, the predicted mixing performance ($\eta_{C^*,mix}$) was approximately 98 percent at the simulated design condition (P_c = 500, MR = 5.2). Also shown are mixing results from single-element tests for analogous conditions. As indicated by the fact that single-element and full-scale injector mixing efficiencies were almost identical, the data suggest that interelement mixing effects are of second order for this particular injector configuration. These results are not too surprising when one considers the low element density of the injector (interelement spacings are about 0.6 in.).

The bottom portion of Fig. 59 shows the results of the tests with BLC flow (6.8 and 9 percent). For comparison, mixing levels as predicted by single-element cold-flow results also are shown. The predicted single-element performance was derived by mass weighting (based on percent of peripheral mass flow) the results from experiments conducted with a performance and a BLC-type element. As indicated, the single-element and full-scale mixing data predict little change in mixing-limited with increased BLC flowrate. The results of the single-element, hot-fire series (Fig. 57) showed that increasing BLC flow had little effect in overall performance.

8.3 FULL-SCALE INJECTOR HOT-FIRE TESTS

8.3.1 Parametric Performance Tests

Hot-fire tests were conducted with parametric variations of injected mixture ratio, pressure throttling, and percentage of BLC flow. Appropriate correction factors were applied to the measured data. A complete discussion of the method of correcting the performance data is presented in Appendix E. Table IX presents a summary of measured and calculated data for all tests conducted with the full-scale injector.

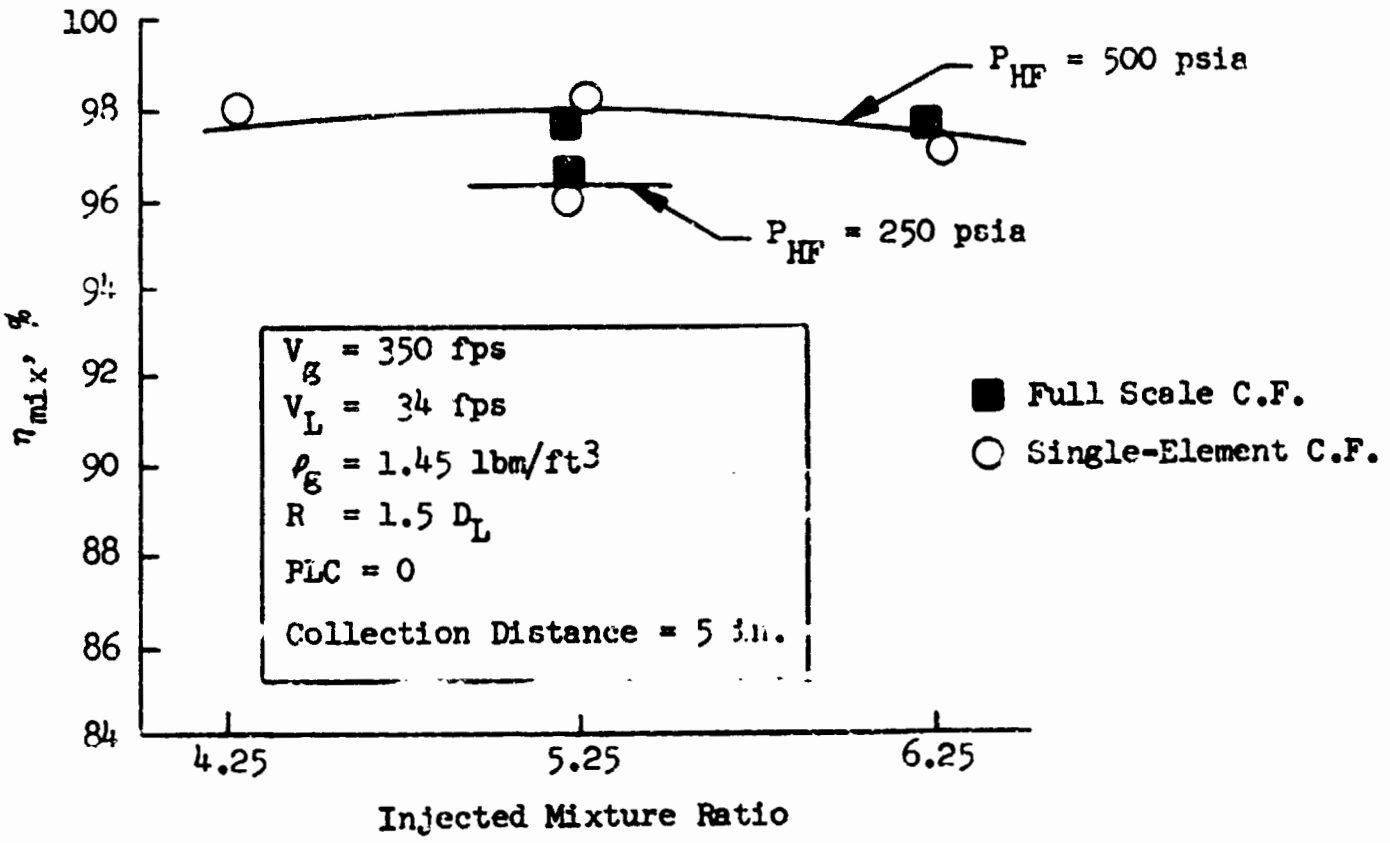

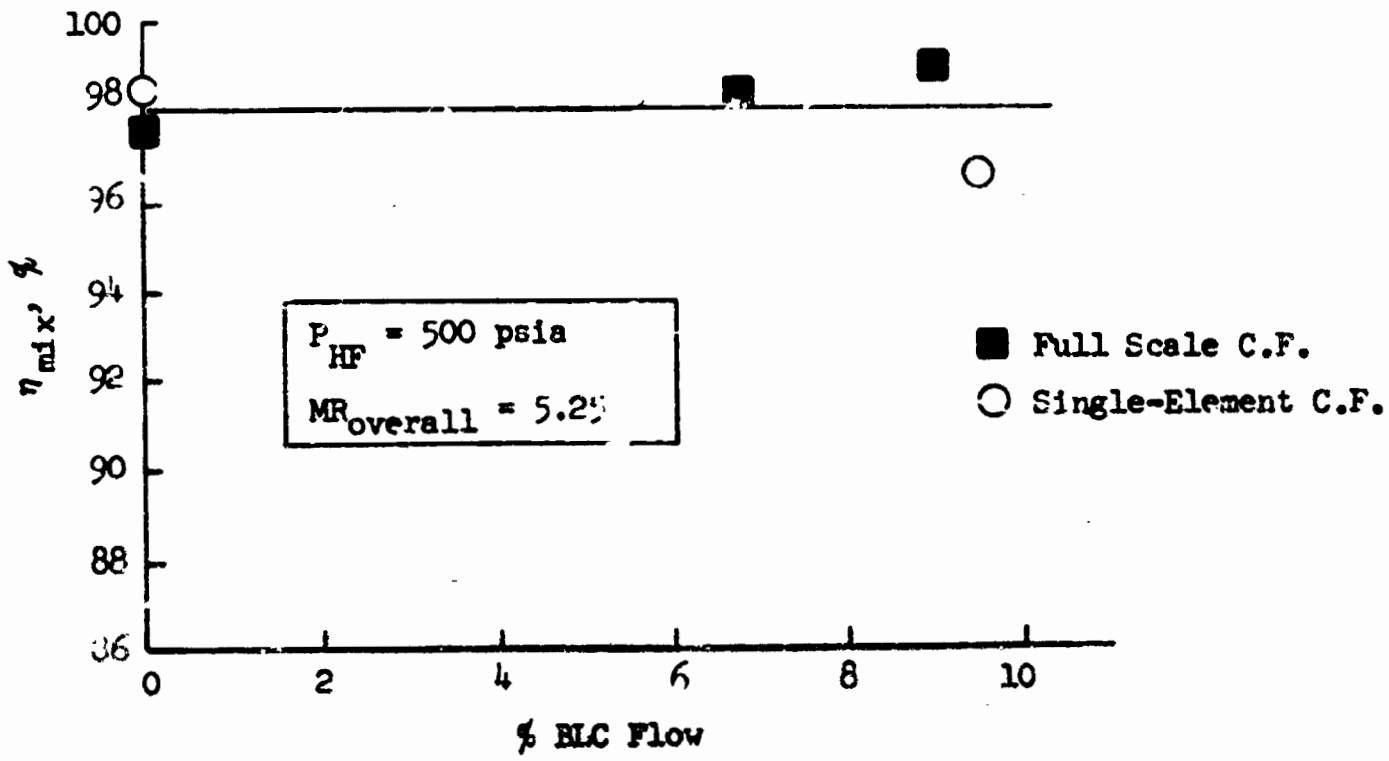

Figure 59. Results of Full-Scale Mixing Tests

FOLDOUT FRAME 1

TABLE IX. SUMMARY OF FULL-SCALE H

(Chamber L* = 40 inche

Rocketdyne Reference Run No.	Chamber Throat Area ($In.^2$)	Oxidizer Flowrate (lbm/sec)	Fuel Flowrate (lbm/sec)	Fuel Injection Temperature (°F)	Chamber Stagnation Pressure (psia)
015	3.955	7.62	1.73	21.5	--
016	3.956	7.61	1.75	9.5	519
017	3.960	7.91	1.47	2.1	512
018	3.971	8.05	1.44	1.9	516
019	3.992	8.50	1.30	-1.4	518
020	4.009	3.87	0.801	15.0	242
021	Malfunction of fuel main valve				
022	4.024	8.25	1.33	-2.6	516
023	4.041	8.16	1.34	-10.0	507
024	4.049	4.08	0.571	0.1	--
025	4.052	1.85	0.262	13.7	106
026	4.059	1.84	0.302	15.8	106
027	4.024	4.18	0.637	-3.0	254
028	3.974	8.07	1.298	-0.4	507
031-1	3.969	7.77	1.35	11.9	506+
031-2	3.973	7.75	1.38	3.8	502+
031-3	3.973	7.75	1.40	3.4	503+
031-4	3.979	7.81	1.44	-10.5	515+
031-5	3.986	7.80	1.45	-20.5	520+
031-6	3.993	7.80	1.49	-25.5	520+

*No pressure taps in chamber for duration test

**Thrust measurement not reliable due to nozzle flow separation effects.

+Injector face pressure

++Chamber heat loss assumed to be negligible for duration test.

FOLDOUT FRAME 2

FULL-SCALE HOT-FIRE DATA

= 40 inches, ε_c = 3:1)

Chamber Stagnation Pressure (psia)	Vacuum Thrust (lbf)	Corrected η_{c^*,P_c} (%)	Corrected $\eta_{c^*,FVAC}$ (T)	Comments
--	--	--	--	1 sec. check-out test
519	3329	100.4	101.8	
512	3312	97.8	98.9	
516	3342	97.3	98.4	
518	3388	97.3	99.3	
242	--**	95.3	--	Throttle test
516	3406	96.7	98.3	W_{BLC} = 0.096 lbm/sec
507	3369	95.9	97.5	W_{BLC} = 0.0320 lbm/sec
--	--**	--	--	Transducer failure
106	--**	95.9	--	Throttle test, W_{BLC} = 0.0199 lbm/sec
106	--**	94.5	--	Throttle test
254	--**	96.1	--	Throttle test, W_{BLC} = 0.0683 lbm/sec
507	3232	96.1	94.9	Bomb test, W_{BLC} = 0.0683 lbm/sec
506+	3254	--*	98.3	W_{BLC} = 0.0982 lbm/sec
502+	3263	--*	98.5	W_{BLC} = 0.0932 lbm/sec
503+	3265	--*	98.5	W_{BLC} = 0.0986 lbm/sec
515+	3314	--*	99.0	W_{BLC} = 0.1005 lbm/sec
520+	3345	--*	100.0	W_{BLC} = 0.1014 lbm/sec
520+	3361	--*	100.3	W_{BLC} = 0.1022 lbm/sec

++ Duration Test 44 Sec

At the design condition (P_c = 500 psia), performance was calculated based on measured thrust and chamber pressure. Figure 60 presents a comparison of injector performance based on these two methods. As indicated, the average performance levels (based on thrust) were approximately 1.3 percent higher than performance based on chamber pressure. The reason for this small discrepancy was not apparent. Thus, performance values for the P_c = 500-psia tests were taken as the average value between those based on thrust and chamber pressure. For the throttled tests, injector performance was based on chamber pressure due only to nozzle separation effects which can invalidate performance values based on thrust measurements.

Figure 61 presents the results of the test series to determine the effects of injected mixture ratio and throttling. In Fig. 61 and 62, the heat loss correction factors were based on measured chamber heat flux levels determined during the short-duration (≤3 seconds) tests. Due to low chamber heat flux levels, this c* correction was not large amounting to approximately 0.7 percent at the design point. The data shown in Fig. 61 for the long-duration test (discussed in subsequent paragraphs) were not corrected for chamber heat loss since calculations showed that, for run times greater than 10 seconds, the chamber operated nearly adiabatically.

At the design point (P_c = 500, MR = 5.25), corrected c* performance was 98.8 percent. Throttling of the injector resulted in reduction of c* efficiency, but to values no lower than about 95 percent.

It should be noted that injected methane temperatures were low (≈2 to 15 F) which resulted in high injected gas densities ($\rho_g \approx 1.8$ lbm/ft^3) and low methane gas gap velicities (≈290 ft/sec). It was previously demonstrated that supplying the methane at higher temperatures (≈120 F) results in substantial increases in performance (Fig. 49). If the methane were supplied at simulated regenerative temperatures (≈800 F), it is estimated that injector performance would be near 100 percent for the range of parameters investigated.

Figure 62 presents the effects of BLC flow (as percent of total CH_4 flow) on injector performance. A nominal BLC flow of 6.0 percent resulted in approximately a 1-percent loss in c* performance. However, note that c* performance was nearly constant over a 5:1 (P_c = 500 to 100 psia) throttling range when BLC was employed. This was not the case when no BLC flow was used. Available instrumentation revealed no instabilities (neither high frequency or chugging) as the engine was throttled from 500 to 100 psia. This lack of any instabilities was noted both with and without BLC flow.

8.3.2 Chamber Wall Heat Flux

Chamber heat flux data were obtained during the short-duration tests by placing small thermocouples in selected locations within the ATJ graphite chamber. Chamber wall heat flux values were then calculated by assuming that the chamber wall was a semi-infinite slab suddenly exposed to constant $\dot{q}/A$ (see Appendix F for a description of the analysis). Knowing a time rate change of temperature in the

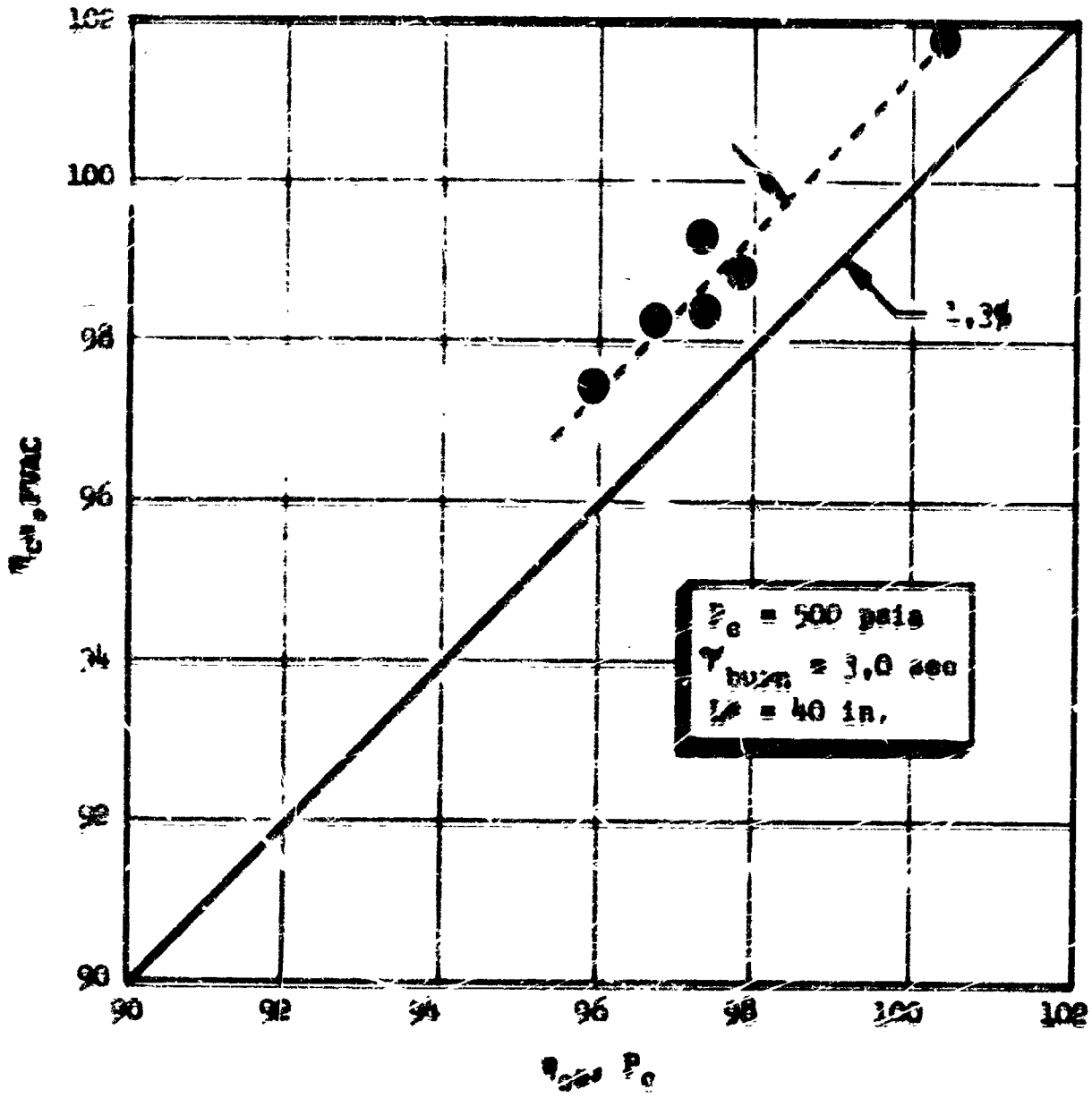

Figure 60. Comparison of Performance Data Based on Thrust and Chamber Pressure Measurements

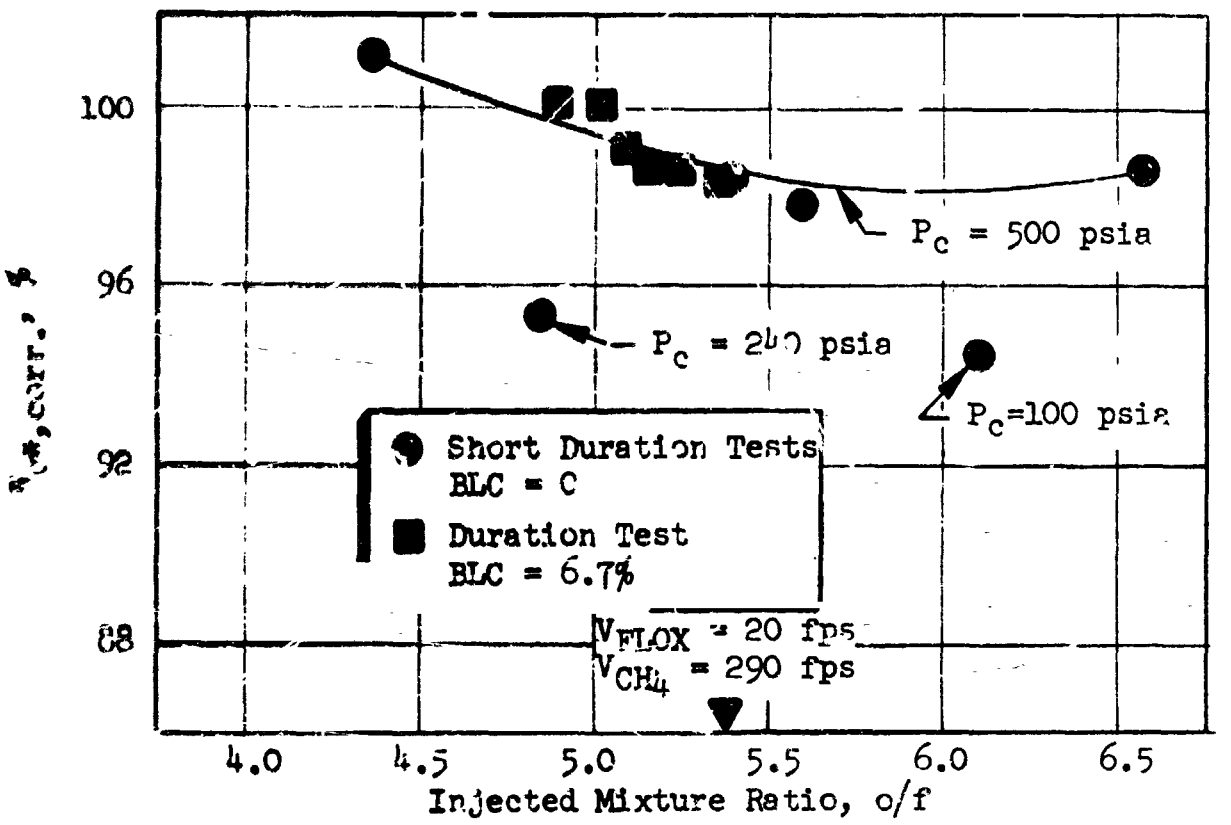

Figure 61. Hot-Fire Performance Data as a Function of Injected Mixture Ratio and Chamber Pressure

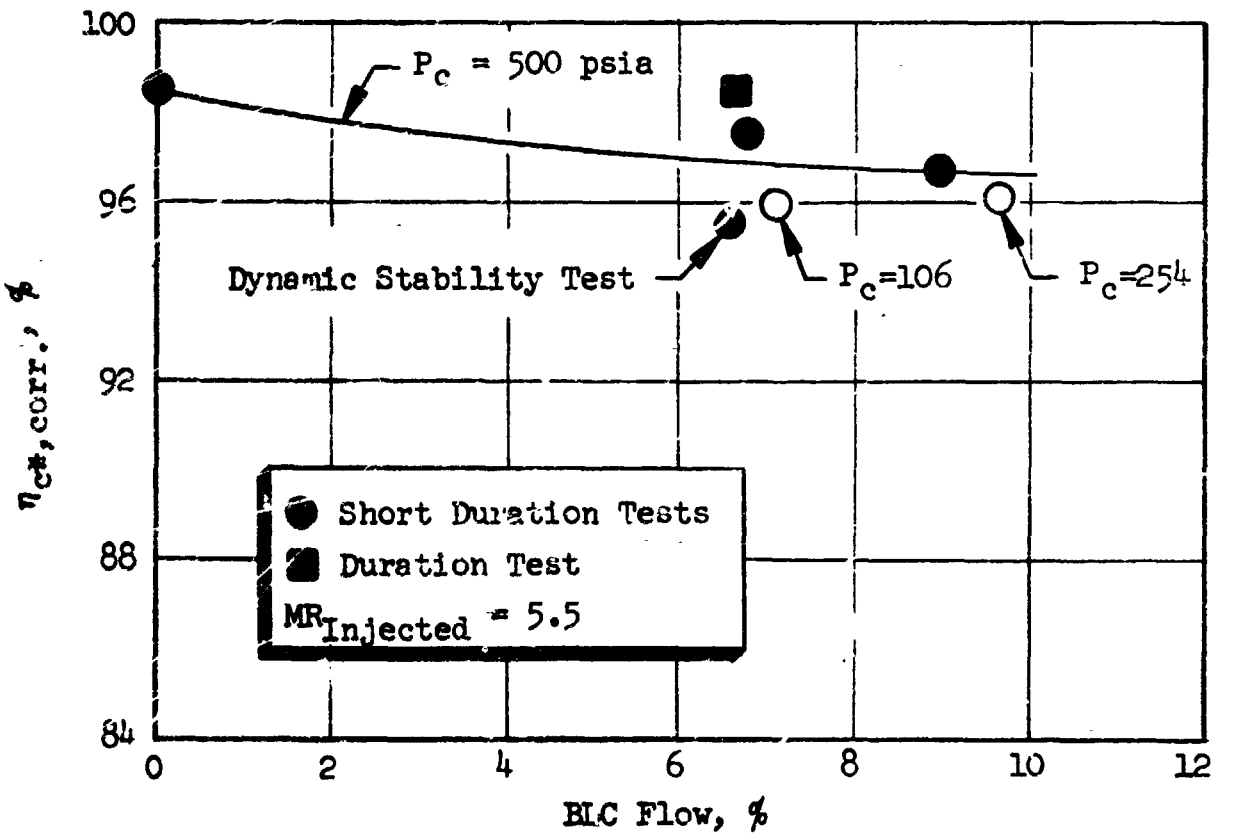

Figure 62. Hot-Fire Performance Data as a Function of Percent BLC Flow and Chamber Pressure

slab (determined by thermocouples located within the graphite liner) and the thermal properties of graphite, the thermocouple outputs were employed to deduce local values of chamber wall heat flux.

Figure 63 presents typical chamber heat flux profiles which show the effect of BLC flow. Also shown in Fig. 63 are injector face heat flux levels which were determined during the parametric tests (discussed in a subsequent paragraph). The data were reduced at a time (≈2.7 seconds in 3-second test) during the run where the chamber wall temperature was calculated (based on measured inner wall temperatures) to be approximately 1000 F. Thus, the chamber wall heat are comparable with regeneratively cooled chamber data with wall temperatures on the order of 1000 F. As expected, the BLC flow was found to be most effective near the injector end of the chamber. Heat flux levels in the convergent section and nozzle throat were found to be independent of percentage of BLC flow, Note, however, that increasing the percentage of BLC flow from 0 to 9 percent resulted in a 50-percent reduction in average chamber wall heat flux*. All experiments were conducted in a L* = 40 in., ε_c = 3:1 chamber.

9.3.3 Comparison of Chamber Heat Flux Levels

Figure 64 presents for comparison chamber heat flux from the present study and those of a Rocketdyne regeneratively cooled thrust chamber program (NAS3-11191, Ref. 19). In the referenced study, both triplet and concentric tube injectors were employed. The concentric tube injector was similar to that employed herein (D_L = 0.106 in., D_p = 0.146 in.; D_g = 0.182 in., R = 1 D_L) except thrust levels were higher (≈5000 lbf) and chamber contraction ratio was larger (ε_c = 4:1). As indicated, significantly lower heat chamber flux levels were measured in the present study.

Examination of Fig. 64 shows that extremely low values of heat flux were measured for the convergent and throat areas of the nozzle. The data are subject to question due to the manner in which the thermocouples were placed within the nozzle. In the cylindrical portion of the chamber thermocouples were embedded in the graphite liner by placing them in drilled holes to within 0.180 in. of the chambers inner surface. In all cases, powdered graphite was placed in the bottom of the drilled hole to minimize or eliminate resistance between the thermocouple tip and the graphite liner. In the convergent and throat areas of the nozzle, the thermocouple tips were placed 0.250 in. from the inner surface due to anticipated higher heat flux levels. Locating the tips at that distance from the surface could have resulted in errors due to lateral heat conditions in the nozzle where, in general, high axial heat flux gradients are established (i.e., see data of NAS3-11191, Fig. 64). In the cylindrical portion of the chamber large axial heat flux gradients are not established; thus, measurement errors due to axial heat condition in that region should be of second order.

*Defined as average chamber wall heat flux level from the injector face to the start of nozzle convergence.

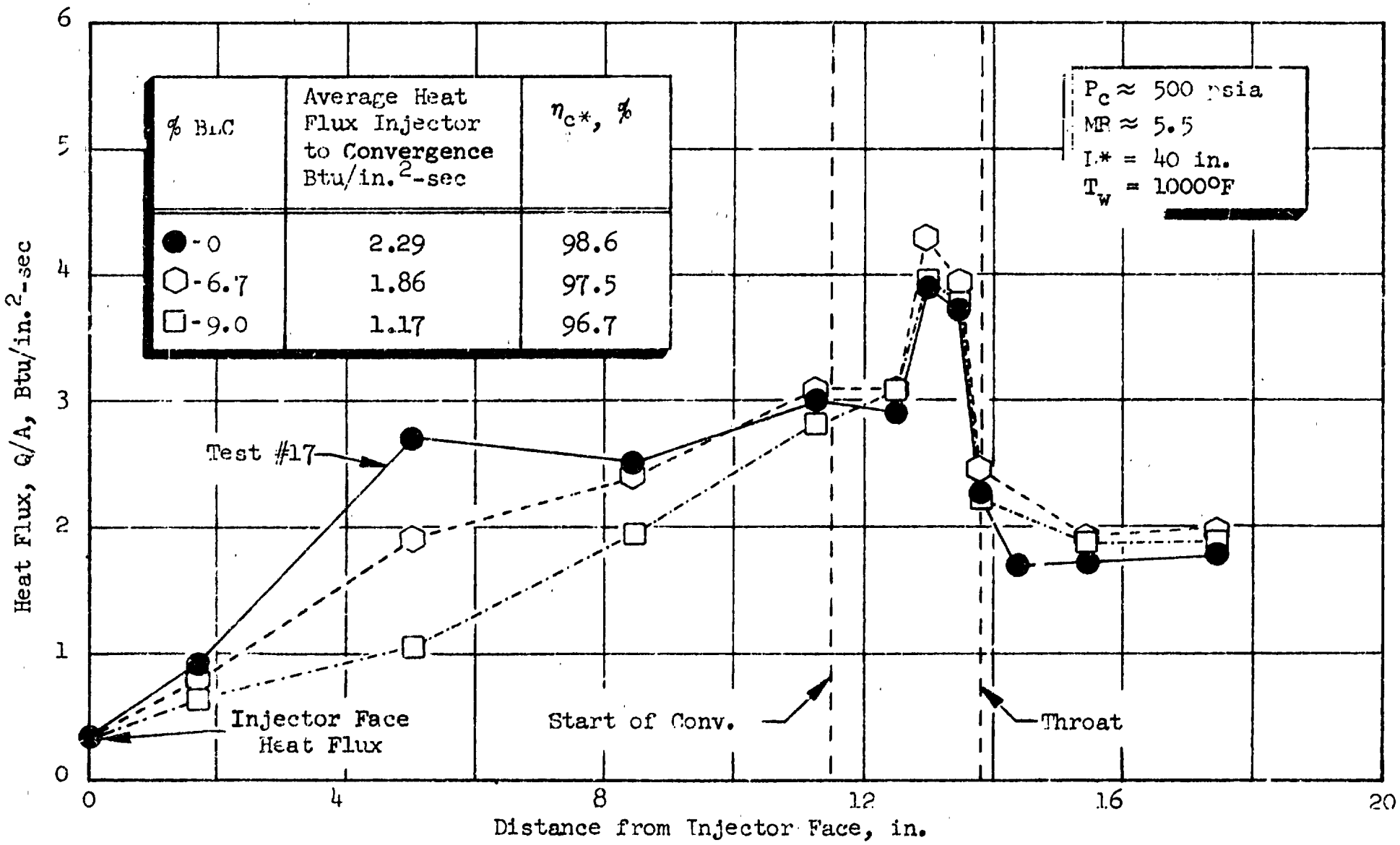

Figure 63. Chamber Heat Flux Profiles as a Function of BLC Flowrate

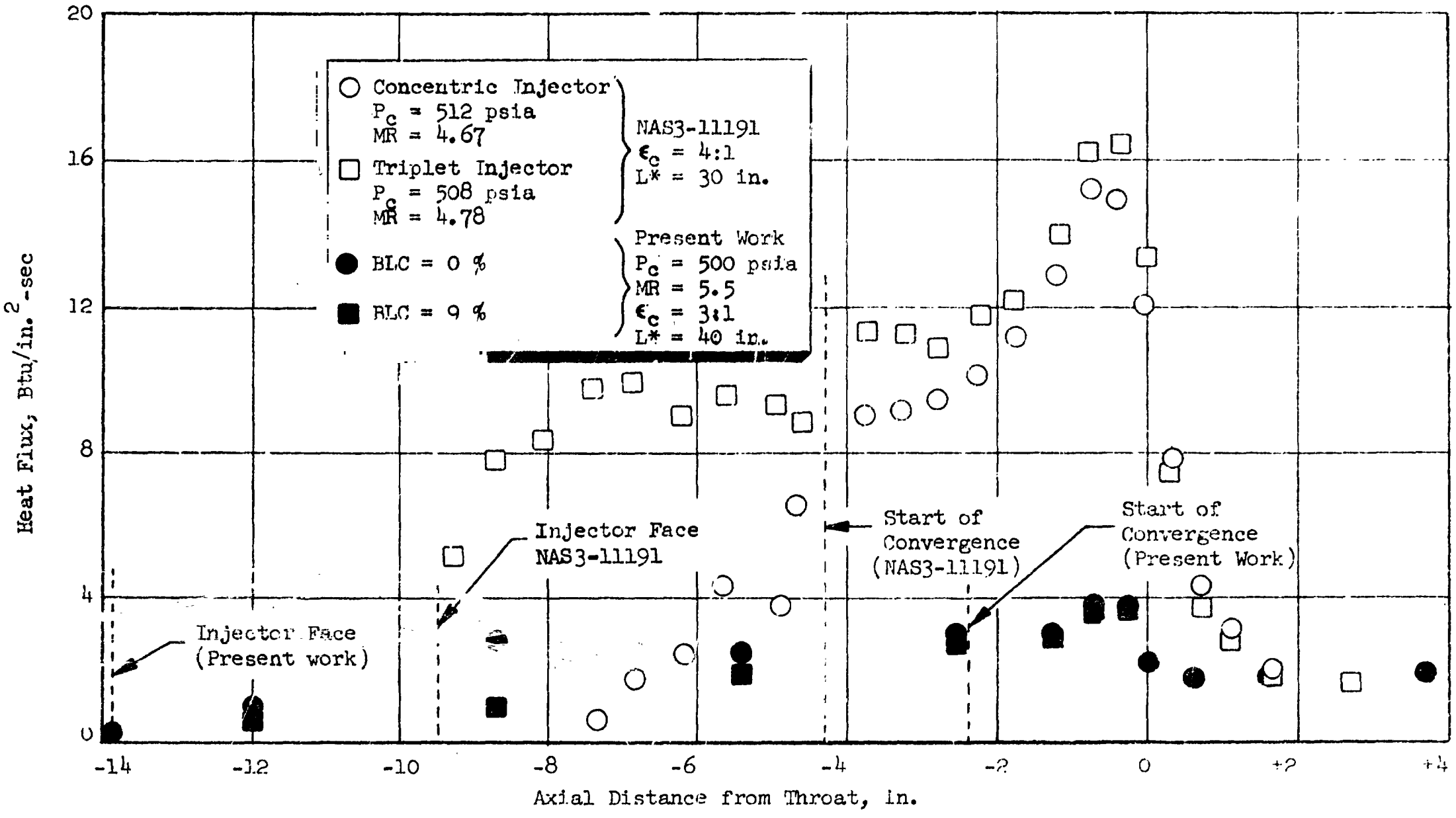

Figure 64. Experimental Heat Flux Profiles

8.3.4 Injector Face Heat Flux

Two thermocouples were installed in the injector face to determine injector face heat flux. One thermocouple was located near the center of the injector face (T/C 1) and the other (T/C 2) in the peripheral zone. Values of injector face heat flux were calculated by the same method which was utilized to calculate chamber wall heat flux (Appendix F). As shown in Table X, the injector heat flux was found to be independent of the percentage of BLC flow. The low values of heat flux are consistant with the lack of any injector face overheating during the parametric hot-firing series. Note also that these heat fluxes are nearly equivalent to those measured in the injector face region with the single-element injector/chamber (Fig. 50).

TABLE X. INJECTOR FACE HEAT FLUX

(P_c = 500 psia, MR≈5.5)

Thermocouple	% BLC	$\dot{q}/A$, Btu/in.^{2}-sec
1	0	0.22
2	0	0.30
1	6.7	0.23
2	6.7	0.35
1	9.0	0 20
2	9.0	0.31

8.3.5 Injector Stability Rating Tests

Injector stability rating tests were conducted at a nominal operating point (P_c = 500 psia, MR = 5.25, 6.7% BLC) by sequentially bombing the engine with bombs of increasing size. The bombs were placed 2.5 in. from the injector face and were circumferentially spaced 90 degrees apart. The centers of the bombs' explosive charges were located approximately 1/2 in. from the chamber walls. Available Photocon data (FLOX and CH_4 manifold pressures) revealed a maximum overpressure of approximately 1100 psi. No injector damage of any kind was sustained during the bomb test. Figure 65 presents a Brush recording of the tape-recorded high-frequency Photocon data which shows the timing of the three bomb pulses. As indicated, considerable instrumentation noise was present in all channels which were recorded. Figure 66 presents an expanded scale Brush record of the No. 3 bomb event where an overpressure of approximately 1100 psi was recorded with damping in less than 15 milliseconds (as determined by examination of the entire expanded Brush record).

8.3.6 Duration Firing

A 44-second duration test was conducted with the injector following the parametric and stability rating tests. The test was conducted using a nominal BLC flow of 6.7 percent in the 40-in. L* chamber. Figure 67 presents measured c* performance based on thrust as a function of time for the duration test. Figure 68 presents measured site thrust for the firing. For this test, pressure taps and thermocouples were not placed in the graphite lined chamber. Note (in Fig. 67) that

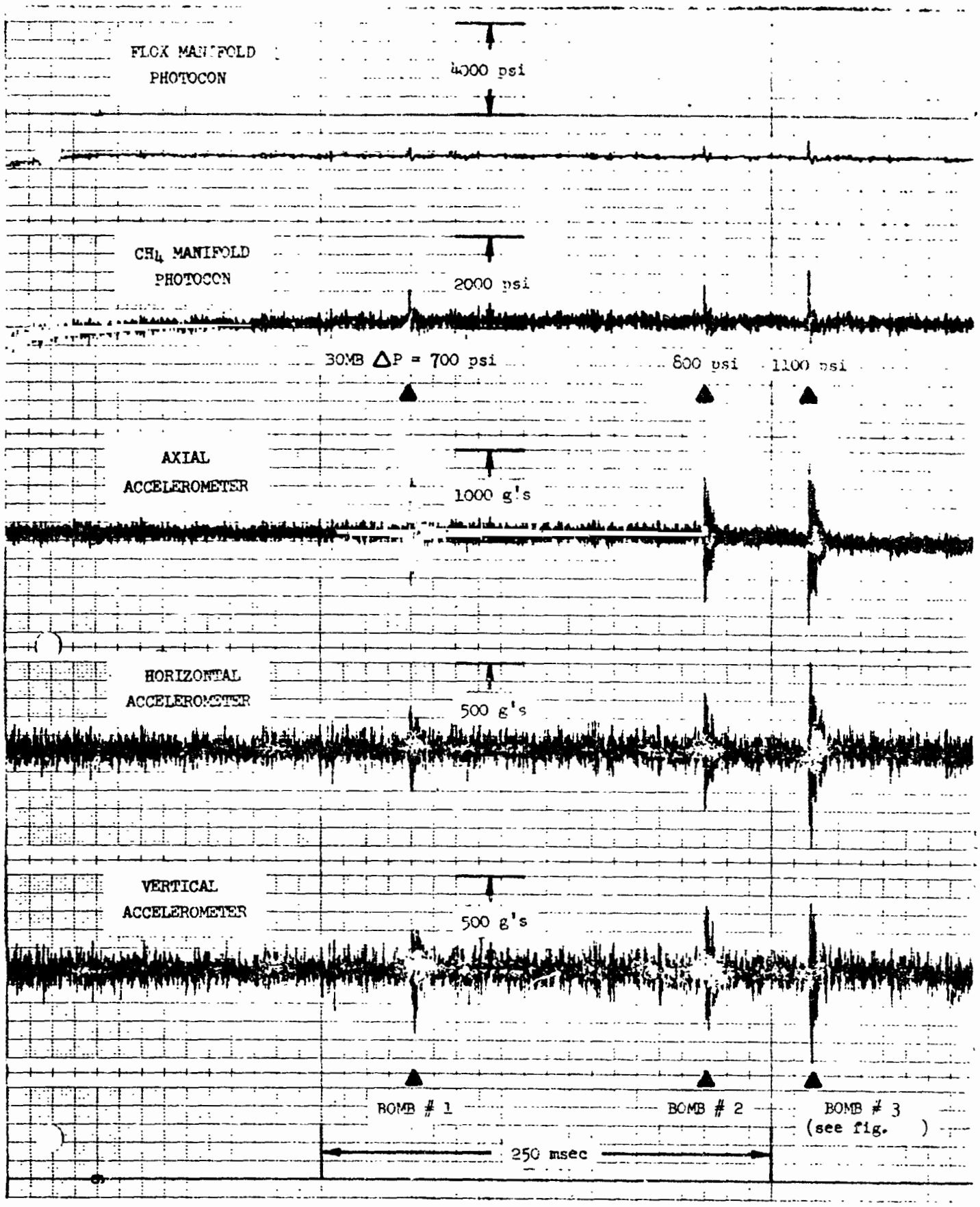

Figure 65. Brush Record of Taped High-Frequency Data

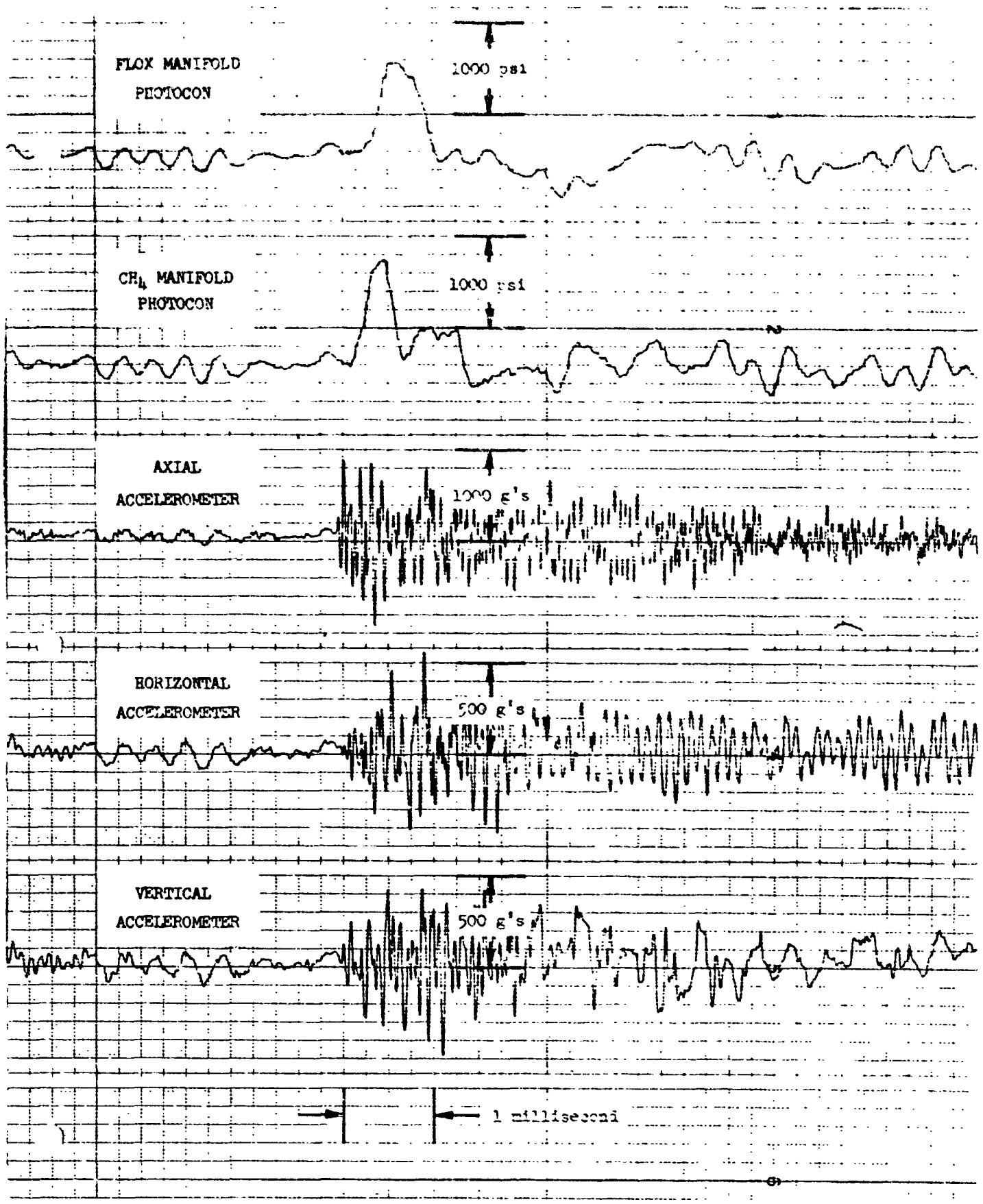

Figure 66. Expanded Brush Record of Bomb No. 3 Event

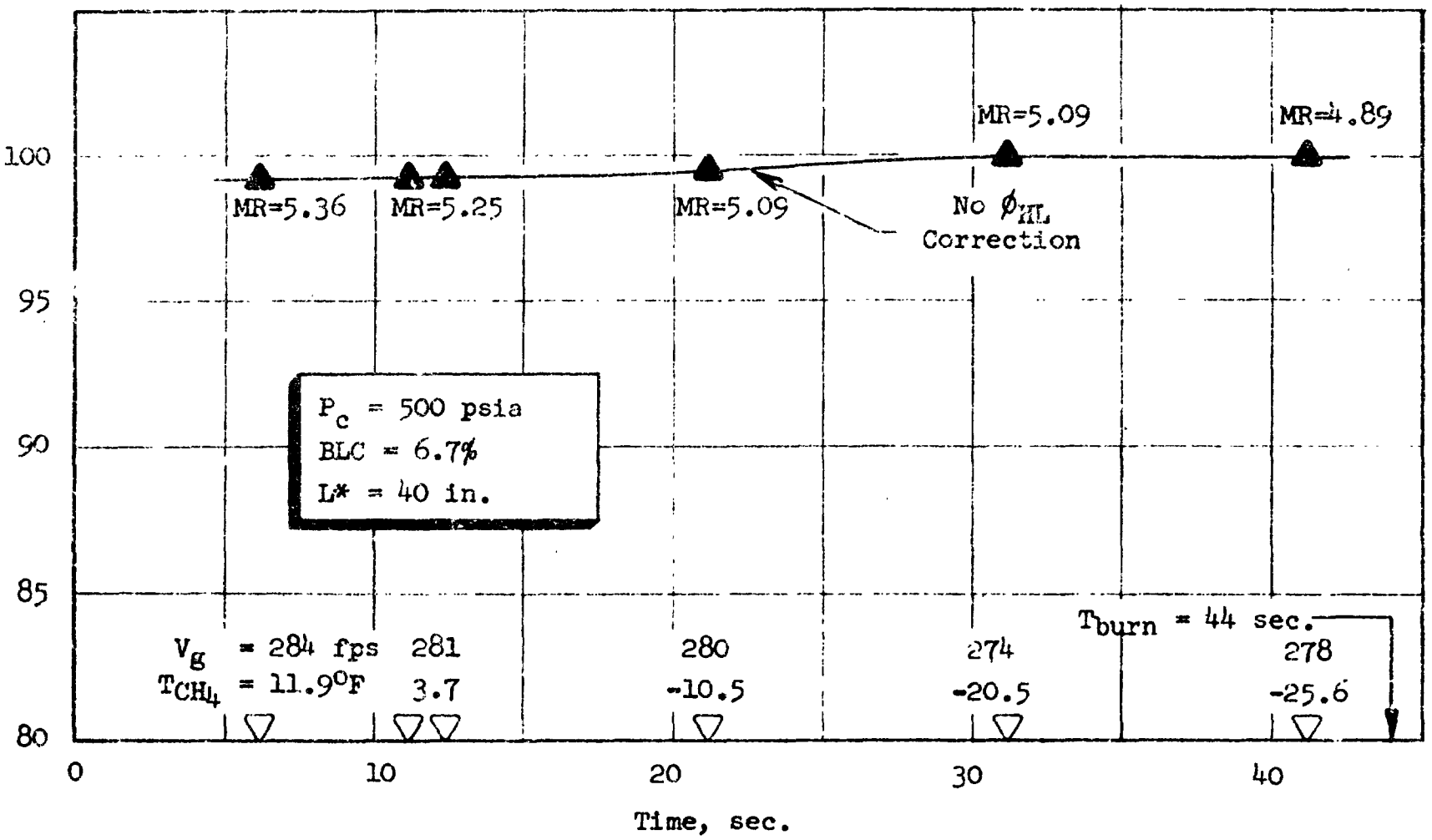

Figure 67. Injector Performance as a Function of Time, 44-Second-Duration Test

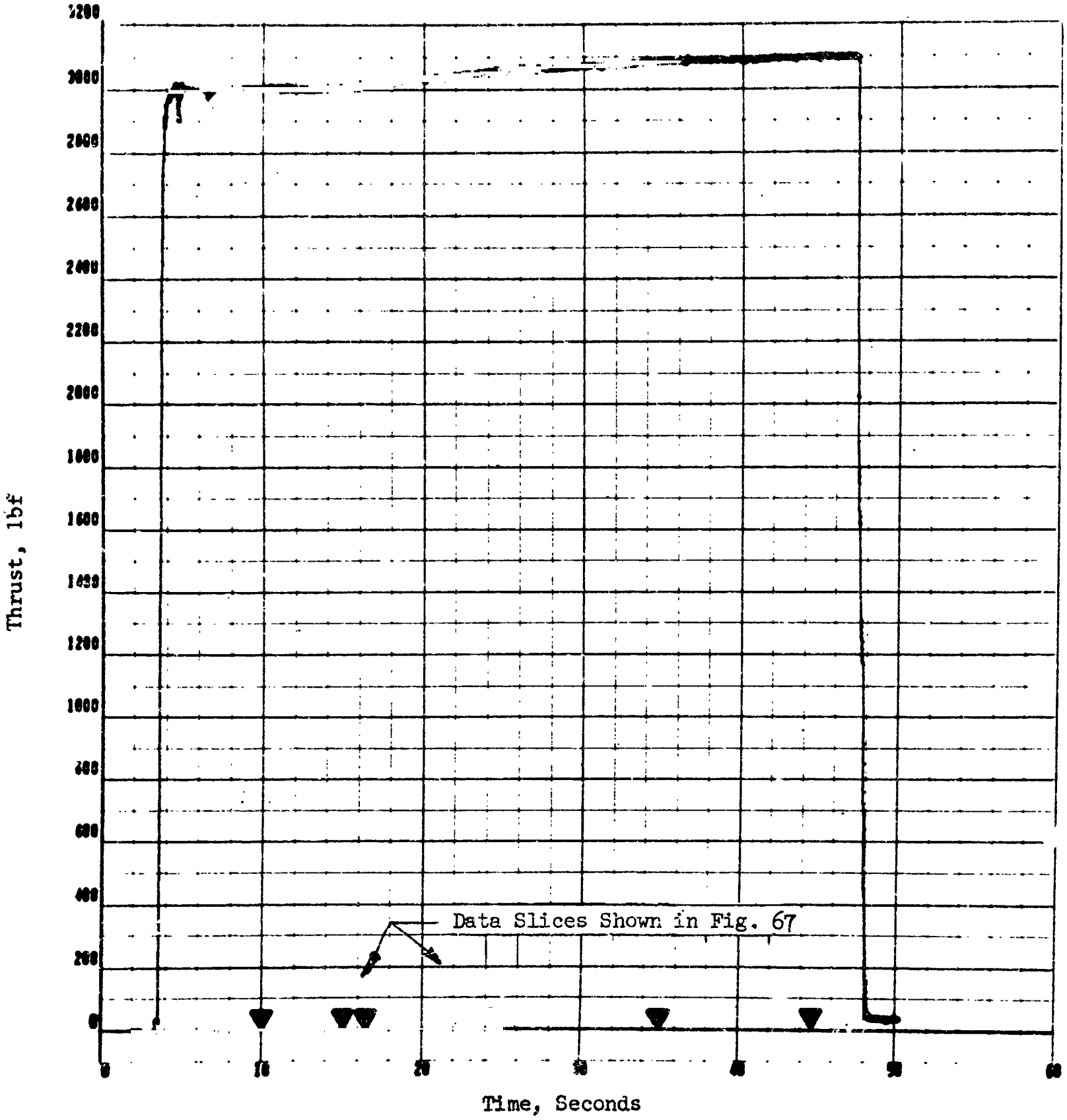

Figure 68. Measured Site Thrust for 44-Second-Duration Test

injected mixture ratio decreased during the firing due to increasing methane flow during the run. The increasing fuel flow was due to the decrease in methane temperature (Joule-Thompson effect) during the run. Measured throat area change during the run was only 0.75 percent.

For times greater than approximately 10 seconds, calculations indicated that chamber wall heat losses would be minimal. Consequently, the data shown in Fig. 67 were not corrected for any chamber wall heat loss (i.e., $\emptyset_{HL} = 1.0$). Note that these data are in essential agreement with the data of Fig. 61, which were corrected for chamber wall heat loss. This agreement substantiates not only the method of correcting for heat loss, but, also, the heat flux data measured during the short duration parametric tests.

The injector face thermocouples revealed an extremely cool face during the duration test. These data are substantiated by the fact that no hardware burning of any kind was evident following the test. Figure 69 presents the face temperature as measured by T/C 1 (located 0.030 in. from the injector face) during the duration test. A heat transfer analysis of the injector face which was made during the design phase had predicted steady-state temperatures of approximately 175 F (for a $\dot{q}/A = 0.25$ Btu/in.^{2}-sec) assuming that $T_{CH4} \approx 70$ F and with no deposition of carbon on the injector face. The substantial (measured) decline in face temperature which began about 6 seconds into the run is attributed to the low methane injection temperatures ($\approx$0 to -26 F) and carbon deposition on the injector's face.

Clearly, for this program, injector face cooling (i.e., Rigimesh, etc.) would have been a needless expense. This point illustrates the value of subscale (single-element) experiments which showed a priority that injector face cooling was not required (Section 6.0).

Figures 70 through 74 are photographs of the injector/chamber hardware following the duration test. Posttest examination of both injector and chamber hardware revealed no significant damage.

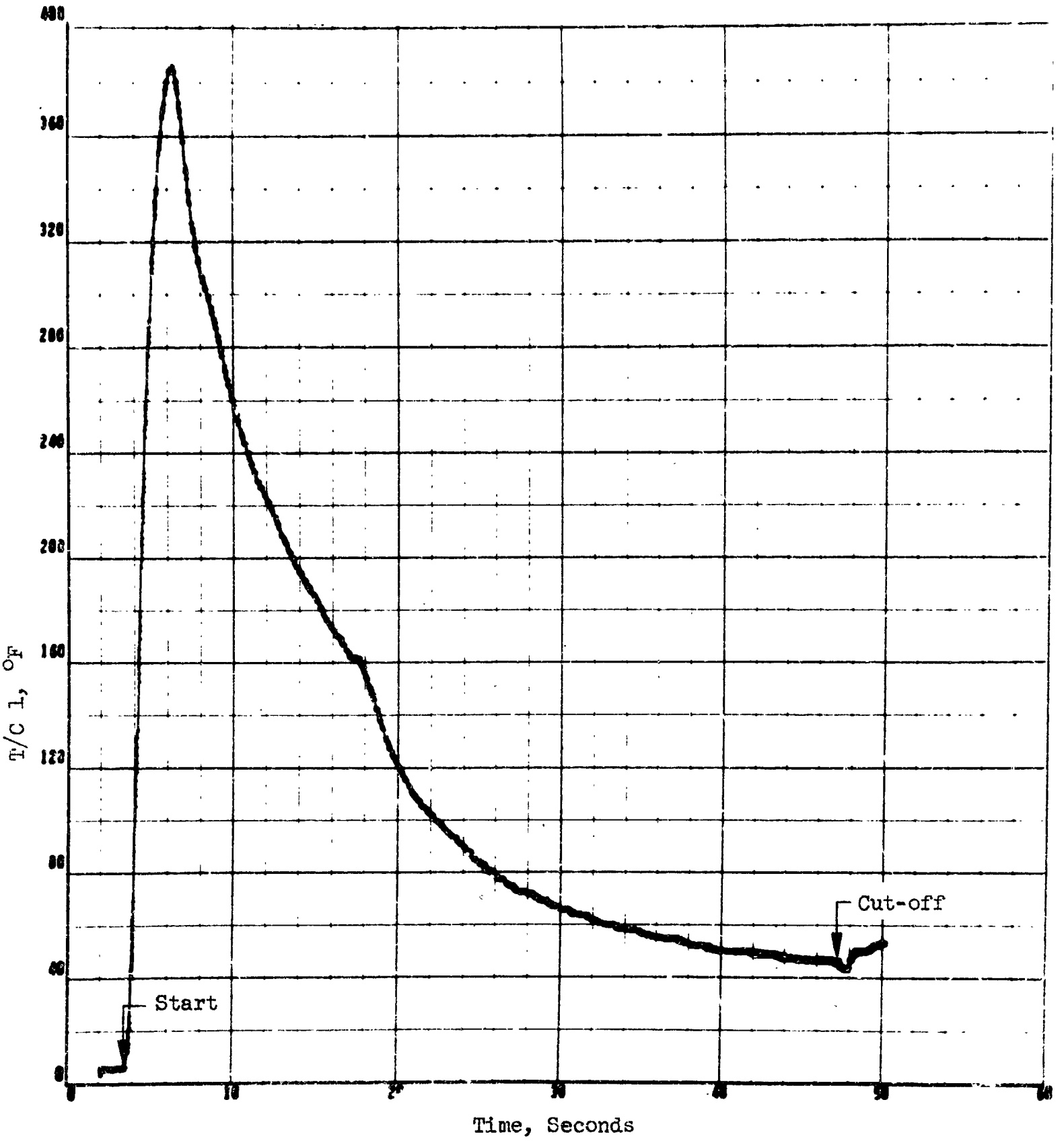

Figure 69. Injector Face Temperature for Duration Test

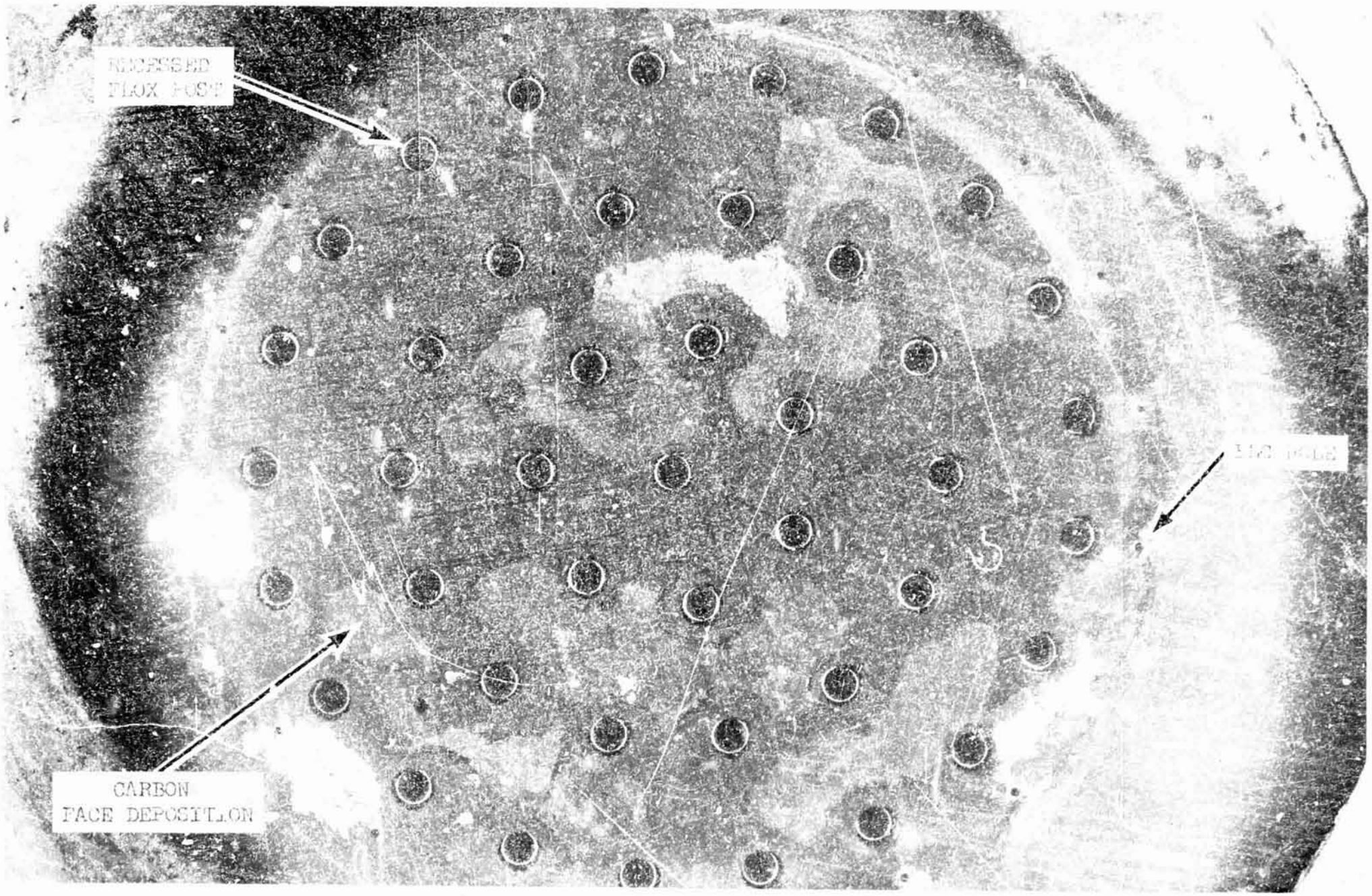

5AA36-10/11/71-S1F

Figure 70. Injector Face Following Duration Firing

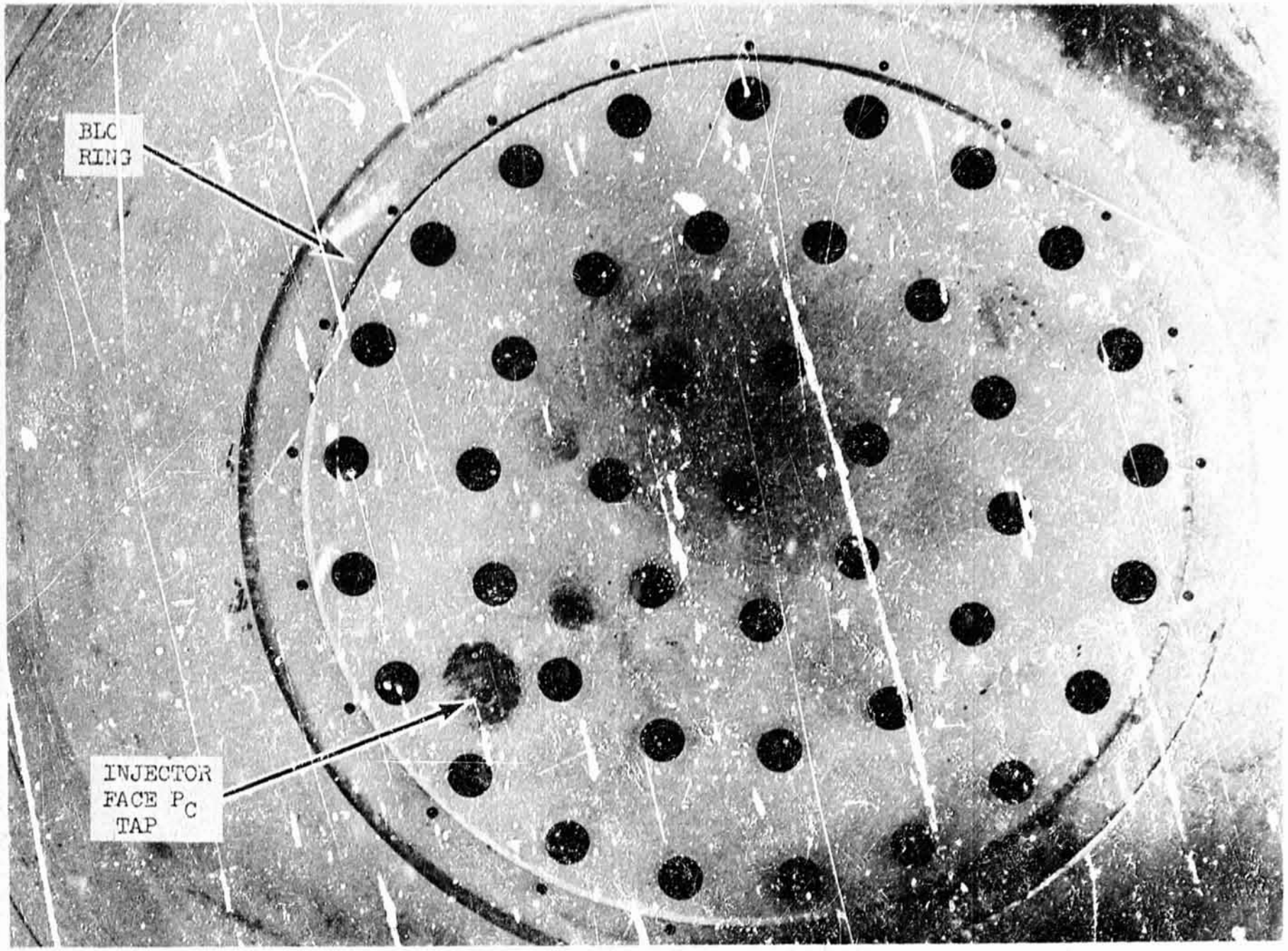

5AA36-10/11/71-S1C

Figure 71. Injector Face Following Carbon Deposition Cleanup

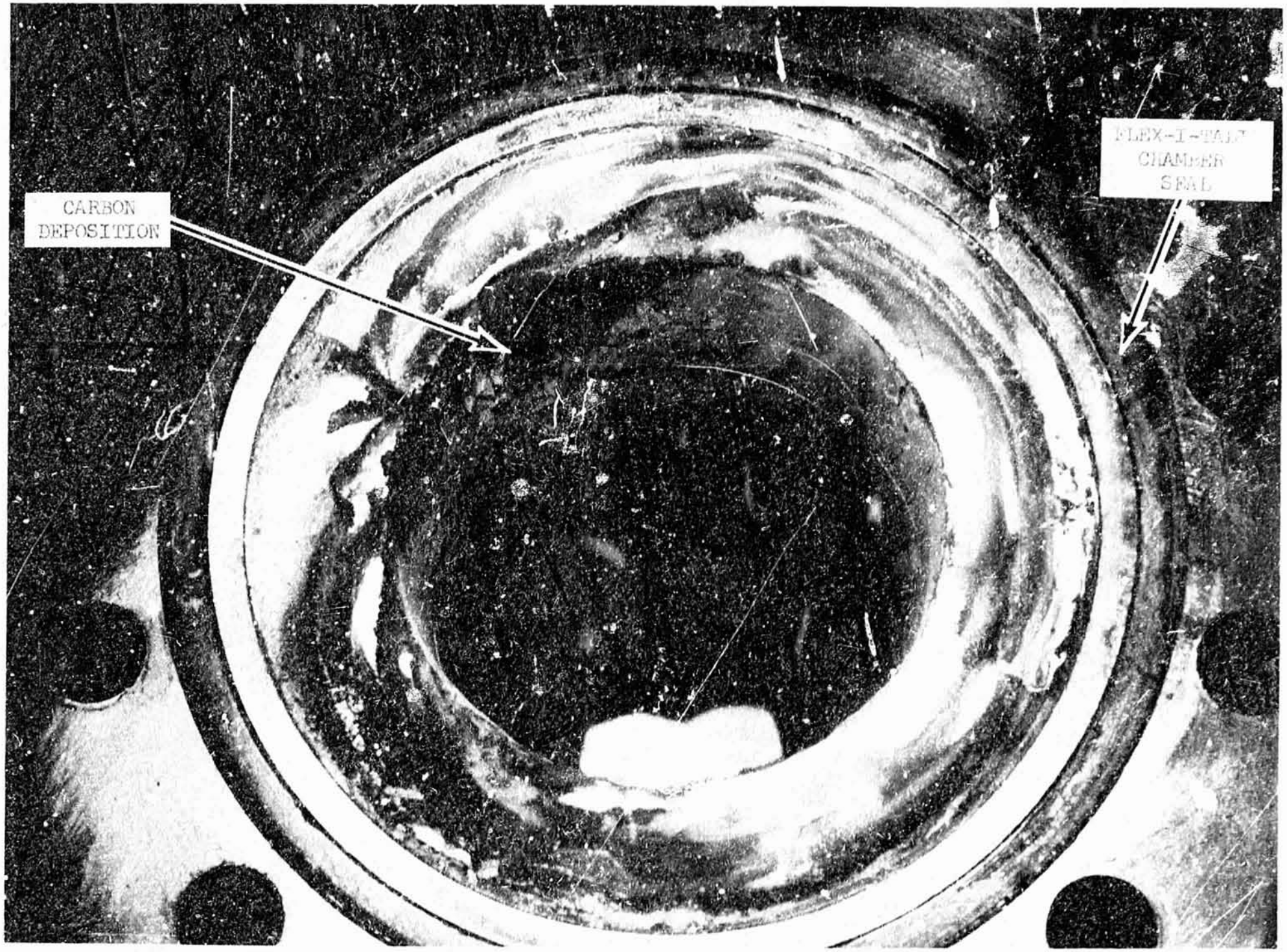

5AA36-10/11/71-S1D

Figure 72. Thrust Chamber Following Duration Test

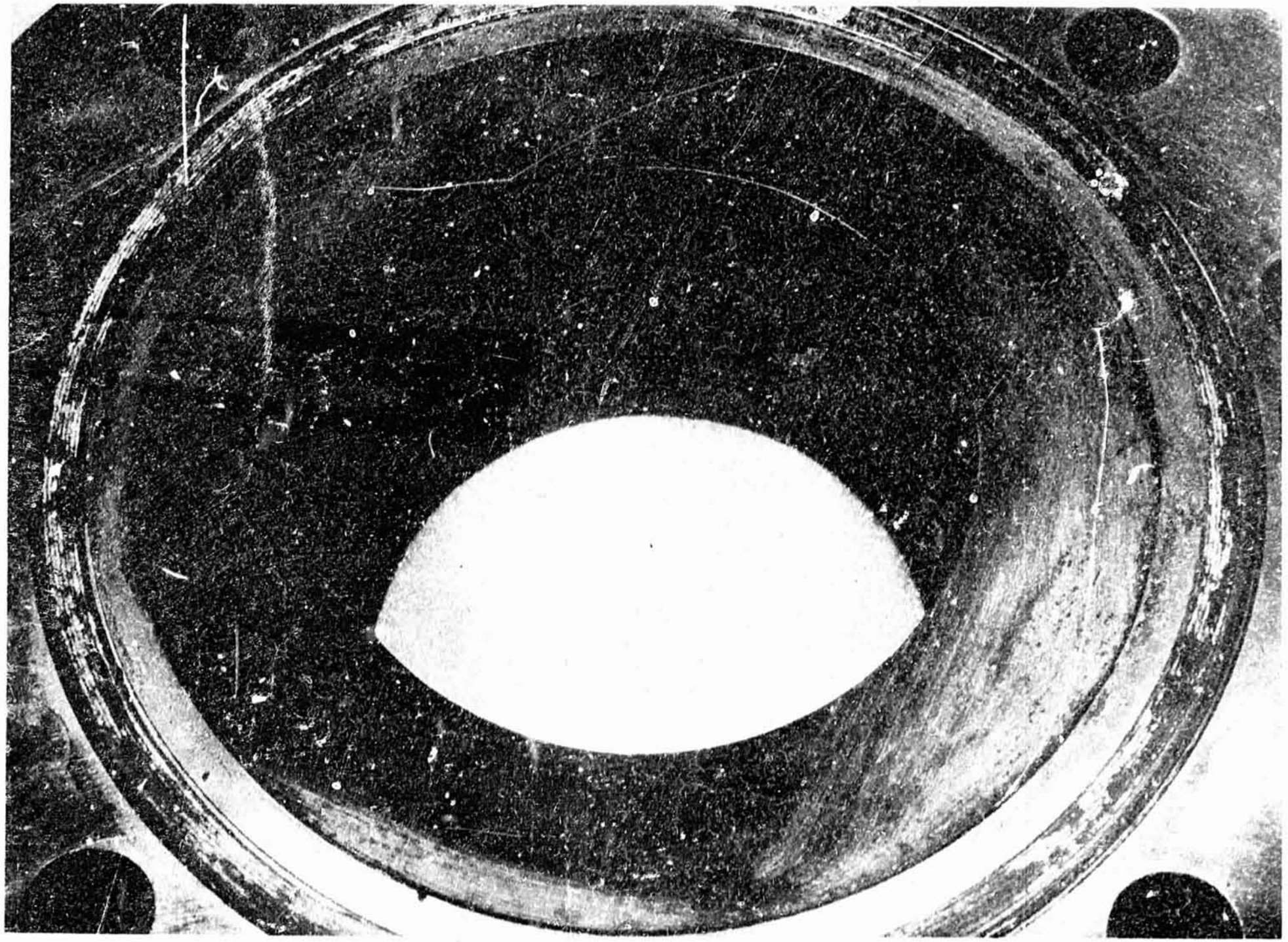

5AA36-10/11/71-S1A

Figure 73. Thrust Chamber Following Carbon Deposition Cleanup

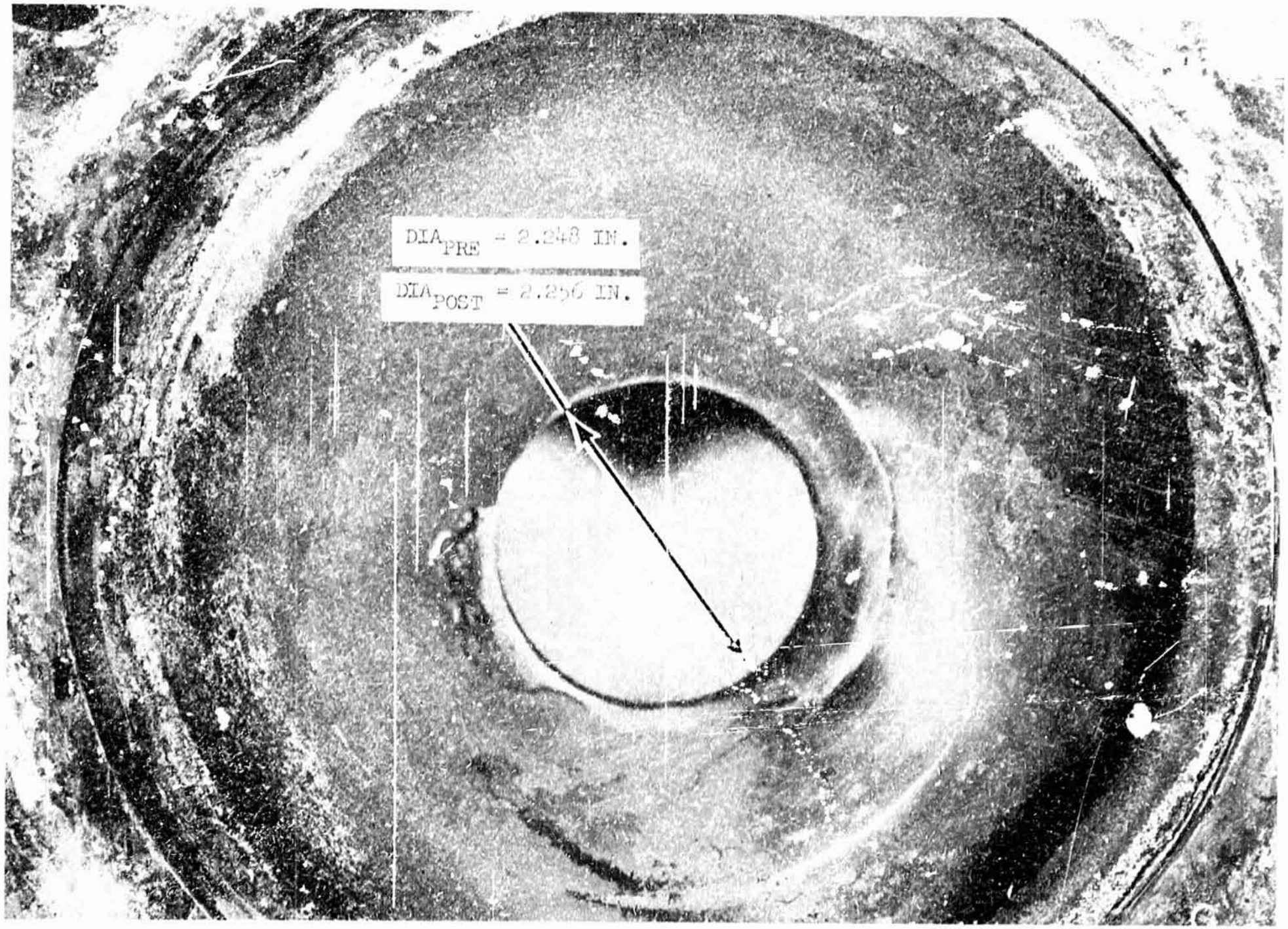

SAA36-10/11/71-S1B

Figure 74. Convergent Portion of Nozzle Following Duration Test

9.0 CORRELATION OF FULL-SCALE INJECTOR DATA

9.1 COLD-FLOW/HOT-FIRE PERFORMANCE CORRELATION

The full-scale cold-flow mixing data of Section 8.0 and the single-element atomization data of Section 5.0 were analyzed to determine the degree of correlation between cold-flow performance predictions and hot-fire results. As in the single-element cold-flow/hot-fire correlation, the overall engine performance was assumed to be the product of a mixing-limited c* efficiency and a vaporization-limited c* efficiency.

The predicted mixing-limited efficiency was determined from the full-scale cold-flow results (Fig. 59). The predicted vaporization efficiency was determined by employing single-element atomization data. As in the single-element correlation analysis, the measured drop sizes (Section 7.0) were corrected for the differences in physical properties of wax and FLOX using the empirical equation of Ingebo. The resultant drop sizes were then used in conjunction with the results of the K-PRIME combustion model to determine a vaporization limited c* efficiency (Section 7.0).

Figure 75 presents the results of the correlation analysis of the cold-flow/hot-fire results for the full-scale injector. The data are plotted in a manner that illustrates the ability of the cold-flow data to predict the parametric variations which were investigated in the hot-firing series (i.e., chamber pressure, injected mixture ratio, and percent BLC flow). The dependent parameter in the three graphs shown in Fig. 75 is the relative change in c* efficiency ($\Delta\eta_{c^*}$) from the efficiency which was determined (in either hot-fire or cold-flow tests) at the nominal design condition (P_c = 500 psia, MR = 5.25, and 0% BLC). As indicated, the cold-flow data successfully predicted reduced performance levels when: (1) the engine was throttled, (2) the overall injected mixture ratio was increased, and (3) the percentage of BLC flow was increased.

To determine if the cold-flow data could predict the absolute performance level of the full-scale injector, the hot-fire test data were analyzed for all conditions at which full-scale mixing tests were performed (Fig. 59). Table XI summarizes the pertinent data employed in the analysis.

TABLE XI. FULL-SCALE HOT-FIRE/COLD-FLOW CORRELATION

Hot-Fire Test No.	P_c, psia	MR	BLC, %	$\bar{D}_{WAX}$, μ	$\bar{D}_{FLOX}$, μ	Cold-Flow $\eta_{c^*,vap}$, %	Cold-Flow $\eta_{c^*,mix}$, %	Cold-Flow η_{c^*} %	Hot-Fire η_{c^*}, %
17 -●	512	5.38	0	600	236	98.0	97.7	95.7	98.4
19 -■	518	6.56	0	720	284	96.0	97.7	93.8	98.3
20 -▼	242	4.84	0	640	252	97.5	96.6	94.2	95.3
22 -◥	516	5.77	6.7	690	271	96.7	98.6	95.4	97.5
23 -◆	507	5.53	9.0	680	258	97.1	99.0	96.2	96.7

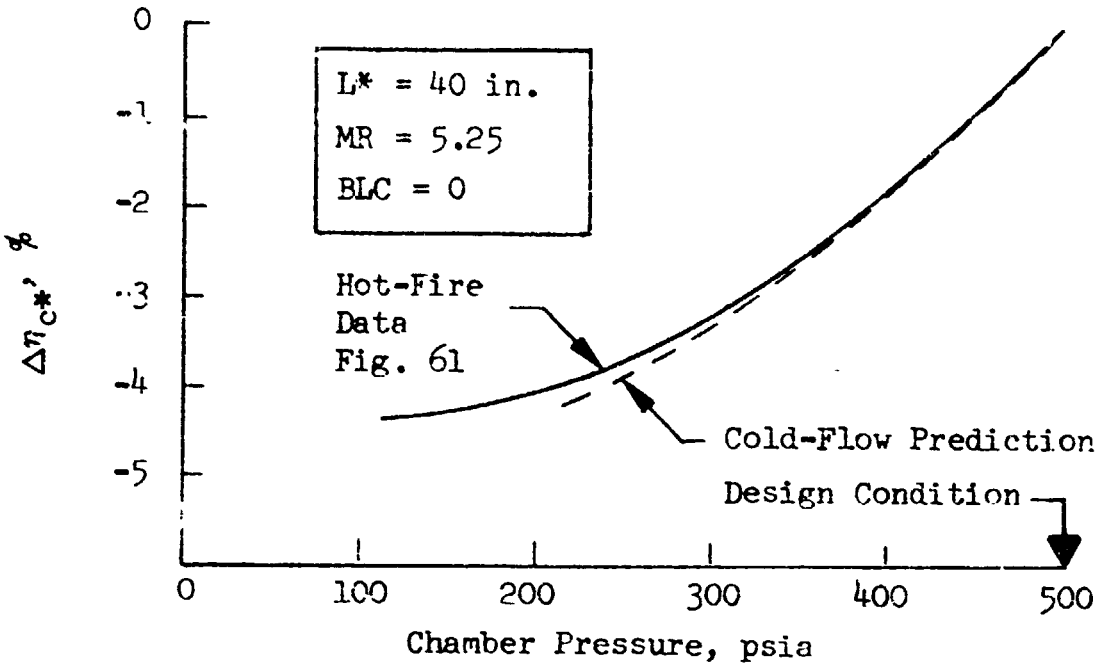

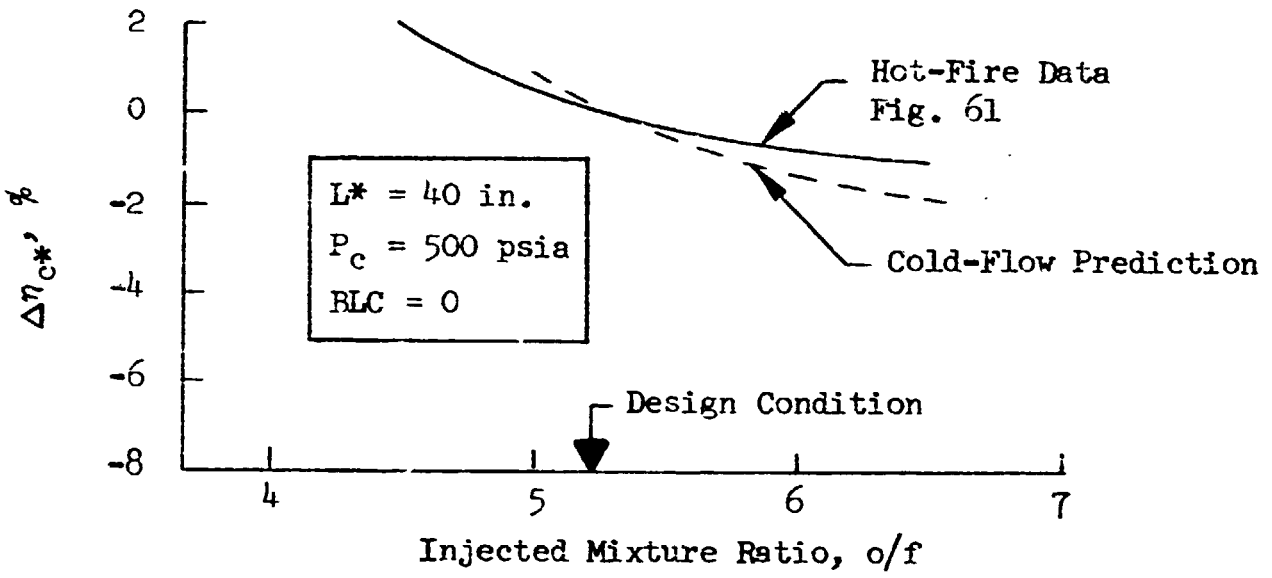

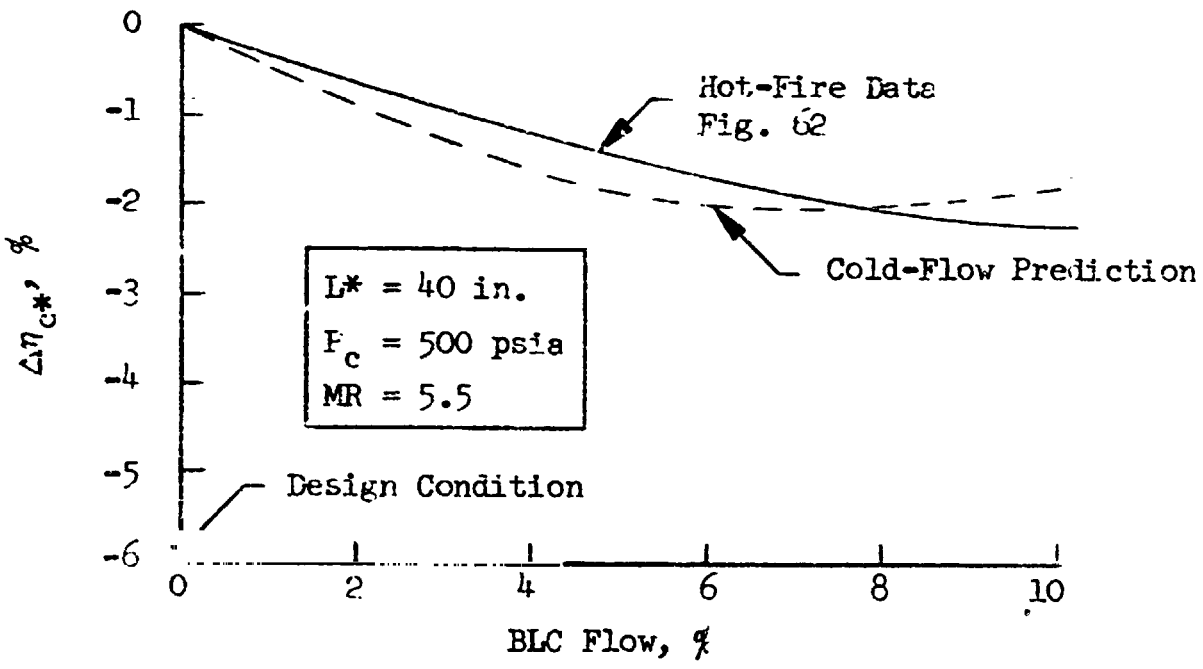

Figure 75. Results of Full-Scale Cold-Flow/Hot-Fire Correlation Analysis

Figure 76 presents the results of the correlation analysis plotted as measured hot-fire performance versus predicted cold-flow performance. As indicated, the average deviation of the five hot-fire tests from the mean correlation line was 2.2 percent.

9.2 CORRELATION OF FULL-SCALE/SINGLE-ELEMENT HEAT FLUX DATA

The heat flux data of the full-scale firings and single-element BLC element hot-firings was compared to determine the relationship between single-element and full-scale chamber heat flux characteristics. Both test series were conducted in $L^* = 40$ in., $\varepsilon_c = 3{:}1$ chambers. The chamber heat flux levels were averaged by integrating the local heat fluxes (Fig. 46, 48, and 63) from the injector face to the start of nozzle convergence. Figure 77 presents the results of the analysis for various levels of BLC flowrate. Based on the data of Fig. 77, it appears that single-element hot-fire data can be employed to predict full-scale chamber heat flux data in the chamber region upstream of the start of nozzle convergence.

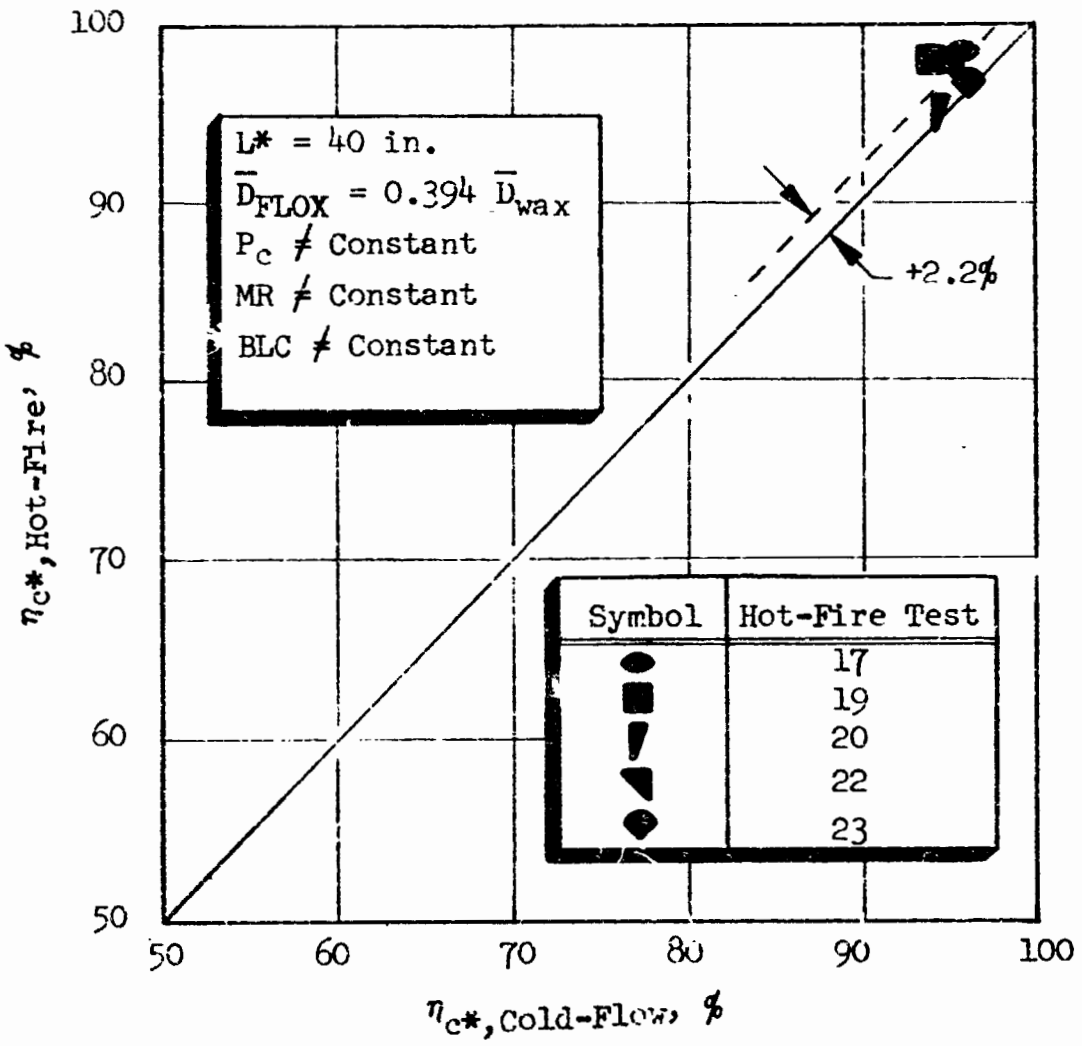

Figure 76. Correlation of Full-Scale Injector Cold-Flow/Hot-Fire Data

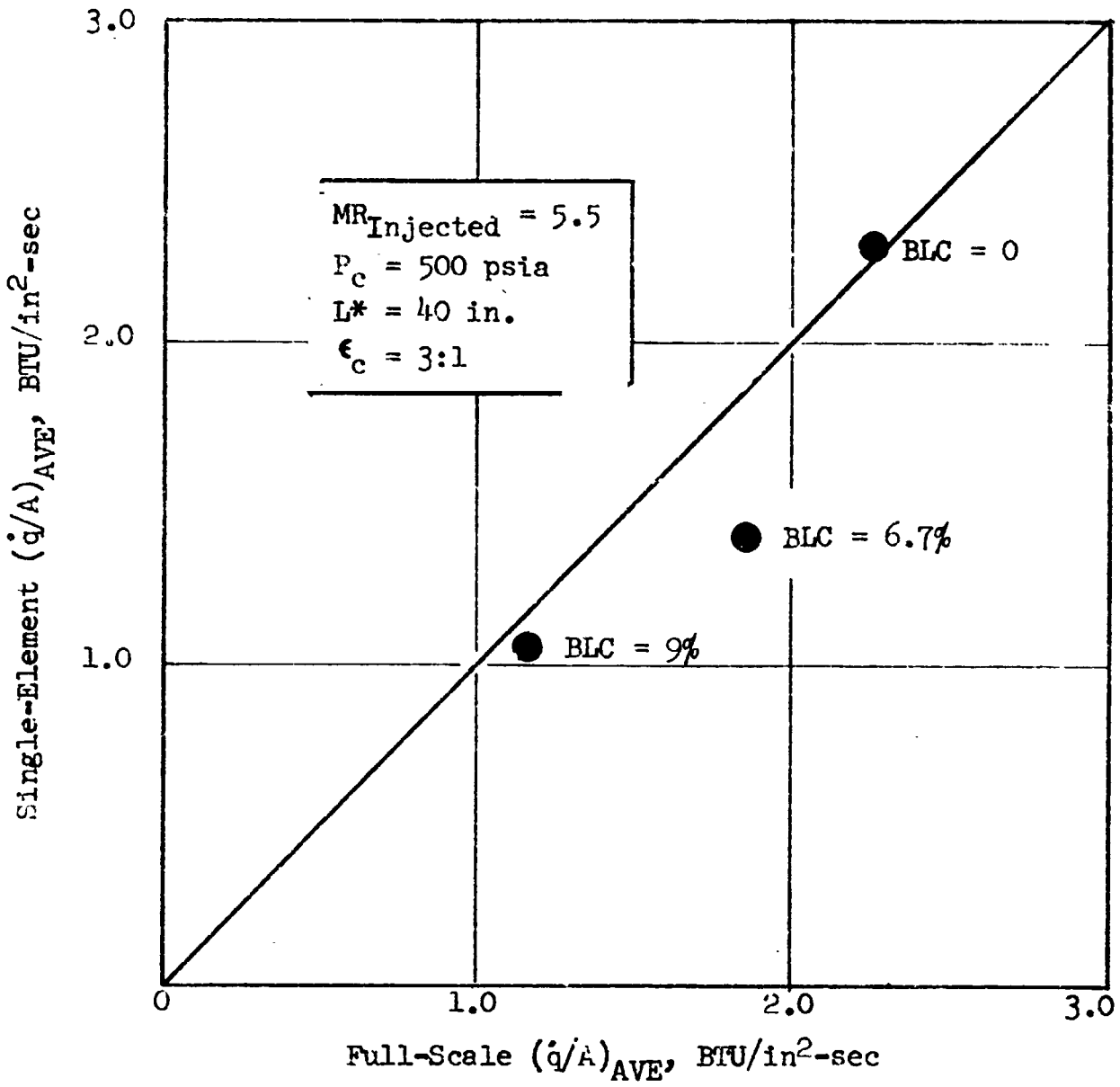

Figure 77. Correlation of Average (Injector to Start of Convergence) Chamber Wall Heat Flux Levels for Single-Element and Full-Scale Hot Firings

10.0 DISCUSSION OF RESULTS

The discussion of the results of this study is divided into three sections: (1) performance/chamber compatibility of the full-scale coaxial injector, (2) use of cold-flow simulation/hot-fire techniques for injector design, and (3) extrapolation of data derived in this program for design of other gas/liquid systems.

10.1 PERFORMANCE/CHAMBER COMPATIBILITY CHARACTERISTICS

As shown in Section 8.0, the injector of this study met the performance and chamber compatibility goals of the program. Injector performance was 99 percent (see Fig. 61 and 67) of the theoretical shifting characteristic velocity at the nominal operating conditions (P_c = 500 psia, MR = 5.25, BLC = 0). Acceptable injector/thrust chamber compatibility was demonstrated both in the short-duration parametric tests (Fig. 67) and in the 44-second duration firing. Injector face temperature data (Fig. 69) from the duration firing indicated that the injector should be operable for an indefinite period of time.

Pressure throttling of the injector was not a requirement of the program. However, throttling tests conducted with the injector resulted in stable firings at high performance levels ($\geq$ 94.5%) over a 5:1 throttling range. In the deeply throttled mode (P_c = 100 psia) the injector exhibited neither low (chugging) nor high frequency instabilities. This is especially noteworthy since, at this operating condition, total injector pressure drop was approximately 18 psi.

Dynamic combustion stability tests (Fig. 65 and 66) conducted at the design condition showed that the injector configuration possessed excellent recovery response to high dynamic pressure disturbances ($\Delta P_{max} \approx$ 1100 psi).

10.2 COLD-FLOW/HOT-FIRE DESIGN TECHNIQUES

The single-element cold-flow/hot-fire techniques (gas/liquid) which were developed in this program and NAS3-12001 have been shown to be a powerful tool for the rational design of high performance injectors. In particular, the pressurized single-element mixing experiments provide the injector designer not only with element mixing levels (i.e., performance) but resulting mass flow and mixture ratio distributions. These data can be employed to determine potential chamber wall heat flux problem areas. They also provide direct physical description of the respective fuel and oxidizer flow distributions, permitting maldistribution to be corrected through specific changes in element design detail.

It was recognized at the inception of the program that cold-flow experiments alone do not provide all inclusive data for the injector designer. That is, combustion effects such as coaxial cup burning can be determined only by hot-firing experiments as demonstrated in this effort. The use of relatively low-cost, single-element hardware allows the experimenter to investigate critical parameters (such as post recess) over a range that would be economically unfeasible with full-scale injector hardware. In addition, due to the small size of the hardware, test modifications are relatively simple and of low cost.

As was demonstrated in this program, single-element, hot-fire data are directly applicable to full-scale injector design. As a specific example chamber wall heat flux data measured in single-element chambers (Fig. 51) suggested that cooling of the full-scale injector face would not be required. Based on these data, the full-scale injector face was not cooled (Fig. 15) and the test results verified that cooling was not required (Table X and Fig. 9). It should be noted also that the heat flux levels measured in the single-element chambers were comparable to those measured in the full-scale thrust chamber (Fig. 48, 63, and 77).

It was demonstrated in this program that the cold-flow simulation techniques which were employed do predict the parametric changes which occur in hot-firing systems. Thus, these techniques can be employed to optimize elements with respect to performance without resulting to expensive hot-firing studies. It should be noted also that the cold-flow data of this program successfully predicted the absolute performance levels of the full-scale injector/chamber.

10.3 USE OF COLD-FLOW DATA FOR OTHER PROPELLANTS

The correlated cold-flow data of this study were presented in a form (Fig 29 and 38) that can be employed to determine element mixing and atomization levels for other gas/liquid propellant combinations (i.e., LOX/GH_2, LOX/propane, etc.). In addition, the correlation of chamber wall heat flux versus chamber wall mixture ratio (Fig. 58) can be employed as a guide in designing elements for enhanced injector/chamber compatibility.

However, caution must be exercised when applying these data to propellant combinations whose elements operate in ranges considerably different than those employed in this study. Specifically, coaxial elements employing LOX/GH_2, in general, operate with significantly higher gas gap velocities ($V_g \approx$ 2000 to 3000 ft/sec) than those using methane ($V_g \approx$ 300 to 500 ft/sec). In addition, LOX/GH_2 elements generally have larger gas gap heights than those reported herein ($h \approx 0.018$ in.). Cold-flow studies (Ref. 2) currently underway at Rocketdyne with LOX/GH_2 coaxial elements indicate that the cold-flow data generated in this study may not be directly applicable to LOX/GH_2. However, injector designers concerned with propellants which operate with similar injection characteristics (i.e., LOX/propane) should be able to utilize the results of this study directly.

11.0 CONCLUSIONS AND RECOMMENDATIONS

The approach and techniques which were employed in the subject program resulted in the direct design of an injector which met or exceeded the performance and chamber compatibility goals of the program without any need for the traditional "cut-and-try" injector development methods. Although the specific application considered was for the propellant combination (FLOX(ℓ)/methane(g), the program resulted in the development of cold-flow/hot-fire techniques which are directly applicable to design of other high performance gas/liquid systems of current interest (i.e., LOX/GH_2, LOX/propane, etc.). Use of these same techniques for the design of injectors using the aforementioned propellants should result in optimum configurations at minimum developmental costs.

Recommendations for future work to further advance gas/liquid injector design technology are:

1. The Rocketdyne CSS combustion model should be made operable with the FLOX/CH_4(g) propellant combination. The CSS model provides coaxial injector cup information which is not available with the K-PRIME combustion model. The addition of FLOX/CH_4(g) property data to the CSS program subroutines would be required. Empirical FLOX jet stripping rate parameters would be derived from available data acquired in the subject program.
2. Cold-flow/hot-fire studies should be conducted with single-element models to investigate the influence of injector element design on cup burning (i.e., fuel annuli wake closure effects, etc.). These results could then be incorporated into analytical combustion models.
3. Additional throttling tests should be performed to verify the stability of the injector design of this study at deeply throttled conditions ($P_c \leq 100$ psia). This would require testing the injectors with thrust chambers instrumented for dynamic pressure measurements.
4. Additional work with thrust chamber configurations should be done to determine an optimum configuration for the coaxial injector. In particular, smaller L* chambers (L* < 40 in.) and lower contraction ratios (ε_c < 3:1) should be investigated.
5. Firings with the injector of this study should be made in a regeneratively cooled thrust chamber to confirm or deny the low heat flux levels which were measured in the chamber convergent and nozzle throat areas.

APPENDIX A

K-PRIME COMBUSTION MODEL

This appendix presents a brief description of the Rocketdyne K-RIME combustion model. More detailed descriptions of the model can be found in Ref. A-1 and A-2.

To determine the degree of propellant vaporization, the combustion model (K-PRIME) takes into consideration:

1. Compressible combustion gas flow with mass and energy addition
2. Droplet drag in the accelerating combustion gas flow field
3. Droplet vaporization with convective heat transfer from the hot combustion gas

These factors result in an analytical description of the "bootstrap" combustion processes typical of rocket engines. The model calculates axial profiles of chamber pressure, combustion gas velocity, vaporization from a range of droplet sizes corresponding to the droplet size distribution produced by the injector, droplet velocities, and the overall percentage of oxidizer which is vaporized.

The combustion model takes into account the compressible flow of combustion gases by the normal gas-dynamic equations; taking into account the effects of mass and energy addition from the vaporizing and reacting propellants.

Droplet drag, for the distribution of droplet sizes produced by the injector, is accounted for by the scaler equation shown below:

$$\frac{dV_D}{dt} = 3/4 \times \frac{C_D \rho_g (V_g - V_D)^2}{\rho_L D} \qquad \text{(A-1)}$$

where

V_D = droplet velocity, ft/sec
t = time, seconds
C_D = drag coefficient (a function of droplet Reynolds number)
ρ_g = combustion gas density, lbm/ft^3
ρ_L = droplet liquid density, lbm/ft^3
V_g = combustion gas velocity, lbm/ft^3
D = droplet diameter, feet

Droplet vaporization is accounted for by an equation similar to:

$$\frac{d(D^2)}{dt} = k' = \frac{144 \times 8\lambda_g}{\rho_L C_{p_v}} \ln\left[1 + \frac{C_{p_v}}{\Delta H_v}(T_g - T_v)\right]\left(1 + 0.6\, Pr^{1/3}\, Re^{1/2}\right) \qquad \text{(A-2)}$$

where

- k' = droplet vaporization constant, in./sec
- D = droplet diameter
- λ_g = combustion gas thermal conductivity
- ρ_L = liquid density
- C_{p_v} = vaporized propellant heat capacity
- ΔH_v = liquid propellant heat of vaporization
- T_g = combustion gas temperature
- T_L = liquid propellant boiling temperature
- Pr = Prandtl number for the combustion gas
- ρ_g = combustion gas density
- Re = Reynolds number for combustion gas

For computer solution of Eq. A-2, the application is more complex. The simplified expression presented above shows the effects of the various physical parameters on droplet vaporization rate. The last bracketed term on the right-hand side of Eq. A-2 represents the effects of forced convection on droplet vaporization, and the remainder of the terms represent the effects of propellant physical properties and combustion gas properties on droplet vaporization rate (Ref. A-3).

For gas/liquid systems, incomplete oxidizer vaporization degrades c* performance by reducing the total amount of combustion gas produced which results in the burned gas mixture ratio being different from the injected mixture ratio, thereby affecting the temperature, molecular weight, etc. of the burned gas. This effect has been included by Priem (Ref. A-4) in the following equation which allows the determination of $\eta_{c^*,vap}$ from parameters calculated by the combustion model computer program:

$$\eta_{c^*,vap} = \left(\frac{\dot{w}_B}{\dot{w}_I}\right)\left(\frac{c^*_B}{c^*_I}\right) \qquad \text{(A-3)}$$

where

- $\dot{w}_B$ = flowrate of burned gas at the geometric throat
- $\dot{w}_I$ = injection flowrate of fuel plus oxidizer
- c^*_B = theoretical c* corresponding to the composition of the burned gas at the geometric throat
- c^*_I = theoretical c* corresponding to the injection mixture ratio of liquid fuel and oxidizer

This computerized combustion model, the general nature of which is described in very brief form by Eq. A-1 through A-3 was used to parametrically investigate the effects of design and operating variables on $\eta_{c^*,vap}$ for the FLOX/CH_4(g) propellant combination (see Section 3.0).

The two most important variables affecting $\eta_{c^*,vap}$ are propellant drop size and combustion chamber geometry. From Eq. A-2, it is seen that the residence time required to completely vaporize a droplet is proportional to the square of the droplet diameter. Equally important, the geometry of the combustion chamber dictates the total residence time during which the droplets must vaporize. If this residence time is too short, the droplets will not be completely vaporized.

Equation A-2 is an implicit expression showing that propellant vaporization efficiency is governed by droplet acceleration and heating by the high-temperature combustion gas. For thrust chambers having contraction area ratios greater than about 2, combustion gas flow can be considered incompressible; therefore, chamber L* is a good index of combustion gas residence time. From continuity, combustion gas velocity for the 2-to-1 chamber will always be higher than that for the 4-to-1 chamber. Higher combustion gas velocities will generally be accompanied by an increased velocity lag between combustion gas and propellant droplets. However, the lower contraction area ratio chambers (L* = constant) will tend to result in longer residence time for the droplets. The higher relative velocity between the combustion gas and propellant droplets will also tend to enhance convective heating and resultant droplet vaporization.

An assumption made in the one-dimensional combustion model program input is the amount of combustion which occurs within the initial injection region. This is required to arrive at a nearly one-dimensional region, and eliminate calculations in the grossly nonuniform injection region (Ref. A-2). It is usually assumed that 10 percent of the propellants have vaporized and reacted within 1 inch of the injector face. This initial condition has proved adequate and permits good correlation with observed experimental results. To assess the effect of variations in this assumption, 5, 10, and 20 percent of the propellants consumed were analytically considered and found to have an insignificant influence on performance. Performance variation due to assumption of 5 to 20 percent initial propellants vaporized instead of 10 percent was $\leq \pm 0.5$ percent in the range of drop size ($D_{30} \leq 150$) and L* (15 inch $\leq L \leq$ 60 inch) considered. Effects of injection velocity and percent of propellants initially reacted were only significant when the propellant drop size is large or when geometric restrictions favored lowered performance.

REFERENCES

A-1. Lambiris, S. L., L. P. Combs, and R. S. Levine, "Stable Combustion Processes in Liquid Propellant Rocket Engines," Combustion and Propulsion, Fifth AGARD Colloqium: High-Temperature Phenomenon, The MacMillan Co., New York, 1962, pp. 596-636.

A-2. Combs, L. P., Liquid Rocket Performance Computer Model with Distributed Energy Release, Final Report, NAS7-746, Rocketdyne, a division of North American Rockwell, Canoga Park, California, November 1971.

A-3. Sutton, R. D. and M. D. Schuman, "Liquid Rocket Combustion Analysis for Coaxial Jet Injection of Gas/Liquid Propellants," CPIA Publication 204, Vol. I, 7th JANNAF Combustion Meeting, February 1971, p 511.

A-4. Priem, R. J. and Heidmann, M. F., Propellant and Vaporization as a Design Criterion for Rocket Engine Combustion Chambers, NASA TR R-67, 1960.

APPENDIX B

PRESSURIZED COLD-FLOW MIXING FACILITY

INTRODUCTION

Early in the like-doublet portion of the subject program, an analytical investigation was conducted to develop appropriate cold-flow modeling criteria for hot-fire gas/liquid injector systems (Ref. B-1). The analysis considered the flow field of a simple injection system consisting of an axisymmetric gas jet into which a liquid jet is introduced at some arbitrary angle. Cold-flow modeling criteria were derived from consideration of available experimental data and an analysis of the governing conservation equations. In general, it was found that, to satisfy all of the cold-flow modeling criteria for a gas/liquid system, the cold-flow experiments would need to be performed in a pressurized environment. Pressurization was required in order to model the density and dynamic pressure of the hot-fire gas phase (fuel).

MEASUREMENT SYSTEM

To characterize the spray fields generated by gas/liquid rocket motor injectors, a system was developed to determine local values of gas and liquid mass flux under pressurized conditions. Knowing local values of gas and liquid mass flux, the "mixedness" (i.e., E_m) of the two-phase spray field was determined. In addition, examination of local values of mass flux was used to characterize peripheral element/candidates for injector-thrust chamber compatibility (see Section 5.0).

A schematic of the complete measurement system for the characterization of dense gas/liquid spray fields is shown in Fig. B-1. Mixing experiments were performed with both single-element and multi-element gas/liquid injectors. The apparatus consisted essentially of a pressurized test section in which the deceleration probe (described in subsequent paragraphs) was positioned in r-θ coordinates. The system contained several "water traps" to ensure that water, which can accumulate during extended test periods, does not plug critical pressure lines in the system. A photograph of the system, which is located at the Combustion and Heat Transfer Laboratory, is shown in Fig. B-2.

A problem associated with the characterization of spray fields generated with single-element injectors was the suppression of the flow-field recirculation caused by the injection of high-velocity streams into a finite closed volume. High levels of recirculation within the test section precluded the accurate determination of the gas-phase flow field. To eliminate flow field recirculation, a low-velocity (7 to 12 ft/sec) uniform "base bleed" flow surrounded the single-element injector. These values of base bleed velocity are in accord with the Craya-Curtet criterion for the elimination of recirculation (Ref. B-2).

One additional problem associated with the characterization of spray fields generated with single-element injectors was the determination of the local mass flux of the injectant gas. As the gas/liquid flow field moves through the surrounding environment on its way from the injector to the probe tip, much of the gas in the environment (base bleed) was ingested into the flow field. Therefore, the gas

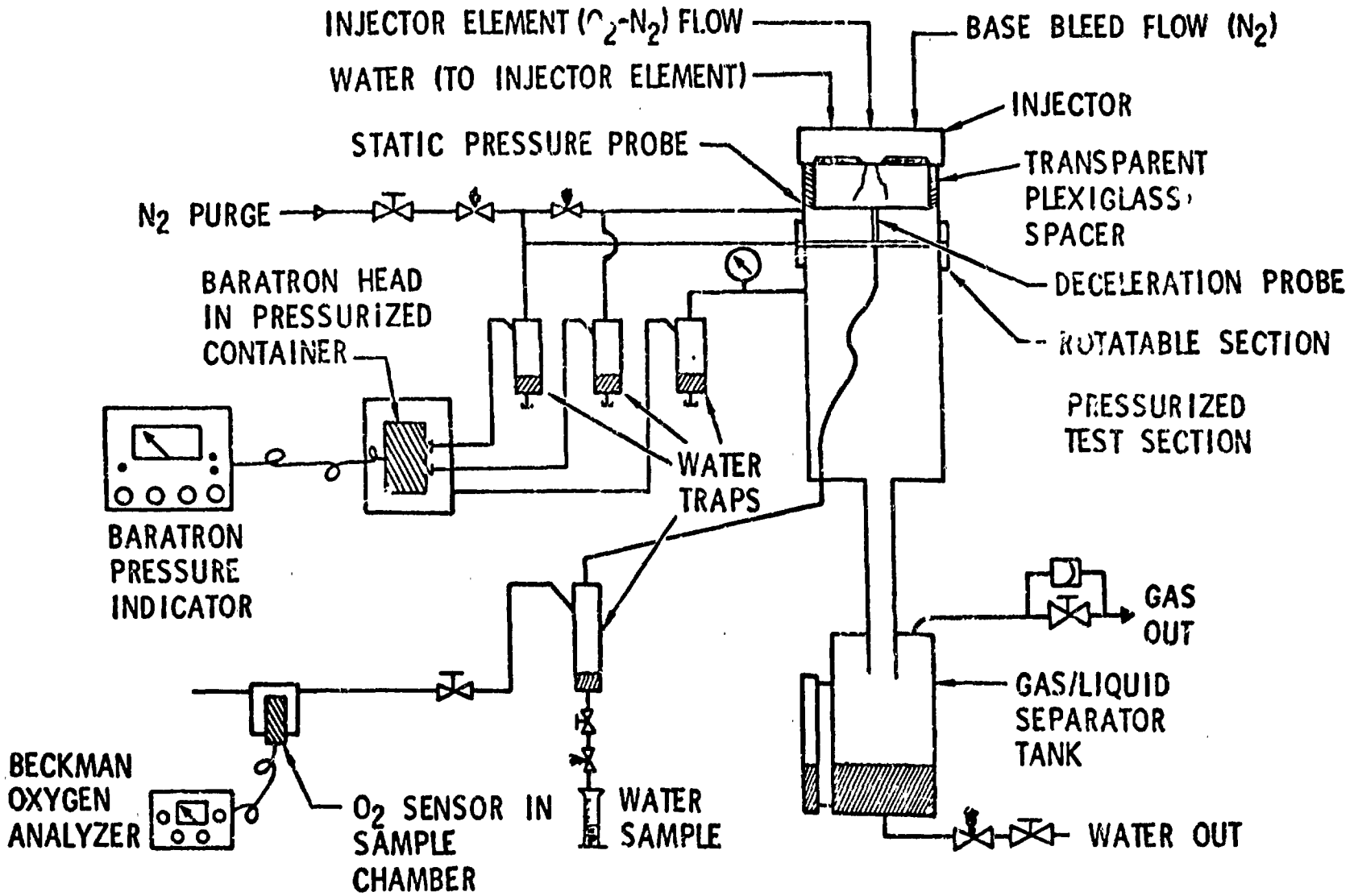

Figure B-1. Schematic of Pressurized Gas/Liquid Mixing Facility

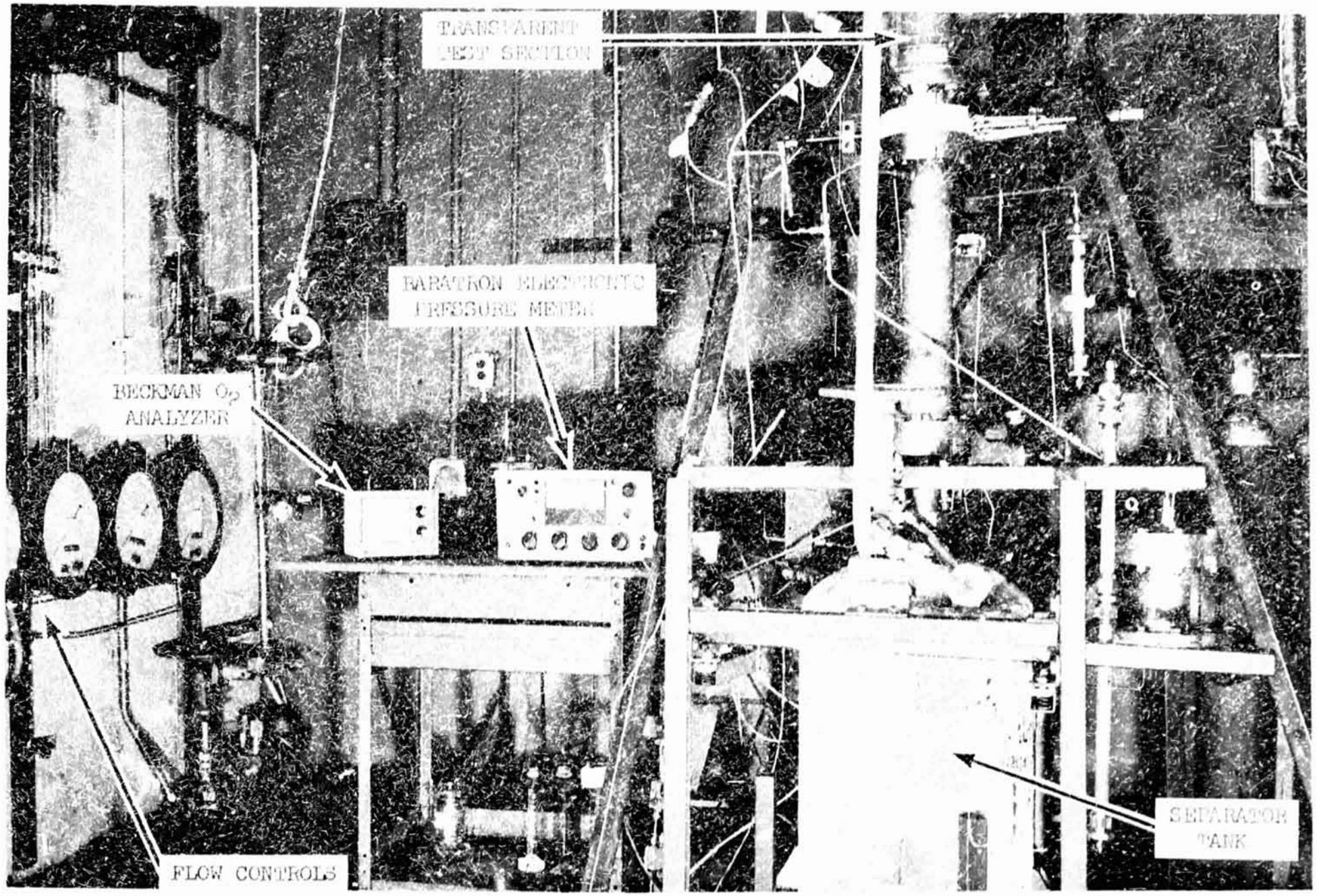

Figure B-2. Pressurized Gas/Liquid Mixing Facility

flowrate measured by the probe was composed both of gas that was injected and gas that was ingested. These two components were segregated to determine the injected portion (for calculation of E_m). To accomplish this, nitrogen and oxygen were mixed in known quantities and injected through the injector element while pure nitrogen was used as a base bleed fluid. The sample which arrived at the probe tip was processed through a Beckman oxygen analyzer (Fig. B-1). The concentration of the oxygen in the sample was then used to determine the concentration of the injected/gas phase.

TWO-PHASE DECELERATION PROBE

The two-phase deceleration probe, which was used for the determination of local values of gas and liquid mass flux, was developed jointly under the subject program and NAS3-12001. Only a brief description of the probe will be presented herein; for a more detailed description see Ref. B-3.

The concept of a deceleration probe for the measurement of gas-phase stagnation pressures, for the determination of gas velocity, in two-phase flow fields was first introduced by Dussourd and Shapiro (Ref. B-4). However, the referenced probe design was operated only in low mass flux ratio (particle flowrate/gas flowrate > 0.2) flow fields. In addition, the probe design of Dussourd and Shapiro was utilized only in ambient-pressure flow fields.

The deceleration probe which was developed was utilized both for the determination of gas-phase stagnation pressures and local liquid mass flux. The probe has been demonstrated to operate successfully in high mass flux ratio (liquid mass flux/gas mass flux 0.2 to 20) two-phase flow fields (Ref. B-5). In addition, measurements have been made in dense gas/liquid flow fields at static pressures up to 500 psia.

A schematic of the deceleration probe, termed the concentric tube two-phase impact probe, is presented in Fig. B-3. The probe was constructed of two concentric tubes (A and B) with a specially designed tip attached to tube B. The tip was designed to prevent the passage of water (termed flooding) into the annulus formed by tubes A and B when the probe is utilized in high mass flux ratio flow fields. The problem of flooding is a serious limitation of the probe design described in Ref.B-4.

The operating principle for the determination of the gas-phase stagnation pressure by the concentric tube two-phase impact probe is illustrated in Fig. B-4. Basically, the intent is to decelerate the gas and measure the gas-phase stagnation pressure in a manner that minimizes momentum exchange from the condensed phase upstream of the measurement location. Particles (or droplets) and gas (each at their own velocity) encounter the probe tip but the gas phase is stagnated at the probe tip where the pressure is approximately equal to the gas-phase stagnation pressure. Deviation from true gas-phase stagnation pressure is due to momentum exchange between the particles and the gas in the near flow field of the probe tip (termed overpressure error). A particle, due to its higher inertia, passes through the probe tip and is decelerated to zero velocity in the stagnation chamber formed by

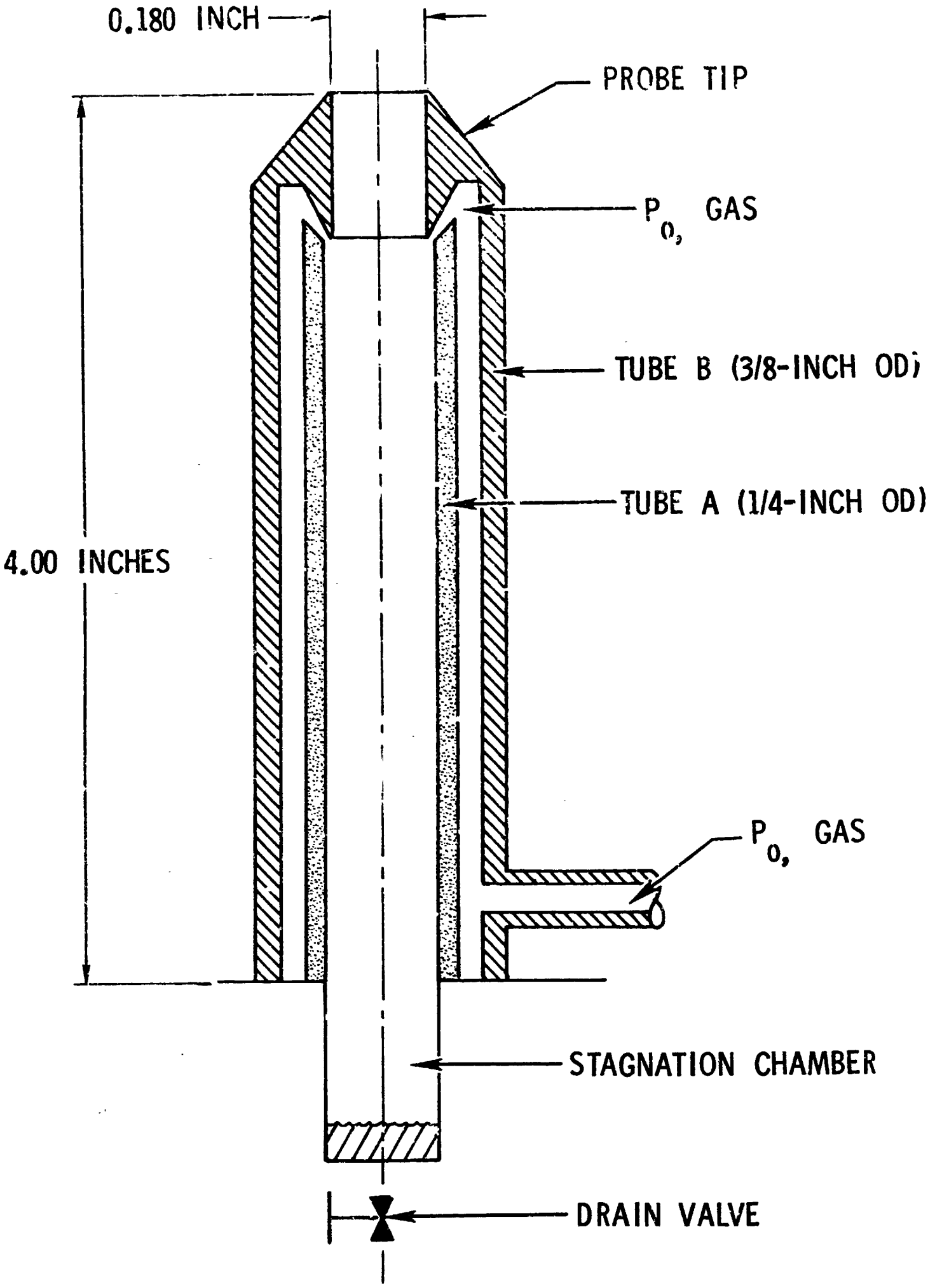

Figure B-3. Schematic of Concentric Tube Two-Phase Impact Probe

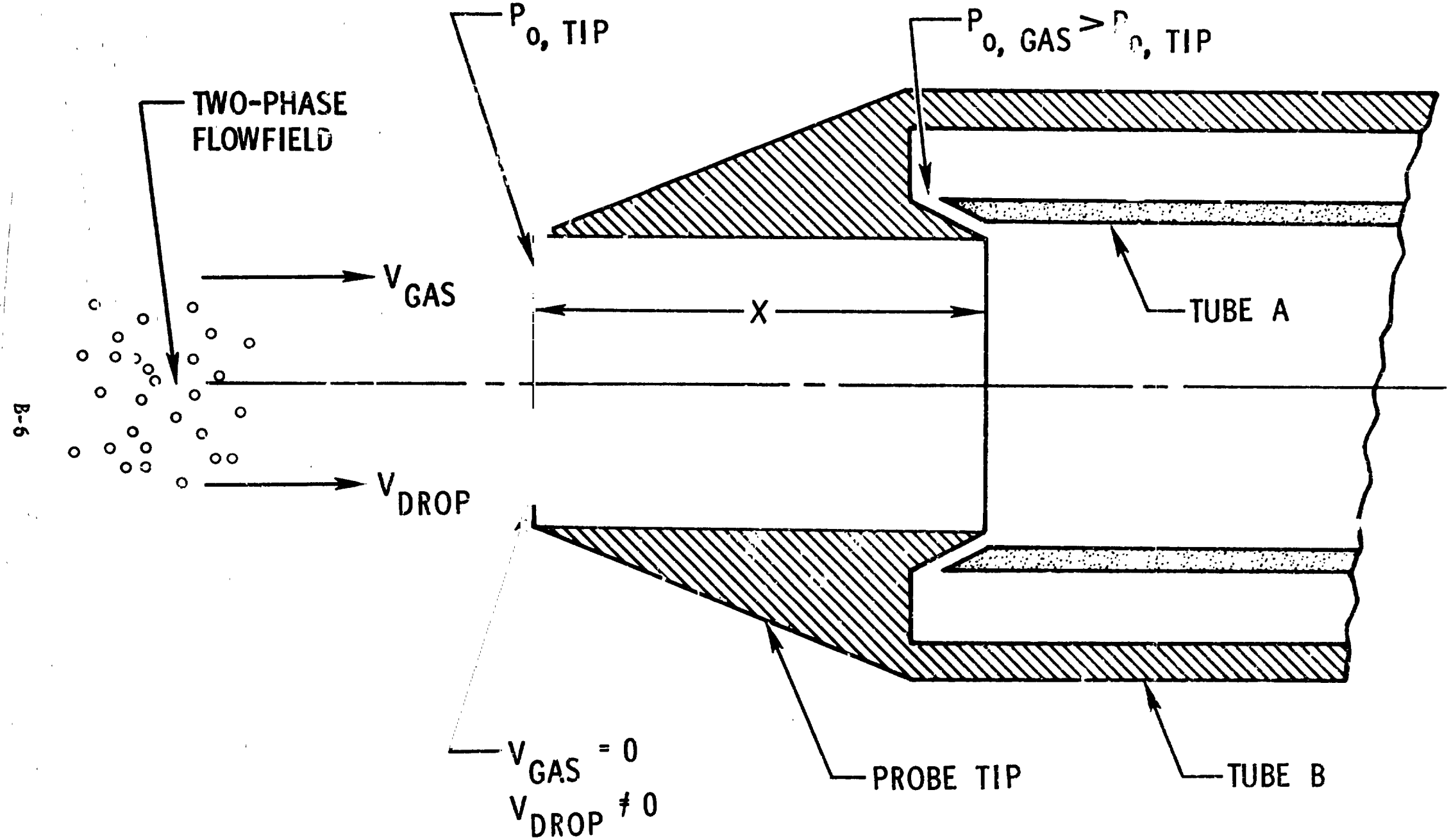

Figure B-4. Principle of Operation

tube A. However, due to momentum exchange between the particles and the stagnated gas, the particles decelerate in the probe tip to some extent over the distance X (see Fig. B-4). The gas-phase stagnation pressure $P_{o,gas}$, as measured in the probe annulus, is greater than the gas-phase stagnation pressure, $P_{o,tip}$. The difference between the two aforementioned pressures can be made small if the distance X is minimized. However, the total overpressure error (due to particle/gas momentum exchange both near and within the probe tip) can be determined by proper calibration of the probe in known two-phase flow fields (Ref. B-3).

The gas-phase stagnation pressure was measured in the 360-degree annulus at the probe tip rather than at a single point as was done on the probe described in Ref. B-4. Tests conducted with both the subject probe and one of the Ref. B-4 designs in high mass flux ratio (> 3) flow fields demonstrated that the concentric tube probe eliminated the pressure oscillations encountered with a probe of Ref. B-4 design. In addition, the concentric tube probe design avoids the need for an external pressure line at the probe tip that could create flow field disturbances. The gas-phase stagnation pressure in the probe annulus was measured with an MKS Baratron Type 77 electronic pressure meter.

Local values of liquid mass flux were determined by capturing a liquid sample in the probe stagnation chamber (Fig. B-2) for a known time interval. However, since the droplet capture efficiency of the probe design is less than 1 (≈ 0.95) small corrections must be made to the captured liquid mass to determine a value of local liquid mass flux. Values of the probe capture efficiency were determined by calibration of the probe in known two-phase flow fields.

A photograph of the two-phase probe and its traversing mechanism is shown in Fig. B-5. The probe is shown located in the rotatable portion of the test section.

REFERENCES

B-1. Burick, R. J., "Development of Experimental Cold-Flow Modeling Criteria for Gas/Liquid Injectors," 18 June 1969, IT-69-341-24, Rocketdyne Internal Memo.

B-2. Becker, H. A., H. C. Hottle, and G. C. Williams, "Mixing and Flow in Ducted Turbulent Jets," Ninth Symposium (International) on Combustion, Academic Press, 1963.

B-3. Burick, R. J., C. H. Scheuerman, and A. Y. Falk, "Determination of Local Values of Gas and Liquid Mass Flux in Highly Loaded Two-Phase Flow," Paper No. 1-5-21, Symposium on Flow--It's Measurement and Control in Science and Industry, 10-14 May 1971, Pittsburgh, Pa., Paper No. 1-5-21, to be published in Symposium Proceedings.

B-4. Dussourd, F. L. and A. H. Shapiro, "A Deceleration Probe for Measuring Stagnation Pressure and Velocity of a Particle Laden Gas Stream," Jet Propulsion, pp 24-34, January 1958.

B-5. Mehegan, P. F., et al., NASA CR-72703, Investigation of Gas-Augmented Injectors, Rocketdyne, a division of North American Rockwell Corporation, Canoga Park, California, September 1970.

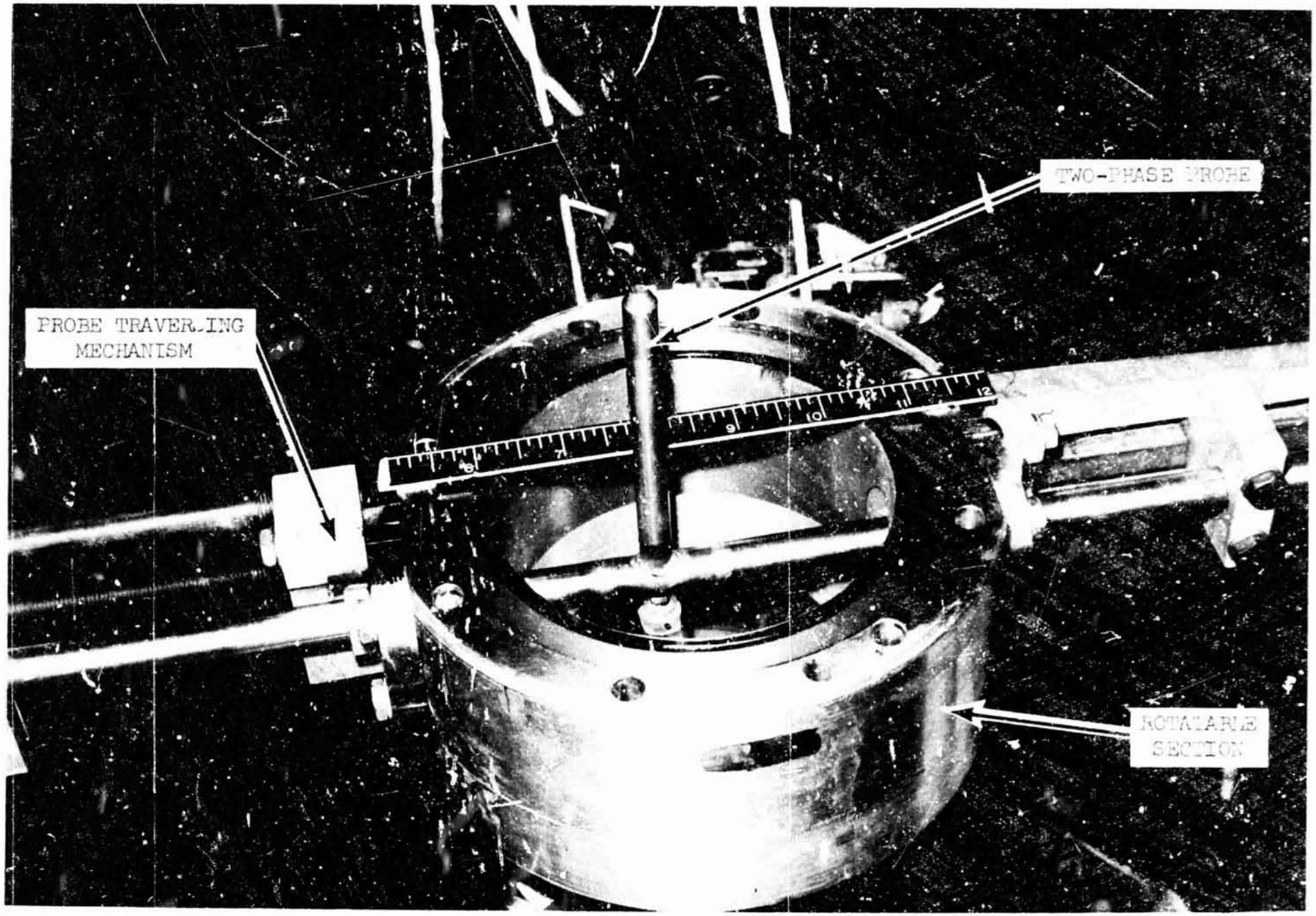

5AA36-11/19/70-S1B

Figure B-5. Two-Phase Impact Probe in Rotatable Section

APPENDIX C

PRESSURIZED COLD-FLOW ATOMIZATION FACILITY

INTRODUCTION

The operating conditions and injector dynamics that control the gas/liquid mixing processes also influence the atomization processes. Thus, early in the coaxial characterization program, work was initiated on the construction of a pressurized atomization facility. The facility is located at the Combustion and Heat Transfer Laboratory. The pressurized system was an addition to an existing molten wax facility which has been used successfully to characterize injector spray fields in a number of programs (Ref. C-1 and C-2). The use of a pressurized environment in the investigation of gas/liquid atomization processes was accomplished for the first time during the subject program.

EQUIPMENT TECHNIQUE

To simulate the dynamic injection conditions of hot-fire propellant systems, the atomization experiments were conducted at simulated gas-phase densities. In this case, gaseous nitrogen and molten wax (Shell-270) were used as nonreactive fuel/oxidizer simulants, respectively. In this molten wax technique, the wax droplets freeze prior to collection and are subsequently subjected to sieve analysis after drying.

A series of 23 standard sieves ranging in size from 53 to 2380 microns (53 to 2380 x 10^{-6} in.) was available for sample sieving. For any particular sample, only 12 of the sieves were used, the particular sieve sizes which were used depended on the anticipated size range. The particular wax sample ($\approx$10 grams) was placed on the largest screen of the selected set of 12 sieves. The sieves were shaken on a RO-TAP automatic shaker for 30 minutes. After the sieving operation was completed, the mass of particles on each sieve was weighed on an electric balance. A total recovery of 96 to 98 percent of the mass originally introduced into the sieves was possible. The mass fraction of sample on each sieve was then plotted as a function of sieve size to determine a mass median drop size.

EXPERIMENTAL FACILITY

A schematic of the pressurized atomization facility that was employed in these studies is presented in Fig. C-1. The system consisted of a 600-gallon cylindrical tank in which a single-element injector model was mounted. Molten wax and heated GN_2 were supplied to the injector from a system that was heated with circulating hot oil. All lines and valves in the wax supply system were oil jacketed to prevent wax freezing. Heated GN_2 was supplied to the injector at a temperature above the melting point of the wax ($\approx$200 F) so that the resulting wax droplets did not freeze prior to the completion of the liquid jet breakup and atomization processes. A water flush was supplied to the inner tank walls during testing to ensure that molten wax did not adhere to the tank walls. A photograph of the pressurized atomization facility is shown in Fig. C-2.

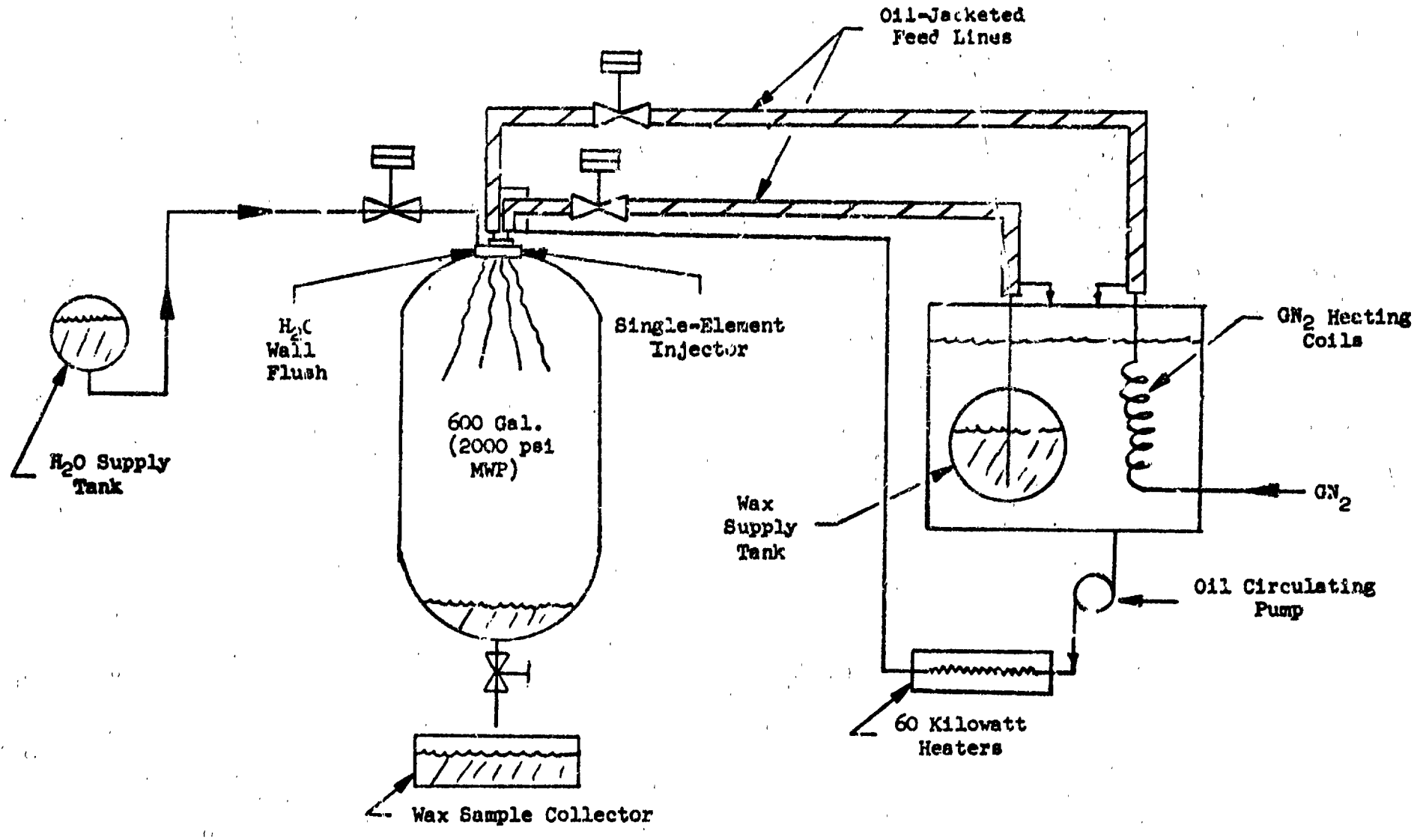

Figure C-1. Schematic of Pressurized Atomization Facility

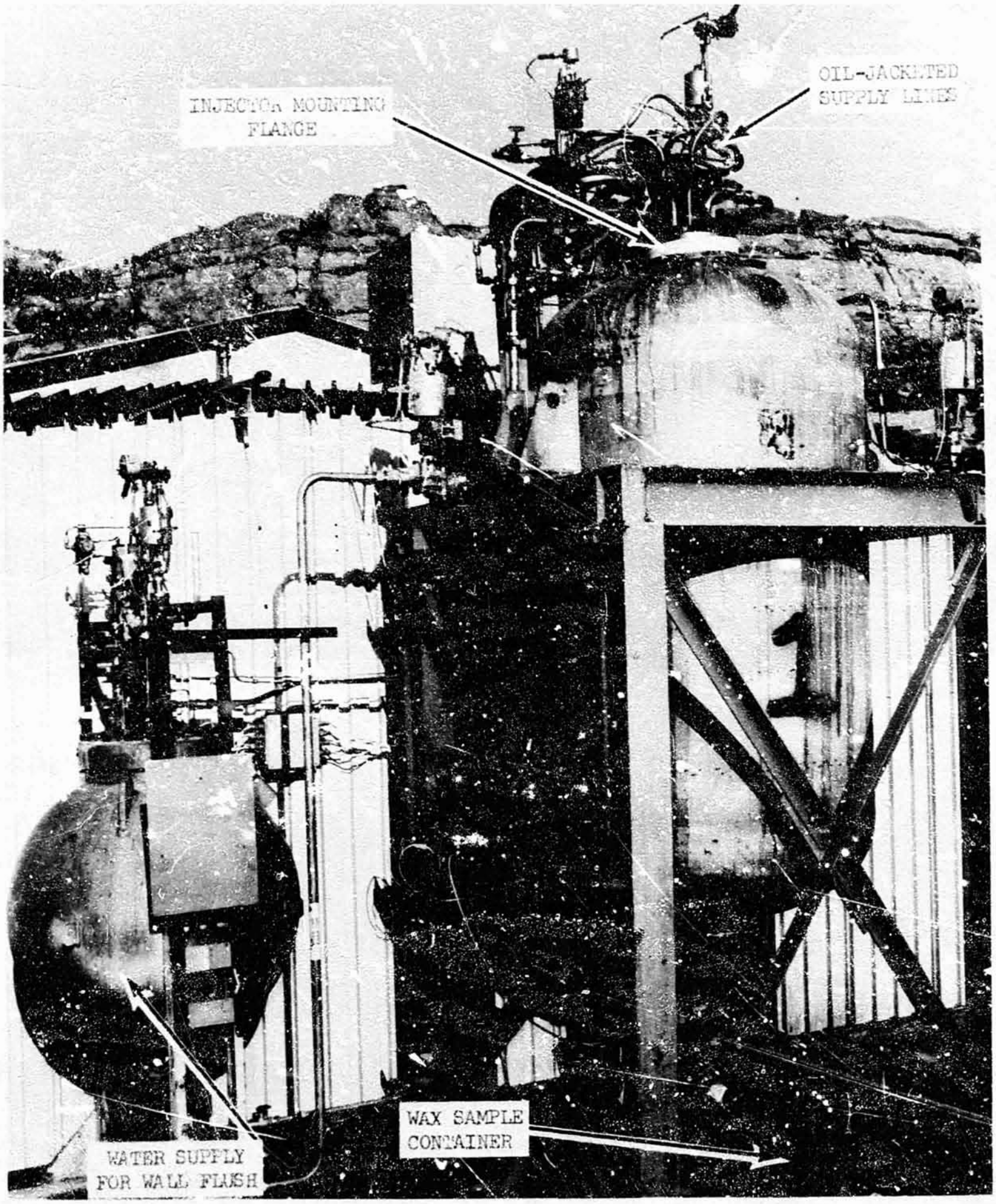

5AA36-11/20/70-S1B

Figure C-2. Pressurized Atomization Facility

REFERENCES

C-1. Dickerson, R., et al., Correlation of Spray Injector Parameters with Rocket Engine Performance, Report AFRPL TR-68-147, Rocketdyne, a division of North American Rockwell, Canoga Park, California, June 1968.

C-2. Mehegan, D. F., et al., NASA CR-72703, Investigation of Gas-Augmented Injectors, Rocketdyne, a division of North American Rockwell, Canoga Park, California, September 1970.

APPENDIX D

HOT-FIRE FACILITIES AND PROCEDURES

INTRODUCTION

Detailed description of the hot-firing test stand instrumentation, data recording (test documentation) procedures, and pertinent experimental procedures, utilized during the program are presented in this appendix. The single-element hot firings were conducted on Uncle stand and the full-scale injector firings were conducted on Willie stand. Since both stands are nearly identical in purpose, only Willie stand will be described in detail.

HOT-FIRING TEST FACILITY

The full-scale hot-fire experimental portion of the program was conducted on test stand Willie at Rocketdyne's Propulsion Research Area (PRA) test complex. This is the same test stand that was used for the like-doublet, full-scale injector firings under the subject program. A schematic flow diagram of the test facility (Willie stand) with instrumentation locations is presented in Fig. D-1.

The FLOX system was identical to that employed in numerous fluorine programs at Rocketdyne. FLOX is stored in the 300- and 120-gallon, vacuum-jacketed, tri-wall storage tanks. FLOX was transferred from the storage tank to the run tank (43 gallons, 2000-psi MWP) prior to each day's testing. Procedures for storage, transfer, and handling of the FLOX have been established on previous programs at Rocketdyne. Prior to assembly, all facility and experimental hardware was thoroughly cleaned in accordance with prescribed procedures.

The (jacketed) FLOX system was completely chilled with liquid nitrogen from the storage tank to the engine. In addition, provisions were made to permit prerun chilldown of the oxidizer dome and injector by means of a liquid nitrogen bleed directly through the injector and thrust chamber, thus preventing the propellant from flashing in the initial portion of the firing and minimizing flow transients. Dried, filtered helium was used for FLOX tank pressurization.

The fuel (gaseous methane) was supplied to the engine from a gaseous methane manifold. The methane was stored in industrial cylinders (K-bottles). Approximately 20 cylinders were connected to the supply manifold.

The engine was mounted horizontally. Tank and purge pressures were set by motorized dome loaders in conjunction with electrically operated tank vent and control valves. Dried and filtered gaseous nitrogen purges were used on the propellant lines.

Test operations and data acquisition were conducted through a central control and recording center. The data recording systems, particular transducers to be used for the various types of measurements, and calibration procedures are briefly described below.

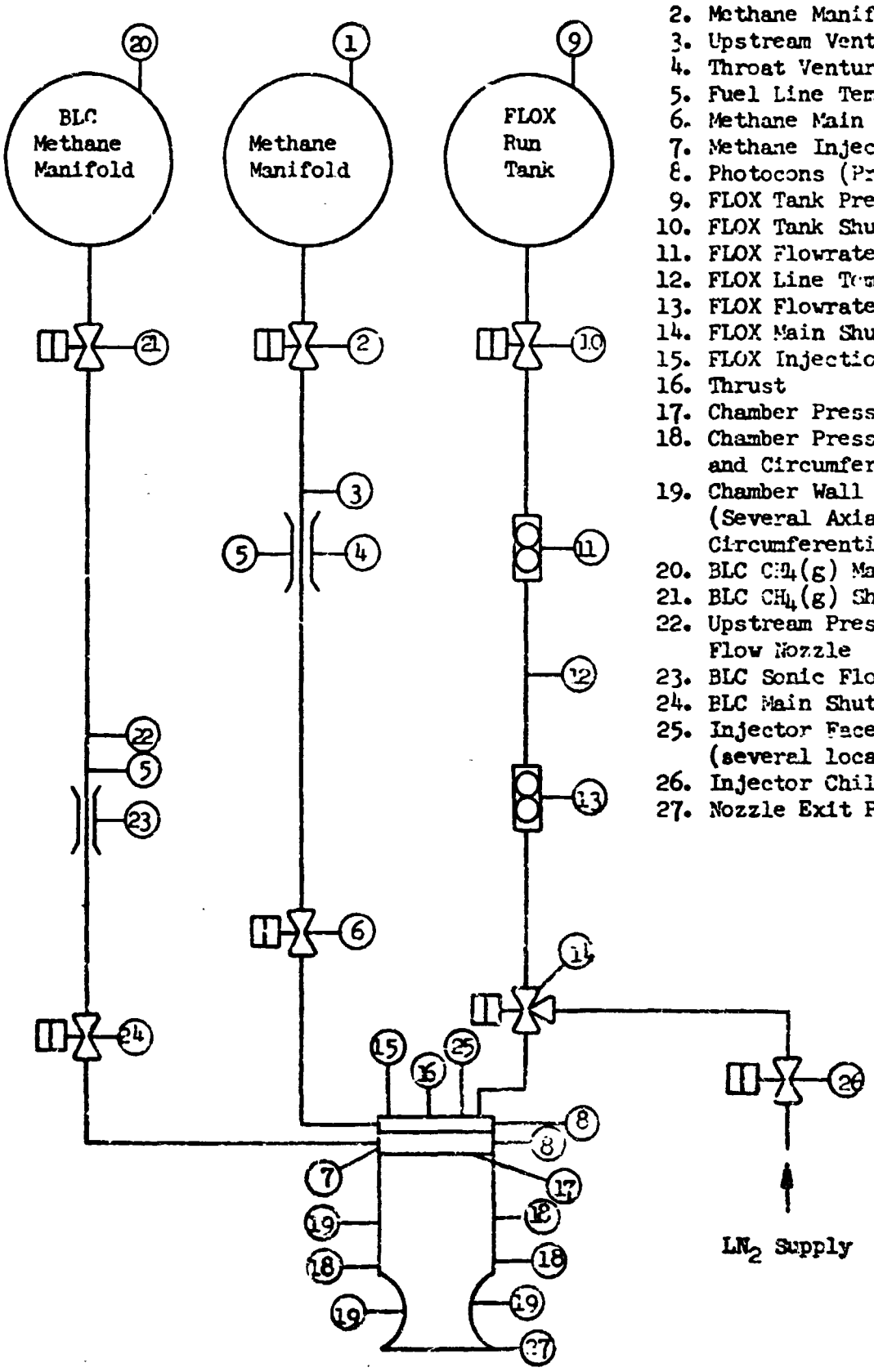

1. Methane Manifold Pressure
2. Methane Manifold Shutoff Valve
3. Upstream Venturi Pressure
4. Throat Venturi Pressure
5. Fuel Line Temperatures
6. Methane Main Shutoff Valve
7. Methane Injection Pressure
8. Photocons (Propellant Manifolds)
9. FLOX Tank Pressure
10. FLOX Tank Shutoff Valve
11. FLOX Flowrate #1
12. FLOX Line Temperature
13. FLOX Flowrate #2
14. FLOX Main Shutoff Valve
15. FLOX Injection Pressure
16. Thrust
17. Chamber Pressure (Injector Face)
18. Chamber Pressure (Several Axial and Circumferential Locations)
19. Chamber Wall Temperature (Several Axial and Circumferential Locations)
20. BLC $CH_4(g)$ Manifold Pressure
21. BLC $CH_4(g)$ Shutoff
22. Upstream Pressure, BLC Sonic Flow Nozzle
23. BLC Sonic Flow Nozzle
24. BLC Main Shutoff Valve
25. Injector Face Temperature (several locations)
26. Injector Chill Valve
27. Nozzle Exit Pressure

Figure D-1. Schematic Flow Diagram of Hot-Fire Test Facility Showing Location of Instrumentation (Full-Scale Coaxial Injector)

Hot Firing, Test Instrumentation, and Data Recording

Facility instrumentation locations are shown in Fig. D-1. Redundant measurements were made on the important experimental parameters (e.g., chamber pressure, flowrates, etc.) to increase data reliability. The particular transducers used for the various types of measurements are described below.

Thrust

The thrust chamber mount was supported on flexures, which allowed free movement parallel to the engine axis (horizontally), restrained in the thrust direction by a Baldwin-Lima-Hamilton double-bridge load cell.

Pressures

Pressures were measured with bonded strain-gage transducers (Taber "Teledyne" Series 206 or equivalent). Chamber pressures were measured at several circumferential and axial positions in the chamber. Redundant measurements were made at pertinent axial locations.

Flowrates

Oxidizer flowrate was measured by Fischer-Porter turbine flowmeters that measure the volumetric flowrate. The oxidizer line had two flowmeters in series to increase data reliability. The fuel flowrate to the injector core was measured by calibrated sonic venturi meters and the BLC flowrate was measured with calibrated sonic flow nozzles. For the single-element firings on Uncle stand, FLOX flowrates were measured by a cavitating venturi. The cavitating venturi was calibrated employing a small turbine flowmeter with FLOX at LN_2 temperatures.

Temperatures

Reliable measurement of cryogenic propellant flowrates requires accurate determination of liquid density as well as volumetric flowrate. Density of cryogenic propellants is a sensitive function of temperature; therefore, it is important to make careful measurements of propellant temperature as close to the flowmeters as practical. This was accomplished by use of shielded platinum resistance bulbs (Rosemont Model 176) immersed in the liquid stream. These instruments are very sensitive to temperature changes in the cryogenic region and are the preferred method of measurement. Oxidizer temperature was measured between the two flowmeters and in the injector manifolds. Fuel temperature was measured in the venturi plenum and injector manifolds using iron-constantan thermocouples.

Temperature histories of the chamber and/or nozzle were measured by chromel-alumel thermocouples embedded in the graphite chamber wall.

Special Instrumentation

Photocon pressure transducers were used to monitor high-frequency pressure oscillations in the fuel/oxidizer manifolds of the full-scale injector.

Calibration Procedures

Transducer calibrations were employed not only to obtain appropriate factors for test data reduction, but to develop statistical histories for each transducer, so that estimates of short- and long-term deviations could be made, and probable error bands calculated. The calibration methods which were employed for the various types of transducers are described below.

The thrust-measuring load cell was calibrated in-place by a permanently mounted, manually operated, hydraulic force cell, which deflects the load cell exactly as does the engine, i.e., through a yoke tension-rod system. Known loads were applied to the force cell through a Morehouse compression-type, temperature-compensated, proving ring calibrated by the National Bureau of Standards (NBS). A thrust calibration was conducted prior to testing on each test day.

Pressure transducers were calibrated end-to-end by mounting them on stand manifolds in which pressures were read with high-precision Heise-Bourdon tube gages. The latter were calibrated periodically on Ruska deadweight testers. Maximum length of pickup line from pressure tap to transducer was less than 1/2 foot.

The turbine flowmeters in the oxidizer line were calibrated prior to the initial test firing and at the conclusion of the test series. The sonic venturi meters were calibrated by the manufacturer to determine the discharge coefficient (C_D).

Resistance of the platinum thermometers to be used in the cryogenic propellant lines was converted to millivolt output by a triple-bridge system. This was calibrated by substituting a decade resistance box for a sensor and setting it at various resistances corresponding to a temperature-resistance calibration for each instrument. These precision platinum resistance sensors have no significant calibration drift. Chamber thermocouples were employed on the basis of the standard NBS millivolt/temperature tables. Thermocouple records were electrically calibrated.

Data Recording Systems

Pertinent pressure, temperature, and flow measurements were recorded on tape during each firing by a Beckman Model 210 Data Acquisition and Recording System. This system acquires analog data from the transducers, which it converts to digital form in binary-coded decimal format. The latter were recorded on tapes, which were then used for computer processing.

The Beckman Data Acquisition Unit sequentially samples the input channel at a range of 5625 samples per second. Programmed computer output consists of tables of time versus parameter value (in engineering units) printed out at approximately 10-millisecond intervals during the firing, together with calibration factors, prerun and postrun zero readings, and related data. The same computed results are machine plotted and displayed as CRT outputs on approximately scaled and labeled grids for simple determination of gradients, establishment of steady state, etc.

Primary data recording for the firings, and subsequent calculation of performance, were on the Beckman 210 system. In addition, the following auxiliary recording systems were employed:

1. An 8-channel, Brush, Mark 200 recorder was employed in conjunction with the Beckman unit, primarily to establish time intervals for computer data reduction and, additionally, for "quick-look" information on the most important parameters. This is a direct-inking system, with display on high-gloss, graduated paper moving at 20 mm/sec.
2. A CEC, 36-channel, direct-reading oscillograph was used as backup for the Beckman 210 system and for indication of any oscillatory combustion.
3. Direct-inking graphic recorders (DIGR's), either Dynalog rotary chart or Esterline-Angus strip chart, were used to set prerun propellant supply pressures, to provide quick-look information, and as secondary backup to the Beckman and oscillograph recorders.

APPENDIX E

CALCULATION OF CORRECTED C* EFFICIENCY

INTRODUCTION

The index of injector performance used in this experimental program was corrected c* efficiency. This parameter was calculated by two independent methods for the full-scale injector tests, one based on measurement of chamber pressure and the other on measurement of thrust. Performance data for the single-element hot-firing were based on chamber pressure due to the difficulty of accurately measuring small thrust levels ($\approx$70 pounds) on a 5000-pound-thrust stand. Details of the computational procedures and of the corrections applied are given in this appendix. A numerical example is included.

CALCULATIONS BASED ON CHAMBER PRESSURE

Characteristic velocity efficiency based on chamber pressure is defined by the following equation

$$\left(\eta_{c^*}\right)_{P_c} = \frac{(P_c)_o \ (A_t)_{eff} \ g_c}{(\dot{w}_T) \ (c^*)_{theo}} \qquad \text{(E-1)}$$

where

$(P_c)_o$ = stagnation pressure at the throat, psia

$(A_t)_{eff}$ = effective thermodynamic throat area, $in.^2$

g_c = conversion factor (32.174 lbm-ft/lbf-sec^2)

$\dot{w}_T$ = total propellant weight flowrate, lbm/sec

$(c^*)_{theo}$ = theoretical characteristic velocity based on shifting equilibrium, ft/sec

Values calculated from Eq. E-1 are referred to as "corrected" c* efficiencies, because the factors involved are not measured directly, but are obtained by application of suitable corrections to measured parameters. Thus, stagnation pressure at the throat was obtained from measured static pressure near the start of nozzle convergence by assumption of isentropic expansion; effective throat area was estimated from measured geometric area by allowing for radius changes during firing and for nonunity discharge coefficient; and chamber pressure was corrected to allow for energy losses from the combustion gases to the chamber wall by friction and measured heat transfer rates. Equation E-1 may therefore be written as follows:

$$\left(\eta_{c^*}\right)_{P_c} = \frac{P_c \ A_t \ g_c \ f_p \ f_{TR} \ f_{DIS} \ f_{FR} \ f_{HL}}{(\dot{w}_o + \dot{w}_f) \ (c^*)_{theo}} \qquad \text{(E-2)}$$

where

P_c = measured static pressure near the start of nozzle convergence, psia

A_t = measured geometric throat area, $in.^2$

$\dot{w}_o$ = oxidizer weight flowrate, lbm/sec

$\dot{w}_f$ = fuel weight flowrate, lbm/sec

f_P = factor correcting observed static pressure to throat stagnation pressure

f_{TR} = factor correcting for change in throat radius during firing

f_{DIS} = factor correcting throat area for effective discharge coefficient

f_{FR} = factor correcting measured chamber pressure for frictional drag of combustion gases at chamber wall

f_{HL} = factor correcting measured chamber pressure for heat losses from combustion gases to chamber wall

Methods of estimation of the various correction factors are described in the following paragraphs.

Pressure Correction (f_p)

Measured static pressure near the start of convergence was converted to stagnation pressure at the throat by assumption of no combustion in the nozzle and application of the isentropic flow equations.

For calculations of a "valid" performance value, care must be taken to ensure measurement of a "valid" static chamber pressure near the start of nozzle convergence. Experience gained on this and related programs (Ref. E-1) at Rocketdyne indicates that a definite increase in static pressure can occur near the start of convergence. This increase in pressure appears to be caused by subsonic deceleration effects associated with the turning of the combustion gases by the converging walls prior to acceleration in the nozzle. The magnitude of this increase is dependent upon the geometric configuration of the nozzle. Measurement of the static chamber pressure must be taken sufficiently upstream of the start of convergence so that its value is not affected by the subsonic decelerating effects discussed above. Furthermore, chamber pressure must be measured where combustion is nearly complete.

During this program, chamber pressure taps were located 0.50, 0.75, 1.00, and 1.25 inches upstream of the start of nozzle convergence. Measured pressures at these four locations were found to be essentially identical for all runs. Consequently, the four pressure readings were averaged to determine a mean static chamber pressure.

The values of f_p, the stagnation-to-static pressure ratio, was estimated to be 1.026, for the 3:1 contraction ratio chamber. Variations in the shifting equilibrium specific heat ratio were minor over the range of test conditions (chamber pressure, mixture ratio) employed. This same correction factor (f_p = 1.026 for ϵ_c = 3) was, therefore, considered applicable over the entire test matrix.

Throat Radius Correction (f_{TR})

Temperature gradients produced in an uncooled nozzle wall by radiative and convective heat transfer from the hot combustion gases result in thermal stresses which can affect the throat radius. Consequently, the geometric throat diameter measured in an ambient-temperature nozzle is not necessarily the same as that which exists during firing. Furthermore, throat diameter during firing will be a function of time, as well as of the physical properties of the throat material, the temperature and pressure of the combustion gases, and the nozzle geometry (i.e., wall thickness, etc.).

A throat radius correction factor, f_{TR}, was used for all tests and is defined as:

$$f_{TR} = \frac{A_{t\ hot}}{A_{t\ cold}} \qquad \text{(E-3)}$$

During the hot-firing tests, the thrust chamber throat diameter and area would increase (compared to the ambient dimensions) as a function of the wall temperature. The "hot" throat area was computed for each test as follows:

$$A_{t\ hot} = \left[(\alpha\ \Delta T_{avg} + 1)\ D_{t,\ cold}\right]^2\ \pi/4 \qquad \text{(E-4)}$$

where

α = thermal expansion coefficient (ATJ graphite)

$\Delta_{T_{avg}}$ = change in average throat wall temperature during the test

$D_{t,cold}$ = cold throat diameter (pretest)

The average change in throat wall temperature was based on measured throat heat flux data (see Fig. 60). For the short duration tests, average wall temperature was calculated (based on nozzle thermocouple measurements) to be approximately 965 F. Thus, ΔT_{avg} was taken as 885 F for all short duration tests. A value of $\alpha = 1.16 \times 10^{-6}$ in./in. F was employed for the thermal expansion coefficient for the ATJ graphite throat. Based on the aforementioned data, Eq. E-3 yields a throat radius correction factor, f_{TR}, equal to 1.002.

The average wall temperature for the long duration test was estimated to be approximately 3000 F based on previous Rocketdyne experience with similar propellants and thrust chambers. Thus, Eq. E-3 yields a throat radius correction factor of 1.007 for the long-duration test.

Throat Discharge Coefficient (f_{DIS})

The discharge coefficient is defined as the ratio of actual flowrate through the throat to the theoretical maximum based on geometric throat area and ideal, uniform, one-dimensional flow with no boundary layer. Values of the discharge coefficient may be estimated either analytically or from correlations of the results of experimental studies of gas flow through nozzles.

Experimental conical nozzle discharge coefficients obtained with air by various investigators are plotted in Fig. E-1 against the indicated geometric parameters. Data sources also are listed in Fig. E-1.

Based on the correlating curve shown and the nozzle geometry of the thrust chamber, the throat discharge correction factor is $f_{DIS} = 0.991$.

Frictional Drag Correction (f_{FR})

Calculation of c* efficiency based on chamber pressure is concerned with chamber phenomena up to the nozzle throat. Drag forces to this point are generally small. For the present application, measured chamber pressure should be (and was) corrected for frictional losses only from the injector to the point where the chamber pressure was measured. Details of the method of estimation of f_{FR} are presented below. This discussion is general and applies to frictional losses for performance based on thrust as well as chamber pressure. Differences between the values of frictional losses for thrust and chamber pressure calculated performance are associated with the different regions over which the frictional losses are integrated.

This factor (f_{FR}) corrects for the energy losses caused by drag forces resulting from the viscous action of the combustion gases on the thrust chamber walls. Its magnitude, which is the integral of the local friction forces over the chamber inside wall, has been estimated by a boundary layer analysis utilizing the integral momentum equation for turbulent flow (Ref. E-2). The analysis accounted for boundary layer effects from the injector to the nozzle exit by suitable description of the boundary layer profile and local skin friction coefficient. A computer program was used to carry out a numerical integration of the equation, including effects of pressure gradient, heat transfer, and surface roughness. The program required a potential core solution of the nozzle flow which was obtained from the variable-property, axisymmetric method of characteristics calculation of the flow field outside the boundary layer; corresponding properties for the subsonic combustion chamber flow field were also calculated.

The above-mentioned program was not run specifically for the thrust chamber which was utilized in this program. However, parametric data generated in NAS3-11199 (FLOX/LPG) was sufficient to interpolate a value of the frictional drag losses for the chamber which was utilized in this study. The value employed for f_{FR} was 1.0036 which is similar to that reported in a recent FLOX/CH_4 program which utilized a similar thrust chamber configuration (f_{FR} = 1.0025, Ref. E-3).

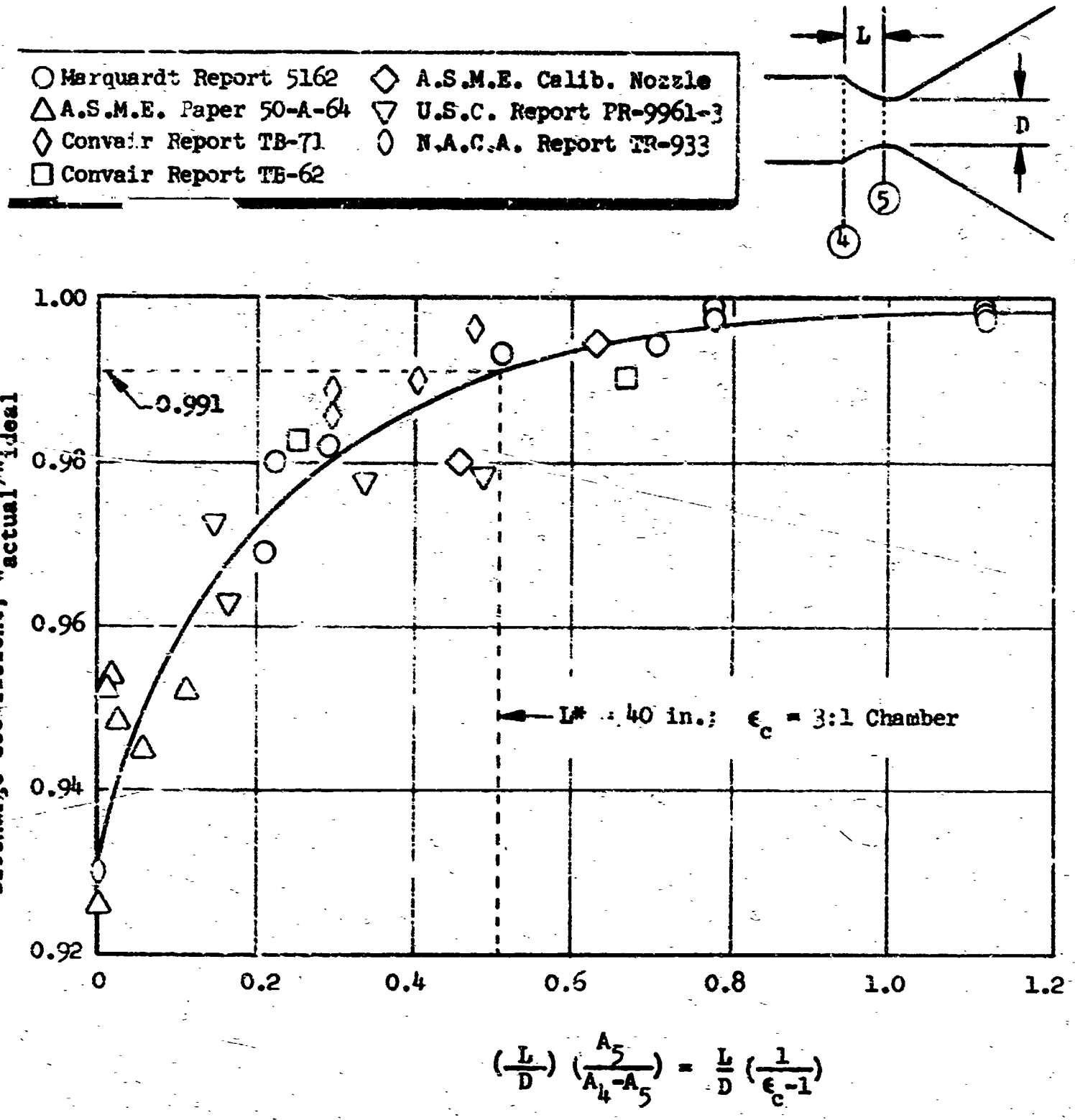

Figure E-1 Discharge Coefficient as Function of Nozzle Dimensions; A_4 = Cross-Sectional Area of Chamber, A_5 = Cross-Sectional Area of Throat (Data Taken From Indicated References for Cold Flows With Air.)

Heat Loss Correction (f_{HL})

Heat transfer from the combustion gases to the walls of an uncooled thrust chamber results in loss of enthalpy and thus decreases chamber pressure and thrust. This enthalpy loss is substantially reduced in a graphite chamber and is effectively recovered in a chamber cooled regeneratively by one of the propellants, whose initial enthalpy is raised by the heat absorbed. To obtain a true indication of performance efficiency in an uncooled chamber, measured chamber pressure must be corrected by a factor which accounts for heat loss to the walls. Heat transfer to the injector was neglected in this correction because the injector surface area and heat flux was small relative to that of the chamber (see Section 8.0) and because a major portion of injector heat flux is absorbed by the injected propellants.

Using the following equation, f_{HL} was estimated:

$$f_{HL} = \left\{ 1 + \left[\frac{c^*_{theo}}{c^*_{meas}} \right]^2 \left[\frac{\Sigma (\dot{q}/A)A}{\dot{w}_T . c_{p_m} . T_c} \right] \right\}^{1/2} \qquad (E\text{-}5)$$

where

c^*_{theo} = theoretical characteristic velocity at test conditions, based on full shifting equilibrium

c^*_{meas} = measured characteristic velocity, corrected for the previously discussed losses

$\Sigma (\dot{q}/A)A$ = measured heat loss to chamber walls

$\dot{w}_T$ = total propellant flowrate

c_{p_m} = mean specific heat of combustion chamber gases at test conditions

T_c = theoretical combustion gas temperature at test conditions

The basis for use of this equation is presented in Ref. E-4 and E-5.

Only heat losses to the chamber wall between the injector and the chamber pressure taps employed for calculation of performance based on chamber pressure are included in Eq. E-5.

Due to the low chamber heat flux levels which were measured in this program, f_{HL} was not large amounting to approximately 1.007 at the design point. For the 44-second duration test, f_{HL} was assumed to be 1.000 since the chamber was essentially operating adiabatically.

CALCULATIONS BASED ON THRUST

An alternate determination of corrected c* efficiency is based upon the following defining equation:

$$(\eta_{c^*})_F = \frac{F_{vac}\, g_c}{(C_F)_{vac}\, \dot{w}_T\, (c^*)_{theo}} \qquad \text{(E-6)}$$

where

F_{vac} = measured thrust corrected to vacuum conditions by the equation: $F_{vac} = F + P_a A_e$, lbf

F = measured thrust, lbf

P_a = ambient pressure, psia

A_e = area of nozzle exit, in.^{2}

g_c = conversion factor (32.174 lbm-ft/lbf-sec^2)

$(C_F)_{vac}$ = theoretical shifting thrust coefficient (vacuum)

$\dot{w}_T$ = total propellant flowrate, lbm/sec

$(c^*)_{theo}$ = theoretical shifting-equilibrium characteristic velocity, ft/sec

Corrected values of vacuum thrust may be obtained by application of suitable corrections to measurements of thrust made at sea level. With these values, which include allowances for all important departures from ideality, theoretical thrust coefficients may be used for calculation of c*. That is, C_F coefficient is 100 percent if there is no combustion in the nozzle, if chemical equilibrium is maintained in the nozzle expansion process, and if energy losses from the combustion gases are taken into account.

Applicable corrections to measured thrust are specified in the following equation:

$$(\eta_{c^*})_F = \frac{(F + P_a A_e)\, g_c\, \phi_{FR}\, \phi_{DIV}\, \phi_{HL}}{(C_F)_{vac}\, (\dot{w}_o + \dot{w}_f)\, (c^*)_{theo}} \qquad \text{(E-7)}$$

where

$(C_F)_{vac}$ = theoretical shifting thrust coefficient (vacuum)

$\dot{w}_o$ = oxidizer weight flowrate, lbm/sec

$\dot{w}_f$ = fuel weight flowrate, lbm/sec

ϕ_{FR} = correction for frictional losses

ϕ_{DIV} = correction for nozzle divergence

ϕ_{HL} = correction for heat losses to chamber and nozzle walls

The correction factors in Eq. E-7 were applied to vacuum thrust ($F \bullet P_a A_e$) instead of to measured site thrust (F) because, for convenience, the correction factors were calculated as changes in efficiency based on theoretical vacuum parameters, so that the total correction was of the form $\Delta F/F_{vac}$.

Although they do not appear explicitly in Eq. E-7, corrections to geometric throat area and to measured static chamber pressure at start of nozzle convergence are implicit in the use of theoretical C_F values. Thus, calculation of corrected c* efficiency from thrust measurement includes all the corrections described above for calculations from chamber pressure measurement plus an additional one to account for nonparallel nozzle exit flow. However, because $(C_F)_{vac}$ is essentially independent of the very small changes in chamber pressure and contraction ratio which are involved in corrections to P_c and A_t, these corrections are of no practical significance in calculation of c* from thrust measurements.

Corrections for Frictional Drag (ϕ_{FR})

The basis for and method of calculation of this factor were discussed under calculation of performance based on chamber pressure.

The value of ϕ_{FR} which was used for the 40-in. L* chamber was 1.015 at the design operating condition. This value is similar to that reported in a similar FLOX/CH_4 program (Ref. E-5, ϕ_{FR} = 1.018, L* = 40 in., ϵ_c = 4:1).

Correction for Nozzle Divergence (ϕ_{DIV})

The one-dimensional theoretical performance calculations assume that flow at the nozzle exit is uniform and parallel to the nozzle axis. The correction factor, ϕ_{DIV}, allows for nozzle divergence (i.e., for nonaxial flow) and for nonuniformity across the nozzle exit plane. It has been calculated by a computer program which utilized the axisymmetric method of characteristics for a variable-property gas (Ref. E-6).

The geometric efficiency was essentially independent of chamber pressure and mixture ratio for the entire test matrix. A value of ϕ_{DIV} = 1.018 was employed to correct for nozzle divergence losses.

Correction for Heat Losses (ϕ_{HL})

Heat loss correction factors for performance calculated from measured thrust are similar to those for performance calculated from chamber pressure, except that heat fluxes in the nozzle are included in the calculations. Thus, Eq. E-5 was employed with the measured heat flux summed from the injector to nozzle exit (Fig. 33).

A computer program was used to calculate ϕ_{HL} from the measured heat flux value. In the 40-in. L* chamber, at design operating conditions, the value of ϕ_{HL} was approximately 1.008.

NUMERICAL EXAMPLE

The method of performance data reduction and correction are illustrated by the following numerical example. This example is typical of all tests. Data from test No. 17 (full-scale injector) are analyzed in this example. The subject test was conducted in the graphite lined chamber (L^* = 40 in., ε_c = 3) at nominal design operating conditions (P_c 500 psia, MR = 5.38, 0% BLC). Pertinent steady-state raw data (static chamber pressure, propellant flowrates, measured thrust, etc.) from this test are presented in Table E-1. Figure 60 presents the chamber heat flux characteristics for the subject test. CRT printouts of the pertinent parameters (as a function of Beckman time) were used to determine when steady-state had been achieved. Analog Beckman traces of static chamber pressure, measured thrust, oxidizer flowrate, and fuel venturi pressures for test No. 17 are shown in Fig. E-? through E-7. The data slice interval for calculation of performance is noted. Steady-state performarce was determined at approximately 2.0 seconds into the 2.5-second test. These traces are representative of the hot-fire tests conducted during the program. Digital Beckman data were used for calculation of all performance values.

Performance Based on Chamber Pressure

Corrected c* efficiency based on chamber pressure measurement was calculated using Eq. E-2. Values of the measured parameters ($\dot{w}_{ox}$, $\dot{w}_f$, and A_t) and the theoretical C* used in Eq. A-2 are shown in Table E-1. The average static chamber pressure measured upstream from the start of nozzle convergence was used for calculation of performance.

Methods of estimation of the various correction factors in Eq. E-2 were outlined previously. Estimation of these correction factors for test No. 17 is described in the following paragraphs.

Pressure Correction (f_{pt}). Measured static pressure was converged to stagnation pressure at the throat by assumption of no combustion in the nozzle and application of the isentropic flow equations. The value of f_p, the stagnation-to-static pressure ratio, was estimated to be 1.026 for the 3:1 contraction ratio chamber.

Throat Radius Connection (f_{TR}). Throat area changes were minor over the time interval of interest. For the subject configuration/operating conditions, f_{TR} was estimated to be 1.002.

Throat Discharge Coefficient (f_{DIS}). For all experiments, the throat discharge coefficient was estimated to be 0.991.

Frictional Drag Correction (f_{FR}). For the subject test conditions, f_{FR} was estimated to be 1.0036.

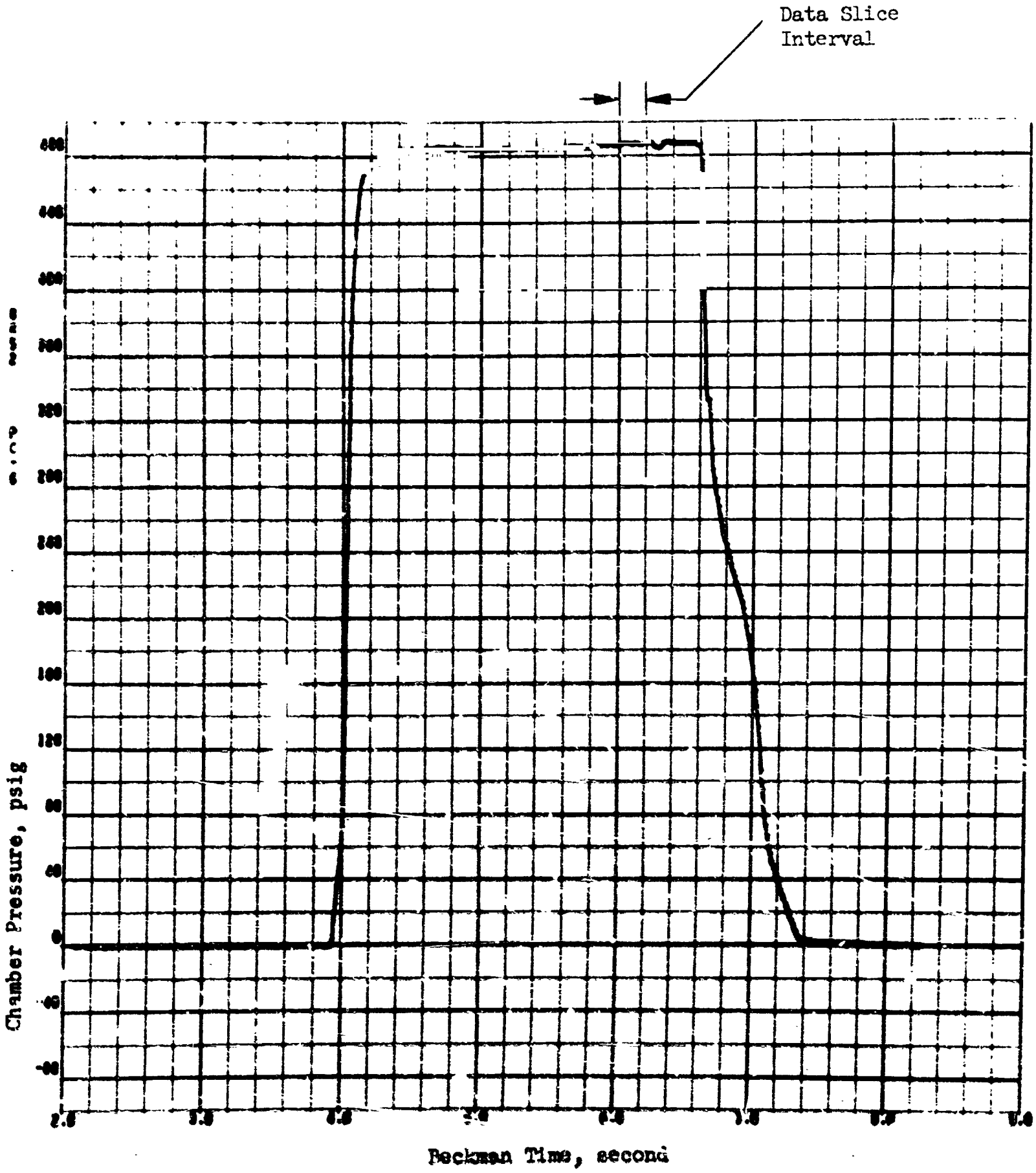

Figure E-2. Static Chamber Pressure (at Position No. 6) as a Function of Beckman Time for Test No. 17

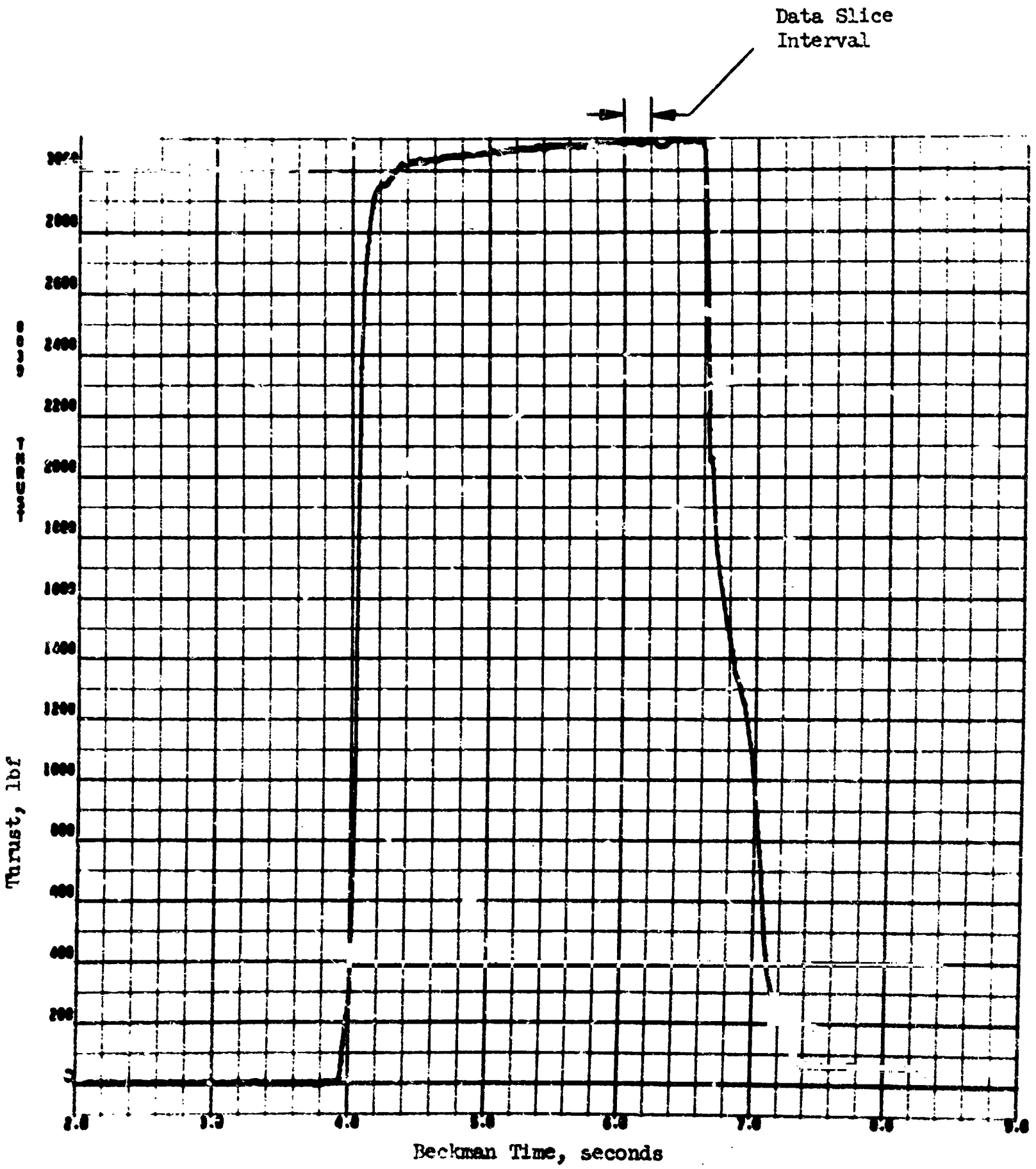

Figure E-3. Measured Site Thrust as a Function of Beckman Time for Test No. 17

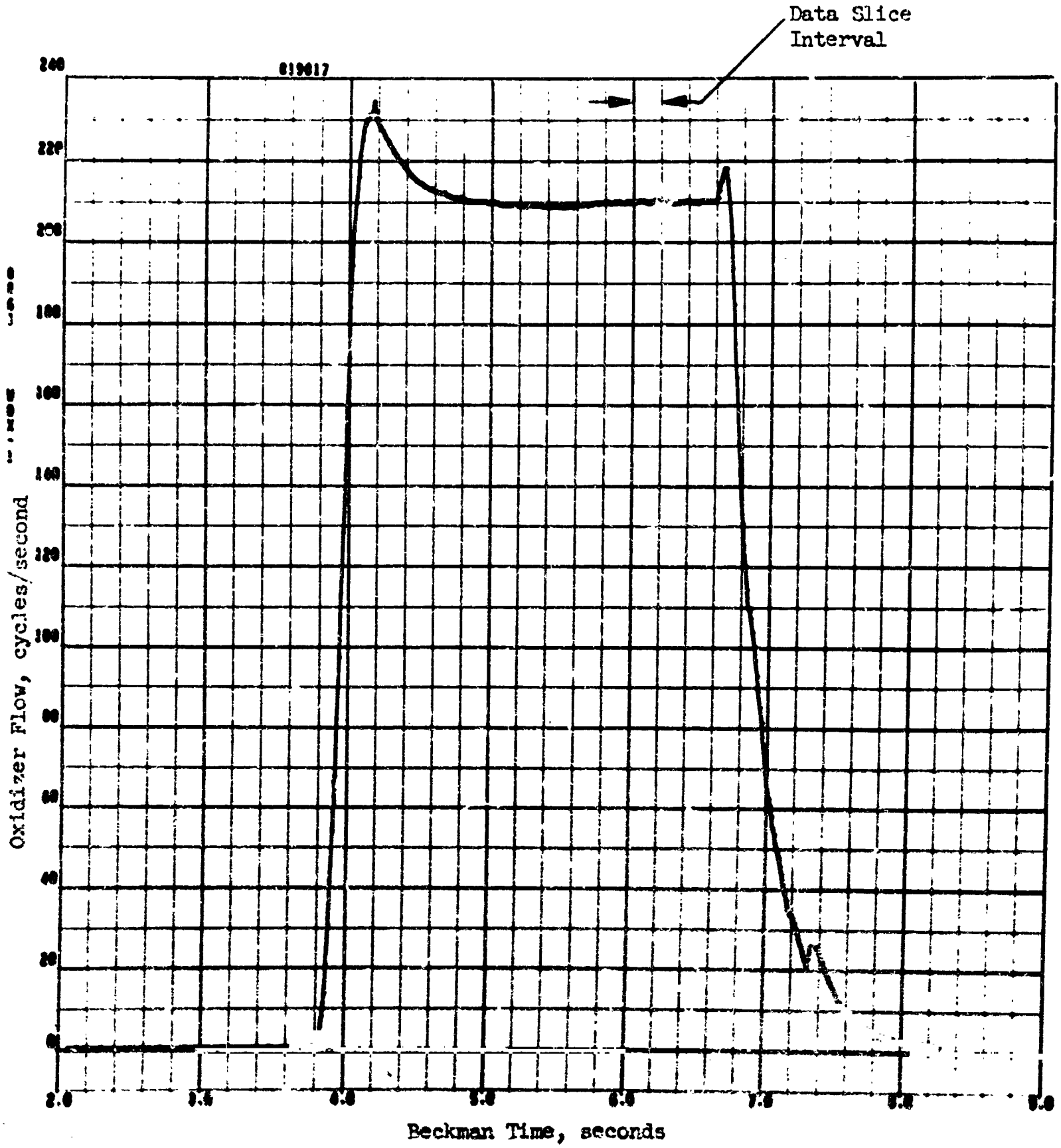

Figure E-4. Oxidizer Flowrate (No. 1 Meter, Cycles/Second) as a Function of Beckman Time for Test No. 17

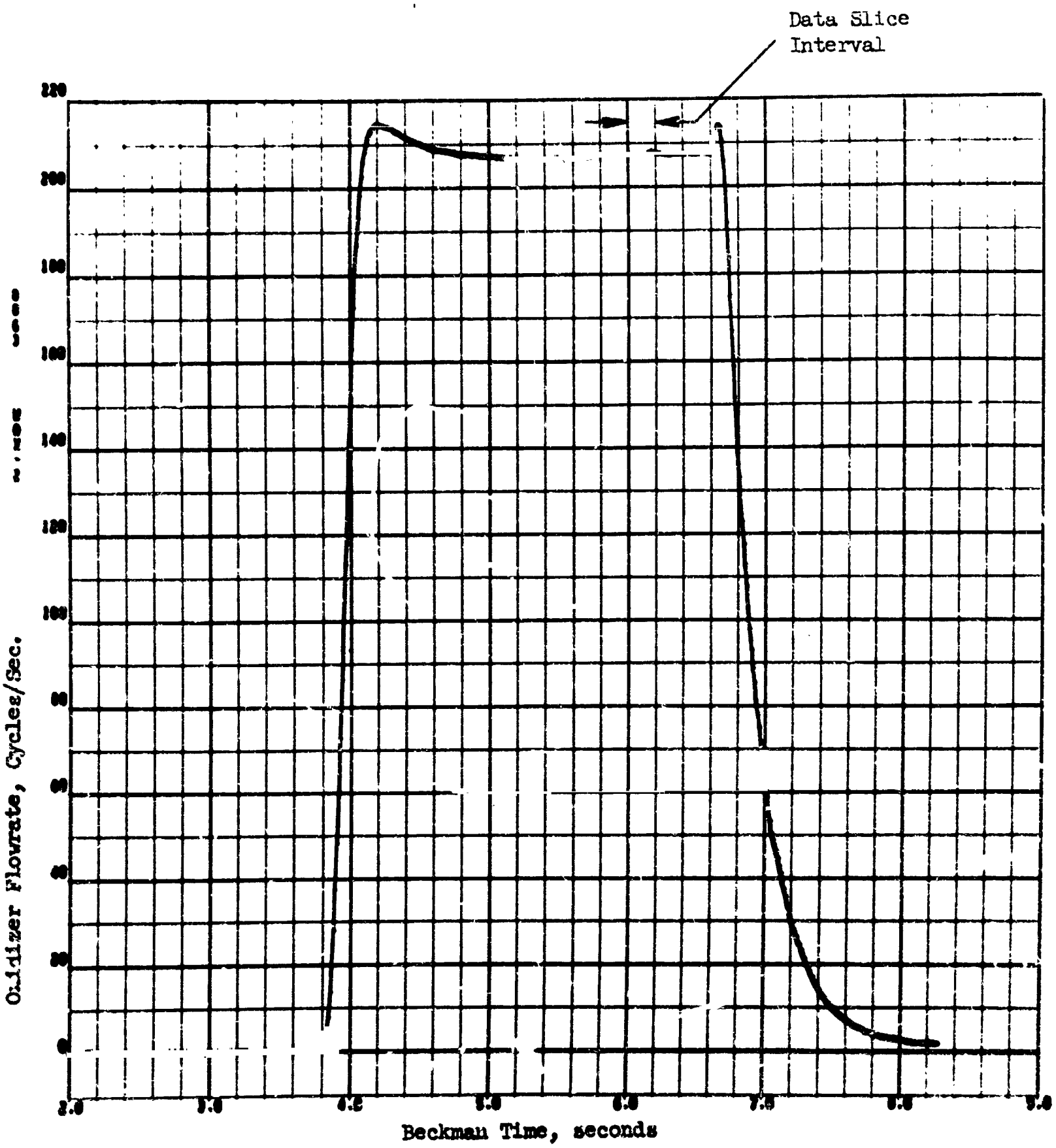

Figure B-5. Oxidizer Flowrate (No. 2 Meter, Cycles/Second) as a Function of Time for Test No. 17

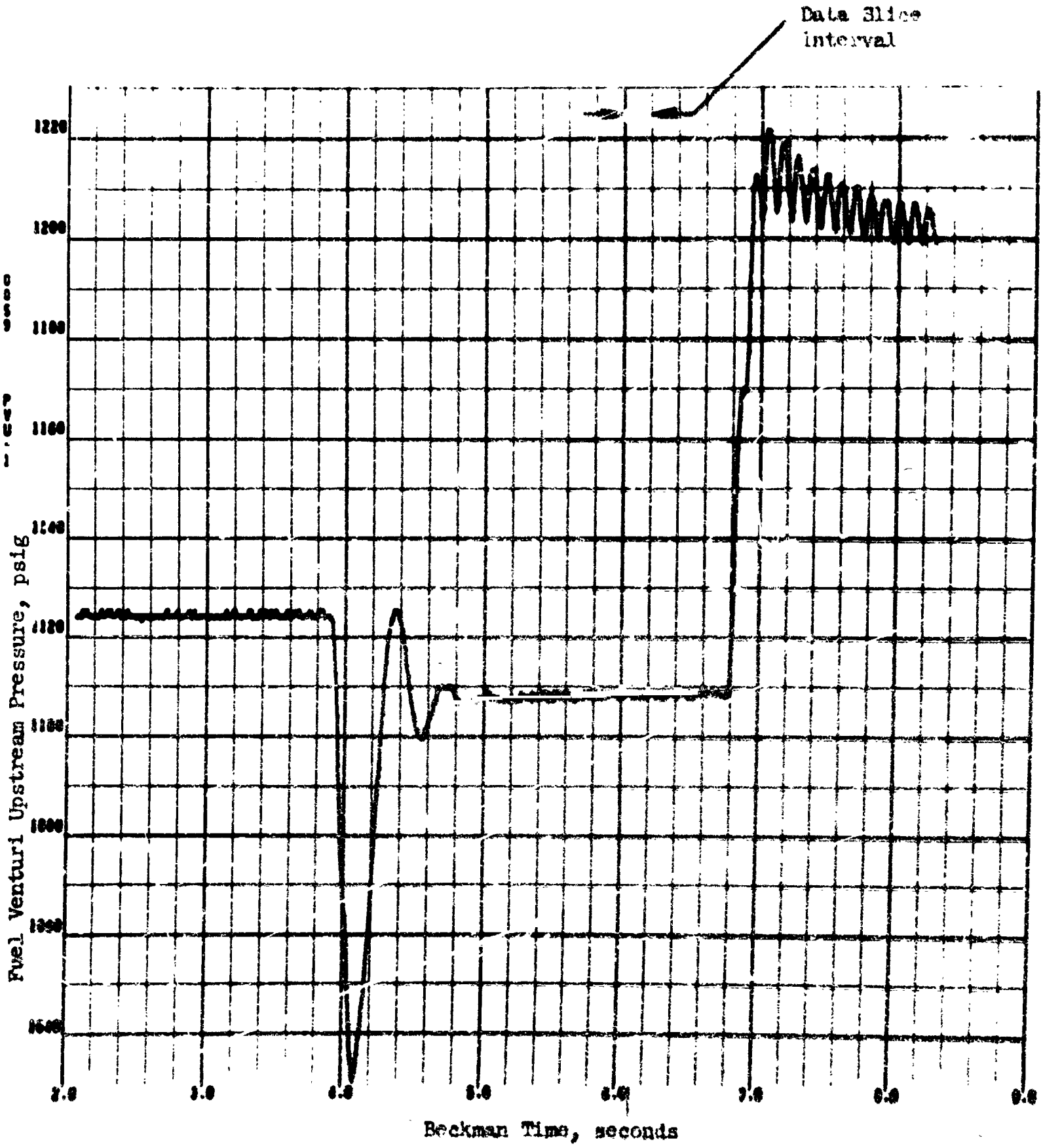

Figure E-6. Upstream Venturi Pressure (Fuel) as a Function of Beckman Time for Test No. 17

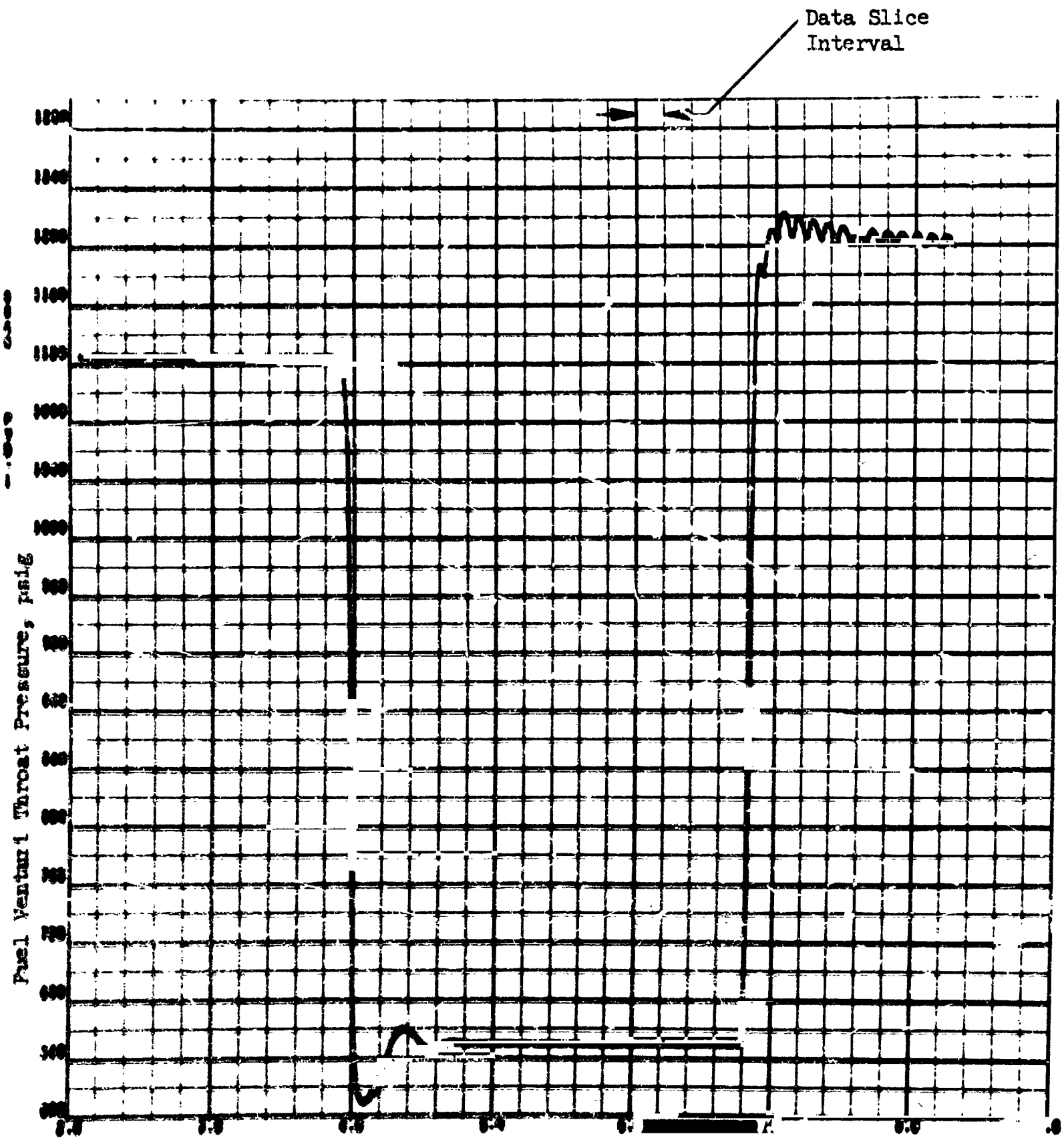

Figure E-7. Venturi Throat Pressure (Fuel) as a Function of Beckman Time for Test No. 17

TABLE E-1. DATA FROM TEST NO. 17

Static Chamber Pressure ①	(484.57 + 480.63 + 491.88 + 485.46)/4 = 485.6 psig = 509.4 psia
Oxidizer Flowrate ②	(7.926 + 7.895)/2 = 7.911 lbm/sec
Fuel Flowrate ②	1.471 lbm/sec
Throat Area ④	3.960 in.
Mixture Ratio	5.38
c* Theoretical	7139 ft/sec
$(C_V)_{VAC}$	1.6746

① Average value of two rows of pressure taps 180 degrees apart

② Value is average of two turbine flowmeters in series

③ Calculated from calibrated sonic venturi pressure measurements

④ Measured with hardware at ambient temperatures (≈75 F)

Heat Loss Correction (f_{HL}). The heat loss correction was estimated from the measured performance and observed chamber heat flux values by use of Eq. E-5. Terms in Eq. E-5 were calculated and defined as follows:

c^*_{theo} = theoretical characteristic velocity at test conditions (based on full shifting equilibrium) = 7139 ft/sec

c^*_{meas} = measured characteristic velocity (corrected for the previously determined losses

$$= \frac{P_c \, A_t \, f_p \, g_c \, f_{TR} \, f_{DIS} \, f_{FR}}{\dot{w}_T}$$

= 6958 ft/sec

T_c = 8142 R

c_{p_m} = 0.431 Btu/lbm R

$\dot{w}_T$ = 9.382 lbm/sec

$\Sigma(\dot{q}/A)(A)$ = heat losses to the chamber wall

= 399.2 Btu/sec (see Fig. 63 for $\dot{q}/A$ profile)

The heat loss correction factor, f_{HL}, for this test is calculated below:

$$f_{HL} = \left\{ 1 + \left[\frac{c^*_{theo}}{c^*_{meas}} \right]^2 \left[\frac{\Sigma(\dot{q}/A) \cdot (A)}{\dot{w}_T \cdot c_{p_m} \cdot T_c} \right] \right\}^{1/2}$$

$$f_{HL} = \left\{ 1 + \left[\frac{7139.0}{6958.0} \right]^2 \left[\frac{399.2}{9.382 \times 0.431 \times 8142} \right] \right\}^{1/2}$$

$$f_{HL} = \left[1.0128 \right]^{1/2} \approx 1.007$$

B

Equation E-2 with the appropriate numerical values shown is presented below for test No. 17:

$$(\eta_{c^*})_{P_c} = \frac{P_c\, A_t\, g_c\, f_p\, f_{TR}\, f_{DIS}\, f_{FR}\, f_{HL}}{(\dot{w}_o + \dot{w}_f)\ (c^*)_{theo}}$$

$$(\eta_{c^*})_{P_c} = \frac{(509.39)(3.960)(32.174)(1.026)(1.002)(0.991)(1.0036)(1.007)}{(7.911 + 1.471)\ (7139.0)}$$

$$(\eta_{c^*})_{P_c} = 97.8\%$$

Thus, for test No. 17, corrected c* efficiency based on chamber pressure was 97.8 percent.

Performance Based on Thrust

Corrected c* efficiency based on thrust measurement was calculated using Eq. E-7. Initially, vacuum thrust was calculated from the measured thrust, ambient pressure, and nozzle exit area as follows:

$$F_{vac} = F_{meas} + P_a\, A_e = 3024.6 + (13.7)\ (20.99) = 3312.0 \text{ lbf}$$

This was necessary because the corrections to be applied were calculated as changes in efficiency based on theoretical vacuum parameters.

Methods of estimation for the correction factors to be applied to the vacuum thrust in the calculation of c* efficiency were presented previously. Estimation of the values used for test No. 17 are described below in the following paragraphs.

Corrections for Fractional Drag (ϕ_{FR}). For the subject test conditions ϕ_{FR} was estimated to be 1.015.

Nozzle Divergence Correction (ϕ_{DIV}). For all experiments, the nozzle divergence losses were estimated to be 1.8 percent (i.e., $\phi_{DIV} = 1.018$).

Heat Loss Correction (ϕ_{HL}). As was the case for the heat loss correction factor for performance based on chamber pressure, (f_{HL}), the heat loss correction factor was estimated using Eq. E-5. For this case, however, the measured c* is based on thrust and total chamber heat losses are employed (i.e., heat losses are summed from injector face to nozzle exit). Terms in Eq. E-5 were calculated and defined as follows:

c^*_{theo} = 7139.0

T_c = 8142 R

c_{p_m} = 0.431 Btu/lbm-R

$\dot{w}_T$ = 9.382 lbm/sec

$(C_F)_{vac}$ = 1.6746

$$c^*_{meas} = \frac{F_{vac}\, g_c\, \phi_{FR}\, \phi_{DIV}}{(C_F)_{vac}\, \dot{w}_T}$$

$$= \frac{(3312)\ (32.174)\ (1.015)\ (1.018)}{(1.6746)\ (9.382)}$$

= 7008.1 ft/sec

$\Sigma(\dot{q}/A)(A)$ = heat losses to the chamber wall between the injector face and nozzle exit

= 504.6 Btu/sec (see Fig. 63 for $\dot{q}/A$ profile)

The heat loss correction factor, ϕ_{HL}, was calculated as follows:

$$\phi_{HL} = \left\{ 1 + \left[\frac{c^*_{theo}}{c^*_{meas}} \right]^2 \left[\frac{\Sigma(\dot{q}/A)\ (A)}{\dot{w}_T \cdot c_{p_m} \cdot T_c} \right] \right\}^{1/2}$$

$$= \left\{ 1 + \left[\frac{7139}{7008.1} \right]^2 \left[\frac{504.6}{9.382 \times 0.431 \times 8142} \right] \right\}^{1/2}$$

$$= \left[1.015 \right]^{1/2} \approx 1.008$$

Equation, E-7 with the appropriate numerical values shown, is presented below for test No. 17:

$$(\eta_{c^*})_F = \frac{(F + P_a A_e)\, g_c\, \phi_{FR}\, \phi_{DIV}\, \phi_{HL}}{(C_F)_{vac}\ (\dot{w}_o + \dot{w}_f)\ (c^*)_{theo}}$$

$$(\eta_{c^*})_F = \frac{(3312)\ (32.174)\ (1.015)\ (1.018)\ (1.008)}{(1.6746)\ (9.382)\ (7139)}$$

$(\eta_{c^*})_F$ = 98.9 %

Thus, corrected c* efficiency (based on thrust) for this test was 98.9 percent as compared to 97.8 percent based on chamber pressure measurements.

REFERENCES

E-1. LAP 68-411 (RC), Static Pressure Measurement for Contract NAS8-1229 Combustion Chamber, Rocketdyne, a Division of North American Rockwell Corporation, 19 August 1968.

E-2. Falk, A. Y., et al., NASA CR-72487, Space Storable Propellant Performance Study, Final Report, Rocketdyne, a Division of North American Rockwell, Canoga Park, California, November 1968.

E-3. Carter, W. A., NASA CR-72708, Gas-Liquid Space Storable Propellant Performance, TRW Systems Group, Redondo Beach, California, June 1970.

E-4. Arbit, H. A., and S. D. Clapp, Fluorine-Hydrogen Performance Evaluation. Part I: Analysis, Design, and Demonstration of High-Performance Injectors for the Liquid Fluorine-Gaseous Hydrogen Propellant Combination, Research Report No. 66-10, Rocketdyne, a Division of North American Rockwell Corporation, Canoga Park, California, April 1966.

E-5. Chamber Technology for Space Storable Propellants - Task II, Prepared for for National Aeronautics and Space Administration, Contract NAS7-304, Report No. R-6028-2, Rocketdyne, a Division of North American Rockwell Corporation, Canoga Park, California, 13 October 1965.

E-6. Hauenstein, C. A., Alternate Throat Development Program for the Apollo Command Module Reaction Control Engines, Report No. R-5941, Rocketdyne, a Division of North American Aviation, Inc., Canoga Park, California, 16 November 1964.

APPENDIX F

HEAT TRANSFER DATA REDUCTION TECHNIQUE

Local values of chamber wall and injector face heat flux were determined by analysis of transient thermocouple data acquired during short duration firings (~3 seconds). The transient thermocouple data were reduced to equivalent heat flux values by assuming that the graphite chamber wall was a semi-infinite slab initially at a uniform temperature which is suddenly exposed to a constant heat flux. The expression for the resulting temperature distribution in the slab is given as (Ref. F-1):

$$T - T_o = 2 \frac{\dot{q}}{A} \left[\frac{\sqrt{\alpha\, \theta}}{k} \quad \text{ierfc} \quad \frac{x}{2\sqrt{\alpha\, \theta}} \right] \tag{F-1}$$

where

T_o = initial temperature of the slab

q/A = the local heat flux

α = the thermal diffusivity

k = the thermal conductivity

x = the distance from the surface, and

θ = the time

Rewriting Eq. F-1 yields

$$T - T_o = 2 \left(\frac{\dot{q}}{A}\right) \frac{\sqrt{\alpha\, \theta}}{k} \left[\frac{1}{\sqrt{\pi}} e^{-\frac{x^2}{4\alpha\theta}} - \frac{x}{2\sqrt{\alpha\theta}} + \left(\frac{x}{\sqrt{\alpha\theta}} \quad \text{erf} \frac{x}{\sqrt{\alpha\, \theta}} \right) \right] \tag{F-2}$$

The error function was expressed in terms of its infinite series, and the expression differentiated with respect to time. The resulting expression is closely approximated by the following:

$$\frac{\partial T}{\partial \theta} = \frac{\dot{q}}{A} \left[\frac{1}{k} \sqrt{\frac{\alpha}{\pi\theta}}\, e^{-\frac{x^2}{4\alpha\theta}} \right] \tag{F-3}$$

or

$$\frac{\dot{q}}{A} = \frac{\partial T / \partial \theta}{K_1}$$

where K_1 is a function of the physical properties of the wall, the location of the thermocouple, and the time.

By knowing the location of the thermocouple from the chamber wall and its thermal properties, the local value of heat flux was computed employing Eq. F-3 by utilizing the slope of the temperature-time output trace of the thermocouple.

As an example, Fig. F-1 shows the temperature time history for one thermocouple located 5 inches from the face of the full-scale injector for the experiment using 6.7 percent BLC flow (test No. 22). For the data slice at 6.2 seconds (Beckman time), Eq. F-3 yields a local heat flux value of 1.89 Btu/in.^{2}-sec.

Figure F-2 presents values for the thermal diffusivity and conductivity of ATJ graphite (Ref. F-2) as a function of temperature which were employed for calculation of local values of chamber wall heat flux.

REFERENCES

F-1. Carslaw, H. S., and J. C. Jaeger, Conduction of Heat in Solids, The Clarendon Press, Oxford, England, 1959, pp 75-77.

F-2. Lowrie, R., Research on Physical and Chemical Principals Affecting High Temperature Materials for Rocket Nozzles, National Carbon Co., Contract No. DA-30-069-ORD-2787, December 1963.

At Slice Point:

$$\frac{\partial T}{\partial \Theta} = 210\ ^\circ F/sec$$

$$\alpha = 0.048\ in.^2/sec$$

$$k = 0.00094\ BTU/in.\text{-}sec\text{-}^\circ R$$

$$X = 0.018\ in.$$

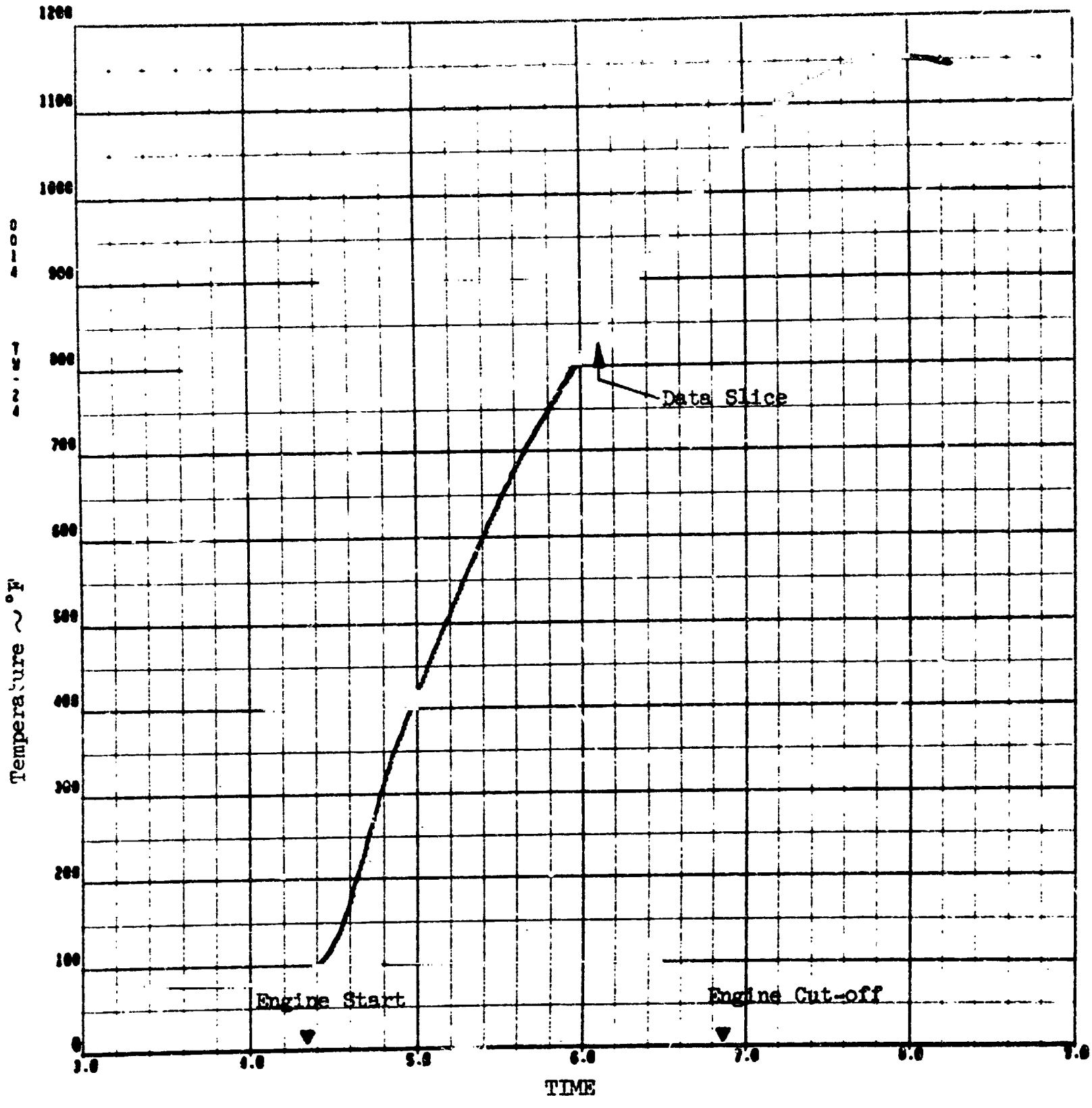

Figure F-1. Typical Temperature-Time History for Chamber Thermocouple

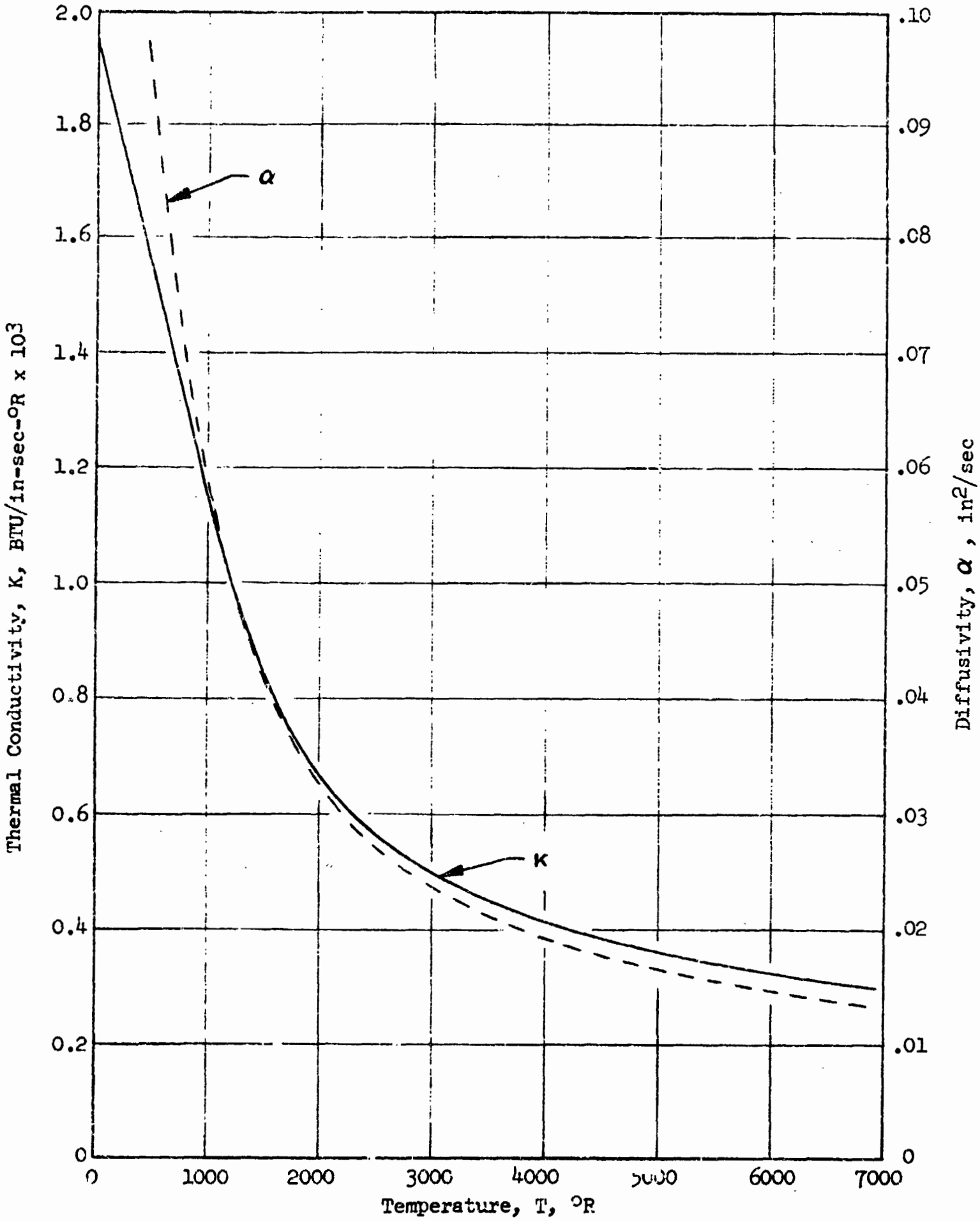

Figure F-2. Thermal Conductivity and Diffusivity as a Function of Temperature for ATJ Graphite

APPENDIX G

PHYSICAL PROPERTY AND THEORETICAL PERFORMANCE SUMMARY

The theoretical performance, combustion temperature, and physical properties of the propellants used for this program are presented in this appendix.

THEORETICAL PERFORMANCE

Theoretical performance of the liquid FLOX (82.6% F_2)/gaseous methane combination is presented in this section. Theoretical shifting equilibrium characteristic velocity (c*) is shown in Fig. G-1 as a function of mixture ratio and chamber pressure. The theoretical combustion temperature as a function of mixture ratio and chamber pressure are presented in Fig. G-2. These data were generated employing Rocketdyne's Propellant Performance Program.

PROPELLANT PROPERTY DATA

The physical properties of the propellants used for this program are tabulated in Tables G-1 and G-2. The density and vapor pressure of FLOX (82.6% F_2) are presented in Fig. G-3 and G-4, respectively. Figures G-5 and G-6 present values for methane for the specific heat ratio, γ, and the compressibility factor, Z, respectively. These property data, in conjunction with the venturi manufacturer's C_D calibration factors, were employed for the determination of methane fuel flowrates.

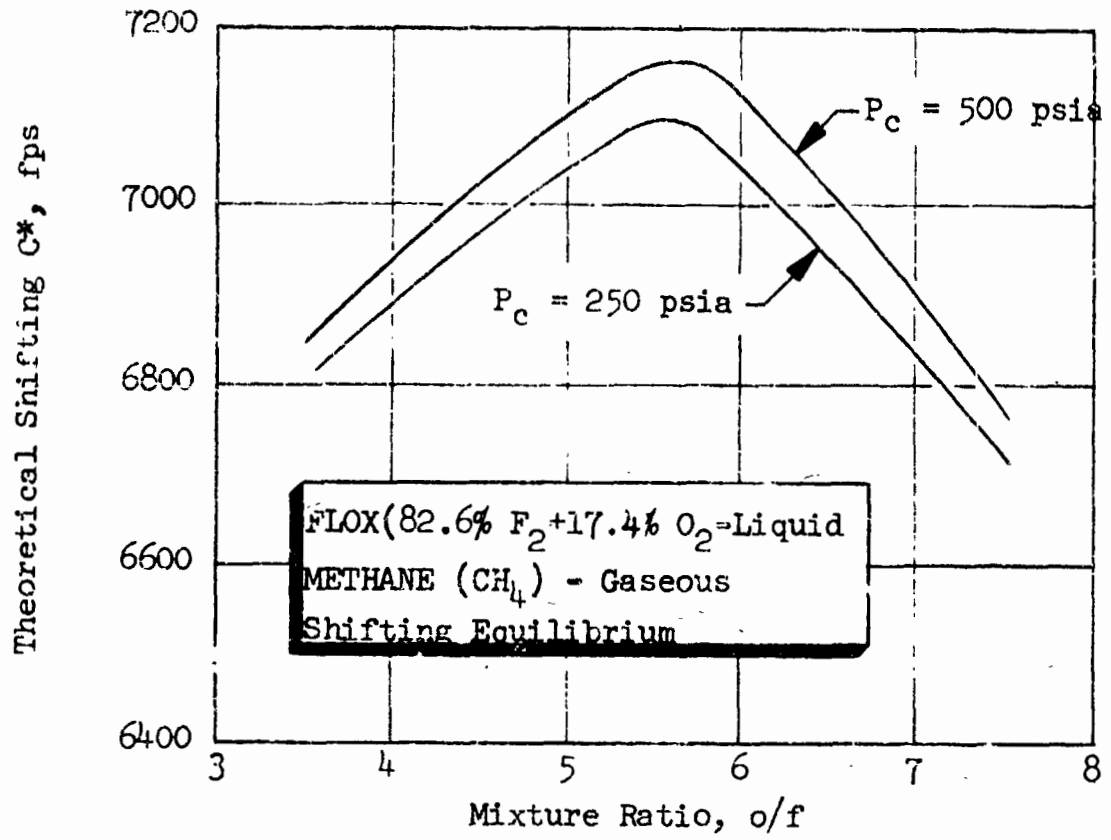

Figure G-1. Theoretical Combustion Temperature as a Function of Mixture Ratio and Chamber Pressure

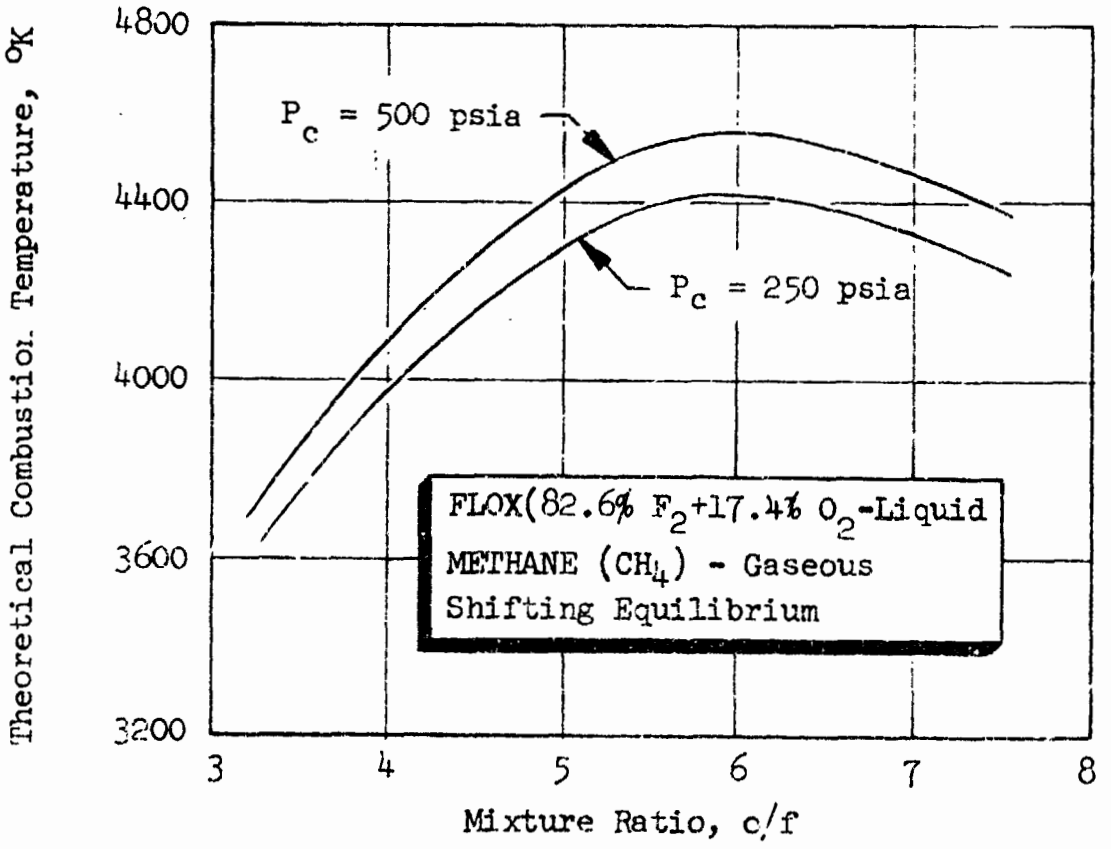

Figure G-2. Theoretical Combustion Temperature as a Function of Mixture Ratio and Chamber Pressure

TABLE G-1. FLOX PROPERTY SUMMARY

(Ref.: NASA SP-3037)

Chemical Formula	82.6% F_2 + 17.4 O_2
Normal Freezing Point, ^{o}R	--
Normal Boiling Point, ^{o}R	154^{o}R
Liquid Density at NBP, lb/ft^3	91
Critical Temperature, ^{o}R	--
Critical Temperature, ^{o}R	--
Critical Pressure, psia	--
Critical Volume, ft^3/lb	--
ΔH (vaporization) at NBP, Btu/lb	74.5
ΔH (fusion), Btu/lb	--
Viscosity at NBP, $lb/(sec)(ft^2)$	5.0
Thermal Conductivity at NBP, Btu/ft-hr-^{o}R	0.090
Specific Heat at NBP, Btu/lb-^{o}R	0.372
Specific Heat, Gas at 60^{o}F	
C_p, Btu/lb-^{o}R	0.200
C_v, Btu/lb-^{o}R	
Ratio, C_p/C_v	
Viscosity at 60^{o}F, centipoise	0.0216
Viscosity, gas, 32^{o}F, 1 atm, centipoise	0.0203
Gas Constant, R, $ft\text{-}lb_f/lb_m\ ^{o}R$	40.8

TABLE G-2 METHANE PROPERTY SUMMARY

(Ref.: Pratt & Whitney Aircraft, PWA FR-1443)

Chemical Formula	CH_4
Molecular Weight	16.042
Normal Freezing Point, ^{o}R	163.2
Normal Boiling Point, ^{o}F	200.8
Liquid Density at NBP, lb/ft^3	26.48
Critical Temperature, ^{o}R	43.3
Critical Pressure, psia	673
Critical Volume, ft^3/lb	0.0989
ΔH (vaporization) at NBP, Btu/lb	219.22
ΔH (fusion), Btu/lb	25.25
Viscosity at NBP, lb/ft-sec	7.0×10^{-5}
Thermal Conductivity at NBP, Btu/ft-hr-^{o}R	0.1075
Specific Heat at NBP, Btu/lb-^{o}R	0.80
Specific Heat, Gas at 60^{o}F	
C_p, Btu/lb-^{o}R	0.5271
C_v, Btu/lb-^{o}R	0.4032
Ratio, C_p/C_v	1.307
Viscosity at 60^{o}F, centipoise	0.012
Viscosity, Gas, 32^{o}R, 1 atm, centipoise	0.009
Gas Constant, R, ft-lbf/lbm-^{o}R	96.31
Gas Density at 32^{o}F, 1 atm	0.045 lb/ft^3
70^{o}F, 1 atm	0.041
70^{o}F, 100 psia	0.285
70^{o}F, 500 psia	1.495
70^{o}F, 1000 psia	3.17
70^{o}F, 2000 psia	6.80*
70^{o}F, 4000 psia	11.77*
70^{o}F, 6000 psia	14.60*

*Calculated from theoretical compressibility curve.

(1) Thermodynamic Properties of Fluorine: Allied Chemical Corp., Jan. 1965

(2) Thermodynamic Data on Oxygen and Nitrogen ASD-TR-61-625 Wright-Patterson AFB, Sept. 1961

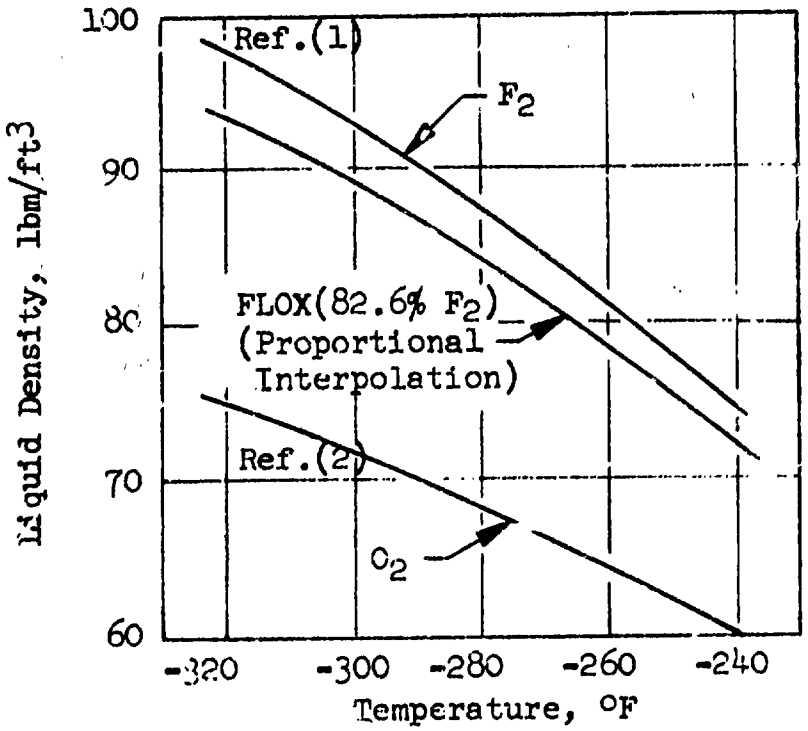

Figure G-3. Liquid Fluorine, Oxygen and FLOX Density as a Function of Temperature

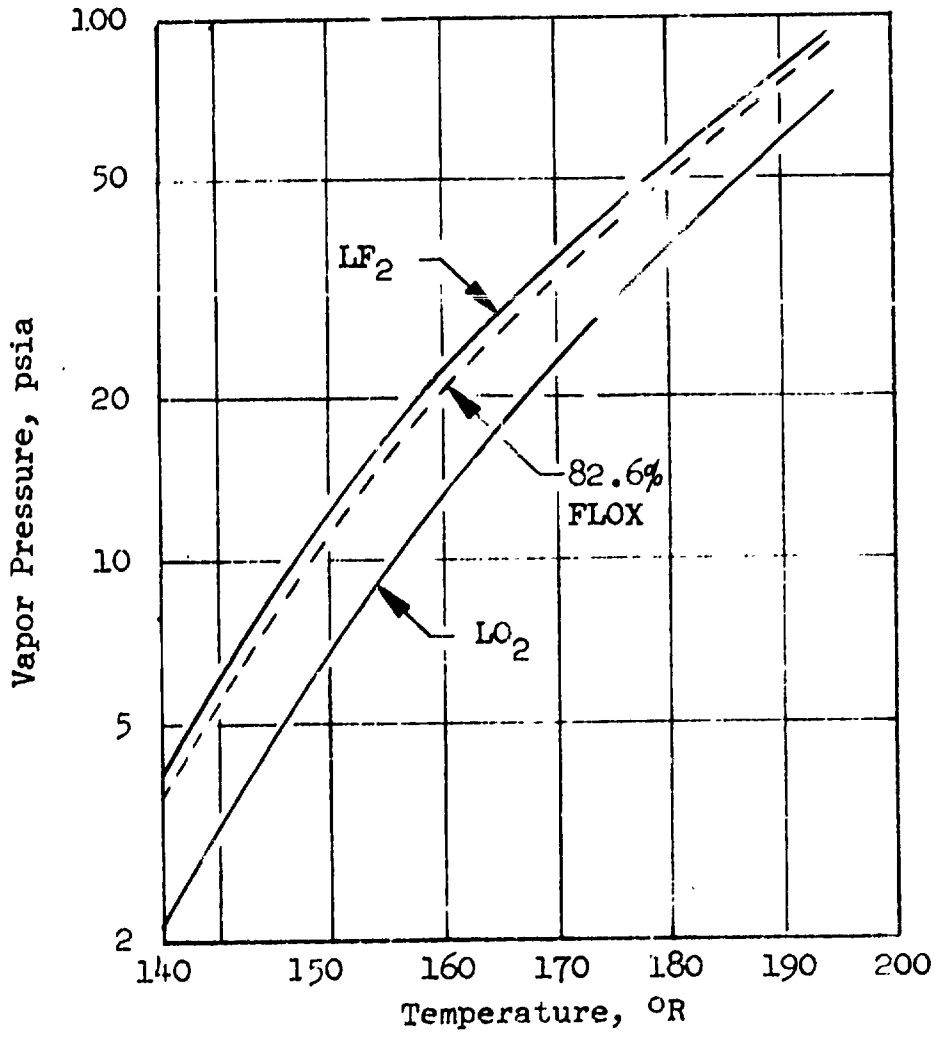

Figure G-4. Vapor Pressure of Liquid Fluorine, Oxygen and FLOX as a Function of Temperature

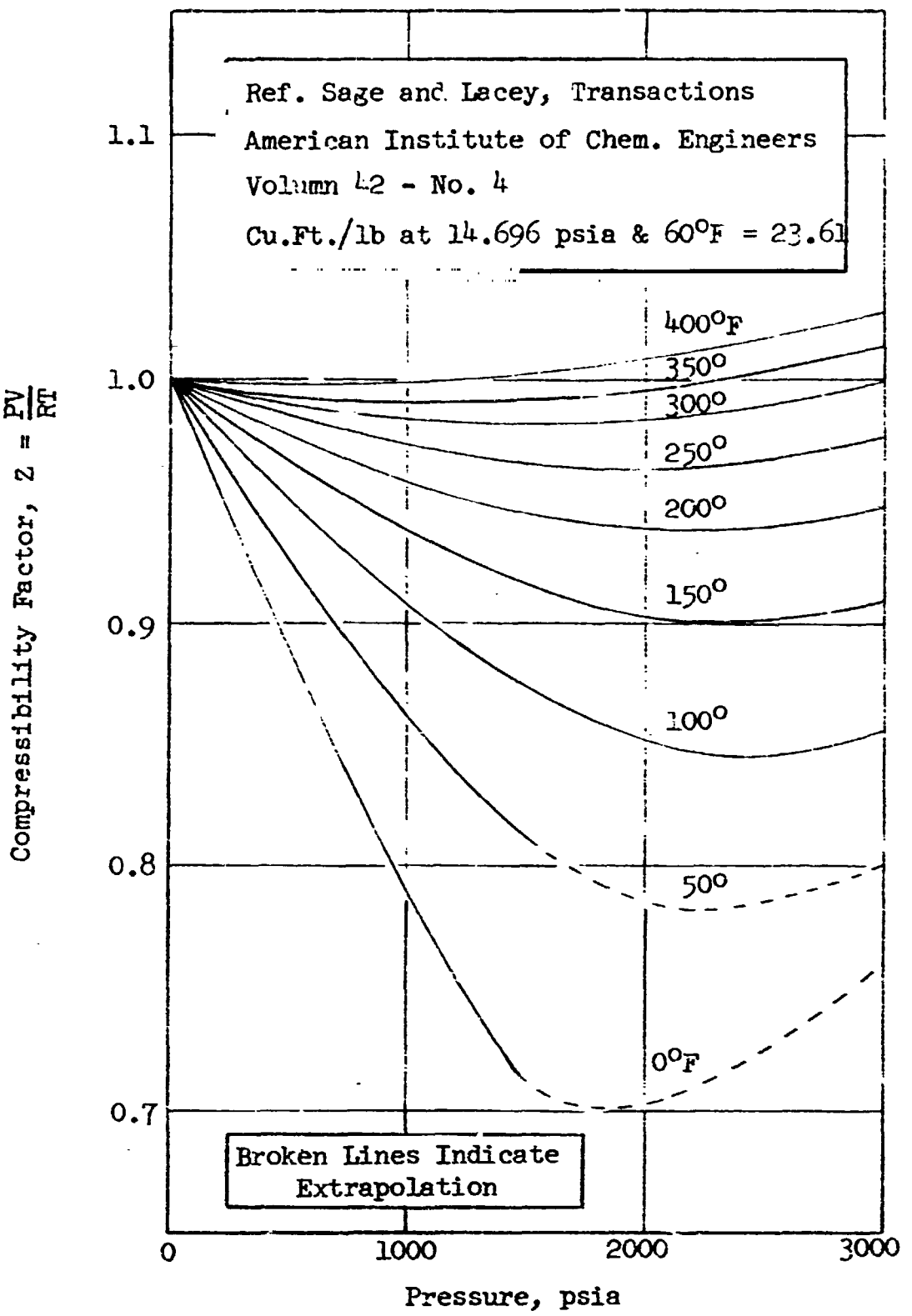

Figure G-5. Compressibility of Methane Gas as a Function of Temperature and Pressure

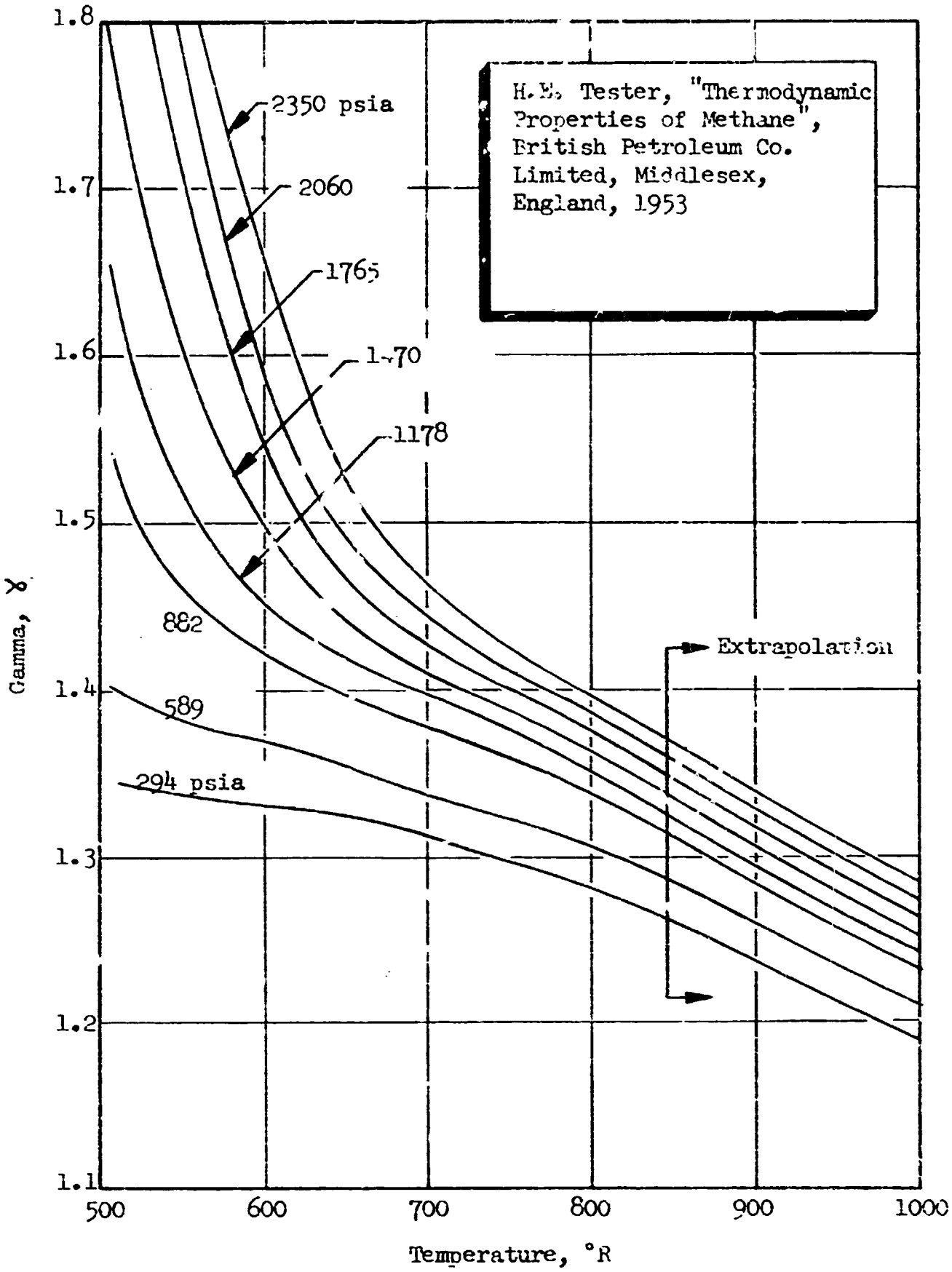

Figure G-6. Specific Heat Ratio of Methane Gas as a Function of Pressure and Temperature

APPENDIX H

PERFORMANCE DATA MEASUREMENT ERROR ANALYSIS

INTRODUCTION

Because it is not possible to measure the true value of any physical property or parameter, the error limits, or uncertainty interval associated with any experimental measurement should be specified. It is the purpose of this appendix to indicate the reliability of the experimental results of this program by estimation of the errors inherent in the data acquisition processes and/or in the calculation procedures. This will permit determination of the range within which, at a given confidence level, the true values of the measured or calculated parameters may be expected to fall.

If error is defined as departure of an experimental measurement from the "true" value, its magnitude can never be completely known; if it were known, it would become a correction which could be systematically applied. Hence, error limits can only be stated within probability limits. Performance data (c* efficiency) precision was estimated by two separate methods, one based on static calibration of the individual transducers, and the other on analysis of repeated firings of the rocket engine.

In the present application, the data precision analysis based on static calibration of the individual transducers was made by an error analysis procedure which consisted of the following steps:

1. Estimation of the uncertainty intervals of the individual transducers, including the measuring systems in which they were used.
2. Combination of the uncertainty intervals of duplicate or redundant sensors into an uncertainty interval for the measurement.
3. Combination of the uncertainty intervals of several measurements (e.g., flowmeter frequency and propellant density) into an uncertainty interval for the parameter they determine (e.g., flowrate).
4. Combination of the uncertainty intervals of the parameters (e.g., chamber pressure, flowrate, and throat area) entering into calculation of the value of the desired variable (e.g., characteristic velocity efficiency) to estimate the uncertainty interval of the calculated result.

As noted above, the second method used to estimate the uncertainty (confidence) interval associated with the experimental determination of characteristic velocity efficiency was by analysis of data from repeated firings of the rocket motor. For this case, the test data were analyzed as a completely randomized design, by use of the analysis-of-variance technique.

Two types of errors are possible in any measurement:

1. Systematic Errors. These are associated with the particular system, with the experimental techniques employed, or with the calibration procedures. They cannot be estimated by statistical methods, and are minimized primarily by careful calibration with the best available standards, by requirements for consistency and traceability of the experimental and calibration techniques, and by critical examination of experimental data.

2. Random Errors. These arise from unpredictable and unknown variations in the experimental situation and are generally assumed to follow a normal distribution to permit simple statistical analysis. Error analysis is concerned only with random errors and implicitly assumes that systematic errors can be eliminated in a carefully conducted experimental program.

SENSOR PRECISION

A measurement analysis program (Random Walk measurement analysis program) is employed at Rocketdyne which uses transducer calibrations to provide appropriate factors for test data reduction. In addition, statistical histories for each transducer are developed so that estimates of short- and long-term deviations can be made and probably error bands calculated. This program is discussed in detail in Appendix I.

The precision of a measurement obtained as the output of a physical instrument or sensor is a quantitative estimate of the uncertainty associated with that measurement. (The word sensor means not only the transducer itself, but the complete system which converts the transducer signal to a numerical value of its physical parameter analog.) This estimate is made by statistical analysis of the outputs of the sensor when repeatedly acted upon by known inputs. The known inputs, of course, have uncertainty limits of their own but, for practical purposes, it is assumed that they are accurate (i.e., identical to true values) within the limits required by the experimental situation. Ultimately, these inputs must be directly traceable to established standards, such as those of the National Bureau of Standards.

When a sensor is calibrated against known inputs, precision may be considered as the certification of an error and within the calibrated interval and within a given confidence level. Thus, it provides a measure of "closeness to truth" of the reduced data. Precision may be numerically expressed as the standard deviation of a measurement, which has the same units as the measurement itself, or as the coefficient of variation (C_V), which permits valid comparisons between measurements in different units. It also permits valid comparisons to be made between large and small things. Coefficient of variation (C_V) is the standard deviation (σ) expressed as a percentage of the mean, thus making it dimensionless:

$$C_V = \frac{\sigma}{\mu} 100 \qquad \text{(H-1)}$$

where

σ = the standard deviation

μ = sample mean value

C_V = coefficient of variation

Pressure

The coefficients of variations of the pressure transducers were obtained by application of the Random Walk measurement analysis program to the calibration data. Chamber pressure values ranged from 0.25 to 0.53 percent for static calibrations made on a pressure manifold mounted on the thrust stand.

For all tests, redundant sensors were used to measure the chamber pressure. Two or three independent transducers were used to measure this important parameter in order to increase the measurement reliability.

Other errors in pressure measurement may arise in addition to the random statistical uncertainty limits. In measurement of chamber pressure through a drilled wall tap, as herein, erroneous values of stream pressure may be indicated because of the effect of the hole itself upon the flow. Estimated magnitudes of this error, which is a function of stream velocity, were based on experimental data obtained with water and gas (Ref. H-1). For the experimental situation herein, these errors are insignificant. Coupling errors, arising from effects of the tubing joining the pressure taps to the transducers were also insignificant in the present series of experiments (Ref. H-2). The locations of the pressure taps from which combustion chamber throat stagnation pressure (or performance) is calculated is quite critical. Procedures were followed to ensure that the proper static pressure measurement was employed. Thus, this source of error is assumed to be insignificant.

Thrust

Values of coefficient of variation obtained by application of the Random Walk measurement analysis program to thrust calibrations were in the 0.23- to 0.35-percent range. A possible source of error in thrust measurement arose from the necessity of taking system prerun zeros with the same degree of propellant line chill as existed during the firings. On the basis of thrust calibrations made with chilled and unchilled propellant lines, the above C_V values should be applicable. The coefficient of variation increase due to line chill variations between tests should (and is assumed to) be negligible.

Throat Area

Geometric throat diameter was measured with an expansion micrometer prior to, and following, each firing. The maximum coefficient of variation of the calculated areas was 0.42 percent. Throat area variation during firing was observed to be small.

Volumetric Flowrate

The coefficients of variation of the turbine flowmeters used to measure the propellant flowrates were determined from flow-bench calibration data. Each meter was calibrated prior to the start, and at the end, of the program. The meters were calibrated with water. Redundant (two) flowmeters, in series, were placed

in the oxidizer line. A C_v value for the oxidizer flowmeter was 0.02. In addition, however, there are predictable water-to-cryogenic calibration shifts (Ref. H-3) which introduce additional sources of error. The coefficient of variation arising from this course is approximately 0.5 percent (Ref H-4).

Temperature

The platinum resistance thermometers (Rosemount bulbs) were precision calibrated by the manufacturer. These calibrations were checked by taking several emf readings with the sensors immersed in LN_2 and in LO_2 at atmospheric pressure; they were correct within the limits of readability. Root-sum-square (RSS) error limits of these sensors based on specifications of repeatability, insulation, time lag, friction heating, and interchangeability are approximately 0.1 percent (Ref. H-5). Voltage readout of the transducers was adjusted to calibration values by a standard decade resistance box with error limits of 0.2 percent.

COMBINED ERROR ESTIMATION

Redundant Measurements

Redundant transducers were used to measure the most important parameters in order to increase the measurement reliability. The most probable value of a redundant measurement is the weighted average. The variance of the weighted mean value, σ_m^2, is given by the following equation:

$$\frac{1}{\sigma_m^2} = \frac{1}{\sigma_1^2} + \frac{1}{\sigma_2^2} + \ldots + \frac{1}{\sigma_n^2} = \sum_{i=1}^{n} \frac{1}{\sigma_i^2} \qquad \text{(H-2)}$$

where

σ_m^2 = the variance of the weighted mean

σ_i^2 = the variance of the i^{th} measurement

Clearly, the variance of a weighted mean is less than any of the individual variances.

Combined Measurements

When several measured variables are combined algebraically to yield an experimental result, the standard deviation of the result, which takes into account the propagation of the individual error, is given by the following equation (Ref. H-6):

$$\sigma_R = \sqrt{\left[\frac{\partial R}{\partial X_1}\ \sigma_1\right]^2 + \left[\frac{\partial R}{\partial X_2}\ \sigma_2\right]^2 + \ldots + \left[\frac{\partial R}{\partial X_n}\ \sigma_m\right]^2} \qquad \text{(H-3)}$$

where

σ_R = the standard deviation of the calculated result

$X_1, X_2, \ldots, X_n$ = measured variables

$R = f(X_1, X_2, \ldots, X_n)$

$\sigma_1, \sigma_2, \ldots, \sigma_n$ = standard deviations of $X_1, X_2, \ldots, X_n$, respectively

When the individual measurements are combined by addition, and are independent, the standard deviation is given by Ref. H-6:

$$\sigma_R = \sqrt{\sigma_1^2 + \sigma_2^2 + \ldots + \sigma_n^2} \qquad \text{(H-4)}$$

DATA PRECISION

Static Calibration Precision Analysis

Characteristic velocity can be calculated by two methods, one based on chamber pressure (P_c) measurement and one on thrust (F) measurement, as given below:

$$c^* = \frac{(P_c)_o \, A_t g_c}{\dot{w}_t} \qquad \text{(H-5)}$$

or

$$c^* = \frac{F_{vac} \, g_c}{(C_F)_{vac} \, \dot{w}_t} \qquad \text{(H-6)}$$

where

c^* = characteristic velocity (calculated), ft/sec

$(P_c)_o$ = stagnation pressure at the throat, psia

A_t = measured geometric throat area, $in.^2$

g_c = conversion factor (32.174 lbm-ft/lbf-sec^2)

$\dot{w}_t$ = total propellant mass flowrate, lbm/sec

$(C_F)_{vac}$ = theoretical shifting thrust coefficient (vacuum)

F_{vac} = measured thrust corrected tc vacuum conditions by the equation: $F_{vac} = F + P_a A_e$, lbf

F = measured thrust, lbf

P_a = ambient pressure, psia

A_e = area of nozzle exit, $in.^2$

It should be noted that these expressions yield uncorrected characteristic velocity.

The standard deviation of the characteristic velocity based on both methods of calculation can be determined by application of Eq. H-3 to Eq. H-5 and H-6. The standard deviation of the uncorrected characteristic velocity (based on chamber pressure) is calculated as follows:

$$(\sigma_{c^*})_{P_c} = \sqrt{\left[\left(\frac{A_t\ g_c}{\dot{w}_t}\right)\sigma_{P_c}\right]^2 + \left[\left(\frac{(P_c)_o\ g_c}{\dot{w}_t}\right)\sigma_{A_t}\right]^2 + \left[\left(\frac{(P_c)_o\ g_c}{\dot{w}_t^{\,2}}\right)\sigma_{\dot{w}_t}\right]^2} \qquad \text{(H-7)}$$

The resulting expression for the standard deviation of the characteristic velocity, based on thrust, is:

$$(\sigma_{c^*})_F = \sqrt{\left[\left(\frac{g_c}{C_{F_{vac}}\ \dot{w}_t}\right)\sigma_{F_{vac}}\right]^2 + \left[\left(\frac{F_{vac}\ g_c}{C_{F_{vac}}\ \dot{w}_t^{\,2}}\right)\sigma_{\dot{w}_t}\right]} \qquad \text{(H-8)}$$

Substitution of numerical values into these expressions yield the resulting standard deviations. As far as random errors only are concerned, there was no significant difference in the estimated standard deviations based on chamber pressure or thrust. The standard deviation of the uncorrected characteristic velocity was approximately 35 ft/sec. This corresponds to a coefficient of variation of approximately 0.5 percent for the uncorrected c* efficiency. Therefore, the uncorrected c* efficiencies determined in the present program are estimated to have an error band of approximately ±1.0 percent at the 95-percent (2σ) confidence level).

Application of the corrections to measured uncorrected characteristic velocities could cause an increase in the error associated with corrected characteristic velocities. Assuming proper application of these corrections, however, the resulting characteristic velocity efficiencies reported herein are estimated to be within ±1.0 percent of the true value.

Calculation of approximate values for σ_{P_c}, σ_{A_t}, and $\sigma_{F_{vac}}$ for use in Eq. H-7 and H-8 are straightforward. Estimation of $\sigma_{\dot{w}_t}$ is more complicated and, therefore, is discussed briefly herein.

For the turbine flowmeter, the propellant mass flowrate ($\dot{w}_i$) is a function of the flowmeter frequency (f_i) and the propellant density (ρ_i):

$$\dot{w}_i = \dot{w}_i\ (f_i,\ \rho_i) \qquad \text{(H-9)}$$

In particular,

$$\dot{w}_i = (f_i)(\rho_i)(\text{flowmeter constant})_i \quad (K) \qquad \text{(H-10)}$$

where

f_i = flowmeter output frequency, cps $\equiv \chi_i$

ρ_i = propellant density, lbm/ft^3

$(\text{flowmeter constant})_i$ = flowmeter constant, gal/cycle

K = conversion factor = $(1/7.48)$ ft^3/gal

Therefore, the standard deviation of each meter's flowrate is given by

$$\rho_{\dot{w}_i} = \sqrt{\left(\frac{\partial \dot{w}_i}{\partial f_i}\ \sigma_{f_i}\right)^2 + \left(\frac{\partial w_i}{\partial \rho_i}\ \sigma_{\rho_i}\right)^2} \qquad \text{(H-11)}$$

or

$$\sigma_{\dot{w}_i} = \left[K(\rho_i)\ (\chi_i)\ (\sigma_{f_i})\right]^2 + \left[f_i\ (\chi_i)\ (\sigma_{\rho_i})\ K\right]^2$$

Actually, flowrate is a function of flowmeter frequency and propellant temperature (assuming no significant error in conversion of propellant temperature to equivalent density). Thus, Eq. H-11 may be written as follows:

$$\sigma_{\dot{w}_i} = \left[K(\rho_i)\ (\chi)_i\ (\sigma_{f_i})\right]^2 + \left[(f_i)\ (\chi)_i\ (\sigma_T)_i\ K\right]^2 \qquad \text{(H-12)}$$

Standard deviation is converted to coefficient of variation by use of Eq. H-1. The standard deviation of each propellant flowrate is then determined by application of Eq. H-2 to the redundant measurements. The coefficient of variation of the total propellant flowrate may be obtained from the coefficients of variation of its component parts by use of the following equation:

$$(C_v)_{\dot{w}_t} = \sqrt{\frac{r^2 (C_v)^2_{\dot{w}_o} + (C_v)^2_{\dot{w}_f}}{(r+1)^2}} \qquad \text{(H-13)}$$

where

r = mixture ratio = $\dot{w}_o/\dot{w}_f$

The standard deviation of the total propellant flowrate can then be obtained from Eq. H-1.

Dynamic Precision Analysis

The estimates of expected standard deviations in characteristic velocity calculated above are based on static calibrations of pressure/thrust sensors and, hence, may not be strictly applicable to the dynamic system represented by a firing

rocket motor. It is generally assumed, however, that such calibration data may be extended without significant change to dynamic systems oscillating at very low frequencies and amplitudes and that steady-state stable combustion is such a system.

An indication of the possible magnitude of the uncertainty interval associated with the experimental determination of characteristic velocity efficiency may be obtained by analysis of repeated firings of a rocket motor with the same set of transducers. If systematic errors are assumed to be insignificant, variations from indicated "correct" values (i.e., those which are on the best curve through the experimental points) may be ascribed to random errors and hence are subject to statistical analysis. The usefulness of such an analysis is a direct function of the number of data points used to obtain the correct or average values. With only three or four data points available for determination of efficiency at a given condition, statistical calculation of measurement reliability has no great absolute value but may be used for comparisons with those estimated from transducer calibrations.

During this program, several different test conditions were duplicated. These test data were analyzed as a completely randomized design (Ref. H-7) by use of the analysis of variance technique. (This is, perhaps, the most powerful and widely used statistical technique.) On the basis of this analysis, the experimental c* efficiencies determined in the present program are estimated to have an error band of approximately ±1.0 percent at the 95-percent confidence level.

SUMMARY

Both methods of estimation of the performance data precision indicates that the experimental c* efficiencies determined in the present program have an error band of approximately ±1.0 percent at the 95-percent (2σ) confidence level. Of course, both of these estimates are based on the assumption that the corrections applied to the uncorrected c* efficiencies (Appendix E) are valid.

REFERENCES

H-1. Dean, R. C., Jr., Aerodynamic Measurements, Gas Turbine Laboratory Massachusetts Institute of Technology, Cambridge, Massachusetts, 1953.

H-2. Thomson, D. B., The Effect of Tubing on Dynamic Pressure Recording, TN-61-3, Rocketdyne, a division of North American Rockwell, Canoga Park, California, 28 February 1961.

H-3. Bucknell, R. L., "Calibration Systems and Turbine-Type Flow Transducers for Cryogenic Flow Measurements," Advances in Cryogenic Engineering, Vol. 8, Plenum Press, New York, 1963, pp 360-369.

H-4. Alspach, W. J., and T. M. Flynn, "Considerations When Using Tubine-Type Flowmeters in Cryogenic Service," Advances in Cryogenic Engineering, Vol. 10, Plenum Press, New York, 1965, pp 246-252.

H-5. Research Report No. 66-10, Fluorine-Hydrogen Performance Evaluation. Part I: Analysis, Design, and Demonstration of High-Performance Injectors for the Liquid Fluorine-Gaseous Hydrogen Propellant Combination, Arbit, H. A. and Clapp, S. D., Rocketdyne, a division of North American Rockwell, Canoga Park, California, April 1966.

H-6. Arkin, H. and Colton, R.R., Statistical Methods, Barnes and Nobel, Inc., N.Y.

H-7. Ostle, B., Statistics in Research, The Iowa State College Press, Ames, Iowa.

APPENDIX I

RANDOM WALK MEASUREMENT ANALYSIS PROGRAM

INTRODUCTION

The primary purpose of a sensor measurement analysis program is to provide a function which relates observed sensor outputs to estimates of corresponding system inputs, together with quantitative indications of the precision of this conversion. The function and the precision estimates are established on the basis of sensor calibration history, that is, upon a sequence of periodic calibrations of the sensor and its associated measuring and recording system against known inputs.

Because calibrations must of necessity be made at a time differing from the actual firing time by several hours to several days, the changes in random sensor error with time must be established. In the Random Walk measurement analysis program (Ref. I-1) this is accomplished by assuming that the input-to-output ratio at a particular input level performs a random walk in time which has normal distribution and variance. It assumes also that there is a random measurement error in the observed datum which is independent of the random walk and which is also normally distributed. Mathematical foundations and development of the program are given in Ref. I-2 and I-3.

On the basis of a sequence of periodic calibrations, the Random Walk program provides the following:

1. A function, either linear or cubic, which converts observed system outputs into estimates of true system inputs;
2. Coefficients of short-term and random walk variations, as well as a combined value valid at specified times; and
3. A decision, based upon the calculated coefficient of variation and a prespecified imprecision limit, as to whether the sensor should be used as is, recalibrated immediately, or discarded, and the maximum allowable interval to next calibration.

MEASUREMENT PROGRAM OUTPUT

A typical Random Walk computer program output is shown in Fig. I-1. The first line of output gives the test stand name and number (Willie, 0019), recording system (Beckman), transducer serial number (651705), ID number for data cards (01 0), and the physical parameter being calibrated (P_c-4).

The next set of numbers ("Latest Output") is the most recent raw calibration data. On the left are the readings (in Beckman counts) for the listed calibration input steps ("Input"); on the right are the precalibrate throw zero (Z1), the calibrate throw reading (CT), the postthrow zero (Z2), the precalibration zero (Z3), the postcalibration zero (Z4), and the date of calibration ("Time").

WILLIE BKM 651705 900 019050 PC4

LATEST OUTPUT																Z1	CT	Z2	Z3	Z4	TIME
498		1246		1998		2740		3484								124	3078	124	124	124	12-23-69
Y(1)	X(1)	Y(2)	X(2)	Y(3)	X(3)	Y(4)	X(4)	Y(5)	X(5)	Y(6)	X(6)	Y(7)	X(7)	TIME							
100.0	0.1266	300.0	0.3798	500.0	0.6344	700.0	0.8856	900.0	1.1374					12-23-69							
100.0	0.1255	300.0	0.3789	500.0	0.6329	700.0	0.8850	900.0	1.1367					12-15-69							
100.0	0.1259	300.0	0.3790	500.0	0.6335	700.0	0.8846	900.0	1.1360					12-15-69							
100.0	0.1269	300.0	0.3794	500.0	0.6345	700.0	0.8853	900.0	1.1371					12-15-69							
100.0	0.1266	300.0	0.3794	500.0	0.6332	700.0	0.8846	900.0	1.1371					12-15-69							

SHORT TERM COEFFICIENT OF VARIATION (PRECISION) = 2.54461E-01 PERCENT
RANDOM COEFFICIENT OF VARIATION = 2.52085E-02 PERCENT/DAY
OFFSET COEFFICIENT OF VARIATION = 7.13511E-02 PERCENT
COEFFICIENT OF VARIATION REQUIRED FOR SYSTEM = 1.500000E 00 PERCENT
COEFFICIENT OF VARIATION REQUIRED FOR DATA REDUCTION MODEL = 1.500000E 00 PERCENT

DATA REDUCTION MODEL(1) IS Y = (7.9101E 02)*X
COEFFICIENT OF VARIATION OF MODEL(1) = 1.5834E-01 PERCENT
STANDARD DEVIATION OF MODEL(1) = 7.9171D-01
DEGREES OF FREEDOM OF MODEL(1) = 23

DATA REDUCTION MODEL(2) IS Y = (-4.0926E-01) + (7.9150E 02)*X
COEFFICIENT OF VARIATION OF MODEL(2) = 1.5611E-01 PERCENT
STANDARD DEVIATION OF MODEL(2) = 7.8054D-01
DEGREES OF FREEDOM OF MODEL(2) = 22

SYSTEM SHOULD BE CALIBRATED ON OR BEFORE 1-22-70

Figure 1-1. Typical Random Walk Computer Output

The first two zeros (Z1 and Z2) are averaged and subtracted from the throw to obtain a reduced throw. For each calibration step, a linear interpolation is made between the last two zeros (Z3 and Z4) and the interpolated result is subtracted from the reading to obtain a reduced reading. Each reduced reading is then divided by the reduced throw to obtain a scaled output. All scaled output values from all calibrations in the system history are then listed ("Scaled Output") under the appropriate input pressures, with one calibration per line and its date ("Time") listed at the right of each line.

The first three lines following the scaled output table are estimates of the measurement variance (σ_m^2) in the input-to-scaled output ratio, the random walk variance (σ^2) in the input-to-scaled output ratio, and the ratio (k) of the former (short-term) variance to the latter (long-term) variance. The variances (σ_m^2 and σ^2) are used in computing the data reduction imprecision, which is defined as the standard deviation of an estimated input about the true input.

The next line of output gives the coefficient of short-term variation, which is the standard deviation (σ_m) expressed as a percentage of the average input-to-scaled output ratio. This quantity is generally the largest component of data reduction imprecision. The following entry gives the coefficient of random walk (long-term) variation, which is the standard deviation (σ) also expressed as a percentage of the average input-to-scaled output ratio. This item is meaningful only after calibrations are obtained over a period of time. The final listing in this block is the prespecified maximum limit of data reduction imprecision expressed as coefficient of variation.

The program now calculates revised scaled output values corresponding to the state of the system at the time of the most recent calibration. These values are then fit by least squares with either a linear or cubic function by the following procedure. The null hypothesis is that the function is linear, and the specified error (the probability that a truly linear function is mistakenly concluded to be nonlinear) is printed out. If the linearity hypothesis is rejected, a cubic fit is made. In either case, the formula for converting scaled outputs to estimated inputs is then given, and, if the relationship is cubic, an input-output table is printed out for convenience in data reduction.

The next line gives the result of the second test, which checks whether or not the input-output model is consistent with the estimate of σ_m (the root-mean-square estimate for the calibration curve fit and $_m$ should be approximately equal). If it is, then the model is labeled "SATISFACTORY"; if not, the model is labeled "UNSATISFACTORY," indicating a significant intercept or an error in the input data.

The following item indicates the ability of the system to meet the specified imprecision requirement. On the basis of the calibration data, three situations are recognized:

1. The system can never meet required precision, and should be replaced
2. The system will fail the requirement within the next two days and should be recalibrated immediately

3. The system will meet the requirement up to a certain date (30 days maximum), on or before which it should be recalibrated. In this case, the estimated data reduction imprecision is given for test data taken two days after the most recent calibration and on the specified recalibration date.

In the present program, the system transducers were calibrated weekly, regardless of the leeway allowed by reason of little or no random walk variation and consequent minimum degradation in precision.

The final item is a 2 by 2 matrix, denoted by R, which is used to estimate data reduction imprecision at any other time of interest and for any scaled output by the following expression:

$$P = \left[V + s^2 \left(h\sigma^2 + \sigma_m^2\right)\right]^{1/2}$$

where

P = estimated standard deviation for a reduced datum

s = scaled output

h = number of days after most recent calibration

V = matrix product: $(s, s^3)\ R\ \begin{pmatrix} s \\ s^3 \end{pmatrix}$

Application of the results of this sensor measurement analysis program to estimation of random experimental errors and to measurement reliability is given in Appendix G.

REFERENCES

I-1. Rothman, D.: Random Walk Program for Measurements Analysis of Static Systems, RM-1119-351, Rocketdyne, a division of North American Rockwell, Canoga Park, California, 25 January 1965.

I-2. Rothman, D.: A Random Walk Model for Non-Uniform, One-Parameter, Static, Linear Measurement Systems, RR-59-47, Rocketdyne, a division of North American Rockwell, Canoga Park, California, 15 December 1959.

I-3. Rothman, D.: Gaussian Random Walk with Gaussian Measurement Errors, SORUM-63-9, Rocketdyne, a division of North American Rockwell, Canoga Park, California, 24 September 1963.

APPENDIX J

REFERENCES

1. NAS3-11191, "Space Storable Regenerative Cooling Investigation."
2. NAS9-9528, "Noncircular Orifice Holes and Advanced Fabrication Techniques for Liquid Rocket Injectors."
3. NAS3-12001, "Investigation of Gas-Augmented Injectors."
4. Falk. A. Y., NASA CR-120935, Space Storable Propellant Performance Study - Gas/Liquid Like-Doublet Injector Characterization, Final Technical Report, R-8973-1, Rocketdyne, a division of North American Rockwell, Canoga Park, California, October 1972.
5. NAS3-11199, "Space Storable Propellant Performance Study."
6. Contract FO4611-67-C-0081, Correlation of Spray Injector Parameters with Rocket Engine Performance, AFRPL-TR-68-147, June 1968.
7. Falk, A. Y., et al., NASA CR-72487, Space Storable Propellant Performance Study, Rocketdyne, a division of North American Rockwell, Canoga Park, California, November 1968.
8. Lambiris, S., L. P. Combs, and R. S. Levine: "Stable Combustion Processes in Liquid Propellant Rocket Engines," Combustion and Propulsion, Fifth AGARD Colloquim: High-Temperature Phenomenon, The MacMillan Co., New York, N. Y., 1962, pp 596-636.
9. Combs, L. P., NASA CR-114462, Liquid Rocket Performance Computer Model with Distributed Energy Release, Final Report, R-8888, Rocketdyne, a division of North American Rockwell, Canoga Park, California, June 1972.
10. Sutton, R. D.,and M. D. Schuman, "Liquid Rocket Combustion Analysis for Coaxial Jet Injection of Gas/Liquid Propellants," CPIA Publication 204, Vol. 1, 7th JANNAF Combustion Meeting, February 1971, p 511.
11. Pieper, J. L., L. E. Dean, and R. S. Valentine, "Mixture Ratio Distribution--Its Impact on Rocket Thrust Chamber Performance," J. Spacecraft Rockets, Vol. 4, No. 6, pp 786-789, June 1967.
12. Rupe, J. H., A Correlation Between the Dynamic Properties of a Pair of Impinging Streams and the Uniformity of Mixture-Ratio Distribution in the Resulting Spray, Progress Report No. 20-209, Jet Propulsion Laboratory, Pasadena, California, 28 March 1956.
13. Rupe, J. H., An Experimental Correlation of the Nonreactive Properties of Injection Schemes and Combustion Effects in a Liquid-Propellant Rocket Engine, Technical Report No. 32-255, Jet Propulsion Laboratory, Pasadena, California, 15 July 1965.
14. Riebling, R. W., "Criteria for Optimum Propellant Mixing in Impinging Jet Injection Elements," J. Spacecraft Rockets, Vol. 4, No. 6, pp 817-819, June 1967.
15. Wrubel, J. R., "Some Effects of Gas Stratification on Choked Nozzle Flows," AIAA Paper 64-266, 1964.

16. Rupe, J. H., The Liquid Phase Mixing of a Pair of Impinging Streams, Progress Report No. 20-195, Jet Propulsion Laboratory, Pasadena, California, 6 August 1953.

17. McDonald, A. T. and R. W. Fox, "An Experimental Investigation of Incompressible Flow in Conical Diffusers," International Journal of Mechanical Sciences, Vol. 8, pp 125-139, 1965.

18. Contract NAS7-304, Chamber Technology for Space Storable Propellants, 3rd Interim Report, Rocketdyne, a division of North American Rockwell, Canoga Park, California, May 1967, CONFIDENTIAL.

19. Pauckert, R. P., NASA CR-72705, Space Storable Regenerative Cooling Investigation, Rocketdyne, a division of North American Rockwell, Canoga Park, California, June 1970.

20. LAP 68-411 (RC): Static Pressure Measurement for Contract NASw-1229 Combustion Chamber, Rocketdyne, a division of North American Rockwell, Canoga Park, California, 19 August 1968.

21. Mehegan, P. F., et al., NASA CR-72703, Investigation of Gas-Augmented Injectors, Rocketdyne, a division of North American Rockwell, Canoga Park, California, September 1970.

22. NASA CR-72704, Space Storable Regenerative Cooling Investigation, Pratt & Whitney Aircraft, Florida Research and Development Center, West Palm Beach, Florida, October 1971.

23. Zajac, L. J., Correlation of Spray Dropsize Distributions and Injector Variables, R-8455, Rocketdyne, a division of North American Rockwell, Canoga Park, California, November 1971.

24. Ingebo, R. D., et al., Dropsize Distribution for Crosscurrent Breakup of Liquid Jets in Airstreams, NACA TN-4087, 1957.